Studies of Metamaterial Structures

by

Angela Demetriadou

Thesis submitted for the degree of
Doctor of Philosophy of the University of London
and the
Diploma of Imperial College London

Condensed Matter Theory Group
The Blackett Laboratory
Imperial College of Science, Technology and Medicine
London

January 2010

Abstract

Metamaterials have had a tremendous development in the past few years, since they can artificially show several novel electromagnetic properties (i.e. negative refraction, perfect lensing, cloaking). In this thesis, various metamaterial designs are studied, where several problems involving the behaviour of the structures are addressed, investigated and solutions are proposed. The first chapter serves as an introduction to metamaterials, by displaying a review of some of the important and pioneer ideas in the literature for this research field. The rest of the thesis is divided in three main parts, for three different metamaterial structures that are discussed.

In part I, wire-metamaterials are investigated, which simulate the electromagnetic behaviour of a low-density electron plasma. Spatial dispersion is a significant disadvantage of wire metamaterials. In this chapter, we investigate the effect of spatial dispersion between connected and non-connected wire-mesh metamaterials. Consequently, we propose two different ways to minimize spatial dispersion in wire metamaterials, by re-designing the unit cell and increasing either the capacitance or the inductance of the metamaterial system.

In the next part of this thesis, Swiss Roll metamaterials are investigated. Initially, the non-chiral Swiss Roll structure is studied numerically and compared with analytical work that is already discussed in the literature, where an excellent agreement was found. Then, the more complicated design of chiral Swiss Rolls is investigated initially analytically and then compared with numerical results, where a notable agreement was found as well. Furthermore, the chirality found for Swiss Rolls is significantly higher compared with other chiral metamaterials discussed in the literature, which allows for the wave polarization to rotate more than 90° in less than a wavelength.

Finally, in part III, high-dielectric spherically-shaped particles are investigated that behave as low-loss magnetic resonators though the excitation of their first magnetic

Mie mode. A double negative metamaterial is also proposed, by embedding the high-dielectric crystals in a wire-mesh metamaterial. In this way, the losses induced from conductor-based magnetic metamaterials (i.e. split-ring resonator) are minimized.

Contents

List of Figures

Acknowledgments

It is a pleasure to thank those who made this thesis possible.

This thesis would not have been possible without my supervisor Professor Sir John B Pendry, that through his Socratic questioning and discussions I managed to acquire a physical insight and knowledge on novel ideas, that 'subsumed' me in the magical world of metamaterials. Despite his pioneer work and novel ideas, that basically started this research field and gave him tremendous fame and popularity, he is always down to earth, kind and polite with everyone. Above all I would like to thank him for the financial support and valuable advices he gave me during the past three years, not only about research but for a professional career in general as well.

I would also like to thank Dr. Ben Wood, that I met at the beginning of my PhD, for the many invaluable discussions. I am also indebted to my many student colleagues for providing a fun environment in which to learn and grow: Sam, Wei Hsiung, David, Josh, Evgeni, Aimee and Miguel.

Away from the academia side, I am very grateful to my parents, for the emotional and financial support whenever I needed it. Last but not least, I would like to thank my sister Marina and Demetris for their kind hospitality, especially during the past three months.

Chapter 1

Introduction to Metamaterials

The electromagnetic properties of a homogeneous material in nature are determined by its molecular composition. The macroscopic electric and magnetic fields of a wave propagating in a material are recognized to be the averages of their microscopic fields [6]. Therefore, the electromagnetic behaviour of materials in nature is described by the electric permittivity (ε) and magnetic permeability (μ) parameters.

Recently, this idea was extended to a new class of artificial materials, 'metamaterial', whose sub-units are of a larger scale than molecular (i.e. figure 1.1). For frequencies where the wavelength is much larger than lattice constant of the artificial medium, the wave is too myopic to resolve the geometry of sub-units and therefore the field averages are related to the macroscopic fields [6]. Consequently, the macroscopic fields are related to each other by the macroscopic ε and μ, indicating that metamaterials can be replaced by a homogeneous medium of identical electromagnetic parameters. The electromagnetic parameters of metamaterials usually include description of anisotropic media, where ε and μ are tensor and dispersive quantities (i.e. the parameters are frequency dependent).

The macroscopic behaviour of metamaterials is governed by the geometry of subunits, which are usually composed from conducting materials. By specifically designing the sub-unit geometry, the macroscopic fields can be governed and therefore artificial media with novel electromagnetic properties can be manufactured, giving access to a new range of phenomena, such as negative refraction, perfect lensing and electromag-

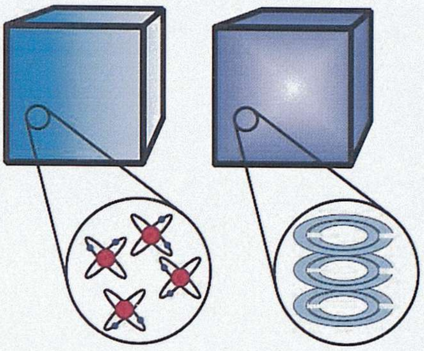

Figure 1.1: Material in nature are composed form molecules (left figure). Metamaterials are artificial media with specifically designed sub-units of several orders of magnitude higher than molecules [1]

netic cloaking.

1.1 Negative Refraction

Veselago in 1968 [7] realized that when a medium has both $Re(\varepsilon)$ and $Re(\mu)$ simultaneously negative, the real part of the refractive index is negative. The statement above can be explained by considering causality in real systems, which requires that both ε and μ to be dispersive with frequency and therefore $\varepsilon(\omega)$ and $\mu(\omega)$. Taking into account that real material are always slightly lossy, then we should consider a small positive imaginary part for $\varepsilon(\omega)$ and $\mu(\omega)$. Let us consider the refractive index formula: $n = \sqrt{\varepsilon\mu}$ which arises from Maxwell's equations. When the real parts of both $\varepsilon(\omega)$ and $\mu(\omega)$ are positive, the positive square root is chosen. For frequencies where $Re(\varepsilon) \rightarrow 0$, $\sqrt{\varepsilon}$ has a branch point. A solution can be found considering that causality force us to take a trajectory above the branch point, giving a positive imaginary solution for $\sqrt{\varepsilon(\omega)}$ when $Re(\varepsilon) < 0$ [1, 2]. Similarly for $Re(\mu) \rightarrow 0$, $\sqrt{\mu(\omega)}$ takes a positive imaginary solution. Therefore,

$$n = \begin{cases} +\sqrt{\varepsilon(\omega)\mu(\omega)} & \text{for } Re(\varepsilon) > 0 \text{ and/or } Re(\mu) > 0 \\ -\sqrt{\varepsilon(\omega)\mu(\omega)} & \text{for } Re(\varepsilon) < 0 \text{ and } Re(\mu) < 0 \end{cases} \tag{1.1}$$

Note that the imaginary and real parts of the tensors are related with each other with the Kramers-Kronig relations [8]. Therefore, it is clear that media with both $\varepsilon(\omega)$ and

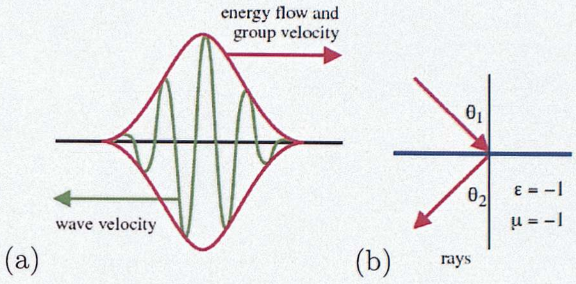

Figure 1.2: (a) A wave propagating in a negatively refractive medium, has the wave velocity and group velocity (i.e. energy) flow propagating in anti-parallel directions (b) A wave incident from a positive to a negative medium, is transmitted in to the negative medium with a negative angle (i.e. at the same side to the normal on the interface) [1]

$\mu(\omega)$ negative for the same frequency range, which are also dispersive and dissipative, show a negative refraction effect.

As Veselago pointed out in 1968 [7], negative refractive media bend the waves the wrong way and obey the left-handed rule. Despite Veselago pointed out the remarkable properties of negative materials, their absence in nature led to omit the subject until a decade ago, when Pendry proposed possible artificial structures for magnetic and consequently negative metamaterials [3, 9]. A negative metamaterial can be simply constructed by combining an electrical and a magnetic resonator with both $\varepsilon(\omega)$ and $\mu(\omega)$ negative for an overlapping frequency range, called doubly negative metamaterials (DNG). The realization of artificially negative structures was predicted theoretically and confirmed experimentally soon afterwards [3, 10]. For microwave frequencies, the most common example is the combination of a wire mesh metamaterial [11, 12, 13] and split-ring resonators [9]. The wire-mesh behaves as a low-density electric plasma with the plasma frequency in the GHz range (explained in greater detail in part I). Split-ring resonators have a magnetic behaviour since they macroscopically look like 'magnetic monopoles' oscillating along them (more detailed discussion in part II). This is a big advantage for magnetic metamaterials, since the magnetic behaviour of most materials in nature tails off at higher frequencies (usually limited to low microwave frequencies). The frequency limit of metamaterials, where the homogenization model

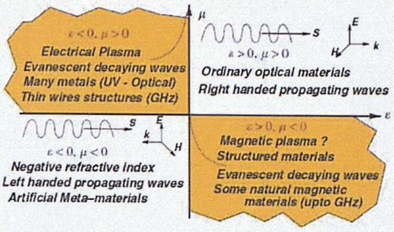

Figure 1.3: Classification of media depends on the sign of $Re(\varepsilon)$ and $Re(\mu)$ [2]

holds, is dependent on the manufacturing process limitations and the behaviour of the conducting elements the sub-units are composed of, at high frequencies.

Waves propagating in a negatively refracting medium show unconventional behaviour. Consider Maxwell's equations,

$$\begin{aligned} \nabla \times \mathbf{E} &= i\omega\mu\mu_0\mathbf{H} \Rightarrow \mathbf{k} \times \mathbf{E} = \omega\mu\mu_0\mathbf{H} \\ \nabla \times \mathbf{H} &= -i\omega\varepsilon\varepsilon_0\mathbf{E} \Rightarrow \mathbf{k} \times \mathbf{H} = -\omega\varepsilon\varepsilon_0\mathbf{E} \end{aligned} \tag{1.2}$$

where $\mathbf{E}$ and $\mathbf{H}$ are the electric and magnetic fields of the form $exp(i\mathbf{kr} - i\omega t)$ (where $\mathbf{r} = x\hat{\mathbf{x}} + y\hat{\mathbf{y}} + z\hat{\mathbf{z}}$). It is easy to see that when both $Re(\mu)$ and $Re(\varepsilon)$ are negative, then the three vectors $\mathbf{k}$, $\mathbf{E}$ and $\mathbf{H}$ obey a left-handed rule. Also note that in this case, the wavevector $\mathbf{k}$ and the Poynting vector ($\mathbf{S} = \mathbf{E} \times \mathbf{H}$) are anti-parallel (figure 1.2(a)). This basically means that the wave (i.e. wave velocity) and the energy of the wave travel in opposite directions [1]. Furthermore, negative refracting media show several interesting properties, which were predicted by Veselago in 1968 [7], such as a reversed Doppler shift and an obtuse angle for Cerenkov radiation. Finally, according to Snell's law, a medium with negative refractive index should refract light in the same side to the normal on the interface as the incident ray, as shown in figure 1.2(b).

Materials can be classified according to the sign of their electromagnetic parameters, since waves behave differently for materials in different sections of figure 1.3. For ordinary optical materials, both $Re(\varepsilon)$ and $Re(\mu)$ are positive where the right-handed rule is obeyed and waves are allowed to propagate in the medium. When both $Re(\varepsilon)$ and $Re(\mu)$ are negative, then the material has a negative refracting index and consequently a reversed Doppler shift, $\mathbf{S}$ and $\mathbf{k}$ are anti-parallel and waves propagating in a negative medium obey the left-handed rule. Only artificial media can support these

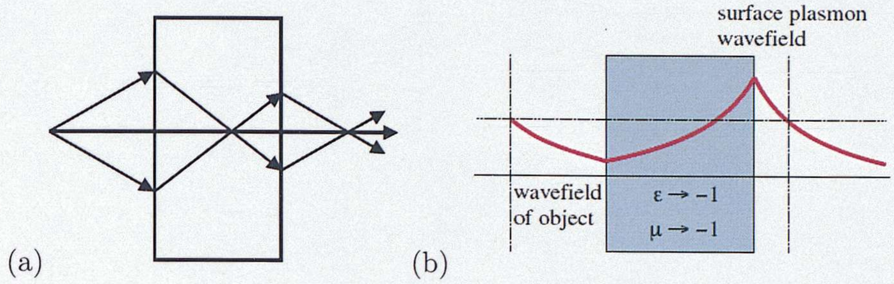

Figure 1.4: (a) Propagating waves focus inside and outside of the negative slab [3] (b) Evanescent waves are amplified inside the negative slab [1]

properties (i.e. metamaterials). Finally, when either $Re(\varepsilon)$ or $Re(\mu)$ are negative, then no wave can propagate in the medium since $\mathbf{k}$ is imaginary. However, evanescent waves exist that are confined at the interface between the two media and decay rapidly.

1.2 Perfect Lensing

In conventional lenses, the image resolution is limited by the wavelength of the incident light, since only the propagating waves can be focused. However, a flat slab of a material with $\varepsilon = -1$ and $\mu = -1$ (i.e. $n = -1$ and $Z = 1 = Z_0$, where Z_0 is the vacuum impedance) focuses both propagating and evanescent waves (i.e. near field). Evanescent waves are confined at the interface between negative and positive media, and decay rapidly. However, inside the negatively refracting slab, the near field is enhanced due to surface modes that exist at the interface, and both the near and far fields are focused as shown in figure 1.4. These lenses are called *super-lenses*. The resolution of super-lenses is limited only from our manufacturing capabilities [3, 14, 2]. Flat super-lenses give an image of the same order as the object. In order to magnify the near-field image created at the focal point, a cylindrical negative lens has to be used as discussed in [14, 15, 16].

A negative slab can also be considered as *optical anti-matter*, in the sense that it cancels out the propagation of a wave though an equally sized positive slab. The scattering, phase and evanescent wave amplitude changes of a wave propagating in a positive medium, are cancelled out by the propagation of the wave in the negative

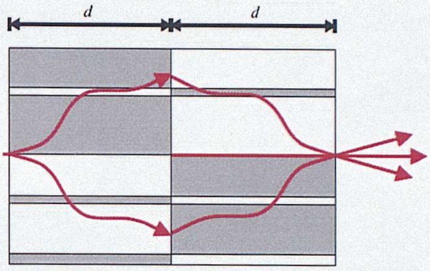

Figure 1.5: The changes on a wave (scattering, phase and amplitude of evanescent waves) imposed by vacuum (white area), are cancelled by the negative slab with $n = -1$ (grey colour) [1].

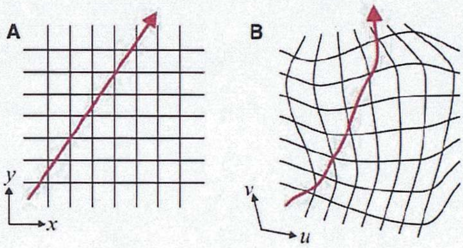

Figure 1.6: (left)The free space field line (red line) in a Cartesian coordinate grid. (right)Distorted field line (red line) in distorted coordinates. The red lines represents either **D**, or **B** fields, or Poynting vector and is equivalent to the path of a ray of light [4].

space as shown in figure 1.5 [2, 14].

1.3 Optical Transformations-Electromagnetic Cloaking

Few years ago, Pendry *et.al.* [4] proposed a theoretical way to control electromagnetic waves around an object (i.e. cloaking an object), based on coordinate transformations of Maxwell's equations. He basically suggested to open a hole in the Cartesian coordinate space, in which any object could be concealed.

For a space where there is no medium (i.e. figure 1.6-left), we can write the empty-space Maxwell equations for Cartesian coordinates. Then, a transformation can be performed on Maxwell equations creating a different coordinate system, where the

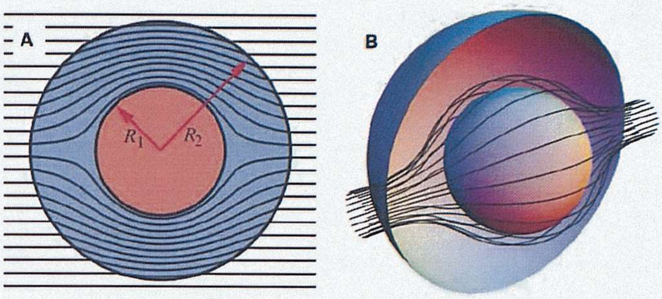

Figure 1.7: The ray trajectories in a spherical cloak (left) two-dimensional cross-section of the system and (right) a three-dimensional representation of the same system. Rays emerge on the other side of the cloak undisturbed [4].

electromagnetic fields follow a different grid (i.e. figure 1.6-right) [4]. The distorted coordinate system can be specifically designed, such that in the Cartesian system a hole in space is induced and therefore a cloak is realized (i.e. figure 1.7) [4]. A cloak smoothly guides the incident rays around the object and the rays emerge on the other side as if they have passed through an empty volume of space (figure 1.7). Hence, an observer cannot see any distortion of the wave and therefore cannot see the object. Note that neither the propagating or evanescent waves see the concealed object for an ideal cloak.

Anisotropic electromagnetic parameters and $Re(n) < 1$ are required to observe this phenomenon, which is easily achieved with metamaterials. However, reaching extremely high or small values of ε or μ can be challenging. Pendry *et.al.* [4] also pointed out possible limitations, such as the singularity for the ray that is incident at the centre of the spherical cloak and the fact that such a cloak is operational for a single frequency. Shortly after Pendry's realization of a cloaking device, Schurig *et.al* [17] tested this idea experimentally in microwave frequencies and managed to 'decrease scattering from the hidden object while at the same time reducing its shadow, so that the cloak and object combined began to resemble empty space'. Also, based on the same idea an acoustic cloak was suggested, where instead of the electromagnetic parameters, the mass density and bulk modulus are determined in order to achieve the minimization of acoustic scattering of an object in a shell [18]. Finally, metamaterials and transformation media can be used to guide electromagnetic waves through any desired route, which is an active and blooming research topic.

Part I

Wire Metamaterials

Chapter 2

Introduction

Generally, electron plasmas obey Drude's model, with the permittivity given by:

$$\varepsilon = 1 - \frac{\omega_p^2}{\omega(\omega + i\gamma)} \tag{2.1}$$

where ω is the frequency of the wave, ω_p the plasma frequency of the electron gas and γ accounts for losses (i.e. for electron plasmas in metals, resistive losses). The plasma frequency (ω_p) can be written in terms of the electron density (n_e), mass (m_e) and charge (e):

$$\omega_p^2 = \frac{n_e e^2}{\varepsilon_0 m_e} = (c_0 k_p)^2 \tag{2.2}$$

where k_p is the plasma wavevector associated with ω_p. Typically, the plasma frequency in metals is in the visible or ultraviolet (UV) region.

Artificial plasmas can be manufactured by thin conducting wires, which is a typical example of a negative permittivity metamaterial. This structure was initially proposed in the 1950's by Brown [19] and Rotman [20], but observed with a new light by Pendry *et.al.* [11, 12]. In order to tune ω_p in microwave frequencies, the electron density n_e needs to be reduced or/and the electron mass m_e to be increased. Wire metamaterials can achieve both, since electrons are constrained to move only inside the wires (i.e. reduce electron density) and the large self-inductance of thin wires enhances the effective electron mass.

In this part of the thesis, wire metamaterials are discussed and is organized as: In chapter 3, the simpler case of thin-parallel wires is discussed, which has already been thoroughly investigated in the literature [5, 21, 22, 23, 24, 25], by presenting numerical and analytical results for the band structure and S-parameters. In chapter 4, wire-mesh metamaterials that have wires along the three orthogonal axes (connected and non-connected) are investigated, by calculating analytically and numerically the dispersion diagrams.

In chapter 5, the problem of spatial dispersion in wire metamaterials that spoils the simple plasma model is explained, by discussing its origination and impact on the behaviour of wire metamaterials. The permittivity tensors are derived, which are dependent on the spatial wavevector. Also, the S-parameters for semi-infinite and finite slabs of parallel and wire-mesh metamaterials are obtained analytically and plotted with numerical results, where the problem of spatial dispersion is apparent. Finally, chapter 6 proposes two ways to minimize spatial dispersion in wire metamaterials, and new possible designs are examined numerically, showing significant minimization of spatial dispersion.

Chapter 3

Thin Parallel Wires

Consider a structure composed of thin-parallel perfectly conducting (PEC) wires of radius r_0 arranged in a square lattice of a and aligned with the z-axes, as shown in figure 3.1. The polarization induced on the wires by applied E_x (or E_y) fields is negligibly small, which results to an insignificant conducting feature in the x-y plane. Therefore, the wave behaves as if it was propagating in vacuum or the dielectric hosting material. For applied E_z-fields (i.e. parallel to wires), the electrons in the wires are flowing up and down the conducting rods, simulating the electromagnetic behaviour of an electron plasma.

The electrons are constrained to move only inside the wires. Therefore, the effective electron density (n_{eff}) of the artificial plasma is reduced, since only a small part of the space is filled with conducting material [12] and depends on the volume fraction

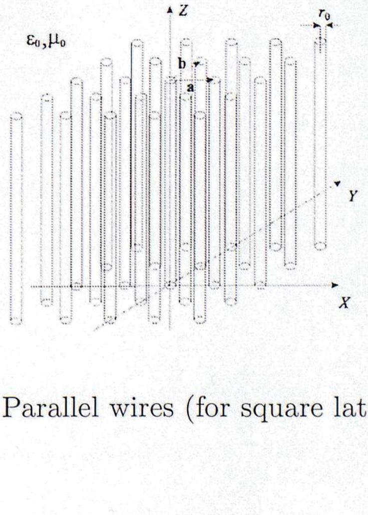

Figure 3.1: Thin Parallel wires (for square lattice a=b=a) [5]

occupied by the wires:

$$n_{eff} = n\frac{\pi r_0^2}{a^2} \tag{3.1}$$

where n is the density of electrons in the wires [11, 12]. A restoring force acting on the electrons has to work both against the rest mass of electrons and the high self-inductance of thin PEC wires. Therefore, considering self-inductance 'as a contribution to the electron mass' [11, 12], the effective electron mass (m_{eff}) is enhanced given by(derivation in Appendix A):

$$m_{eff} = \frac{\mu_0 e^2 r_0^2 n}{2}\left[\ln\left(\frac{a}{2\pi r_0}\right) + F(x)\right] \tag{3.2}$$

where $F(x)$ accounts for contributions from neighbouring wires and for a square lattice $F(x=1) = 0.5275$, (where x =a/b, and a, b are defined in figure 3.1) [5]. Substituting n_{eff} and m_{eff} in (2.2), the plasma frequency for thin parallel-wire structures arranged in a square lattice is given by:

$$\omega_p^2 = (c_0 k_p)^2 = \frac{2\pi c_0^2}{a^2(\ln(\frac{a}{2\pi r}) + 0.5275)} \tag{3.3}$$

This metamaterial can be thought of as an anisotropic low-density artificial plasma with plasma frequency in the GHz range, significantly lower than naturally occurring electron plasmas that usually have ω_p in the UV or visible region.

3.1 Band Structure

The dispersion equations of the parallel-wire metamaterial shown in figure 3.1 are derived analytically (in Appendix B), by considering the averaged electric field over a unit cell ($\overline{E_z}$) and the fluctuation of the electric field across the unit cell ΔE_z (i.e. from the edge of the unit cell until the surface of the wire). The difference $\overline{E_z} - \Delta E_z$ gives the electric field in the wire, which is zero since the wires are made of a PEC material. By solving this equation, it was found that the parallel-wire metamaterial supports three different types of modes [5, 22, 23], which are classified according to their field configuration.

For the case where both the wavevector and the electric field are in the xy-plane and perpendicular to each other (and perpendicular to wires), the transverse electric

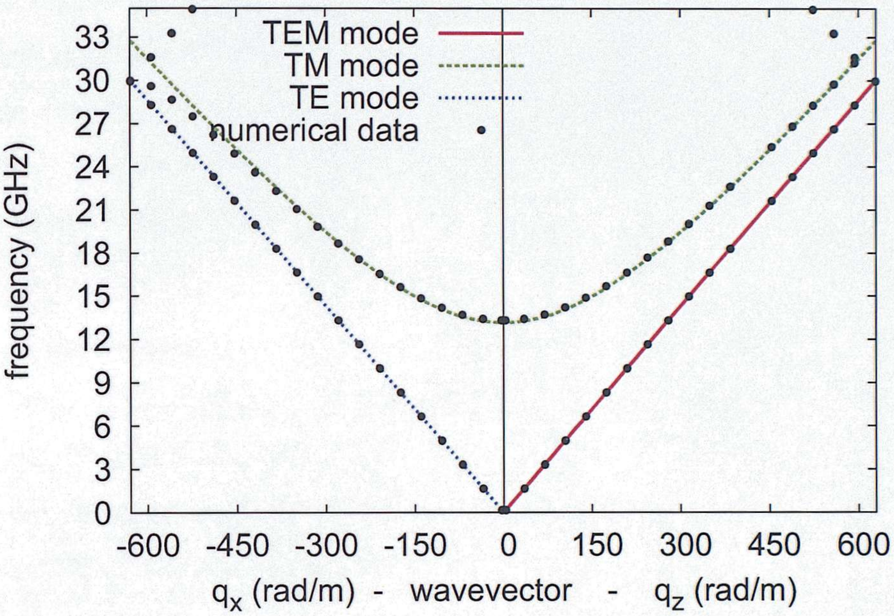

Figure 3.2: The band structure for the thin-parallel-wire medium with the wires along the z-axis. The simulations measurements (dots), the theoretical prediction (as discussed in section 3.1) for the TE mode (dotted blue line), the longitudinal (TM) mode (dashed green line) and the TEM mode (full red line) are plotted for $r/a = 0.01$: (Wire's radius)/(lattice constant). Note that the left part of the figure is a plot for the wavevector across the wires (i.e. along the x-axes) and the right part for the wavevector along the wires (i.e. along the z-axis).

(TE) mode is excited and is given by:

$$\omega = c_0 k_0 = c_0 \sqrt{\frac{q_x^2 + q_y^2}{\varepsilon_{host}}} \tag{3.4}$$

where ε_{host} is the dielectric constant of the hosting material the wires are impended in (in this report vacuum is considered and $\varepsilon_{host} = 1$).Therefore, for q_{xy}-propagation (i.e. $q_z = 0$), the TE mode behaves, as if it was travelling just in the hosting medium, since there is no interaction with the extremely thin wires.

When the wavevector is parallel to the electric field (i.e. $\mathbf{q} \parallel \mathbf{E}$) and $E_z \neq 0$, currents are induced on the wire, and the longitudinal or transverse magnetic (TM) mode is excited and given by:

$$\omega = c_0 \sqrt{q^2 + k_p^2} \tag{3.5}$$

where q is the wavevector in the wire medium, and k_p is the wavevector corresponding to ω_p. At $\omega < \omega_p$, the wave cannot propagate in the metamaterial, and becomes evanescent. Note that the dispersion is independent of the direction of $\mathbf{q}$.

Finally, for q_z-propagation the transmission-line mode or transverse electric and magnetic (TEM) mode is excited and given by:

$$\omega = c_0 q_z \tag{3.6}$$

Although the electric field parallel to the wires is zero ($E_z = 0$), the current in the wires is nonzero. This mode corresponds to the case where $(k_0^2 - q_z^2)$ in (B.14) is zero. The wavevector in the x-y plane can take arbitrary values and is in plane with the electric field. This mode has plane wave solutions for Maxwell equations for all frequencies [5]. These modes travel with the speed of light along the direction of the wires, with no restrictions for the components of the wavevector in the x-y plane. Belov *et.al.* [24, 25] propose sub-wavelength information transferring from one xy-surface to another with the speed of light, a process named 'canalization'.

Summarizing, for q_z-propagation the TM and TEM modes are expected to be excited and for q_x-propagation the TE and TM modes. In figure 3.2, dispersion equations (3.4), (3.5) and (3.6) are plotted with lines for q_x- (left) and q_z-propagation (right) for a structure of $(r_0/a) = 0.01$. Numerical results were calculated using CST

Microwave Studio for both propagation directions and are also plotted in figure 3.2 with black dots for comparison with the analytic work. The TM-mode disperses for $\omega > \omega_p$, TE and TEM modes are degenerate with the light line as expected. However, note that for a hosting medium with $\varepsilon_{host} \neq 1$, the TE mode is no longer degenerate with the light line, while the TEM mode continues to travel with the speed of light [24, 25]. The analytical prediction for the electromagnetic behaviour of the parallel-wire metamaterial agrees perfectly with numerical results. The slight disagreement at $\sim 30GHz$ is due to the band-gap at the Brillouin zone that the analytical work cannot predict, since at these frequencies the homogenization model breaks.

Chapter 4

3D Wire-Mesh Metamaterials

The parallel-wire metamaterial is an anisotropic structure. An isotropic artificial plasma can be realized by considering a metamaterial with wires along the three orthogonal axes, either connected or non-connected. (figures 4.1 and 4.6 respectively). Since only the wires parallel to the electric field are active and contribute to the plasma behaviour of these structures, these metamaterials are expected to simulate the properties of an isotropic low-density electron plasma with plasma frequency given by (3.3).

In this chapter, both configurations of wire-mesh (connected and non-connected) are discussed, by deriving the dispersion equations analytically and comparing the results with numerical calculations.

4.1 Band Structure

In an ideal naturally occurring electron plasma, radiation disperses with two degenerate transverse modes:

$$\omega = c_0\sqrt{q^2 + k_p^2} \tag{4.1}$$

and a dispersion-less longitudinal mode as

$$\omega = c_0 k_p \tag{4.2}$$

which are plotted in figure 4.2 with dotted and dashed lines respectively. Hence, an ideal artificial plasma should follow the same dispersion behaviour.

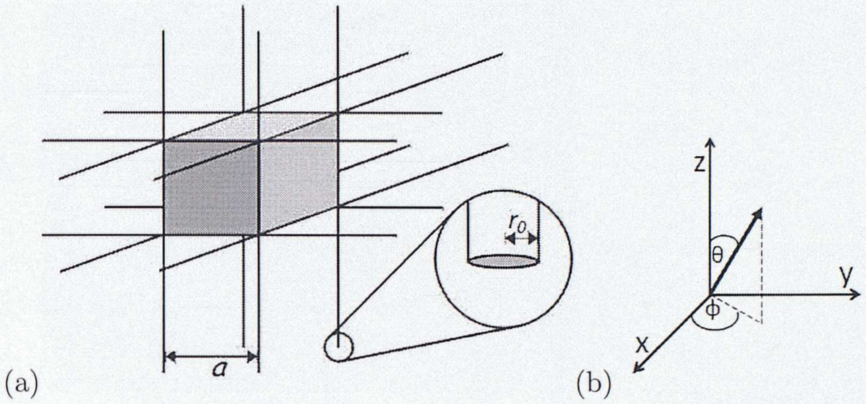

Figure 4.1: (a)3D-connected wire-mesh metamaterial, r_0 is the radius of the wires and a is the lattice constant (b) The wires are aligned with the three orthogonal axes. The translation from orthogonal to spherical coordinates is determined by angles θ and ϕ.

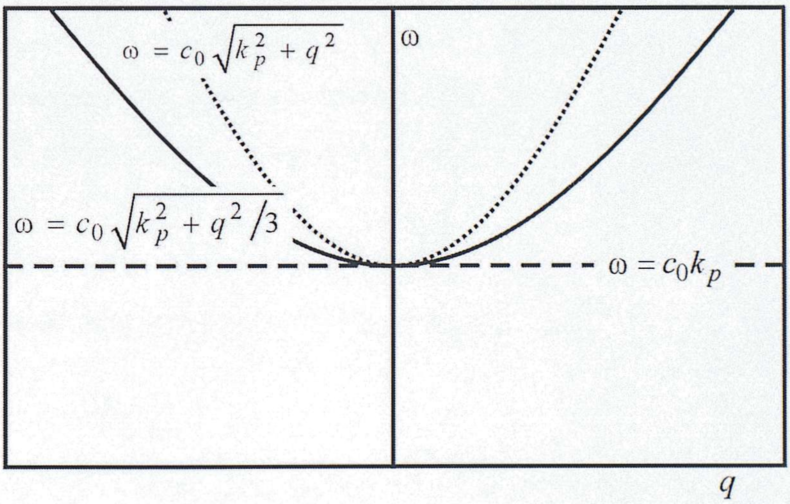

Figure 4.2: Comparison between the wire mesh band structure and the real electron plasma's band structure.

Using the same method as for the previous structure, the dispersion equations for wire-mesh metamaterials are derived in Appendix C, but taking into account the 3D symmetry of the structures. Assuming an electric field oscillating along the x-axes and no neighbouring wire effects, the averaged electric field over a unit cell $\overline{E_x}$ is given by:

$$\overline{E_x} = \left[i\omega\mu_0 j_{0x} - iq_x \frac{\mathbf{j_0} \cdot \mathbf{q}}{\varepsilon_0 \omega} \right] \frac{1}{(q^2 - k_0^2)a^2} \exp(iq_x x + iq_y y + iq_z z - i\omega t) \tag{4.3}$$

where a is the lattice constant, and the variation of electric field across the unit cell ΔE_x (i.e. the difference from the surface of the wire to the edge of the unit cell) is given by:

$$\Delta E_x = i\frac{2}{\pi}\sqrt{\frac{\mu_0}{\varepsilon_0}} \ln\left(\frac{a}{r_0\sqrt{\pi}}\right) \left[\frac{Cq_x - k_0^2 j_{0x}}{4k_0}\right] \exp(iq_x x - i\omega t) \tag{4.4}$$

where j_{0x} is the current induced on the x-wire, q is the wavevector inside the metamaterial and C a term associated with the charge accumulation on the wires (i.e. spatial dispersion). For simplicity a cylindrical unit cell is considered with radius $R_c = a/\sqrt{\pi}$, for the derivation of ΔE_x. Spatial dispersion arises from the periodic charge accumulation induced by longitudinal waves on the wires. Therefore, C takes different values for the connected and non-connected wire-mesh, since charge accumulated at a node, which brings to an electrical contact the three wires, is distributed evenly over the three wires, in contrary to the non-connected structure (discussed in more detail in chapter 5). Therefore, for the connected wire-mesh:

$$C = \frac{\mathbf{q} \cdot \mathbf{j_0}}{3} \tag{4.5}$$

and for the non-connected wire-mesh metamaterial:

$$C = \mathbf{q} \cdot \mathbf{j_0} \tag{4.6}$$

The difference $(\overline{E_x} - \Delta E_x)$ gives the electric field in the wires, which is zero for PEC wires. Therefore, by considering $(\overline{E_x} - \Delta E_x) = 0$, we derive:

$$\frac{\left[k_0^2 j_{0x} - q_x \mathbf{q} \cdot \mathbf{j_0}\right]}{q^2 - k_0^2} + \frac{k_0^2 j_{0x}}{k_p^2} - C\frac{q_x}{k_p^2} = 0 \tag{4.7}$$

The dispersion equations can be obtained by solving (4.7).

4.1.1 Connected Wire Mesh

The nodes of the connected wire-mesh structure in figure 4.1, bring to an electrical contact the three orthogonal wires. Therefore, the charge accumulated at the nodes can be distributed evenly over the three wires and C is given by (4.5). For the transverse modes, $\mathbf{q} \cdot \mathbf{j_0} = 0$ condition applies, and substituting (4.5) into (4.7), the dispersion equation for the transverse modes is obtained:

$$k_0^2 = q_T^2 + k_p^2 \Rightarrow \omega = c_0\sqrt{q_T^2 + k_p^2} \tag{4.8}$$

where q_T is the transverse wavevector. For the longitudinal mode, $\mathbf{q} \times \mathbf{j_0} = 0$ condition applies and the dispersion equation is given by:

$$k_0^2 = (q_L^2/3) + k_p^2 \Rightarrow \omega = c_0\sqrt{\frac{q_L^2}{3} + k_p^2} \tag{4.9}$$

where q_L is the longitudinal wavevector. Note, that the longitudinal and transverse modes must coincide at the plasma frequency as $q \rightarrow 0$ and that the wire-mesh medium supports only two different types of modes, in contrast to the parallel-wire medium that supports three different kind of modes. Note that in contrary to ideal plasmas that have a dispersion-less longitudinal mode, for the connected wire-mesh metamaterial disperses as in (4.9).

If there was no charge accumulation on the wires and $C = 0$, then the dispersion equation of the longitudinal mode would be:

$$k_0^2 = k_p^2 \Rightarrow \omega = c_0 k_p = \omega_p \tag{4.10}$$

which is a flat mode at the plasma frequency, identical to the behaviour of an ideal plasma. In figure 4.2, the band structure of an ideal plasma is plotted together with dispersion equations of (4.8) and (4.9). Note that although the transverse modes of the wire-mesh metamaterial and an ideal plasma follow identical dispersion, the longitudinal mode does not. It disperses with frequency due to charge accumulation on the wires. Electrons are constrained to flow inside the wires. Therefore, when a longitudinal wave is incident on the wire, charge is periodically accumulated on the wires, create a local electric fields opposing to the current flow associated with the plasma behaviour of the metamaterial. Hence, for larger wavevectors, more energy

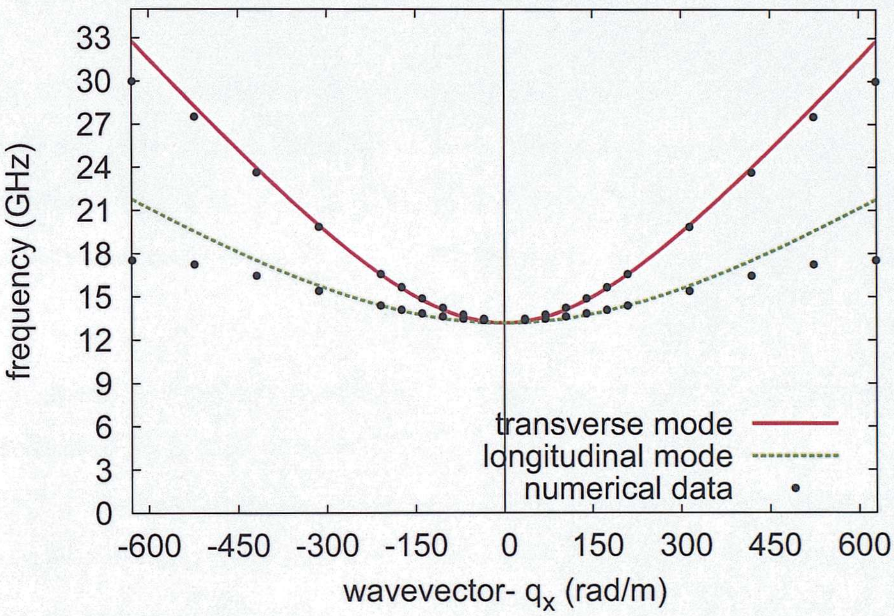

Figure 4.3: The band structure of the wire mesh for propagation along one of the wires. The simulation measurements (dots), the theory predictions for the transverse mode (full red line), the longitudinal mode (dashed green line) and the light line (dotted line) are shown for $r/a = 0.01$: (wire's radius)/(lattice constant)

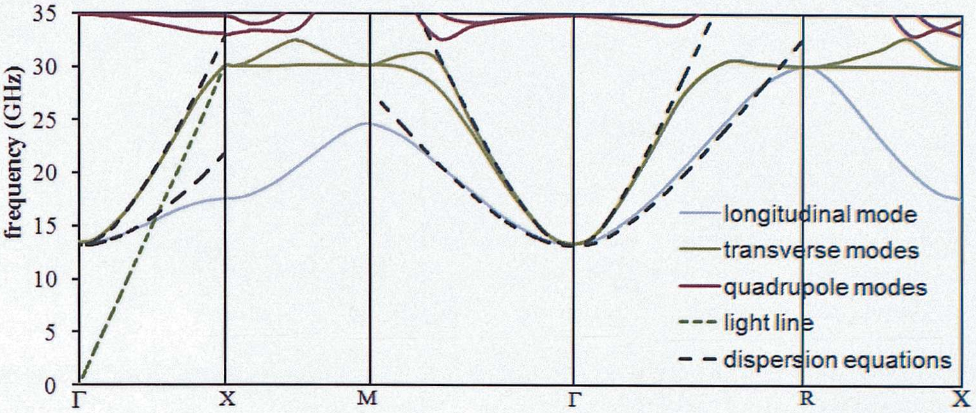

Figure 4.4: The band structure of a 3D connected wire-mesh metamaterial, with dimensions $r : a = 0.01 : 1$ where r is the radius of the wires and a the lattice constant, for propagations $\Gamma(0, 0, 0)$, $X(0, 0, \pi/a)$, $M(0, \pi/a, \pi/a)$ and $R(\pi/a, \pi/a, \pi/a)$. Numerical results are shown with solid coloured lines and analytical results with dashed black lines.

needs to be spend to drive the electrons in the wire, causing the longitudinal mode to disperse with frequency (more details in Chapter 5).

Using CST Microwave Studio, the band structure of the connected wire-mesh was derived numerically and is plotted with dispersion equations (4.8) and (4.9) in figure 4.3 for propagation along one of the wires (i.e. q_x-propagation). Note that for q_x-propagation, there are two degenerate transverse modes and a slower longitudinal mode. The agreement between numerical and analytical results is significant ($\sim 99\%$)

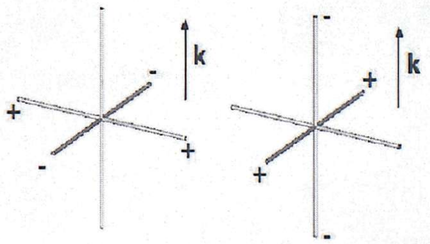

Figure 4.5: The arrangement of charge for the two degenerate quadrupole modes (a) transverse and (b) longitudinal configurations.

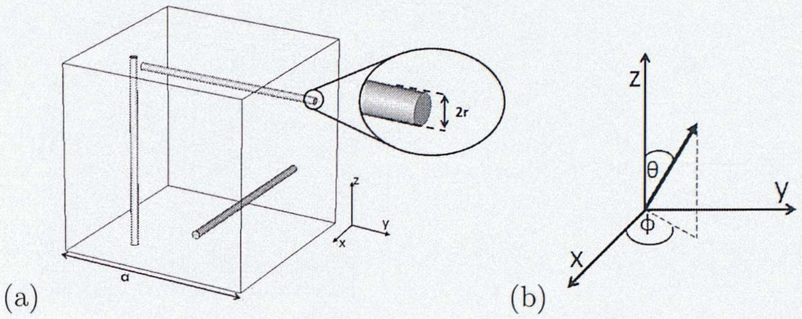

Figure 4.6: (a)3D non-connected wire-mesh metamaterial, where r_0 is the radius of the wires and a the lattice constant. (b) The wires are aligned with the three orthogonal axes, but not in an electrical contact. The translation from orthogonal to spherical coordinates is determined by angles θ and ϕ.

with a small difference at the Brillouin zone, where numerical calculations show a stop-band that the analytical model cannot predict, since it assumes a homogeneous medium. In figure 4.4, the band structure for the connected wire-mesh is shown for various propagation directions, obtained numerically (solid lines) and analytically from (4.8) and (4.9) (dashed black lines).

Furthermore, in figure 4.4, two degenerate flat modes can be seen at $\sim 35GHz$, which are identified as two quadrupole modes arising from the orthogonal nature of the structure and the electronic charge confinement. Note that only two independent quadrupole modes exist, whose electronic distribution is shown in figure 4.5. The loss of their degeneracy for large wavevector values, arises from the fact that one of them is polarized along the wavevector and the other one is not. A difference that becomes more apparent for larger wavevectors (i.e. smaller wavelengths), where the wave is able to resolve the polarization difference.

4.1.2 Non-Connected Wire Mesh

The dispersion equations for the non-connected wire-mesh metamaterial shown in figure 4.6(a) are derived using the same method as for the connected wire-mesh, but taking into account that the three orthogonal wires are not at an electrical contact. Hence, the charge accumulated on the wires cannot be distributed over the three wires.

Therefore, for non-connected wires, where $C = \mathbf{q} \cdot \mathbf{j_0}$, (4.7) can be solved for the transverse mode, where $\mathbf{q} \cdot \mathbf{j_0} = 0$. Therefore, the dispersion equation is given by:

$$k_0^2 = q_T^2 + k_p^2 \Rightarrow \omega = c_0\sqrt{q_T^2 + k_p^2} \tag{4.11}$$

where q_T is the transverse wavevector. For the longitudinal mode $\mathbf{q} \times \mathbf{j_0} = 0$ and the dispersion equation is given by:

$$k_0^2 = q_L^2 + k_p^2 \Rightarrow \omega = c_0\sqrt{q_L^2 + k_p^2} \tag{4.12}$$

where q_L is the longitudinal wavevector. Note that the longitudinal and transverse modes are degenerate. The longitudinal mode disperses over a broader frequency range for the non-connected compared with the connected wire-mesh, demanding approximately three times more energy for the current to overcome the local electric fields induced by charge accumulation. This indicates that spatial dispersion for non-connected wire-mesh is much more significant than for the connected wire-mesh, since the charge accumulated on the wires due to spatial dispersion cannot be distributed over the three wires.

Using CST Microwave Studio, the band structure was derived numerically (dots) and is plotted with the analytical predictions (solid line) of (4.11) and (4.12) in figure 4.7. The agreement between the results is extremely high, with insignificant difference at the Brillouin zone, where a stop-band appears for the transverse mode and the analytical model fails to predict. Comparing figures 4.3 with 4.7 and equations (4.9) with (4.12), it can be concluded that spatial dispersion for the connected wire-mesh is reduced by (1/3), which is in agreement with [26]. In this report, our aim is to design and investigate wire metamaterials that manage to eliminate spatial dispersion and exhibit a dispersion-less longitudinal mode. Therefore, the new proposed designs are all based on the connected wire-mesh structure, since this design already manages to confine the longitudinal dispersion by (1/3).

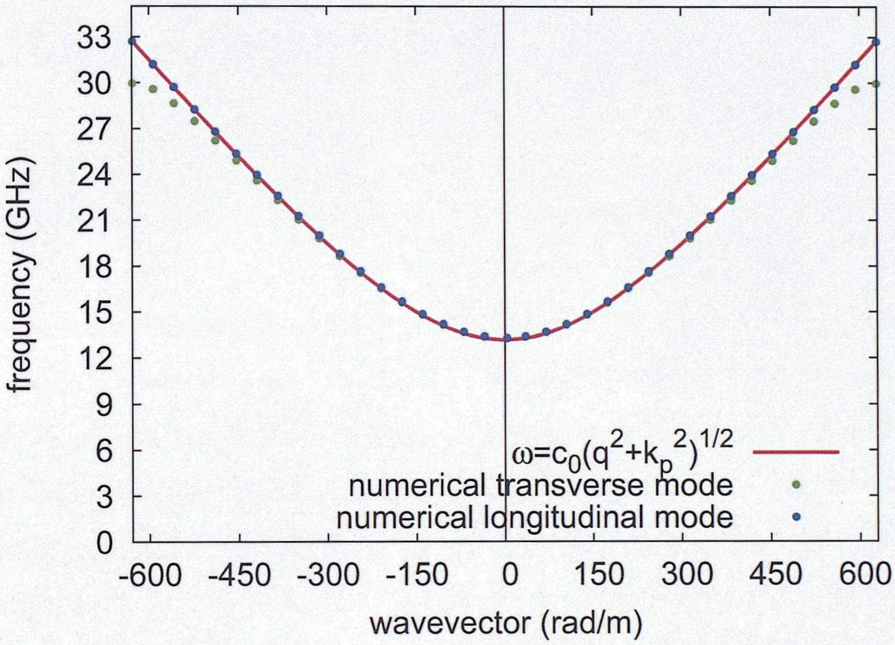

Figure 4.7: The band structure of the non-connected wire mesh metamaterial for propagation along one of the wires of dimensions $r_0 : a = 0.01 : 1$, where r_0 is the radius of the wires and a the lattice constant. The simulations measurements for the longitudinal (blue dots) and transverse modes (green dots) are plotted with analytical predictions (red solid line).

Chapter 5

Spatial Dispersion

The causality of metamaterials that imposes the frequency dispersion of media, usually results to local electromagnetic parameters as well. The non-local behaviour (i.e. spatial dispersion), is usually considered negligibly small for larger wavelengths (i.e. $\lambda \gg a$ - smaller wavevectors). It takes a meaningful sense for smaller wavelengths where $\lambda \rightarrow a$, and results to frequency dispersive electromagnetic parameters that are also dependent on the spatial derivatives of the fields (i.e. q). However, it is well known that spatial dispersion exists in wire metamaterials, even in the short wavevector limit [5], which spoils the simple local model. According to the local model, the permittivity tensor for wire metamaterials obeys the Drude model:

$$\varepsilon(\omega) = 1 - \frac{\omega_p^2}{\omega^2 + i\gamma\omega} \tag{5.1}$$

where ω_p is the plasma frequency and γ accounts for conductivity losses of wires. Unfortunately, this is not the case, since spatial dispersion that induces a spatial wavevector dependence for the permittivity tensor, is significant for both the long and short wavelength limit.

A longitudinal wave propagating along one of the wires (i.e. $\mathbf{q} \parallel \mathbf{E}$) induces periodic charge accumulation on the wire parallel to $\mathbf{q}$. Due to low capacitance of thin wires, the accumulated charge gives rise to strong local electric fields that disturb the current flow in the wire, which is associated with the plasma-like behaviour of the metamaterial. Therefore, the permittivity tensor is dependent on $\mathbf{q}$, in order to take into account the effect of spatial dispersion. However, transverse waves (i.e. $\mathbf{q} \perp \mathbf{E}$)

have no spatial wavevector dependence on the permittivity tensor, since there is no charge accumulation for $\mathbf{q}a \ll 1$ and therefore no spatial dispersion effect. Hence, the transverse permittivity tensor obeys the local-model of (5.1). As a result, two different permittivity tensors are needed to describe wire metamaterials, depending on wave polarization.

In this chapter, spatial dispersion is discussed for the thin-parallel-wire metamaterials (i.e. figure 3.1), the 3D-connected wire-mesh (i.e. figure 4.1) and briefly for the 3D-non-connected wire-mesh metamaterials (i.e. figure 4.6). The permittivity tensors are derived analytically for all three structures, where a dependence on the spatial wavevector is found for longitudinal waves. Furthermore, analytical reflection coefficients for semi-infinite and finite slabs are derived and plotted with numerical results, where the effect of spatial dispersion on scattering parameters is evidently spoiling the simple picture of a local-model.

5.1 Thin parallel wires

Consider the parallel-wire metamaterial shown in figure 5.1. Assume that the parallel wires of radius r_0 are made from a perfect electric conducting (PEC) material, placed in vacuum arranged in a square lattice of a and aligned with z-axes. When the structure is subjected to an electromagnetic field, an electric field is induced, driven by the current flow in the wire. The electric field averaged over the unit cell (i.e. derived in (B.9)) is given by:

$$\overline{E_z} = -\frac{i(k_0^2 - q_z^2)}{\omega\varepsilon_0(k_0^2 - q^2)} j_z \tag{5.2}$$

where $j_z = I exp(iq_x x + iq_y y + iq_z z - i\omega t)/a^2$ is the current flowing in the wire averaged over the unit cell. Approximate the cubical unit cell with a cylinder of radius $R = a/\sqrt{\pi}$ and the variation of the electric field from the surface of the wire to the edge of the cylindrical unit cell (i.e. derived in (B.13)) is given by :

$$\Delta E_z(r_0) = -\sqrt{\frac{\mu_0}{\varepsilon_0}} \frac{i(k_0^2 - q_z^2)}{k_0 k_p^2} j_z \tag{5.3}$$

If a new current source J_z is added, the mean electric field is given by:

$$\overline{E_z} = -\frac{i(k_0^2 - q_z^2)}{\omega\varepsilon_0(k_0^2 - q^2)} (J_z + j_z) \tag{5.4}$$

while $\Delta E_z(r_0)$ remains unaffected. The electric field inside the wires $(E_z - \Delta E_z(r_0))$, has to be zero since PEC wires are considered. Therefore:

$$\begin{aligned} E_z - \Delta E_z(r_0) &= \left[-\frac{i(k_0^2 - q_z^2)}{\omega\varepsilon_0(k_0^2 - q^2)}(J_z + j_z)\right] - \left[-\sqrt{\frac{\mu_0}{\varepsilon_0}}\frac{i(k_0^2 - q_z^2)}{k_0 k_p^2} j_z\right] = 0 \\ \therefore -\sqrt{\frac{\mu_0}{\varepsilon_0}}\frac{i(k_0^2 - q_z^2)}{k_0}\left[\frac{J_z + j_z}{(k_0^2 - q^2)} - \frac{j_z}{k_p^2}\right] &= 0 \end{aligned} \tag{5.5}$$

The additional source affects only the longitudinal mode, which is given by setting the square brackets in the above equation to zero. Therefore, when the longitudinal mode is excited ($\therefore \mathbf{q} = q_z\hat{\mathbf{z}}$), the relation between the two sources is given by:

$$J_z = -j_z + j_z\left(\frac{k_0^2 - q_z^2}{k_p^2}\right) \tag{5.6}$$

Using the continuity equation ($\frac{\partial\rho}{\partial t} + \nabla\mathbf{J} = 0 \Rightarrow -i\omega\rho + iqJ = 0$) and from Maxwell's equations: $\nabla\mathbf{D} = \varepsilon\varepsilon_0\nabla\mathbf{E} + \nabla\mathbf{P} = \rho_{ext} \Rightarrow \varepsilon_0\nabla\mathbf{E} = \rho_{ext} + \rho_{pol}$ (where $\rho_{pol} = -\nabla\mathbf{P}$ is the charge density due to polarization $\mathbf{P}$ and ρ_{ext} is the charge density associated with J_z), then:

$$\begin{aligned} \varepsilon_{zz}(\omega, q_z) &= \frac{\nabla\mathrm{D}}{\varepsilon_0\nabla\mathrm{E}} = \frac{J_z}{J_z + j_z} \\ \therefore \varepsilon_{zz}(\omega, q_z) &= \varepsilon_0\left(1 - \frac{k_p^2}{k_0^2 - q_z^2}\right) \end{aligned} \tag{5.7}$$

The non-local behaviour of the parallel-wire structure results in a permittivity tensor dependent on the spatial component of the wavevector q_z, which is in agreement with the derivations in [5, 23]. Note that for $\varepsilon(\omega, q_z) = 0$, the dispersion equation of the longitudinal mode is obtained. The permittivity tensor along the x- and y-axes is $\varepsilon_{xx} = \varepsilon_{yy} = \varepsilon_0$, since the wires are extremely thin. Hence:

$$\overline{\overline{\varepsilon}}(\omega) = \varepsilon_0(\mathbf{xx} + \mathbf{yy}) + \varepsilon_{zz}(\omega, q_z)\mathbf{zz} \tag{5.8}$$

For the special case that $q_z = 0$ (i.e. TE mode excitation), (5.7) becomes identical to the the local model of (5.1) as expected, since spatial dispersion is negligible for transverse modes. For TEM mode excitation (i.e. $\omega = cq_z$), (5.7) becomes infinite and according to Belov *et.al.* [5], this singularity can be avoided by using: $\mathbf{E} = \overline{\overline{\varepsilon}}^{-1}\mathbf{D}$ to solve Maxwell's equations. Therefore, the solution to Maxwell equations describe a plane wave travelling with the speed of light at q_z-direction. The wavevector and the electric field in the xy-plane take arbitrary values, giving rise to 'canalization' [5].

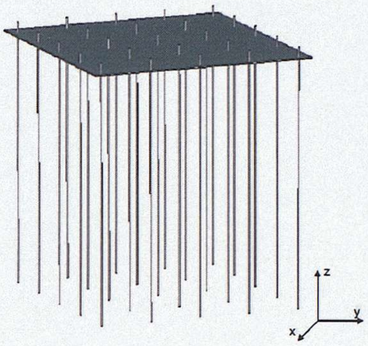

Figure 5.1: Semi-infinite slab of a parallel-wire structure

5.1.1 Scattering Parameters

The effect of spatial dispersion on the behaviour of the wire metamaterial is evident from S-parameter calculations. Initially, the simple local model is used to obtain analytically the reflection coefficient for a semi-infinite slab (as shown in figure 5.1), and is compared with calculations for the non-local model. The difference between the two results is significant, and is clear that the local model neglects to consider one of the propagating modes. Consequently, the non-local model is used to analytically derive the reflection coefficient for a finite-slab, and the results are in excellent agreement with numerical calculations.

Initially, consider a semi-infinite slab of the parallel-wire metamaterial and a surface at $z = 0$ as shown in figure 5.1. By matching the electric and magnetic fields at $z = 0$, the reflection coefficient is derived analytically (in Appendix D) and is given by:

$$R_{non-local} = \frac{q_z k_p^2 + q_x^2 q_z - k_0 k_p^2 - q_x^2 q_{2z}}{q_z k_p^2 + q_x^2 q_z + k_0 k_p^2 + q_x^2 q_{2z}} \tag{5.9}$$

where $q_{2z} = \sqrt{k_0^2 - k_p^2 - q_x^2}$. The non-locality of the medium is apparent, due to its dependence on the spatial wavevector component. The local reflection coefficient is given by:

$$R_{local} = \frac{q_z - q_{2z}}{q_z + q_{2z}} \tag{5.10}$$

which falsely assumes that only one mode is propagating through the medium. The local model leads to a paradox, where the current associated with just one mode excitation is not zero at surface $z = 0$. This is invalid, since the capacitance of thin

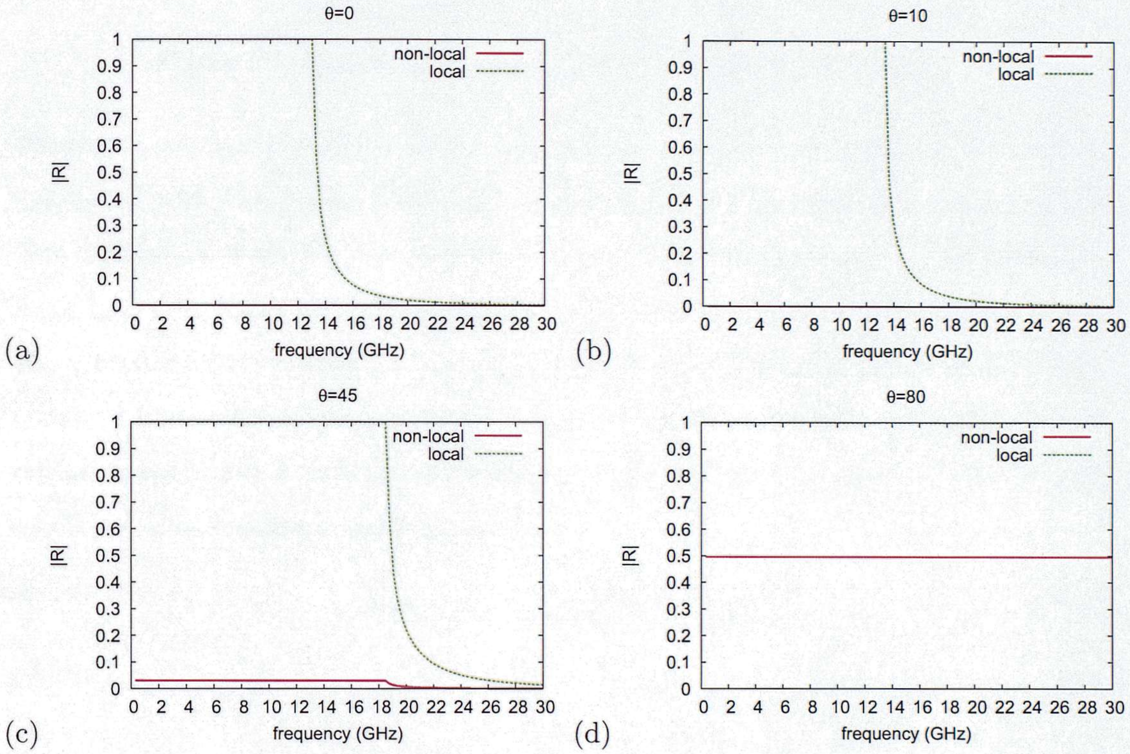

Figure 5.2: The analytic predictions for the reflection coefficient $| R |$ of a wave incident on a semi-infinite slab of a parallel-wire metamaterial are plotted for the local (green dashed line) and the non-local model (red solid line) (a)normal incidence - $\theta = 0°$ (b)$\theta = 10°$ (c)$\theta = 45°$ (d)$\theta = 80°$

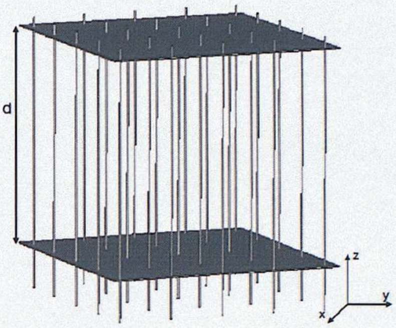

Figure 5.3: A finite slab of a parallel-wire medium of length d.

wires at a surface should be zero. However, non-locality accounts for the current associated with the second mode, which is opposite and equal to the current of the first mode, and therefore the paradox is overcame (more discussion in Appendix D). $R_{non-local}$ and R_{local} are plotted in figure 5.2 for various angles of incidence, where R_{local} predicts a stop-band for $\omega < \omega_p$, since it falsely neglects TEM mode excitation.

For a finite slab of the parallel-wire medium, as shown in figure 5.3, the non-local reflection coefficient is calculated by matching the electric and magnetic fields at both $z = 0$ and $z = d$ surfaces and is given by:

$$R_{non-local} = \frac{1 + A^2 - B^2}{1 + 2B - A^2 + B^2} \tag{5.11}$$

where

$$\begin{aligned} A &= \frac{i}{q_z(k_p^2 + q_x^2)} \left[\frac{k_0 k_p^2}{sin(k_0 d)} + \frac{q_x^2 q_{2z}}{sin(q_{2z} d)} \right] \\ B &= \frac{i}{q_z(k_p^2 + q_x^2)} \left[\frac{k_0 k_p^2 cos(k_0 d)}{sin(k_0 d)} + \frac{q_x^2 q_{2z} cos(q_{2z} d)}{sin(q_{2z} d)} \right] \end{aligned} \tag{5.12}$$

and $q_{2z} = \sqrt{k_0^2 - k_p^2 - q_x^2}$, k_0 is the wavevector of the incident wave and d is the length of the finite slab of the medium as shown in figure 5.3.

In figure 5.4, (5.11) is plotted for various angles of incidence (red solid line), together with numerical results (green dashed line) calculated with CST Microwave Studio [1]. A five-unit-cell slab (as shown in figure 5.3) was simulated for PEC wires of radius $r_0 = 0.05mm$, placed in vacuum and with lattice constant $a = 5mm$, giving an analytic prediction for the plasma frequency from (3.3) of $13.2GHz$.

---

[1] CST GmbH, Darmstadt, Germany

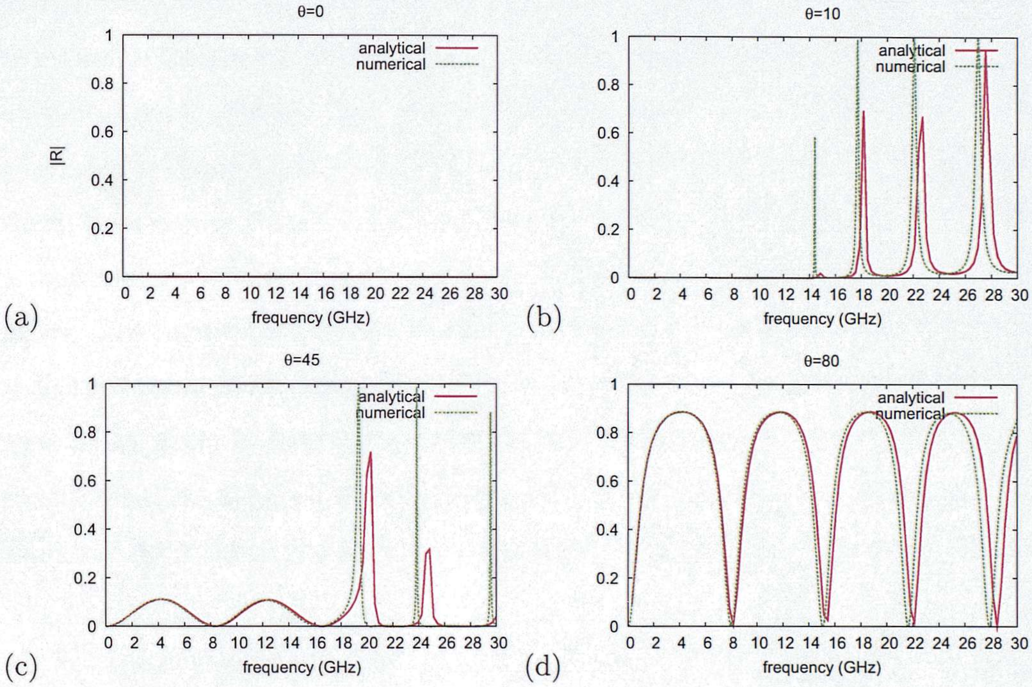

Figure 5.4: The reflection coefficient $\mid R \mid$ plotted with frequency, for a finite slab of a parallel-wire structure with $(r_0 : a) = 0.01 : 1$ for (a) normal incidence - $\theta = 0°$ (b)$\theta = 10°$ (c)$\theta = 45°$ (d)$\theta = 80°$.

For normal incidence (i.e. q_z-propagation), the wave is totally transmitted through the medium (i.e. $|R| = 0$) due to TEM mode excitation, since the electric field is always perpendicular to q_z and the wires. For 10° angle of incidence and $\omega < \omega_p$ just the TEM mode propagates through the medium, due to the stop-band of the longitudinal mode for $\omega < \omega_p$, and the wave is therefore totally transmitted through the metamaterial as well. For $\omega > \omega_p$, the strong internal reflection of the longitudinal mode induces sharp interference fringes, which are not equally spaced, since the longitudinal mode is not linearly dispersive with the frequency as predicted by (3.5). For 45° angle of incidence, interference fringes are observed for $\omega < \omega_P$ due to multiple reflections of TEM mode at the internal surfaces (i.e. Fabry-Perot interferometer). For $\omega > \omega_p$, a mixture of fringes is observed, due to Fabry-Perot interferences induced by TEM mode and sharp interference fringes induced by longitudinal mode. For 80° angle of incidence, a uniform interference pattern is observed, due to strong multiple scattering of TEM mode. The interference fringes are sharper compared with smaller angles of incidence, a characteristic of the Fabry-Perot interferometer, and are equally spaced indicating that TEM mode is linearly dispersive with the frequency, as predicted by (3.6). The longitudinal mode does not contribute to the interference pattern, although is excited, due to its decaying character in the whole range of frequencies at this angle of incidence.

For q_x-propagation (or 90° angle of incidence) and $E_z \neq 0$, only the transverse mode is excited, since q_x is always perpendicular to the electric field and $q_z = 0$. Therefore, the local model for the effective permittivity tensor holds and an analytical prediction for the transmission and reflection of the wave through a finite slab can be derived using the work in [3]:

$$\begin{aligned} T_S &= \frac{tt' exp(iq_x^{'}d)}{1 - r'^2 exp(i2q_x^{'}d)} \\ R_S &= r + \frac{tt'r' exp(i2q_x^{'}d)}{1 - r'^2 exp(i2q_x^{'}d)} \end{aligned} \tag{5.13}$$

where $q_x^{'} = i\sqrt{q_y'^2 - \varepsilon(\omega)k_0^2}$ is the z-component of the wavevector inside the metamaterial slab, $\varepsilon(\omega) = 1 - \omega_p^2/\omega$ and d is the length of the slab. For a medium with $\mu = 1$, the transmission and reflection at the first interface (t and r) of the slab and at the

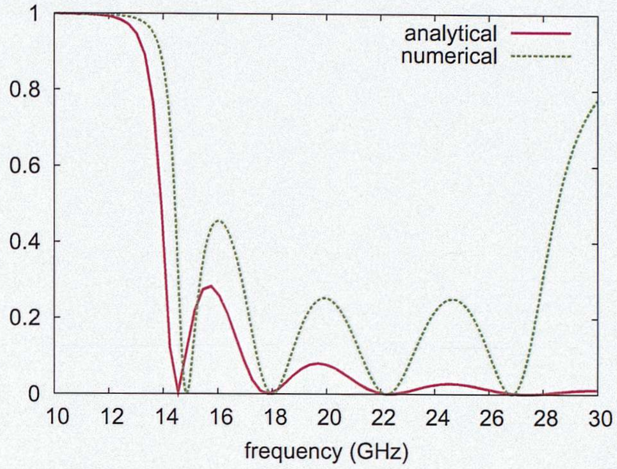

Figure 5.5: The reflection coefficient $| R |$ for parallel-wire metamaterials of radius $r_0 : a = 0.01 : 1$ and q_x-propagation (i.e. perpendicular to the wires). Analytical predictions (red solid line) for S-polarized waves given by (5.13) plotted with numerical calculations (green dashed line) for a five-unit-cell slab.

second interface (t' and r') are given by:

$$\begin{aligned} t &= \frac{2q_x}{q_x + {q'}_x} \\ r &= \frac{q_x - {q'}_x}{q_x + {q'}_x} \\ t' &= \frac{2{q'}_x}{q_x + {q'}_x} \\ r' &= \frac{{q'}_x - q_x}{q_x + {q'}_x} \end{aligned} \tag{5.14}$$

where q_x is the x-component of the wavevector in vacuum. In this case, the S-parameters show interference fringes due to multiple scattering of the transverse mode at the internal interfaces of the finite slab. In figure 5.5, the reflection coefficient of (5.13) (red solid line) is plotted with the numerical results (green dashed line) for a five-unit-cell slab (i.e. $d = 5a$) consisted of parallel, PEC wires of radius $r_0 = 0.05mm$ and lattice constant $a = 5mm$, placed in a square lattice and embedded in vacuum. There is a stop-band for $\omega < \omega_p$, where the local model predicts $\varepsilon < 0$. Also, the agreement with numerical results is significant, confirming that the local model holds for transverse mode excitation and is in agreement with [27]. The difference of the analytic prediction and numerical results at higher frequencies (i.e. $\sim 30GHz$) is due to the band-gap of the transverse mode at Brillouin zone that the analytic work cannot predict.

5.2 Wire-Mesh Metamaterials

Similarly to parallel-wire metamaterials, the plasma behaviour of a wire-mesh is strongly dominated by spatial dispersion. Consider a wire-mesh made of PEC wires with radius r_0, placed in a lattice of a filled with vacuum. The mean electric field induced by an incident wave, averaged over the unit cell (is derived in (C.8)) and given by:

$$\overline{E_x} = \left[i\omega\mu_0 j_{0x} - iq_x\frac{\mathbf{j}_0\cdot\mathbf{q}}{\varepsilon_0\omega}\right]\frac{1}{(q^2-k_0^2)a^2}\exp(iq_xx+iq_yy+iq_zz-i\omega t) \tag{5.15}$$

where $\mathbf{j}_0$ is the current flowing in each unit cell and j_{0x} the current flowing along the wire aligned with the x-axes. Assuming a cylindrical unit cell of radius $R = a/\sqrt{\pi}$, the difference of the electric field from the surface of the wire to the edge of the unit cell (derived in (C.13)) is given by:

$$\Delta E_x = \frac{i}{k_p^2a^2}\left[C\frac{q_x}{k_0} - \frac{k_0^2 j_{0x}}{k_0}\right]\sqrt{\frac{\mu_0}{\varepsilon_0}}\exp(iq_xx+iq_yy+iq_zz-i\omega t) \tag{5.16}$$

where $k_p^2 = \frac{2\pi/a^2}{ln\left(\frac{a}{r_0\sqrt{\pi}}\right)}$ is the plasma wavevector and C is given from (4.5) and (4.6) for the connected and non-connected wire mesh metamaterials respectively. Adding a new source $\mathbf{J}_0$, (5.15) becomes:

$$\overline{E_x} = \left[i\omega\mu_0(j_{0x}+J_{0x}) - iq_x\frac{(\mathbf{j}_0+\mathbf{J}_0)\cdot\mathbf{q}}{\varepsilon_0\omega}\right]\frac{1}{(q^2-k_0^2)a^2}\exp(iq_xx+iq_yy+iq_zz-i\omega t) \tag{5.17}$$

The difference $(E_x - \Delta E_x)$ gives the electric field inside the wires, which is zero since the wires are made of a PEC material, and therefore:

$$\overline{E_x} - \Delta E_x = \frac{i\omega\mu_0(j_{0x}+J_{0x}) - iq_x\frac{(\mathbf{j}_0+\mathbf{J}_0)\cdot\mathbf{q}}{\varepsilon_0\omega}}{(q^2-k_0^2)a^2} - \left[\frac{i}{k_p^2a^2}\left(C\frac{q_x}{k_0} - \frac{k_0^2 j_{0x}}{k_0}\right)\sqrt{\frac{\mu_0}{\varepsilon_0}}\right] = 0 \tag{5.18}$$

5.2.1 Connected Wire-Mesh

For connected wire-mesh metamaterials, as shown in figure 4.1, $C = \mathbf{q}\cdot\mathbf{j}_0/3$. Substituting this into (5.18) and considering q_x-propagation for simplicity, then for the longitudinal mode for which $\mathbf{q} = q_x\hat{\mathbf{x}}$, $\mathbf{J}_0 = J_{0x}\mathbf{q}$ and $\mathbf{j}_0 = j_{0x}\mathbf{q}$, (5.18) becomes:

$$\frac{i}{a^2k_0}\sqrt{\frac{\mu_0}{\varepsilon_0}}\left[\frac{(k_0^2-q_x^2)(J_{0x}+j_{0x})}{(q^2-k_0^2)} - \frac{(q_x^2-3k_0^2)j_{0x}}{3k_p^2}\right] = 0 \tag{5.19}$$

When the square brackets are equal to zero, the relationship between the J_{0x} and j_{0x} sources is:

$$\therefore J_{0x} = -j_{0x}\left(\frac{q_x^2 - 3k_0^2 + 3k_p^2}{3k_p^2}\right) \tag{5.20}$$

Again, using the continuity equation ($\frac{\partial\rho}{\partial t} + \nabla\mathbf{J} = 0$) and Maxwell's equations (i.e. $\nabla\mathbf{E} = \rho_{ext} + \rho_{pol}$, where $\rho_{pol} = -\nabla\mathbf{P}$ and ρ_{ext} is associated with $\mathbf{J_0}$), the longitudinal permittivity tensor is given by:

$$\varepsilon_L = \frac{\nabla\mathbf{D}}{\nabla\mathbf{E}} = \frac{J_{0x}}{J_{0x} + j_{0x}} = \varepsilon_0\left(1 - \frac{3k_p^2}{3k_0^2 - q_x^2}\right) \tag{5.21}$$

Note that for the zeros of (5.21), the dispersion equation for the longitudinal mode arises. A longitudinal wave induces periodic charge accumulation on the wires parallel to q, and due to the low capacitance of thin wires, strong local electric fields arise, disturbing the current flow associated with the plasma-like behaviour of the metamaterial. The strong local electric fields lead to a wavevector dependence for the longitudinal permittivity tensor.

The transverse mode is effectively described by the local-model (similarly to parallel-wire metamaterial), since charge accumulation and spatial dispersion are negligibly small. Therefore, the transverse permittivity tensor can be written as:

$$\varepsilon_T = \varepsilon_0\left(1 - \frac{k_p^2}{k_0^2}\right) \tag{5.22}$$

Summarizing, for the special case of a wave incident to the wire mesh structure along one of the wires (i.e. along the x-axes), the permittivity tensor is given by:

$$\overline{\overline{\varepsilon}}(\omega) = \varepsilon_{xx}\mathbf{xx} + \varepsilon_{yy}\mathbf{yy} + \varepsilon_{zz}\mathbf{zz} \tag{5.23}$$

where

$$\varepsilon_{xx} = 1 - \frac{3k_p^2}{3k_0^2 - q_x^2} \tag{5.24}$$

$$\varepsilon_{yy} = \varepsilon_{zz} = 1 - \frac{k_p^2}{k_0^2} \tag{5.25}$$

This equation suggests that for an incident wave on the wire mesh structure, both the longitudinal and the transverse modes are excited, but have different electromagnetic response, due to different permittivity tensors. A way to deal with this problem is to block the longitudinal mode from propagating in the metamaterial (i.e. flat mode), in order to have a structure that is effectively described only by the local model of ε_T and has a band structure identical to an ideal plasma behaviour.

5.2.1.1 Scattering Parameters

Similarly to parallel-wire metamaterials, the effect of spatial dispersion on the structure's behaviour is apparent from S-parameter calculations. Initially, the local model is used to obtain analytically the reflection coefficient for a semi-infinite slab, and is compared with calculations for the non-local model. The difference between the two results is evident, and is clear that the local model fails for larger angles of incidence, where the spatial component of the wavevector becomes more dominant. For a finite slab of the wire metamaterial, the S-polarized and P-polarized waves have different behaviour, since just the latter has a spatial wavevector component that excites the longitudinal mode. Therefore, by observing the difference of the reflection coefficient for the two polarizations the effect of spatial dispersion on the behaviour of the structure is evident, which basically shows the excitation and dispersion of the longitudinal mode.

Consider a P-polarized wave with wavelength $\lambda \gg a$, incident to a semi-infinite slab of a 3D-connected wire-mesh medium. The reflection coefficient can be calculated by matching the magnetic and electric fields at the surface of incidence (derived in Appendix E) and is given by:

$$R_{non-local} = \frac{q_z q_{Lz}(k_0^2 - k_p^2) - \left[q_{Tz} q_{Lz} k_0^2 + q_x^2 k_p^2\right]}{q_z q_{Lz}(k_0^2 - k_p^2) + \left[q_{Tz} q_{Lz} k_0^2 + q_x^2 k_p^2\right]} \tag{5.26}$$

where $q_{Lz}^2 = 3(k_0^2 - k_p^2) - (q_{Lx}^2 + q_{Ly}^2)$ is the z-axis component of the longitudinal wavevector and $q_{Tz}^2 = k_0^2 - k_p^2 - (q_{Tx}^2 + q_{Ty}^2)$ is the z-axis component of the transverse wavevector. The dependence of (5.26) on q_{Lz} takes into account the excitation of the longitudinal mode and the effect of spatial dispersion associated with it. However, if the longitudinal mode was dispersion-less (i.e. flat mode), then $q_{Lz} \to \infty$ and (5.26) reduces to:

$$R_{local} = \lim_{q_{Lz} \to \infty} R_{non-loc} = \frac{q_z \varepsilon(\omega) - q_{Tz}}{q_z \varepsilon(\omega) + q_{Tz}} \tag{5.27}$$

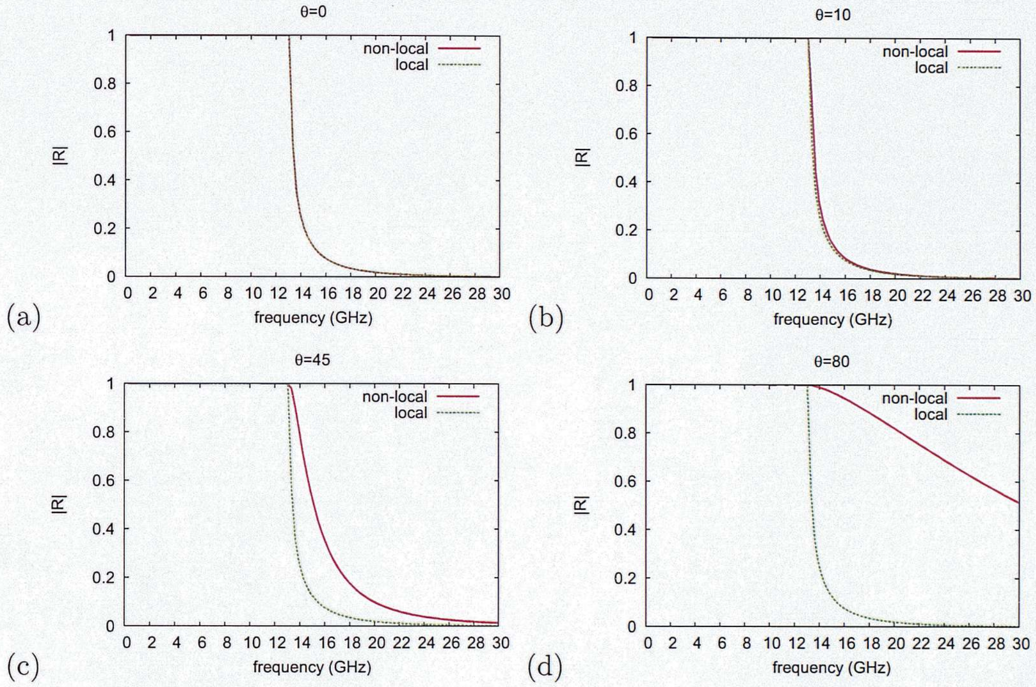

(a) (b) (c) (d)

Figure 5.6: The analytic predictions for the reflection coefficient $\mid R \mid$ of a wave incident on a semi-infinite slab of a 3D-connected wire-mesh metamaterial are plotted for the local (green dashed line) and the non-local model (red solid line) (a)normal incidence - $\theta = 0°$ (b)$\theta = 10°$ (c)$\theta = 45°$ (d)$\theta = 80°$.

where the local model is sufficient to describe the behaviour of the structure and therefore $\varepsilon(\omega) = \varepsilon_L(\omega) = \varepsilon_T(\omega) = 1 - \frac{k_p^2}{k_0^2}$. $R_{non-local}$ and R_{local} are plotted together in figure 5.6 with red solid and green dashed lines respectively. For small angles of incidence, the difference is small, since the component of the wavevector parallel to the electric field is small. However, for bigger angles the discrepancies become larger.

The reflection coefficient for S-polarized (green dashed lines) and P-polarized (red-solid lines) waves were calculated using CST Microwave Studio and are shown in figure 5.7 for various angles of incidence on a finite slab of five unit-cells (i.e. $d = 5a$). It is assumed that the wires are made from PEC material in vacuum. Due to the cut-off frequency at ω_p, it is expected that $|R| = 1$ for $\omega < \omega_p$. P-polarized waves excite both the longitudinal and transverse mode, since a component of the electric field and the wavevector are parallel, both with each other and one of the wires, taking into account non-locality of the metamaterial. S-polarized waves cannot excite the longitudinal mode in a wire-mesh structure, since the electric field is always perpendicular to the wavevector. Therefore, (5.13) expresses the reflection coefficient from a finite slab of a medium obeying the local model and is plotted in figure 5.7 with blue dotted line for comparison with the numerically derived S-polarized reflection coefficient.

For normal incidence, the longitudinal mode is not excited for neither S- or P-polarized waves, since there is no component of the electric field parallel to the wavevector for either polarizations. Therefore, $|R|$ is identical for both polarizations, as shown in figure 5.7(a) and also identical to figure 5.5, since the active wires are those only parallel to the electric field. Consequently, the electromagnetic behaviour of the structure for normal incidence is effectively described by the local model, and an analytic prediction is given from (5.13) and plotted in figure 5.7(a) (blue dotted line). However, for non-normal incidence, both the transverse and longitudinal modes are exited for P-polarized waves. For small angles of incidence, the excitation of the longitudinal mode appears as sharp resonances at $\sim 14GHz$. For larger angles of incidence, the excitation and dispersion of the longitudinal mode destroys the simple picture of the local-model interference pattern. Therefore, spatial dispersion is a problem that prevents the effective local homogenization of wire metamaterials with one simple local model.

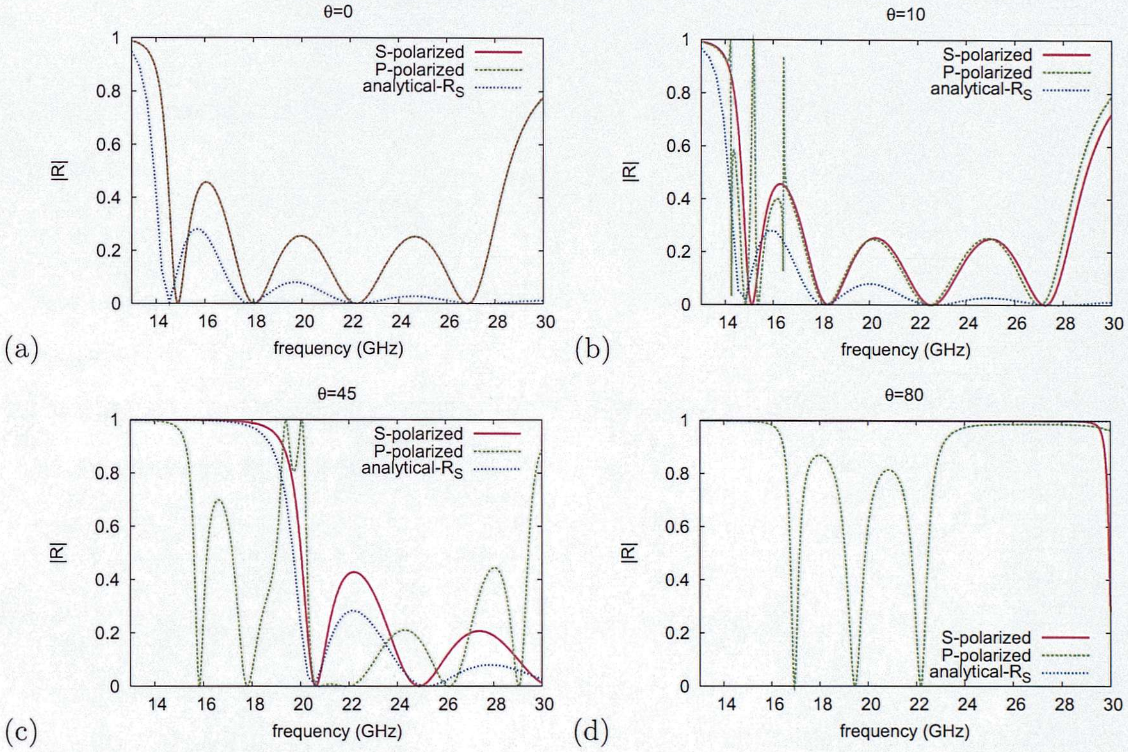

Figure 5.7: The modulus of the reflection coefficient for the connected wire-mesh metamaterial of $r_0 : a = 0.01 : 1$. Numerically calculated reflection coefficients for S-polarized (red solid lines) and P-polarized (green dashed lines) waves plotted with the analytical prediction for a local model (blue dotted line) of (5.13) (a) normal incidence -$\theta = 0°$ (b) $\theta = 10°$ (c) $\theta = 45°$, (d) $\theta = 80°$

5.2.2 Non-Connected Wire-Mesh

For non-connected wire-mesh metamaterials shown in figure 4.6, $C = \mathbf{q} \cdot \mathbf{j_0}$. Following the same derivation procedure as for the connected wire-mesh metamaterial, substitute C to (5.18) and consider q_x-propagation for simplicity. Therefore, the relationship between the J_{0x} and j_{0x} sources is:

$$J_{0x} = -j_{0x} \left(\frac{q_x^2 - k_0^2 + k_p^2}{k_p^2} \right) \tag{5.28}$$

Using the continuity and Maxwell's equations, the longitudinal permittivity tensor is given by:

$$\varepsilon_L = \varepsilon_0 \left(1 - \frac{k_p^2}{k_0^2 - q_z^2} \right) \tag{5.29}$$

Note that for the zeros of (5.29), the dispersion equation for the longitudinal mode arises.

Similarly to the connected wire-mesh metamaterial, the transverse mode is effectively described by the local-model, and therefore:

$$\varepsilon_T = \varepsilon_0 \left(1 - \frac{k_p^2}{k_0^2} \right) \tag{5.30}$$

Equation (5.23) suggests that the effect of spatial dispersion for the non-connected wire mesh is enhanced by a factor of (1/3). Since spatial dispersion arises due to the periodic charge accumulation on the wires, the difference can be recognized at the fact that the wires in the connected wire-mesh are at an electrical contact at nodes. Therefore, the charge is evenly distributed over the three wires at nodes, minimizing spatial dispersion.

For a finite slab of five-unit-cells of the non-connected wire-mesh, the reflection coefficients for S- and P-polarized waves were calculated numerically using CST Microwave Studio and plotted in figure 5.8. Also, an analytical prediction for S-polarized waves, calculated using (5.13), is plotted with the dotted line for comparison with numerical results. The excitation of the longitudinal mode, that is strongly reflected inside the finite slab, creates the sharp resonances seen for the P-polarized wave, even for small angles of incidence. The non-locality of the structure spoils the simple interference pattern of the reflection coefficient for higher angles of incidence. It is clear that

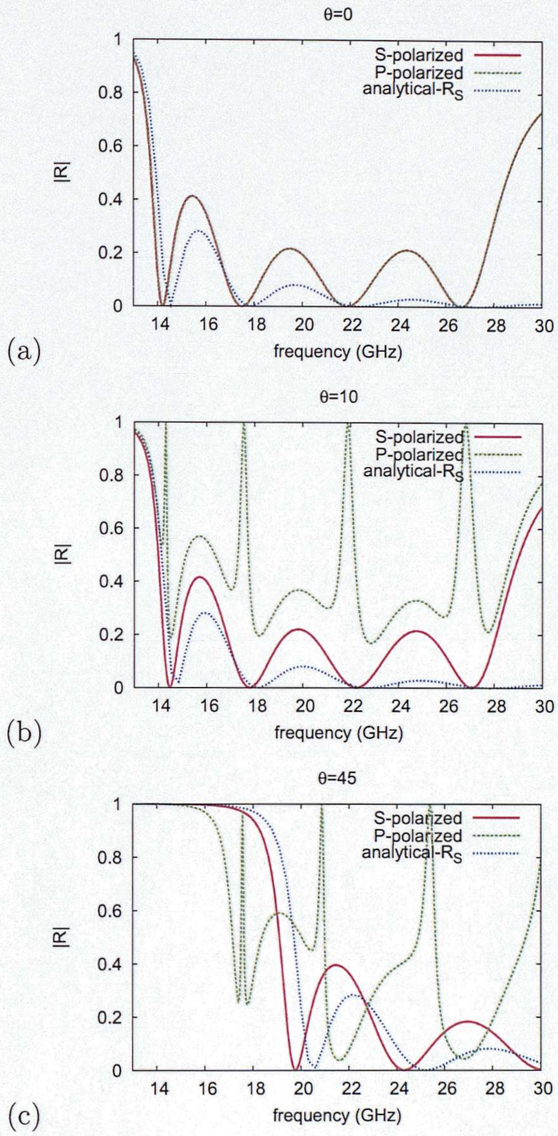

Figure 5.8: The modulus of the reflection coefficient for the non-connected wire-mesh metamaterial of $r_0 : a = 0.01 : 1$. Numerically calculated reflection coefficients for S-polarized (red solid lines) and P-polarized (green dashed lines) waves plotted with the analytical prediction for the local model (blue dotted line) of (5.13) (a) normal incidence -$\theta = 0°$ (b) $\theta = 10°$ (c) $\theta = 45°$

the effect of spatial dispersion is dramatically more significant for the non-connected than the connected wire-mesh. However, neither wire metamaterials are described by a simple local dielectric tensor. In this report (next chapter), new wire-metamaterials are proposed that manage to minimize spatial dispersion and therefore allow for the homogenization of the medium with a simple local model.

Chapter 6

New Wire Metamaterials

Spatial dispersion in wire-mesh metamaterials arises from charge accumulation on the wires for longitudinal waves. Charge accumulation creates strong local electric fields due to the low capacitance of thin wires. These fields disturb the current flow associated with the plasma behaviour of the structure, and introduce a spatial component of the wavevector to the longitudinal permittivity tensor. Two ways are proposed in this thesis that manage to tame spatial dispersion in wire metamaterials, by slightly changing the sub-unit's geometry.

In order to minimize charge accumulation, we initially increase the capacitance of the system, achieved by attaching conducting structures on the wires (i.e. plates, spheres, cubes, cylinders). Now, the electrons are parked on the attached structures and not on the wires, leaving the current flow in the wires unaffected and minimizing the effect of spatial dispersion. An alternative way is to increase the inductance of the system, by coating the wires with a high-permeability material. The magnetic coat enhances the magnetic and consequently the electric field of the wave, which are associated with the plasma behaviour of the structure, but leaves the local electrostatic part (i.e. accumulated charge) unaffected. Therefore, the relative importance of charge accumulation on the wires, compared with the plasma behaviour is reduced (or the plasma behaviour of the structure enhanced).

However, by changing the geometry of the sub-unit, the permittivity tensors and dispersion equations discussed above are not valid for the new wire structures. Therefore, a modelling method for spatial dispersion is proposed, which measures the dependence of the permittivity tensors ($\overline{\overline{\varepsilon}}$) on the spatial wavevector q. This method gives a measure of the effect of spatial dispersion in the system and holds for all designs discussed in this report.

This chapter is organized as follows: in the first section the modelling method is described , where as examples the connected and non-connected wire-mesh metamaterials are used. Consequently, two designs are proposed that have increased capacitance compared with connected wire-mesh and numerical results show significant reduction of spatial dispersion. Finally, a design with increased inductance is proposed and investigated numerically.

6.1 Modelling Spatial Dispersion for a wire structure:

Shapiro *et.al.* [28] model spatial dispersion in connected wire mesh metamaterials, by measuring the dependence of permittivity tensors on the spatial wavevector. We expand this method in order to take into account the polarization of attached conducting structure on the wires by a constant β. The permittivity tensor is then rewritten for q_z-propagation (i.e. for propagation along one of the wires) as:

$$\overline{\overline{\varepsilon}}(\omega) = \varepsilon_{xx}\mathbf{xx} + \varepsilon_{yy}\mathbf{yy} + \varepsilon_{zz}\mathbf{zz} \tag{6.1}$$

where

$$\begin{aligned} \varepsilon_{xx} = \varepsilon_{yy} &= \beta\left(1 - \frac{k_p^2}{k_0^2}\right) + \alpha_2 \frac{q_z^2}{k_0^2} \\ \varepsilon_{zz} &= \beta\left(1 - \frac{k_p^2}{k_0^2}\right) + \alpha_1 \frac{q_z^2}{k_0^2} \end{aligned} \tag{6.2}$$

where α_1, α_2 are frequency dependent spatial dispersion coefficients for the longitudinal and transverse waves respectively. They can be considered as a measure of spatial dependence of the permittivity tensor for the wire-mesh and also depend on the dimensions of the lattice and wires. They can be determined by fitting the numerically calculated band structures (for $q \rightarrow 0$) to [28]:

$$\omega^2 = \omega_p^2 + Aq^2c^2 \tag{6.3}$$

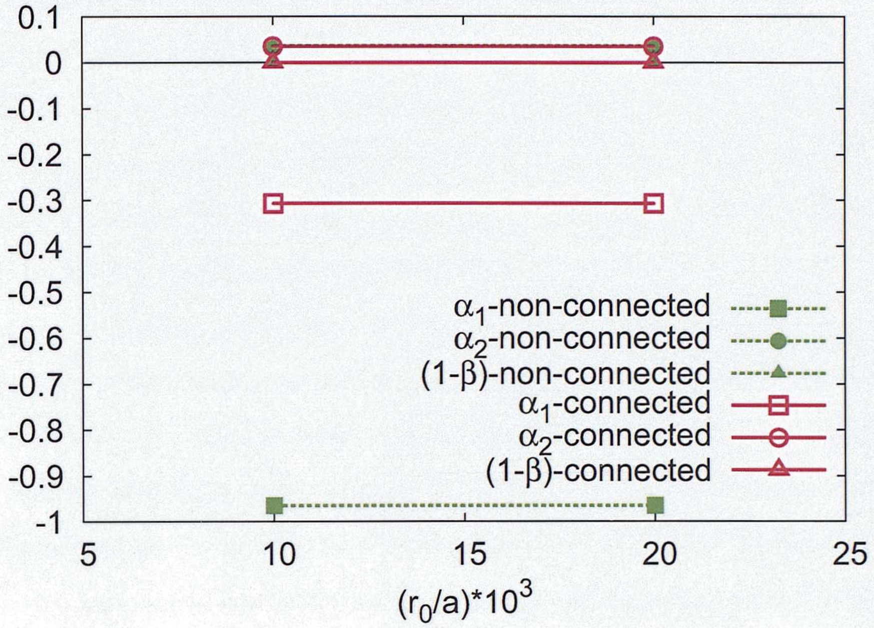

Figure 6.1: The spatial dispersion coefficients α_1 (square points), α_2 (circle points) for the connected (empty red) and the non-connected (full green) wire-mesh structure, plotted with respect of (r_0/a) ratio. Also, $(1-\beta)$ is plotted with triangle shaped points, which is zero for these structures. Where r_0 is the radius of the wires and a the lattice constant.

where A depends on the propagation direction. For the longitudinal mode: $A = -\alpha_1/\beta$ and for transverse modes:$A = (1-\alpha_2)/\beta$. Finally, β can be determined by calculating the band structure for just the added structures, where the dispersion equation has the form: $\omega^2 = (kc)^2/\beta$. Note that $\beta = 1$ for the simple wire-mesh metamaterial. It is clear from equations (6.2), that the permittivity tensor corresponding to a transverse wave (i.e. $\varepsilon_{xx} = \varepsilon_{yy}$) is different from the permittivity tensor corresponding to a longitudinal wave (ε_{zz}), when α_1 and α_2 are different.

As a first example, consider the connected wire-mesh structure shown in figure 4.1 and $(r/a) = 0.01$, whose band structure is shown in figure 4.3. The spatial dispersion coefficients take values: $\alpha_1 = -0.307$, $\alpha_2 = 0.035$ and $\beta = 1$. This means that the spatial dispersion for the transverse mode is negligible for $r \ll a$ and therefore the local model holds where $\varepsilon_{xx} = \varepsilon_{yy} = 1 - \frac{k_P^2}{k_0}$, as expected. On the other hand, the spatial dependence of the longitudinal permittivity tensor is dominated by α_1, which is significant for this structure, even for $r \ll a$. Similarly for non-connected wire-mesh shown in figure 4.6 and for $(r/a) = 0.01$ whose band structure is shown in figure 4.7, the spatial dispersion coefficients take values: $\alpha_1 \sim -1$, $\alpha_2 = 0.035$ and $\beta = 1$. As expected the transverse permittivity tensor has negligible dependence on q and α_1 dominates the longitudinal permittivity tensor.

The spatial dispersion coefficients for both structures and for various (r/a) ratios are plotted in figure 6.1. It is clear that there is no significant dependence on the radius of the wire, as long as $r \ll a$ is valid. As expected from the analytical derivation in chapter 4, spatial dispersion is reduced to (1/3) when the wires are connected, since the charge is distributed over the three orthogonal wires at nodes. Therefore, the new designs of wire metamaterials proposed in this section, use as a base the connected wire-mesh metamaterial.

6.2 Increasing the Capacitance

A way to minimize spatial dispersion in wire metamaterials is to increase the capacitance of the system by attaching conducting structures (i.e. cubes, plates, spheres, cylinders) on the wires. Hence, for a longitudinal wave, the charge is distributed on the surface of the attached structures instead of accumulating periodically on the wires. Therefore, the current flow in the wires, associated with the plasma-like behaviour of the metamaterial, remains unaffected. Various designs were examined using finite integrations algorithms for Maxwell's equations with CST Microwave Studio to calculate the dispersion diagrams and S-parameters for the new designs. Although all new structures showed significant reduction of spatial dispersion, in this thesis, two representative designs are discussed: cubes attached at the joints of a connected wire-mesh metamaterial and thin square plates at the mid-points between nodes of the wires.

6.2.1 Cubical Inclusions

Cubes made of PEC material are introduced at the nodes of a connected wire-mesh metamaterial as shown in figure 6.2(a) and the band structure was numerically calcu-

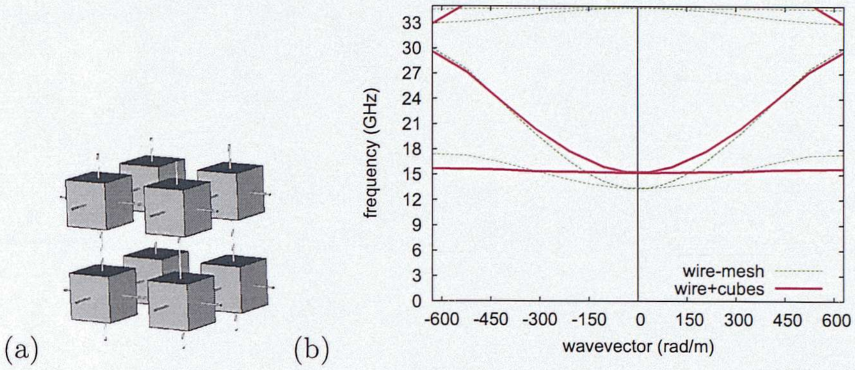

Figure 6.2: (a)The wire mesh with cubes attached at the joints (b) The band structure plotted for q_x-propagation for the structure shown left (red solid lines) (for $r : x : a = 0.01 : 0.5 : 1$ (wire's radius):(cube's side):(lattice constant)) and the connected wire-mesh metamaterial (green dotted lines)

lated using CST Microwave Studio and plotted in figure 6.2(b)(red solid lines) with the dispersion diagram of just the wire mesh (green dashed lines) for comparison. The addition of PEC cubes with side x, has a tremendous impact on the dispersion of the longitudinal mode, which is almost dispersion-less for propagation along one of the wires. In figure 6.3, the dispersion diagram for various propagation vectors is shown, where again the dispersion of the longitudinal mode is limited to $\sim 6GHz$ frequency range compared with $\sim 17GHz$ for the connected wire-mesh metamaterial. However, by introducing cubes on the structure, the wires are shortened causing the effective electron mass of (3.2) to take smaller values. Therefore, ω_p of the new structure takes slightly higher values of $\sim 2GHz$ since $m_{eff}^{wire} > m_{eff}^{cubes+wires}$, as shown in figure 6.2(b).

As discussed in section 6.1, spatial dispersion in a wire-mesh metamaterial can be modelled with coefficients α_1 and α_2, showing the effect of spatial dispersion for the longitudinal and transverse modes respectively. Furthermore, the cubes are getting polarized when subjected to an electromagnetic wave, which gives $\beta > 1$. The dependence of polarization and spatial dispersion coefficients on the cube's dimensions, is plotted in figure 6.4. The transverse α_2 coefficient takes negligible values, similarly to connected wire-mesh metamaterials, indicating that the cubical inclusions do not affect the transverse mode significantly. The longitudinal α_1 coefficient is also dramat-

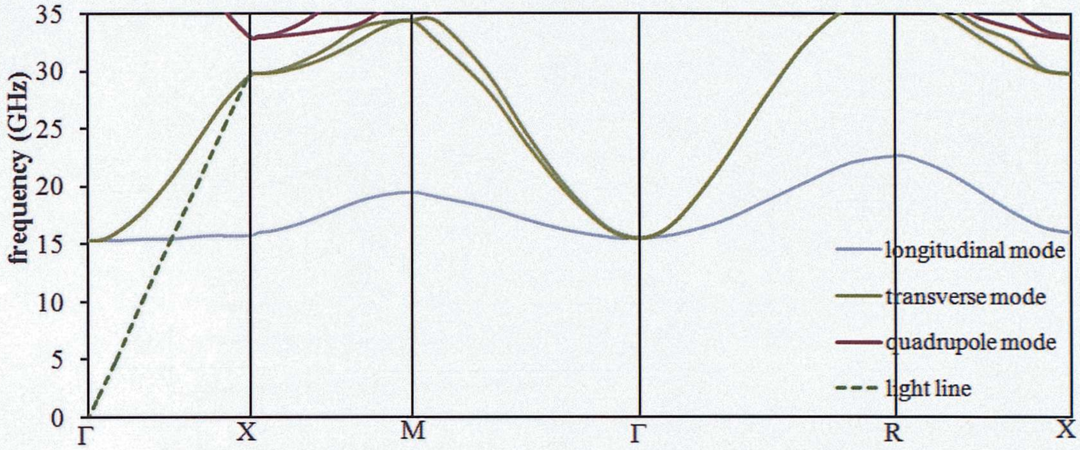

Figure 6.3: The band structure of structure shown in figure 6.2, with dimensions $r : x : a = 0.01 : 0.5 : 1$ where r is the radius of the wires, x the side of the attached cube and a the lattice constant, where $\Gamma(0,0,0)$, $X(0,0,\pi/a)$, $M(0,\pi/a,\pi/a)$ and $R(\pi/a,\pi/a,\pi/a)$.

ically reduced to negligibly small values for all cubical sizes, indicating that the spatial dependence of the longitudinal $\bar{\bar{\varepsilon}}$ is insignificantly small. On the other hand, although β coefficient is increased significantly, has no spatial effect and does not restrict the use of a local model, since the general Drude model can be used:

$$\varepsilon = \varepsilon_1 - \frac{\Omega^2}{\omega(\omega + i\gamma)} \tag{6.4}$$

where Ω and ε_1 are constants and γ represents the losses in the system. This equation is in agreement with the model used in (6.2), since as shown in figure 6.4, both spatial dispersion coefficients take negligible values for the new structure. For cubes of dimensions $(x/a) = 0.5$ attached on wires of $r = 0.05mm$ (with the band structure shown in figures 6.2 and 6.3), the coefficients take values: $\alpha_1 = -0.049$, $\alpha_2 = -0.045$ and $\beta = 1.24$.

The S-parameters of a finite (five-unit cell) slab of the new structure were calculated numerically using CST Microwave Studio, in order to determine the effect of spatial dispersion on the electromagnetic behaviour of the new wire metamaterial. Periodic boundary conditions are applied for the x- and y- directions and five unit cells along z-axes. The reflection coefficients of S- and P-polarized waves are plotted in figure 6.5,

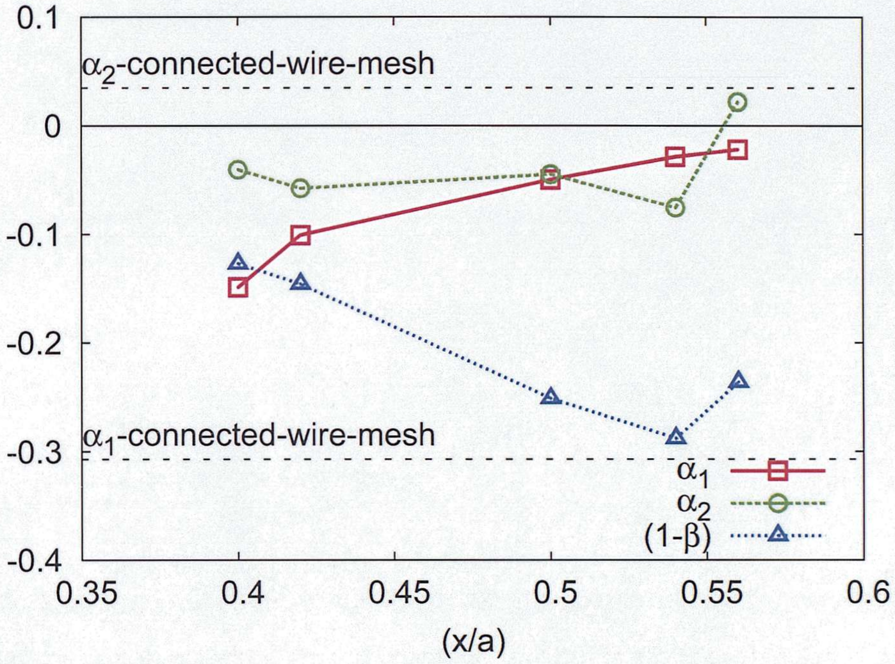

Figure 6.4: The spatial dispersion coefficients α_1 (square red points), α_2 (circle green points) of the structure shown in figure 6.2(a) are plotted against the dimensions of the cube, where x is the side of the cube and a is the lattice constant. Also, $(1 - \beta)$ is plotted with triangle shaped blue points. For all calculations the radius of the wires was constant with $(r/a) = 0.01$ and with black dashed lines the coefficients are shown for just the connected wire-mesh.

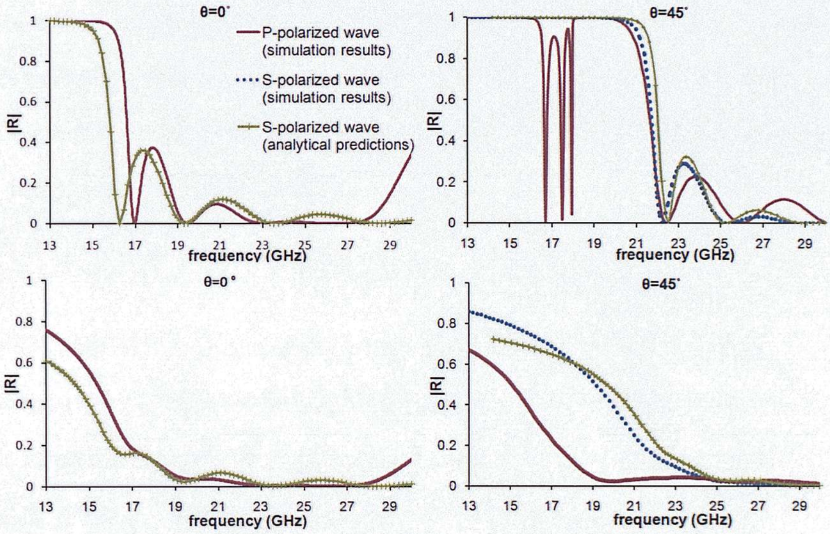

Figure 6.5: The modulus of the reflection coefficient for the structure in figure 6.2 and dimensions $r : x : a = 0.01 : 0.5 : 1$ where r is the radius of the wires, x the side of the attached cube and a the lattice constant. The S-polarized (dashed lines) and P-polarized (solid lines) are plotted for $\theta = 0°$ (left graphs) and $theta = 45°$ (right graphs) angles of incidence. The top graphs are for a loss-free system (i.e. perfect electric conducting (PEC) wires in vacuum with $\varepsilon = 1$ and $\mu = 1$) and bottom graphs for PEC wires in a slightly lossy hosting medium with conductivity $\sigma = 0.111Sm^{-1}$ (i.e. $Im(\varepsilon) = \sigma/(\varepsilon_0\omega)$).

with the analytical prediction of (5.13) for a homogeneous slab with permittivity tensor obeying the general Drude model of (6.4). For normal incidence in figure 6.5, both S- and P-polarized reflection coefficients are degenerate, since the E-field is always perpendicular to the wires and only the transverse mode is excited. The agreement between numerical and analytical calculations is significant, except at frequencies close to Brillouin zone, where there is a band gap and the analytical theory does not predict.

For non-normal incidence on a loss-less system (top graphs), the excitation of the longitudinal mode can be seen at $\sim$ (17 − 18)GHz as sharp resonances for a P-polarized wave. These resonances are attenuated, when the hosting medium of the wires becomes slightly lossy(bottom graphs) with:

$$\varepsilon_{host} = \varepsilon_0 \left(1 + i\frac{\sigma}{\varepsilon_0 \omega}\right) \tag{6.5}$$

where $\sigma = 0.1 Sm^{-1}$ is the conductivity (i.e. at $\omega = 17GHz \rightarrow Im(\varepsilon) = 0.106$) and ω the frequency in s^{-1}. Considering that all materials in nature are always slightly lossy, then the longitudinal mode cannot propagate in the new wire metamaterial. Even if it propagates slightly in the medium, it is extremely slow and is attenuated from the loss of the hosting medium. Therefore, the effect of spatial dispersion is excluded from the new wire metamaterial and can be effectively described by one homogenized medium obeying the simple local model.

6.2.2 Thin-Square-Plate Inclusions

Consider thin square PEC plates attached at the mid-points between the nodes of a connected wire-mesh metamaterials, as shown in figure 6.6(a). The additional surface area of the new wire metamaterial is about six times larger than the design described above. Therefore, a more dramatic effect on spatial dispersion is expected for the thin-plate wire-mesh metamaterial, since the capacitance of the system is remarkably increased. Furthermore, the new wire metamaterial has almost no effect on the value of the plasma frequency, since the wires are negligibly shortened. In figure 6.6(b), the dispersion diagram for propagation along one of the wires is shown plotted together with the band structure of connected wire-mesh for comparison. The longitudinal mode for the new structure is dispersion-less, indicating that it cannot propagate in the

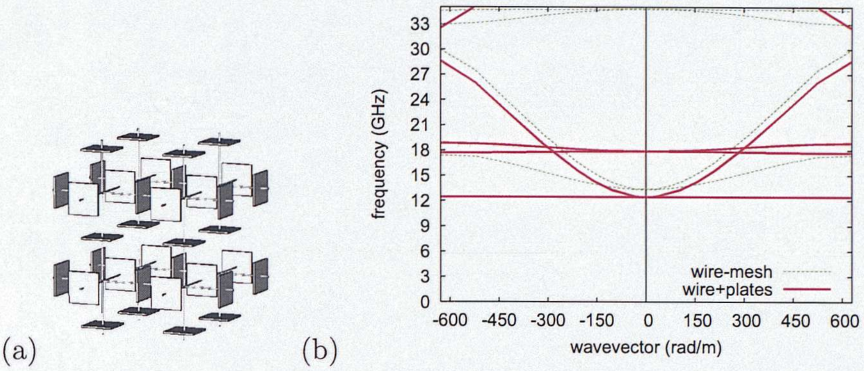

Figure 6.6: (a)The wire mesh metamaterial with thin square plates attached at the mid-points between the joints of the wires (b) The band structure plotted for k_x-propagation for the structure shown no the left (red solid lines) (for $r : x : a = 0.01 : 0.36 : 1$ (wire's radius):(plate's side):(lattice constant)) and the connected wire-mesh metamaterial (green dotted lines)

medium. The dispersion diagram for all propagation directions in shown in figure 6.8, where the dispersion of the longitudinal mode has been confined to ~ 6GHz.

In figure 6.7, the polarization and spatial dispersion coefficients are plotted with respect to plate dimensions. As expected, α_1 takes smaller values for larger plates, where the surface area is larger. For large enough plates it takes positive values, due to additional effects (i.e. the plates interact with each other). Nevertheless, α_1 is reduced to negligibly small values for all plate dimensions, while α_2 is maintained at low values. For square plates with dimensions $(x/a) = 0.36$, spatial dispersion coefficients take values $\alpha_1 \rightarrow 0$, $\alpha_2 = 0.04$ and $\beta = 1.04$. Note that the thickness of the plates does not affect α_1 and α_2 values, but changes slightly the plasma frequency and β.

Furthermore, at $\sim 17GHz$, two flat degenerate modes can be observed in figure 6.8. These are identified as the two quadrupole modes that arise due to the orthogonal nature of the wire structure, with charge arrangement as shown in figure 4.5. They appear at much lower frequencies than for the simple wire-mesh, since charge is stored both on the plates and also distributed at nodes. However, both are flat (i.e. group velocity is zero), meaning that when excited they do not propagate in the metamate-

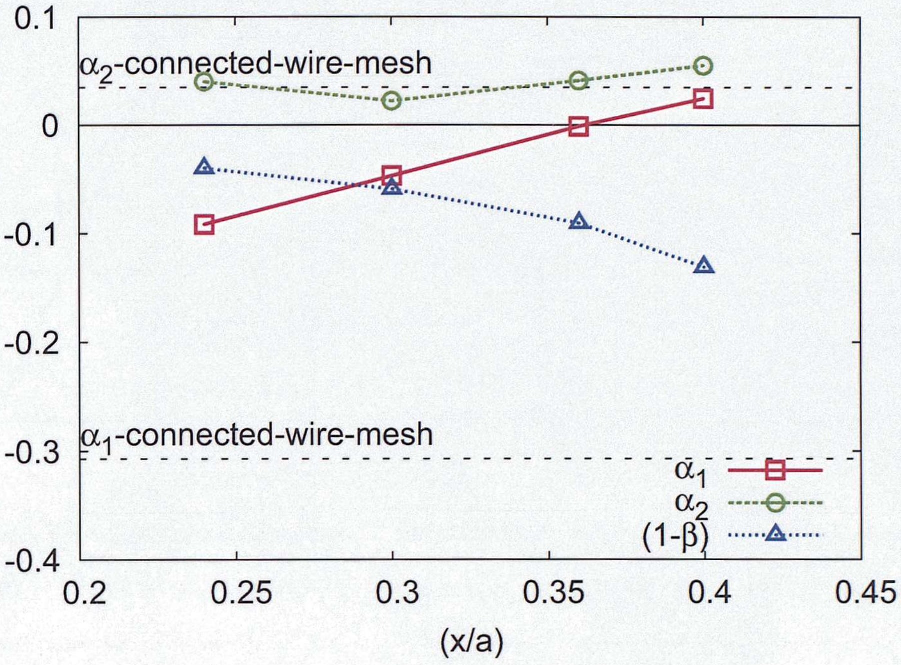

Figure 6.7: Spatial dispersion coefficients (α_1 and α_2) are plotted against the dimensions of the square plates, where x is the side of square plates and a the lattice constant.

rial. Therefore, since neither the longitudinal or quadrupole modes propagate in the medium, then only the transverse mode propagates, suggesting that the local model of (6.4) is valid for describing this wire metamaterial.

The S-parameters were calculated numerically for a five-unit-cell slab in order to observe the reduction of the effect of spatial dispersion on the new wire design and are plotted in figure 6.9. For normal incidence (left figures), both S- and P-polarized waves excite just the transverse modes since the electric field is always perpendicular to the wires, which leads to a degeneracy for the reflection coefficients of the two wave-polarizations. For non-normal incidences, both the longitudinal and transverse modes are excited for P-polarized waves. The longitudinal mode excitation appears as sharp resonances at $\sim 14GHz$ for a loss-less system, which are attenuated for a slightly lossy hosting medium (i.e. $\sigma = 0.1Sm^{-1}$ in (6.5)). Furthermore, at $\sim (18-20)GHz$ sharp resonances appear as well, due to the excitation of the quadrupole modes. These resonances are also attenuated for a slightly lossy hosting medium and similarly to longitudinal mode, do not contribute to the interference pattern. Finally, in figure 6.9,

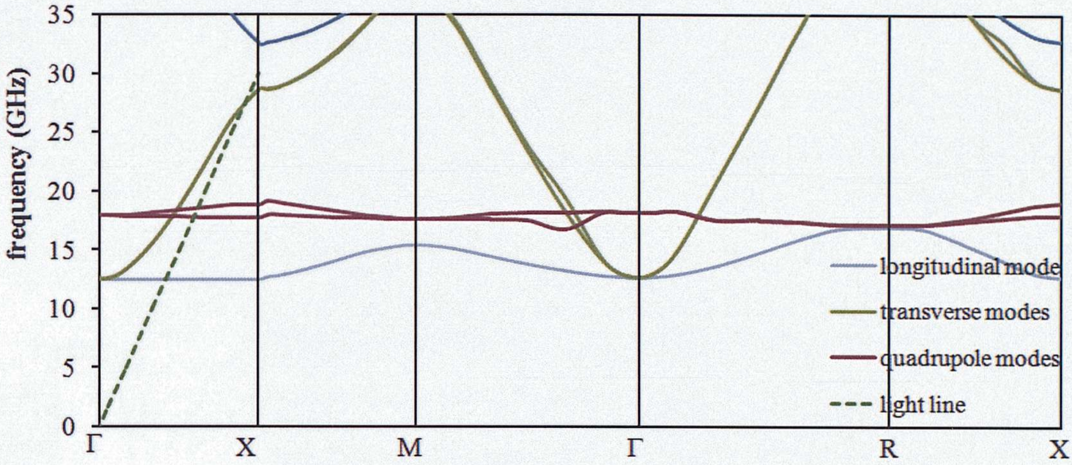

Figure 6.8: The dispersion diagram of the structure shown in figure 6.6 for $r : x : a = 0.01 : 0.36 : 1$ where r is the radius of the wires, x the side of the square plate, a the lattice constant and $\Gamma(0, 0, 0)$, $\mathrm{X}(0, 0, \pi/a)$, $\mathrm{M}(0, \pi/a, \pi/a)$ and $\mathrm{R}(\pi/a, \pi/a, \pi/a)$.

the analytical prediction of (5.13) is plotted for a slab of a homogeneous medium with permittivity tensor obeying the model of (6.4), which shows significant agreement for all angles of incidence.The disagreement between analytical and numerical results seen at $\sim 30GHz$ is due to the band-gap at the Brillouin zone that the analytical model cannot predict.

6.3 Increasing the Inductance

An alternative way to minimize the effect of spatial dispersion in wire metamaterials, is to increase the inductance of the system by coating the wires with a magnetic material, as shown in figure 6.10(a). The coating material enhances the magnetic and consequently the electric field of the wave, which are associated with the plasma behaviour of the structure. However, it leaves the electrostatic (i.e. charge accumulation responsible for spatial dispersion) unaffected. Hence, the relative importance of charge accumulation on the wires is reduced, with respect to the plasma behaviour of the structure.

Figure 6.10(b) shows the band structure for propagation along one of the wires (red solid lines), plotted together with the dispersion diagram of the connected wire-

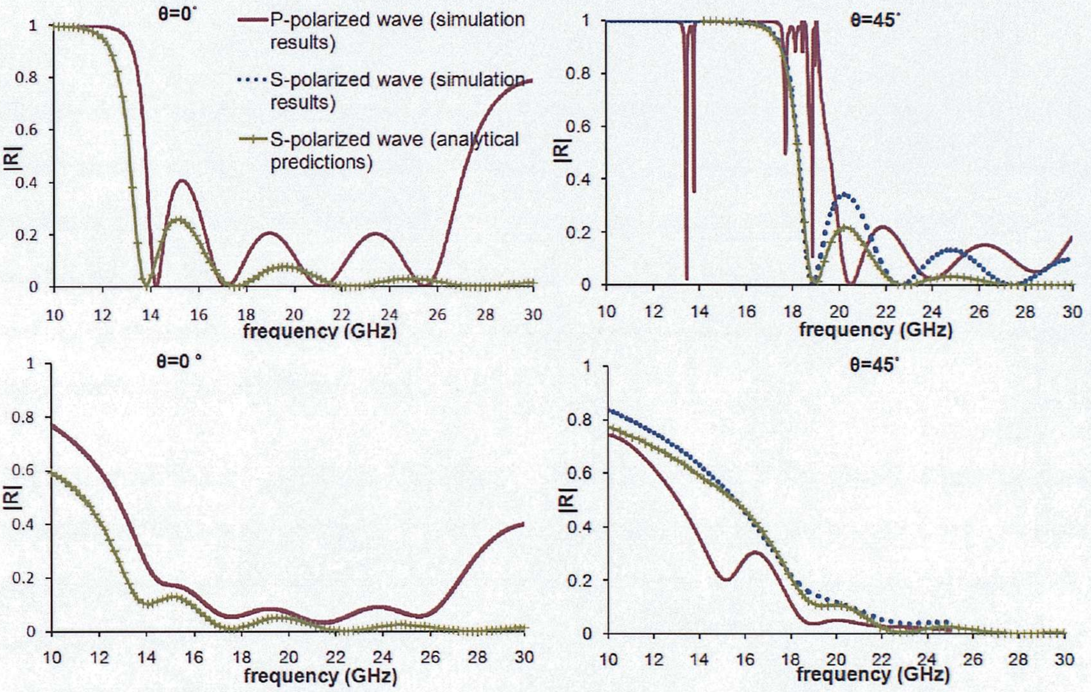

Figure 6.9: The modulus of the reflection coefficient for the structure in figure 6.6. The S-polarized (dashed line) and P-polarized (solid line) are plotted for various angles of incidence. Top graphs show the reflection coefficient for PEC wires in vacuum (i.e. $\varepsilon = 1$ and $\mu = 1$) and bottom graphs PEC wires in a slightly lossy hosting medium with $\varepsilon_{host} = \varepsilon_0 \left(1 + \frac{\sigma}{\varepsilon_0 \omega}\right)$, where $\sigma = 0.111 Sm^{-1}$ is the conductivity.

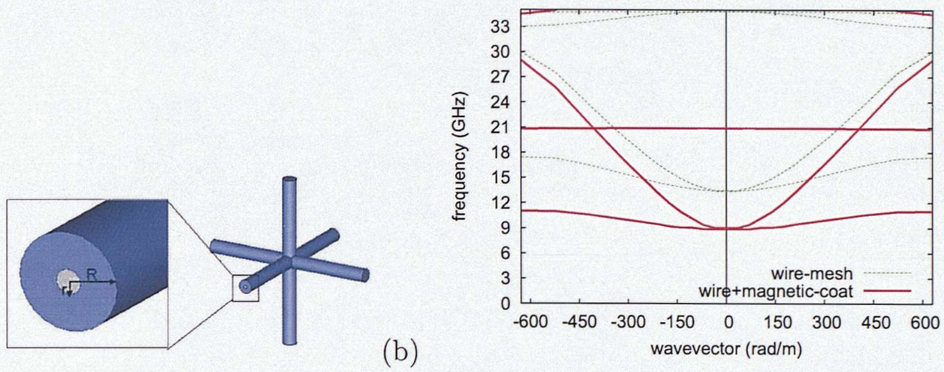

(a) (b)

Figure 6.10: (a)The wire mesh structure, coated with a magnetic material. R is the outer radius of the coating magnetic material of magnetic permeability μ and r the radius of PEC wires.(b) The band structure plotted for k_x-propagation for the structure shown no the left (red solid lines) (for $r : R : a = 0.01 : 0.04 : 1$ (wire's radius):(outer radius of coating magnetic material):(lattice constant)) and the connected wire-mesh metamaterial (green dotted lines)

mesh metamaterial (green gashed lines). The dispersion of the longitudinal mode is reduced, as well as the value of the plasma frequency, which can be explained by taking into account that the self-inductance effects that drive (3.2), are enhanced due to the increased inductance of the wire system (i.e. $m_{eff}^{magn-coat} > m_{eff}^{wire-mesh}$). Spatial dispersion coefficients α_1 and α_2 plotted in figure 6.11 show significant reduction for structures with a magnetic coating of $\mu = 5$. They take negligibly small values for the new wire structure and note that $\beta = 1$, since the magnetic coating material is not polarized by an incident wave. The band structure for various propagation directions is plotted in figure 6.12, where the frequency range of the longitudinal mode dispersion is reduced compare to the simple connected wire-mesh metamaterial.

The S-parameters were numerically calculated using CST Microwave Studio, for a five-unit-cell slab, in order to determine the effect of spatial dispersion on the electromagnetic behaviour of the new design and are plotted in figure 6.13. For normal incidence, the reflection coefficient for both the S- and P-polarized waves is identical, since just the transverse mode is excited. For non-normal incidence, the excitation of the longitudinal mode induces sharp resonances at the interference pattern of P-polarized

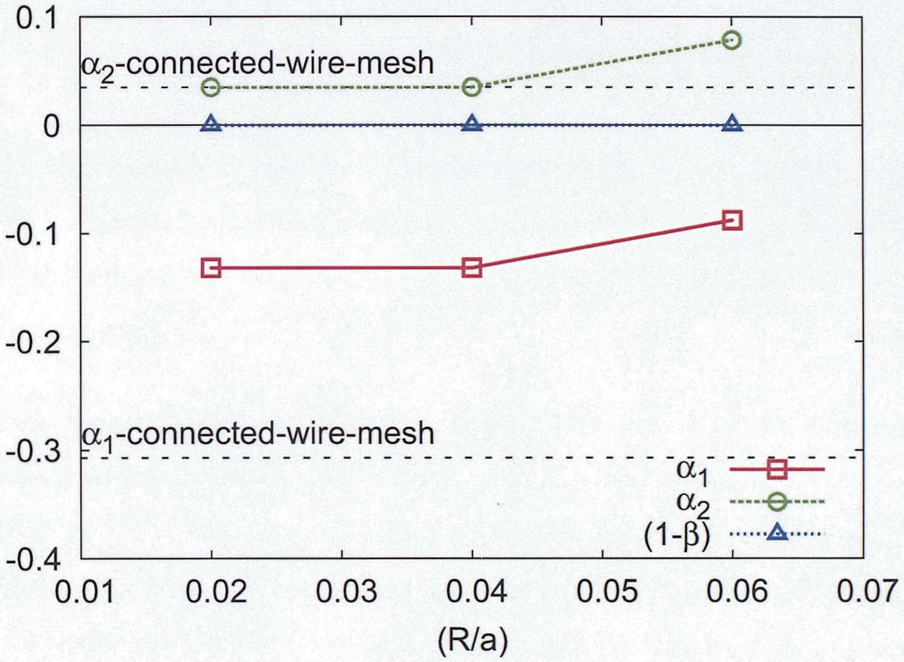

Figure 6.11: Spatial dispersion coefficients (α_1 and α_2) are plotted against the radius of the magnetic coating, where R is the outer radius of the coating material and a the lattice constant. For all calculations $(r/a) = 0.01$ and $\mu = 5$, where r is the radius of PEC wires and μ the magnetic permeability of the coating material.

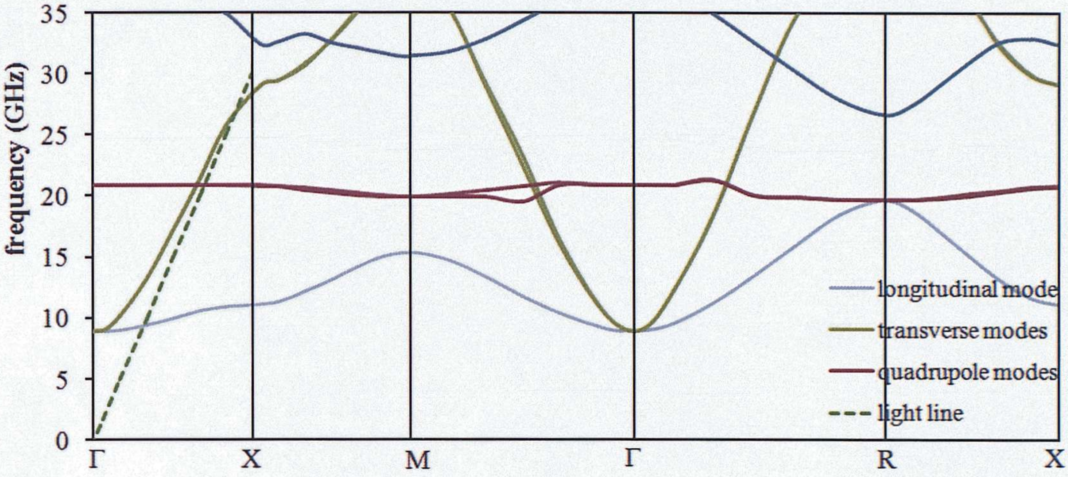

Figure 6.12: The dispersion diagram of the structure shown in figure 6.10 for $r : R : a = 0.01 : 0.04 : 1$ where R is the outer radius of coating magnetic material of $\mu = 5$, r the radius of PEC wires, a the lattice constant and $\Gamma(0, 0, 0)$, $\mathrm{X}(0, 0, \pi/a)$, $\mathrm{M}(0, \pi/a, \pi/a)$ and $\mathrm{R}(\pi/a, \pi/a, \pi/a)$

waves for the loss-less hosting medium (top figures) at $\sim (10 - 12)GHz$. However, the sharp resonances are attenuated in a slightly lossy hosting medium (bottom figures) of $\sigma = 0.08Sm^{-1}$ in (6.5). Furthermore, the quadrupole modes are excited for the loss-less hosting medium and appear as sharp resonances as well at $\sim 20GHz$, which are also absorbed in a slightly lossy hosting medium. Therefore, for any real system where loss is always present, just the transverse mode propagates in the wire metamaterial. Finally, the analytical prediction for the reflection coefficient from (5.13) is also plotted in figure 6.13, assuming a homogeneous medium with a permittivity tensor obeying the general Drude mode of (6.4). The significant agreement indicates that the local model is valid for the new wire structure, and that the effect of spatial dispersion on the new wire structure is negligibly small.

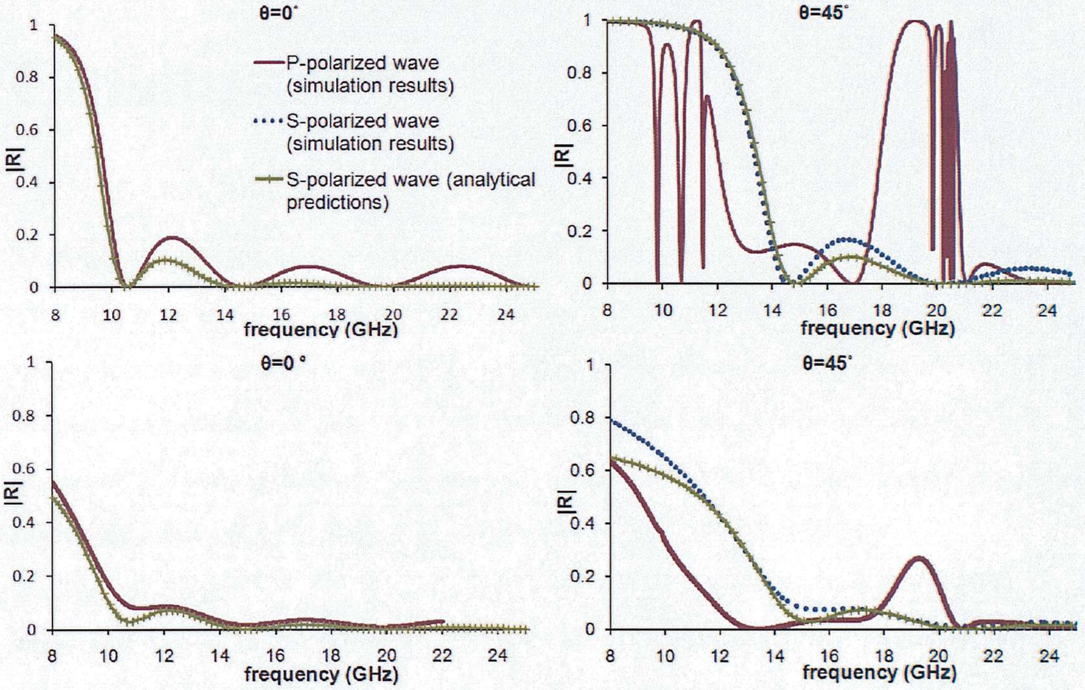

Figure 6.13: The modulus of the reflection coefficient for the structure in figure 6.10. The S-polarized (dashed line) and P-polarized (solid line) are plotted for various angles of incidence. Top graphs show the reflection coefficient for PEC wires in vacuum (i.e. $\varepsilon = 1$ and $\mu = 1$) and bottom graphs PEC wires in a slightly lossy hosting medium with $\varepsilon_{host} = \varepsilon_0 \left(1 + \frac{\sigma}{\varepsilon_0 \omega}\right)$, where $\sigma = 0.083 Sm^{-1}$ is the conductivity.

Chapter 7

Conclusions

A wire-mesh metamaterial simulates the properties of a low-density electron plasma, with the plasma frequency in the GHz range. However, the properties of the artificial plasma are strongly modified by spatial dispersion, which arises from periodic charge accumulation in the wires for longitudinal waves. The longitudinal mode disperses with the frequency and propagates in the metamaterial, preventing the effective homogenization of the wire-mesh with one local permittivity tensor.

Spatial dispersion can be minimized by attaching conducting structures on the wires and therefore increasing the capacitance or by coating the wires with a magnetic material, which increases the inductance of the wire metamaterial. Various structures are proposed and examined numerically that manage to eliminate spatial dispersion and create a dispersion-free longitudinal mode. Hence, the longitudinal mode (and quadrupole modes that are also dispersion-free) are either not excited by externally incident radiation, or propagate extremely slowly in the medium and therefore are rapidly attenuated by the lossy hosting medium. Therefore, the transverse mode is the only mode propagating in the medium, which is well described by the local model, and the new wire-structures can be homogenized by the simple local model.

Part II

Swiss Rolls Metamaterials

Chapter 8

Introduction

The magnetic response of conventional materials disappears at high frequencies, even at few GHz. However, magnetic media can be artificially constructed with sub-unit dimensions much smaller than the wavelength of the incident wave and usually exhibit a resonant magnetic behaviour for frequencies from few MHz to THz, IR and even the visible region [29, 30, 31]. In 1999, Pendry *et.al.* [9] proposed several artificially magnetic structures, composed entirely from conducting materials. Their design is based on an array of wire loops, and therefore, a magnetic field (H_0) induced currents and an electromotive force (emf) that opposes the applied magnetic field. Hence, an effective magnetic response is produced [9].

The majority of the metamaterial community has focused on magnetic materials that operate at higher frequencies (such as split-ring resonators, U-shaped or cut-wires) and allow for the combination with wire-mesh to create a negative refracting medium. However, Swiss Rolls are magnetic metamaterials with different, but equally interesting applications, mainly in the MHZ frequency region. An important advantage of Swiss Rolls is that their resonant frequency can be tuned over a broad frequency range (from MHz to GHz). The most well-known application of Swiss Rolls is for magnetic resonance imaging (MRI) [32, 33, 34] that operates at MHz frequency, where most magnetic metamaterials require at least 100 times larger lattice constant, which is not practically applicable. Furthermore, chiral Swiss Rolls, in addition to MRI applications, are ideal for polarization rotation/selection antenna applications.

Initially, we investigate the non-chiral Swiss Roll metamaterial. Comparison of the already known analytic work [9] with numerical calculations for the band-structure, scattering parameters and effective electromagnetic tensors is presented, where a considerable agreement was found [35]. The lack of numerical work for Swiss Rolls in the literature, is due to the complex design of the structure, which demands an extremely fine modelling mesh and consequently huge computational power and time.

Then, the more complicated design of the chiral Swiss Roll metamaterial is investigated [36, 37]. The chirality of the structure combined with the magnetic resonant behaviour, result to a negative band for one-wave polarization, even for GHz frequencies. In this chapter, the electromagnetic parameters and band structure of a chiral Swiss Roll metamaterial are derived analytically and compared with numerical calculations. Then, the scattering parameters are calculated numerically, where the effect of chirality is apparent, since the transmission coefficient for right-handed and left-handed circularly polarized waves are different. Finally, the electromagnetic and chirality terms are retrieved from numerical scattering parameters, where a significant agreement was found with analytical work as well.

Chapter 9

Non-chiral Swiss-Roll metamaterials

A Swiss Roll metamaterial is made from a thin insulated conducting sheet, wrapped around a cylindrical mandrel in a spiral shape, as shown in figure 9.1(a). When an oscillating magnetic field H_0 is applied along the rolls (along the z-axes), currents are induced on the conducting spiral circumference and therefore an emf arises that opposes the applied magnetic field H_0. Hence, it macroscopically appears that 'magnetic' monopoles are flowing up and down the roll, which can be considered as a magnetic equivalent of conducting wires. Due to structure's self-capacitance and self-inductance, the induced currents are subjected to an LC resonant circuit giving rise to a resonant effective magnetic permeability μ_{zz}^{eff} obeying the Lorentz model and is plotted in figure 9.1.

For a metamaterial consisted from Swiss Rolls arranged in a square lattice of constant a, the fields obey:

$$\begin{aligned} \mathbf{D} &= \varepsilon_{\mathsf{eff}}\varepsilon_0\mathbf{E} - i\kappa\sqrt{\varepsilon_0\mu_0}\mathbf{H} \\ \mathbf{B} &= \mu_{\mathsf{eff}}\mu_0\mathbf{H} + i\kappa^{\mathrm{T}}\sqrt{\varepsilon_0\mu_0}\mathbf{E} \end{aligned} \tag{9.1}$$

where $\varepsilon_{\mathsf{eff}}$ and μ_{eff} are the effective electric permittivity and magnetic permeability respectively, κ the magnetoelectric coupling term that takes into account the bianisotropic nature of the structure.

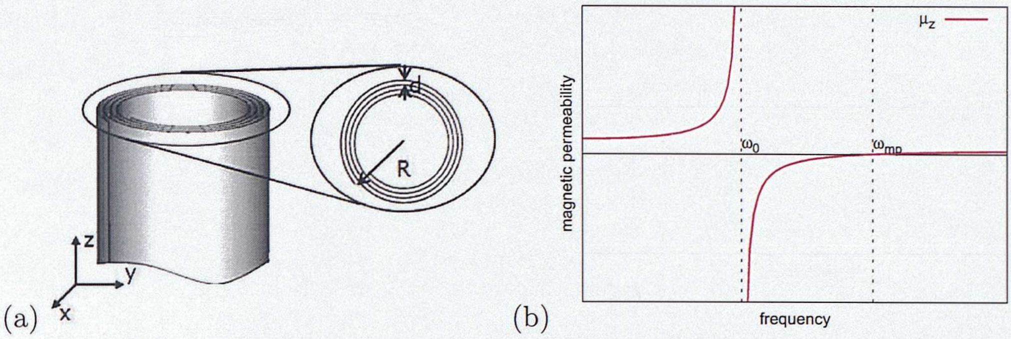

Figure 9.1: (a)A Swiss Roll, where R is the outer radius, d the gap between the conducting sheets. (b)For magnetic fields along the Swiss Roll, the metamaterial has an effective resonant magnetic permeability (μ_z). Note that $\mu_z < 0$ for $\omega_0 < \omega < \omega_{mp}$.

Assuming that the conducting sheet is infinitely thin and that the radius R of the roll is much larger than the gap d (i.e. $R \gg d$), the axial magnetic field along the roll is given by [9]:

$$H_z = H_0 + j - Fj \tag{9.2}$$

where $F = \pi R^2/a^2$ is the filling factor, a is the lattice constant, and j the induced current per unit length of the conducting sheet. The last term of this equation arises due to depolarizing fields, which are assumed to be uniform for infinite rolls. The emf can be calculated using Lenz's law:

$$emf = i\omega(N-1)\pi R^2 \mu_0 \left(H_0 + j - \frac{\pi R^2}{a^2} j \right) \tag{9.3}$$

where N is the number of spiral turns of the conducting sheet. The emf needs to be balanced by the Ohmic drop in potential. Hence:

$$i\omega(N-1)\pi R^2 \mu_0 \left(H_0 + j - \frac{\pi R^2}{a^2} j \right) = 2\pi R \rho j - \frac{j}{i\omega C 2\pi R(N-1)} \tag{9.4}$$

where ρ is the resistance of the conducting sheet per unit area and the term $(2\pi R \rho j)$ accounts for the resistivity losses of conductive elements. The last term accounts for the Ohmic potential due to the capacitive elements of the structure and the capacitance per turn is given by:

$$C = \frac{\varepsilon_d \varepsilon_0}{d(N-1)} \tag{9.5}$$

where ε_d is the dielectric constant of the material in the gap, which we assume to be vacuum (i.e. $\varepsilon_d = 1$).

Solving (9.4), the current (j) induced on the roll can be obtained and therefore the z-component of the effective magnetic permeability is given by:

$$\mu_{zz}^{eff} = \frac{B_{ave}}{\mu_0 H_{ave}} = \frac{\mu_0 H_0}{\mu_0 (H_0 - Fj)} = 1 - \frac{F\omega^2}{\omega^2 - \omega_0^2 + i\Gamma\omega} \tag{9.6}$$

and obeys Lorentz model, where ω is the frequency of the wave, $\Gamma = 2\rho/[\mu_0 R(N-1)]$ accounts for the resistivity losses from the conducting material. The resonant frequency ω_0 is given by:

$$\omega_0 = c_0 \sqrt{\frac{d}{2\pi^2 R^3 \varepsilon_d (N-1)}} \tag{9.7}$$

The magnetic permeability of (9.6) is plotted in figure 9.1(b) and goes to infinity at ω_0-frequency (for loss-less media) and to zero at the 'magnetic' plasma frequency (ω_{mp}) given by:

$$\omega_{mp} = c_0 \sqrt{\frac{d}{(1-F)2\pi^2 R^3 \varepsilon (N-1)}} = \frac{\omega_0}{\sqrt{1-F}} \tag{9.8}$$

Consider an E_z-field oscillating along the Swiss Rolls. For the long wavelength limit (i.e. $\lambda \gg a$), the field would see thick conducting wires and therefore, the electric permittivity along the Swiss Rolls obeys Drude's model:

$$\varepsilon_{zz}^{eff} = 1 - \frac{\omega_p^2}{\omega^2} \tag{9.9}$$

where ω_p is the plasma frequency, which takes extremely high values, since for thick conducting wires, ω_p increases [21, 5]. Therefore, $\omega_p \gg \omega_0$ and $\omega_p \gg \omega_{mp}$, and ε_z is negative for frequencies where Swiss Rolls are magnetically active [11, 12, 13]. This indicates that for k_x-propagation and frequencies around ω_0 and ω_{mp}, the band structure is not doubly degenerate, since (E_z, H_y) mode is forbidden and therefore only the (E_y, H_z) mode propagates.

Now, considering lateral electric or magnetic fields (i.e. in the x-y plane) and neglecting the resistivity losses of the conducting sheet, then the lateral components of ε_{eff} and μ_{eff} are approximately constants [9]. The magnetic lines can not penetrate the rods, and are constrained in the free space around the Swiss Rolls, giving a spatially non-uniform magnetic field and lateral μ^{eff} takes values [38, 39, 6]:

$$\mu_{xx}^{eff} = \mu_{yy}^{eff} \simeq \frac{\sqrt{1-F}}{2} \tag{9.10}$$

Similarly, for the x- and y- components of the electric permittivity:

$$\varepsilon_{xx}^{eff} = \varepsilon_{yy}^{eff} \simeq \frac{2}{\sqrt{1-F}} \tag{9.11}$$

Finally, due to the bianisotropic nature of the structure, a resonant magnetoelectric coupling term (κ) has to be considered, which takes the form:

$$\kappa = \frac{\delta\omega\omega_0^2}{\omega^2 - \omega_0^2} \tag{9.12}$$

where δ is a constant. E_x and E_y applied fields induce electric dipoles on the rolls, causing currents to flow on the outer (j_{out}) and internal (j_{in}) layers of the roll. Consequently, an additional magnetization arises due to E_{xy} fields, accounted by κ. For Swiss Rolls with small d and therefore large (R/d), the magnetoelectric coupling term tends to zero ($\kappa \to 0$) since $j_{in} \to j_{out}$. Therefore, δ takes extremely small values, in contrary to split-ring resonators that have a much stronger magnetoelectric coupling.

9.1 Band Structure

The dispersion equation for a medium consisted from Swiss Rolls in a square lattice and aligned with the z-axes can be found considering Maxwell's equations for a monochromatic wave with frequency ω and wavevector $\mathbf{k}$. For simplicity, assume that $k_y = 0$, and since the medium is magnetically active and electrically inactive along the z-axes, the dispersion equation derived in Appendix F [40] is:

$$\omega = c_0\sqrt{\frac{k_x^2}{\varepsilon_y\mu_z} + \frac{k_z^2}{\varepsilon_y\mu_x}} \tag{9.13}$$

which is plotted in figure 9.2 (red line) for k_x-(left) and k_z-propagation (right). For k_x-propagation and for frequencies $\omega_0 < \omega < \omega_{mp}$, the medium is opaque since $\mu_{zz}^{eff} < 0$ and $\varepsilon_{yy}^{eff} > 0$ introducing a stop band in the dispersion diagram. Also, the band structure is not doubly degenerate for k_x-propagation as expected, since the (E_z, H_y) mode is forbidden for $\omega < \omega_p$. In figure 9.2 (right), the band structure for k_z-propagation is

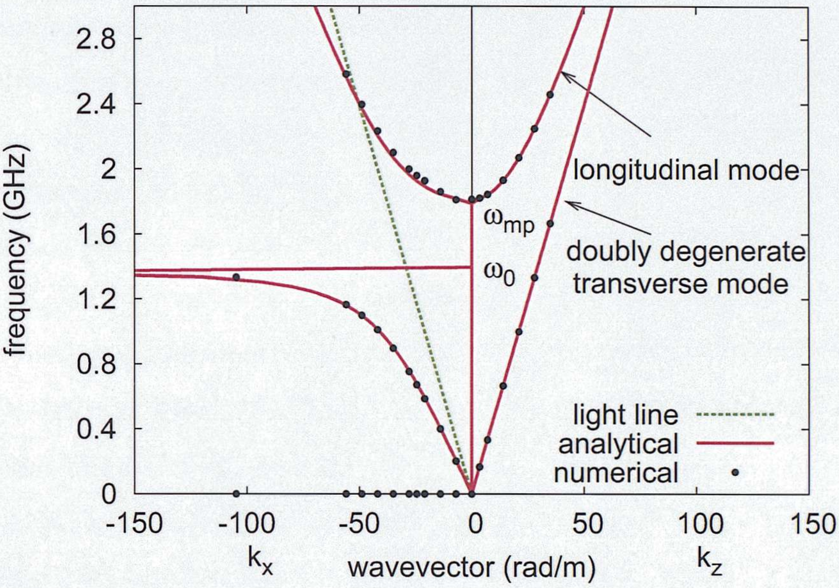

Figure 9.2: The analytical prediction (red solid line) for the band structure at $k \to 0$, plotted with numerical results (dots) for a Swiss Roll metamaterial with dimensions $N = 2$, $d = 0.1mm$, $x = 0.05mm$, $R = 2mm$ and $a = 5mm$. Note that the left part of both plots is the band structure for k_x-propagation and the right part for k_z-propagation. Note that there is a stop band for $\omega_0 < \omega < \omega_{mp}$ and k_x-propagation, where $\mu_z < 0$. The light line is plotted with a green dashed line.

plotted, where the electric and magnetic fields are in the x-y plane. Therefore, there are two doubly degenerate transverse modes (since $\varepsilon_{xx} = \varepsilon_{yy}$ and $\mu_{xx} = \mu_{yy}$), that are also degenerate with the light line since $\sqrt{\varepsilon_{xx}\mu_{yy}} = \sqrt{\varepsilon_{yy}\mu_{xx}} = 1$, as predicted in (9.10) and (9.11).

The Swiss Roll is a rather complex design to be modelled numerically, since it is constructed from a thin conducting sheet arranged in a spiral shape with a relatively big radius and small d (i.e. $R \gg d$) [40, 41]. The fine details of the structure demand a huge computational power and time for adequate numerical accuracy. A way to go around this problem is to calculate the band structure for a Swiss Roll with less fine detail (i.e. thicker conducting sheet-x and a smaller ratio of (R/d)). Initially, the band structure of a Swiss Roll with dimensions $x = 0.05mm$, $d = 0.1mm$, $R = 2mm$, $a = 5mm$ and $N = 2$, was numerically calculated using CST Microwave Studio and is plotted in figure 9.2(black dots) with the analytical prediction (red solid lines) of (9.13). The analytical and numerical results show a significant agreement (i.e. $\sim 90\%$) for both k_x- and k_z-propagations, even though some of the assumptions taken analytically are not valid for numerical calculations.

Figure 9.3 shows the band structure at higher frequencies, where the numerical calculations find equally-spaced flat modes. By carefully studying the H-fields plotted in figure 9.5(c) and (d), these modes are identified as trapped modes inside the spiral gap, which acts as a spiral waveguide. The waveguide modes are observed at frequencies:

$$\omega_g^n = c_0\sqrt{k_{mp}^2 + \left(\frac{n\pi}{S}\right)^2 + k_z^2} \tag{9.14}$$

where n is a positive integer, k_{mp} is the wavevector associated with the‘magnetic plasma’ frequency in (9.8) and S is the length of the spiral waveguide given by:

$$S = \int_0^{2\pi(N-1)} \sqrt{\rho^2 + \left(\frac{d\rho}{d\theta}\right)^2}\, d\theta \tag{9.15}$$

where ρ is the radius of the spiral waveguide and θ the angle created between r_0 and ρ radial vectors. As the number of turns N increase for a Swiss Roll, the length of the spiral waveguide increases as well, leading to more dense waveguide modes. Numerical results agree with (9.14) $\sim 95 - 96\%$, although the open boundary conditions are neglected in (9.14). Also, our results are consistent with the work in [42].

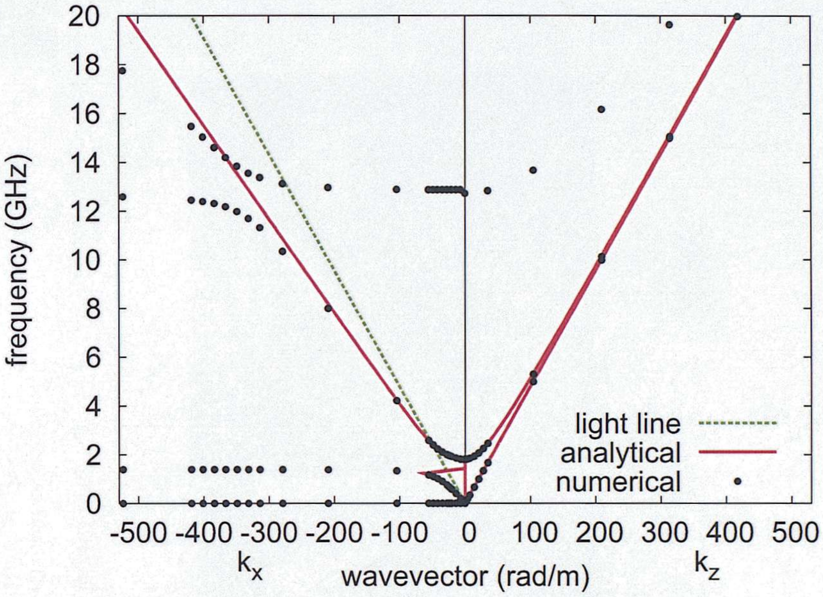

Figure 9.3: The analytical prediction for the band structure (red solid line), plotted with numerical results (dots) for a Swiss Roll metamaterial with dimensions $N = 2$, $d = 0.1mm$, $x = 0.05mm$, $R = 2mm$ and $a = 5mm$. Note that the left part of both plots is the band structure for k_x-propagation and the right part for k_z-propagation at high frequencies, the excitation of the first waveguide mode can be seen. The light line is plotted with a green dashed line.

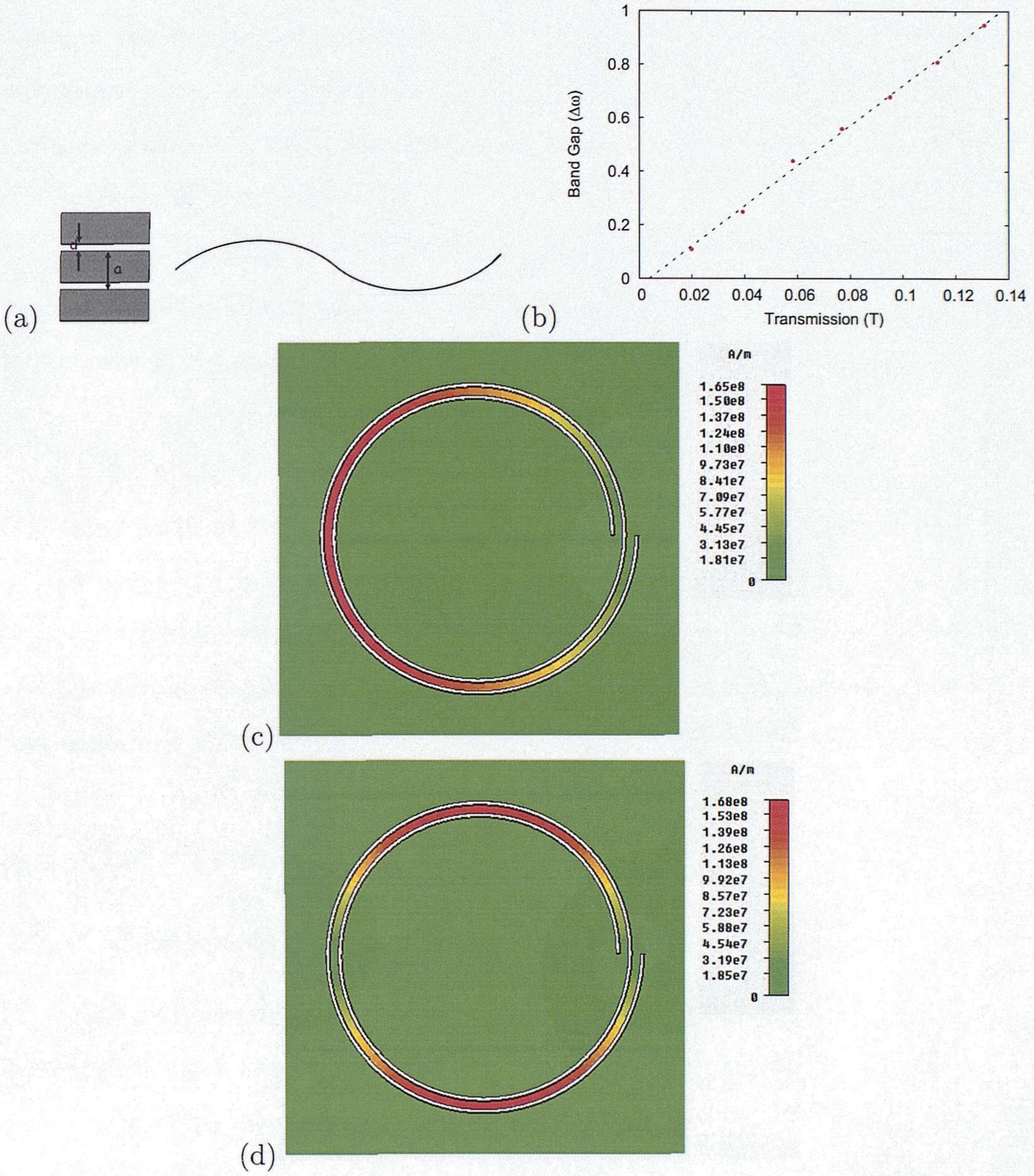

Figure 9.4: (a) Blocks arranged in a periodicity of a and d is the gap between them. (b)The size of the band-gap created due to the coupling of the waveguide and transverse modes is plotted, against the transmission of a wave through the block-medium (i.e. $T = \frac{2d}{d+a}$). (c) the magnetic field amplitude for the first waveguide mode and (d) the second waveguide mode.

However, as seen in figure 9.3 for k_x-propagation, the waveguide mode couples strongly with the transverse mode creating a band gap and the stronger the coupling between the two modes, obviously the bigger the band gap ($\Delta\omega$). A simple way to investigate this, is to model the spiral waveguide, as an array of blocks with gap between them of d and periodicity a as shown in figure 9.4(a), and calculate the transmission of a wave through this medium. The impedance of such a medium is given by $Z = (d/a)Z_0$, where Z_0 is the impedance of the hosting medium (i.e. vacuum). The transmission of the wave trapped in the waveguide is calculated by matching the impedance at the two media and:

$$T = \frac{2Z}{Z + Z_0} = \frac{2d}{d + a} \tag{9.16}$$

The bandwidth of the band-gap $\Delta\omega$ was measured numerically for several values of d, and is plotted in figure 9.4(b) against transmission ($T = \frac{2d}{d+a}$), and as expected they have a linear relationship. Therefore, for more fine dimensions of Swiss Roll (i.e. smaller d) and where ω_0 is in MHz frequencies, the coupling between the waveguide and transverse modes is expected to be weak with a negligibly small band gap.

9.2 Effective Electromagnetic Behaviour

9.2.1 Scattering Parameters

As discussed previously, the scattering parameters give an indirect insight to the electromagnetic behaviour of the structure. In this section an analytic prediction is derived and compared to numerical results.

Assuming that a metamaterial is consisted of Swiss Rolls in a square lattice and aligned with the z-axes, then the scattering parameters of a wave incident on a finite slab can be derived analytically using the method described in [3]. Note that the same method was used for calculating the S-parameters of a wave incident on a finite slab of wire metamaterials, where it was assumed that $\mu = 1$, which does not hold for Swiss

Roll metamaterials. Therefore, (5.13) takes the form:

$$\begin{aligned} T_S &= \frac{tt' exp(iq_x^{'}d)}{1 - r'^2 exp(i2q_x^{'}d)} \\ R_S &= r + \frac{tt'r' exp(i2q_x^{'}d)}{1 - r'^2 exp(i2q_x^{'}d)} \end{aligned} \tag{9.17}$$

where $q_x^{'} = i\sqrt{q'^2_z - \varepsilon_{yy}\mu_{zz}k_0^2}$ is the x-component of the wavevector inside the metamaterial slab of length d, ε_{yy} is given from (9.11) and μ_{zz} from (9.6). The transmission and reflection at the first interface (t and r) and second interface (t' and r') are given by:

$$\begin{aligned} t &= \frac{2\mu_{zz}q_x}{\mu_{zz}q_x + q'_x} \\ r &= \frac{\mu_{zz}q_x - q'_x}{\mu_{zz}q_x + q'_x} \\ t' &= \frac{2\mu_{zz}q'_x}{\mu_{zz}q_x + q'_x} \\ r' &= \frac{q'_x - \mu_{zz}q_x}{\mu_{zz}q_x + q'_x} \end{aligned} \tag{9.18}$$

where q_x is the x-component of the wavevector in vacuum.

For normal incidence $q'_z = 0$, the reflection coefficient of (9.17) is plotted in figure 9.5(a) and(b) (red solid line) with numerical calculations (blue dotted lines) on a 5-unit-cell slab with periodic boundary conditions along the y- and z-directions. The analytical and numerical results have an outstanding agreement of $\sim$ 92% for frequencies up to $9GHz$, with a small difference on the value of ω_0, which is due to the approximations taken analytically and are not valid for the structure simulated (due to modelling difficulties). At frequencies higher than $9GHz$ the agreement breaks since the wavelength becomes comparable to lattice constant and the homogenization model breaks. At these high frequencies, internal scattering within the unit cell takes place and the homogenization theory is not valid. Also, the excitation of the first waveguide mode can be seen in figure 9.5(a), and its value is in agreement with (9.14) at $\sim$ 98%.

9.2.2 Retrieval Method for Bianisotropic Media

Although the scattering parameters show important information about the behaviour of a structure, it is usually preferable to obtain the effective electromagnetic parame-

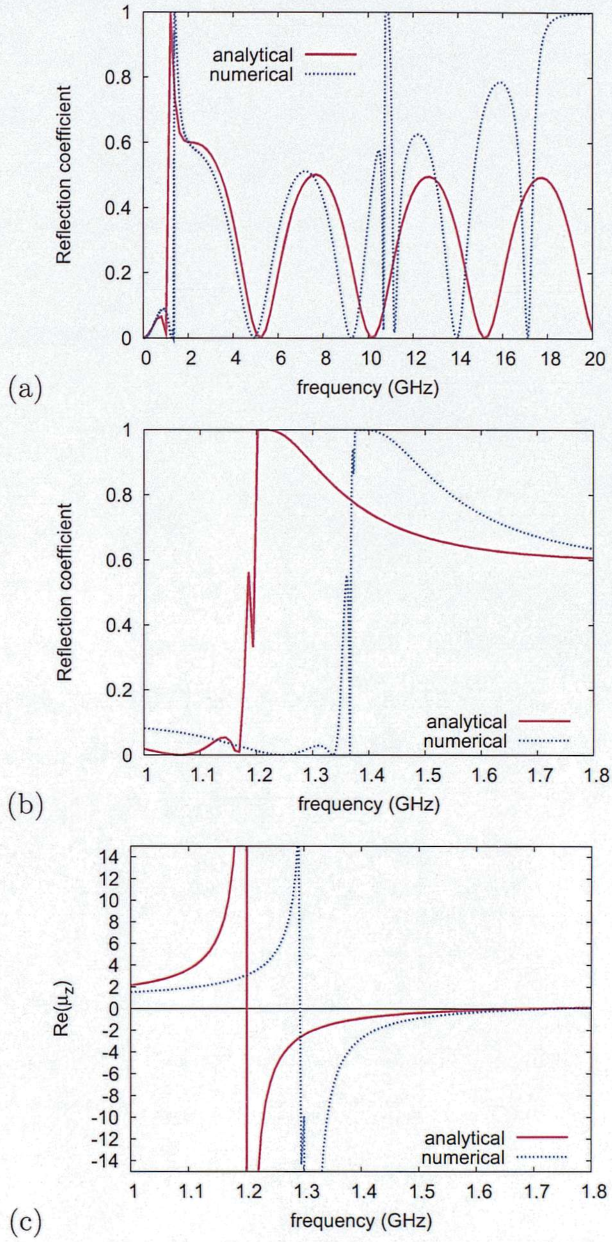

Figure 9.5: The analytic prediction (red solid line) and the numerical result (blue dotted line) for the reflection coefficient ($|R|$) is plotted for normal incidence on a five-unit cell slab of a Swiss Roll metamaterial with dimensions $N = 2$, $d = 0.1mm$, $x = 0.05mm$, $R = 2mm$, $a = 5mm$ and band structure shown in figure 9.2. (a)for a wide frequency range, where the excitation of the first waveguide mode can be seen and (b) for $\omega \rightarrow \omega_o$ (c)The analytical prediction of $Re(\mu_{zz})$ shown in (9.6) (red solid line) plotted with $Re(\mu_{zz})$ retrieved from numerical results (blue dotted line).

ters, since they are directly linking D and B with E and H. The effective parameters can be retrieved from the numerically calculated S-parameters, using methods that are well documented in literature [43, 44] for isotropic media, as well as for anisotropic media in [45] (such as wires combined with split-ring resonators). However, Chen et.al. [46] discuss ε and μ retrieval, specifically for bianisotropic media, like Swiss-Roll metamaterials.

The S_{11} and S_{21}-parameters can be written as [43, 44, 45, 46]:

$$S_{11} = \frac{r_{01}[1 - \exp(i2nk_0ma)]}{1 - |r_{01}|^2 \exp(i2nk_0ma)} \tag{9.19}$$

$$S_{21} = \frac{(1 - |r_{01}|^2) \exp(ink_0ma)}{1 - |r_{01}|^2 \exp(i2nk_0ma)} \tag{9.20}$$

where $r_{01} = (z-1)/(z+1)$, $z_0 = 1$ is the vacuum impedance, z the medium impedance, n the refractive index, k_0 the wavevector of the incident wave, m the number of unit cells in the slab, ma the width of the slab. Note that (9.19) and (9.20) are identical to (9.17), just written in a different format. Solving (9.19) and (9.20), the impedance and refractive index are obtained [46]:

$$z = \sqrt{\frac{DC'' - B'}{A'} - \frac{D^2}{4}} + i\frac{D}{2} \tag{9.21}$$

where

$$\begin{aligned} A &= 2S_{11} - S_{11}^2 - 1 + S_{21}^2 \\ B &= 2S_{11} + S_{11}^2 + 1 - S_{21}^2 \\ C &= S_{11}^2 + S_{21}^2 - 1 \\ D &= \frac{A''B' - A'B''}{A''C'' + A'C'} \end{aligned} \tag{9.22}$$

and $(.)'$, $(.)''$ denote the real and imaginary parts of the operators respectively and:

$$n = -\frac{i}{k_0 d} \ln\left(\frac{r_{01} - S_{11}}{S_{21} r_{01}}\right) \tag{9.23}$$

Note that in order to avoid violating causality we choose the branches of the above equation, where $Re(z) \geq 0$ and $Im(n) \geq 0$. Hence, the electric permittivity along the y-axis is given by:

$$\varepsilon_{yy} = \frac{n - i\kappa}{z} \tag{9.24}$$

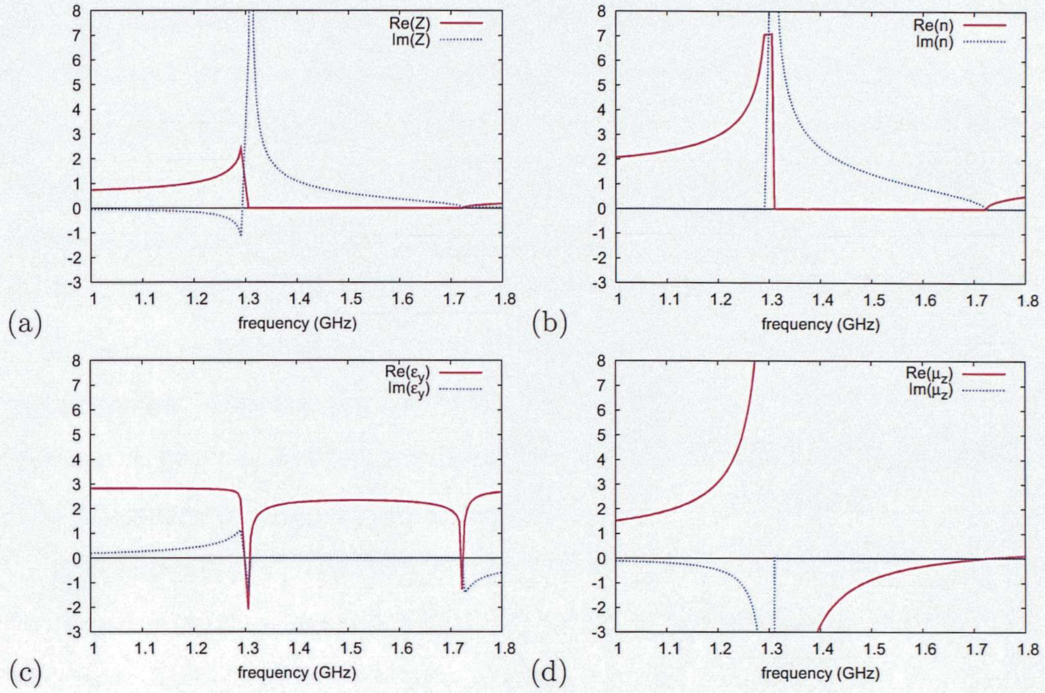

Figure 9.6: The retrieved effective electromagnetic parameters (z, n, ε, μ) from numerical S-parameter results of a Swiss Roll metamaterial with dimensions $x = 0.05mm$, $d = 0.1mm$, $R = 2mm$, $a = 5mm$ and $N = 2$. The electromagnetic parameters are plotted for $\omega \rightarrow \omega_0$ and the real parts are plotted with the red solid line and the imaginary part with the blue dotted line. (a)impedance (Z), (b)refractive index (n), (c)electric permittivity (ε_y) across the Swiss Roll and (d)the magnetic permeability (μ_z) along the roll.

the magnetic permeability along the z-axis:

$$\mu_{zz} = z(n + i\kappa) \tag{9.25}$$

and the magnetoelectric coupling by:

$$\kappa = \frac{1}{2i}\left(\frac{\mu_{zz}}{z} - \varepsilon_{yy} z\right) \tag{9.26}$$

9.2.3 Retrieved Effective Electromagnetic Parameters

Applying the above method to the numerically calculated S-parameters shown in figure 9.5(b), the magnetic permeability is retrieved and plotted (blue dotted line) together with the analytical prediction (red solid line) of (9.6) in figure 9.5(c). They both have the same shape with an exceptional agreement (higher than 92%). This denotes that the modelling of a Swiss Roll metamaterial as a medium with effective parameters given by (9.6) and (9.11) is a sufficiently accurate model. Furthermore, the real and imaginary parts of the retrieved ε_{yy}^{eff}, μ_{zz}^{eff}, refractive index (n) and impedance (z) are shown in figure 9.6. Note that since the metamaterial discussed here is a passive medium, the requirements $Re(z) \geq 0$ and $Im(n) \geq 0$ are applied during the retrieval procedure, in order to avoid violating causality. It can be seen that both the impedance and refractive index real parts are always positive for the frequencies where the metamaterial is passive, and equal to zero for stop-band frequencies, as expected. Also, their imaginary parts have a sharp peak at the resonance frequency.

Furthermore, the dependence of $Re(\mu_z)$ on the size of the gap between the conducting sheets (d) is investigated and is plotted in figure 9.7(a), where the expected behaviour from (9.6) is obtained. However, it is clear from figure 9.7(a) that the agreement between numerical and analytical results depends on the validity of the assumption taken theoretically that $R \gg d$. The disagreement is only on the value of ω_0 and reduces for higher values of (R/d). Also, the dependence of μ_{zz}^{eff} on dielectric constant ε_d of the material inside the gap is plotted in figure 9.7(b), where the behaviour is as expected from (9.6). The disagreement between analytical and numerical results is due to the value of d (i.e. $d = 0.1mm$), where the contribution of various ε_d on the accuracy is almost negligible. Finally, in figure 9.7(c), the retrieved $Re(\mu_z)$ is plotted for various thicknesses of the conducting sheet and for $d = 0.1mm$, $\varepsilon_d = 1$. As the conducting sheet becomes thinner, the value of ω_0 converges. However, the inaccuracy that a thicker conducting sheet induces to numerical results is minor (i.e. $\sim 3-5\%$), with respect to the extreme reduction on the demand of computational power and time.

9.3 Swiss Roll Metamaterials at MHz frequencies

Swiss Roll metamaterials are most commonly used at MHz frequencies [40, 34, 33, 41], where they deploy an infinitely thin conducting sheet and $R \gg d$. Despite the tremendous modelling and computational problems of such a complicated structure, the S-

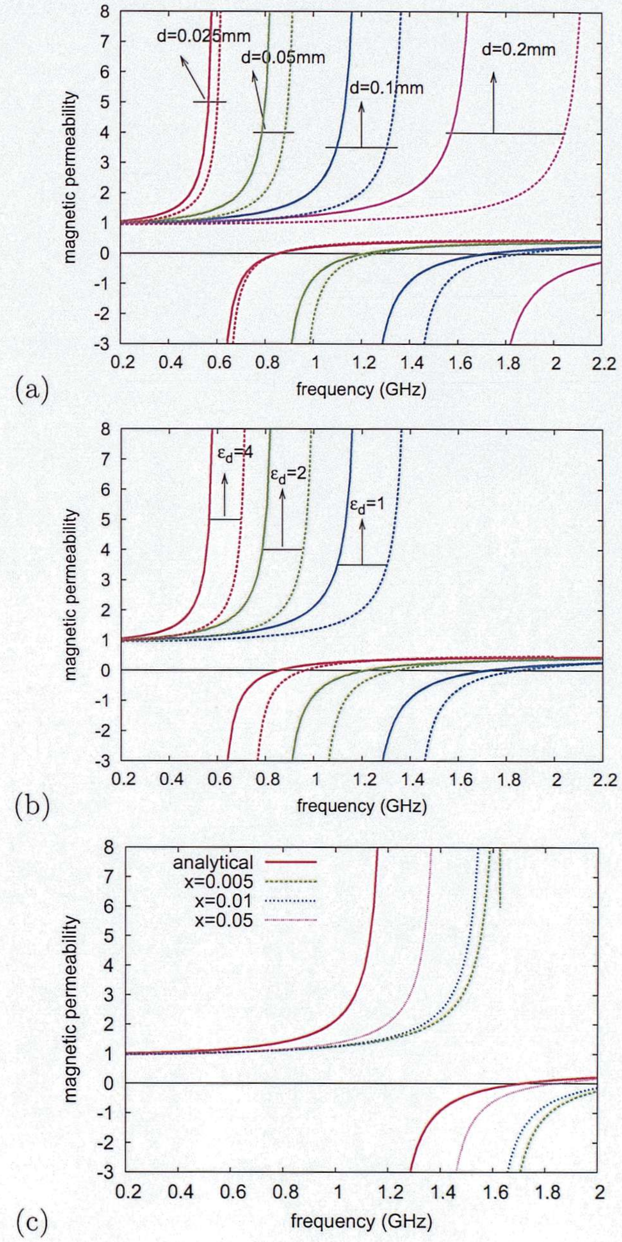

Figure 9.7: For Swiss Rolls with radius $R = 2mm$, lattice constant $a = 5mm$ and $N = 2$ (a) analytical (solid lines) and retrieved (dashed lines) $Re(\mu_{zz})$ is plotted against frequency for various values of d (red: $d = 0.025mm$, green: $d = 0.05mm$, blue: $d = 0.1mm$ and pink: $d = 0.2mm$) filled with vacuum (i.e. $\varepsilon_d = 1$) and for $x = 0.05mm$ (b)Analytical (solid lines) and retrieved (dashed lines) of $Re(\mu_z)$ against frequency for various values of ε_d (red: $\varepsilon_d = 4$, green: $\varepsilon_d = 2$ and blue: $\varepsilon_d = 1$) for $d = 0.1mm$ and $x = 0.05mm$. (c) Analytical (solid lines) and retrieved (dashed lines) of $Re(\mu_z)$ against frequency for various values of the conducting sheet's thickness x ($d = 0.1mm$ and $\varepsilon_d = 1$).

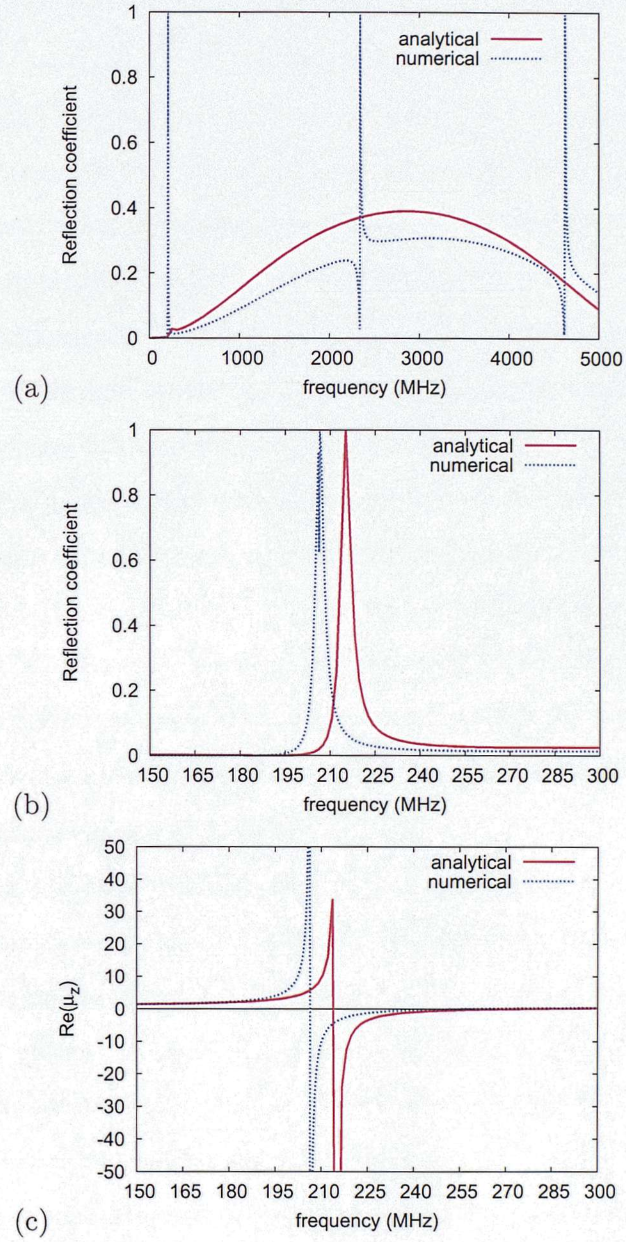

Figure 9.8: The analytic prediction (red solid line) and the numerical result (blue dotted line) for the reflection coefficient ($|R|$) is plotted for normal incidence on a five-unit cell slab of a Swiss Roll metamaterial with dimensions $N = 5$, $x = 5\mu m$, $d = 25\mu m$, $R = 2500\mu m$ and $a = 7000\mu m$. (a)for a wide frequency range, where the excitation of the first two waveguide modes can be seen and (b) for $\omega \rightarrow \omega_o$ (c)The analytical prediction of μ_z shown in (9.6) (red solid line) plotted with μ_z retrieved from numerical results (blue dotted line).

parameters were numerically calculated for a Swiss Roll metamaterial with dimensions $N = 5$, $x = 5\mu m$, $d = 25\mu m$, $R = 2500\mu m$ and $a = 7000\mu m$ using CST Microwave Studio. For normal incidence on a three-unit-cell slab, the analytical (red solid line) and numerical (blue dotted line) results for $|R|$ are plotted in figure 9.8(a) and (b). The analytical prediction was calculated with (9.17). The agreement between analytical and simulation results is $\sim 95\%$ for frequencies around ω_0. The S-parameters were also calculated numerically for a broader frequency range, where the excitation of the first and second waveguide modes can be seen as sharp resonances in figure 9.8(a). The waveguide frequencies are also well predicted by (9.14), with an agreement of $\sim 99\%$.

The retrieved μ_{zz}^{eff} is plotted with the analytical prediction of (9.6), in figure 9.8(c). Both have the same behaviour, with a slight shift on the value of ω_0 and the electromagnetic parameters (ε_{yy}^{eff}, n, z and μ_{zz}^{eff}) retrieved from numerical S-parameter results are plotted in figure 9.9. The real parts of the impedance and refractive index are always positive, or zero for frequencies where μ_{zz} takes negative values. The main difference from the GHz-structure is that ε_{yy} has a weaker resonance, which approaches even more the approximation taken initially in (9.11).

Finally, using the retrieved ε_{yy}^{eff} and μ_{zz}^{eff} shown in figure 9.9 and the analytical dispersion equations of (9.13), an estimate for the band structure for a Swiss Roll metamaterial with dimensions $N = 5$, $x = 5\mu m$, $d = 25\mu m$, $R = 2500\mu m$, $a = 7000\mu m$ was derived and plotted in figure 9.10, since it was not possible to model the structure and derive the band structure directly from numerical calculations. In figure 9.10(a), the band structure is plotted for $k_x \rightarrow 0$ and in figure 9.10(b), for higher frequencies, where the first waveguide mode can be seen. Also note that since d is much smaller, the waveguide mode coupling with the transverse mode is considerably weaker, as expected from (9.16).

The agreement between analytical and numerical results for a frequency range from few MHz to tens of GHz is remarkable. An important advantage of Swiss Rolls over other artificially magnetic media (such as Split-Ring-Resonators), is the fact that their resonance frequency can be tune over a very broad frequency range by simply changing d (figure 9.7(a)), ε_d(figure 9.7(c)), R or a. Furthermore, they are magnetically active for low frequencies without demanding large unit cells, since ω_0 can be tuned by simply

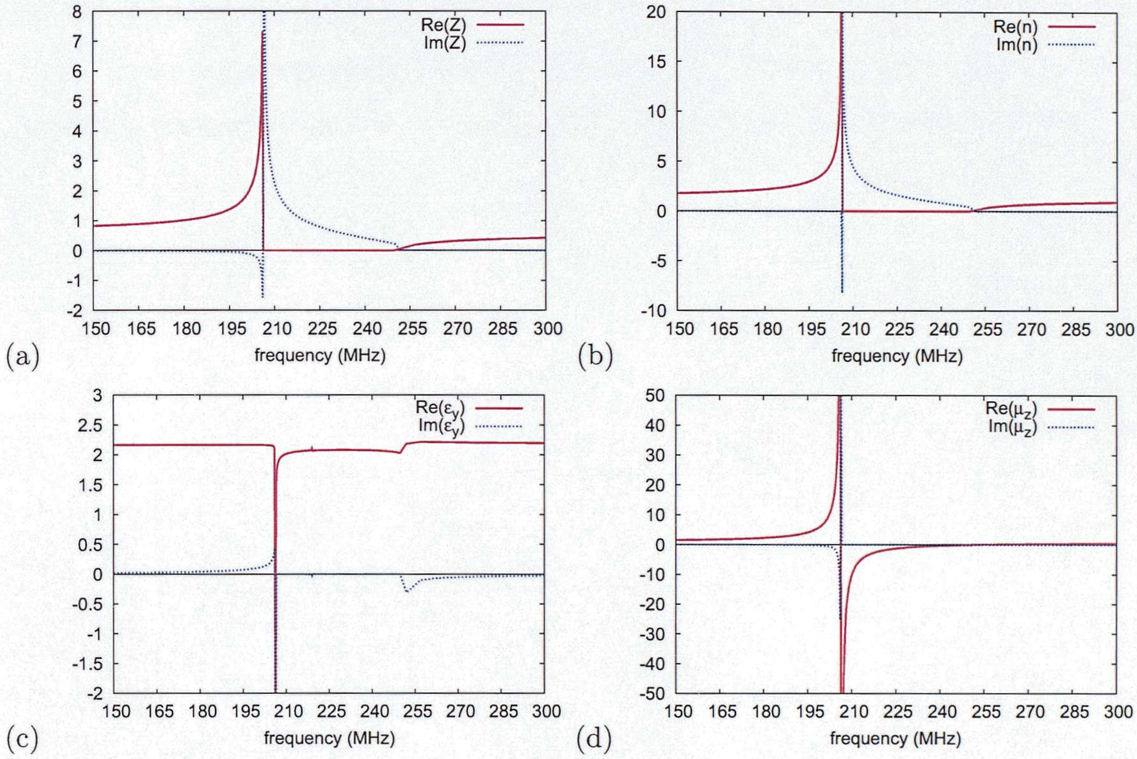

Figure 9.9: The retrieved effective electromagnetic parameters (z, n, ε, μ) from numerical S-parameter results of a Swiss Roll metamaterial with dimensions $N = 5$, $x = 5\mu m$, $d = 25\mu m$, $R = 2500\mu m$ and $a = 7000\mu m$. The electromagnetic parameters are plotted at $\omega \rightarrow \omega_0$ and the real parts with the red solid line and the imaginary part with the blue dotted line: (a)impedance (Z), (b) refractive index (n), (c)electric permittivity across the rolls (ε_y) and (d) magnetic permeability along the rolls (μ_z)

increasing the number of turns N, a property that makes them handy and easier to be used for devices operating in the MHz range, such as Magnetic Resonance Imaging (MRI) and for antenna applications.

The agreement between theory and numerical results is outstanding and allows us to move to the even more complicated structure of chiral Swiss Rolls, firstly introduced in [36]. As discussed in [36, 37], the magnetic resonant behaviour of chiral Swiss Rolls arises in the same way as for the non-chiral structure. However, due to chirality and magnetic resonant behaviour, a negative band for one wave polarization is obtained.

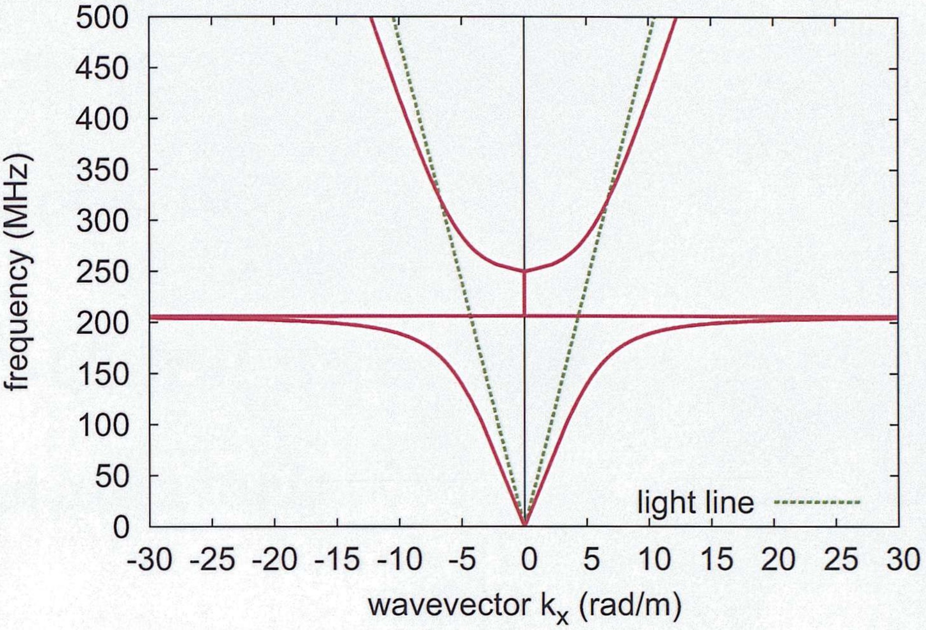

(a)

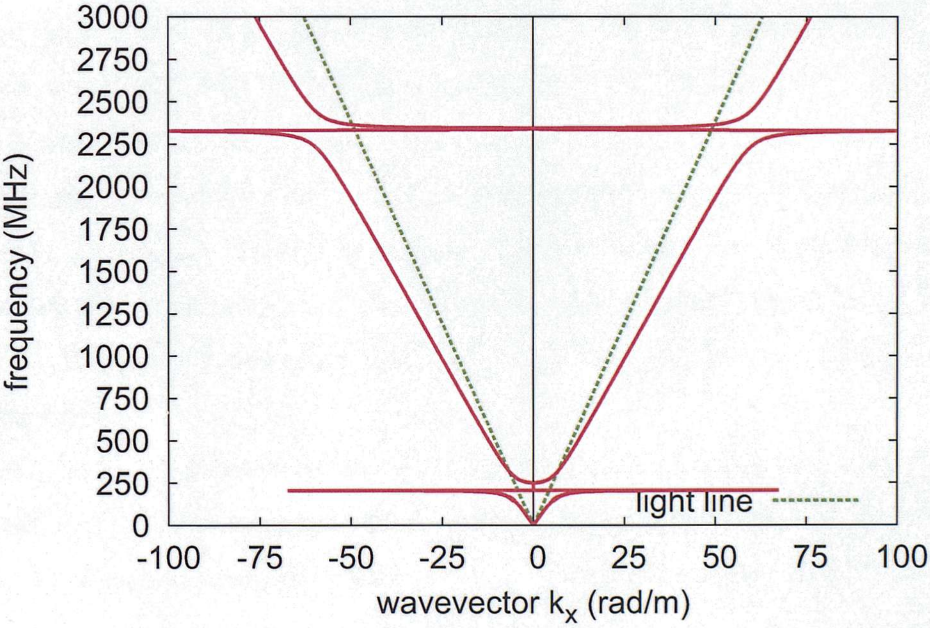

(b)

Figure 9.10: The band structure for k_x-propagation in a Swiss Roll metamaterial with dimensions $N = 5$, $x = 5\mu m$, $d = 25\mu m$, $R = 2500\mu m$ and $a = 7000\mu m$. (a) The band structure for $\omega \rightarrow \omega_0$ and (b) for a wide frequency range, where the first waveguide mode cam be seen.

Chapter 10

2D-Chiral Swiss-Roll metamaterials

As discussed in section 1.1, negative refraction is one of the most well-known and notable properties that metamaterials are able to achieve. Veselago in 1968 [7] pointed out that a material with both $Re(\varepsilon(\omega))$ and $Re(\mu(\omega))$ simultaneously negative, exhibits a negative refractive index. This can be analytically proved by considering causality and dispersion in real media, as well as the fact that from Maxwell's equations, $n = \sqrt{\varepsilon(\omega)\mu(\omega)}$. Therefore, a straightforward design for a negatively refracting metamaterial is to combine an electric and a magnetic resonant structure, with their resonance frequency tuned such that $Re(\varepsilon)$ and $Re(\mu)$ to be negative for the same frequency range.

Shelby *et. al.* [10] constructed and experimentally tested the first negatively-refracting metamaterial. It was composed of an artificial plasma (i.e. wire-mesh metamaterial [11, 12, 13]), and a magnetic resonator (i.e. split-ring resonators [9]), which provide the negative permittivity and negative permeability respectively. These metamaterials are usually called Doubly Negative Metamaterials (DNG), since two different resonant structures are combined to provide a negative refracting index over a frequency range, and a typical band structure of a DNG metamaterial is plotted in figure 10.1. Note that the dispersion diagram is not continuous at the transition from the negative to positive band [36]. Finally, the applications of DNG metamaterials are considerably

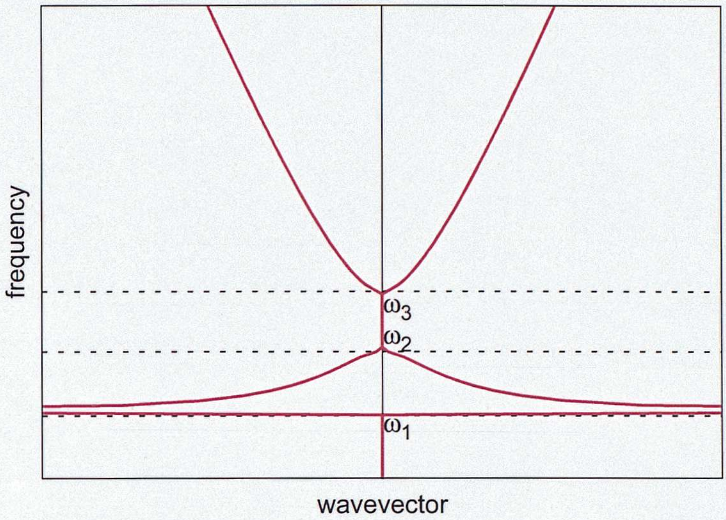

Figure 10.1: The band structure of a typical doubly negative metamaterial, consisted from a wire mesh and Split Ring resonators, where ω_1 is the resonant frequency of the split ring resonators, ω_2 is the magnetic plasma frequency of the split ring resonators and ω_3 is the plasma frequency of the wire mesh.

limited due to resonance losses and manufacturing limitations of artificially magnetic structures at high frequencies.

Several alternative metamaterial structures are discussed in the literature that support negative refraction and manage to overcome some of DNG-metamaterial's limitations, such as chiral media. Chiral metamaterials exhibit a backward wave without requiring both ε and μ to be negative [36, 47, 48, 49, 50]. Generally, a structure is said to be chiral if it is not identical to its mirror image and a chiral medium macroscopically rotates the wave's polarization. Hence, the electromagnetic fields in a chiral medium can be written as [36]:

$$\begin{bmatrix} \mathbf{D} \\ \mathbf{B} \end{bmatrix} = \begin{bmatrix} \chi_{EE} & \chi_{EH} \\ \chi_{HE} & \chi_{HH} \end{bmatrix} \begin{bmatrix} \mathbf{E} \\ \mathbf{H} \end{bmatrix} \tag{10.1}$$

where $\mathbf{D}$ is the electric displacement vector, $\mathbf{E}$ the electric field intensity, $\mathbf{B}$ is the magnetic induction field and $\mathbf{H}$ the magnetic field intensity. The parameters χ_{EE} and χ_{HH} are the electric permittivity and magnetic permeability of the medium, respectively, and χ_{EH} and χ_{HE} are the chirality terms, whose values determine the rotation

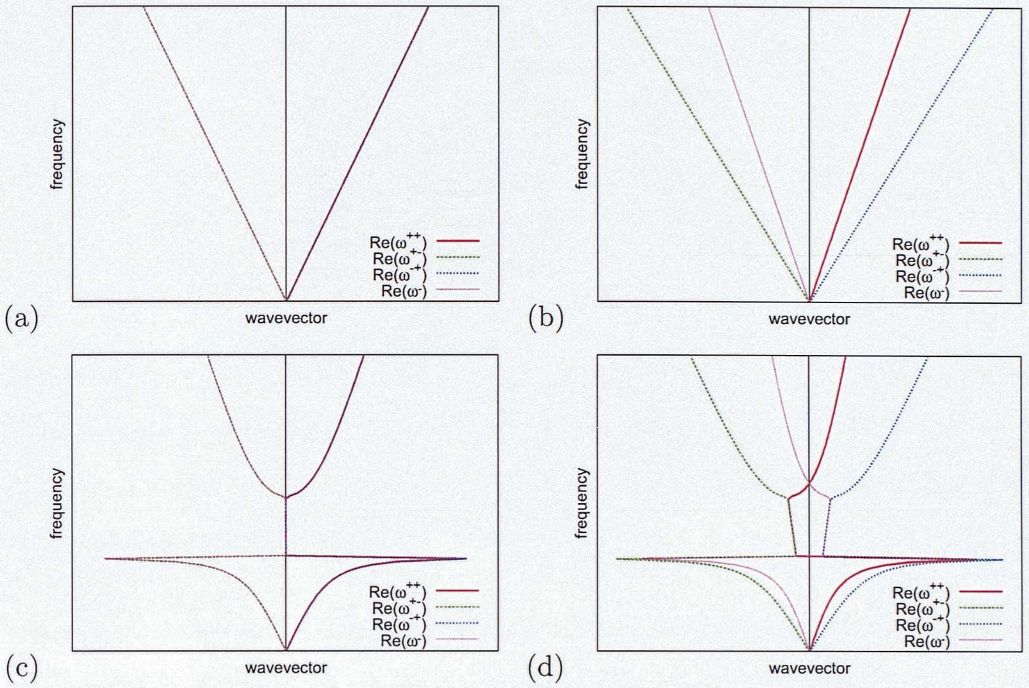

Figure 10.2: The band structure of a homogeneous isotropic medium (a) without chiral inclusions (b) with chiral inclusions. The band structure of a magnetically (or electrically) resonant structure (c) without chiral inclusions (d) with chiral inclusions

of the wave's polarization.

A homogeneous medium with constant ε and μ has a doubly degenerate transverse mode as shown in figures 10.2(a). Note that where ω^{ij}, i shows the wave's polarization and j the group velocity of the wave. If chiral inclusions are introduced in this medium, then the two degenerate modes split, producing the band structure shown in figure 10.2(b). Similarly, a dipole medium (electric or magnetic) has two degenerate modes, with a stop-band for frequencies where ε or μ is negative as shown in figure 10.2(c). If chiral inclusions are introduced, the degenerate modes split and give rise to a negative band for one of the wave polarizations, as shown in figure 10.2(d) [36]. Hence, chiral metamaterials are able to achieve negative refraction with a continuous transition between negative and positive bands and requiring just one resonant structure in contrary to DNG. Here, it is worth mentioning that chiral inclusions of aligned handedness ensure macroscopic rotatory power. If half of them have opposite handed-

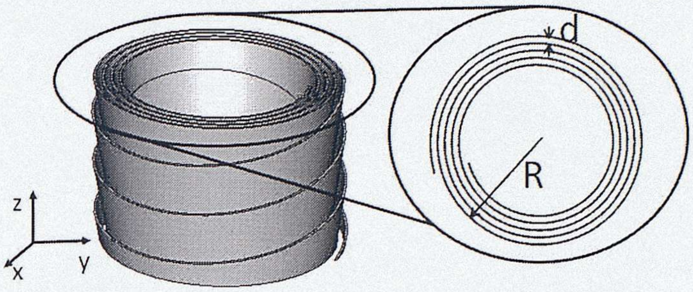

Figure 10.3: A chiral Swiss Roll is constructed by winding an insulated conducting sheet around a cylindrical mandrel, creating an overlapping helix. The cross section of a chiral Swiss Roll is shown as well, where R is the radius and d the gap between the conducting sheet.

ness, the rotatory power disappears [51] creating a racemic medium. Examples of chiral metamaterials are helically-shaped conducting wires [50, 52], chiral Swiss Rolls [36, 37], twisted crosses [53] and twisted-crossed "S" symbols [47, 49, 54]. In this chapter, chiral Swiss Roll metamaterials are discussed (figure 10.3) and is shown that they exhibit an enormous chirality compared with other chiral structures reported previously in the literature.

10.1 Effective Electromagnetic Parameters

A chiral Swiss Roll can be constructed by winding an insulated conducting sheet around a cylindrical mandrel, creating an overlapping helix as shown in figure 10.3. Each layer of the conducting sheet is separated by distance d, filled with a dielectric material of ε_d (or vacuum $\varepsilon_d = 1$). The external radius of the rod is R and N is the number of turns measured at a cross-section. The unwrapped conducting sheet has the shape shown in figure 10.4 with width given by $w = 2\pi RN \sin\theta$ and length $l = N2\pi R\tan\theta$. When wrapped around a mandrel creates a chiral Swiss Roll with periodicity $p = 2\pi R\tan\theta$.

The structure has a magnetic resonance, arising in the same way as for non-chiral Swiss Rolls. When a magnetic field (H_0) is applied along the roll, currents are induced on the conducting elements of the structure. Hence, an emf opposing H_0 arises and it

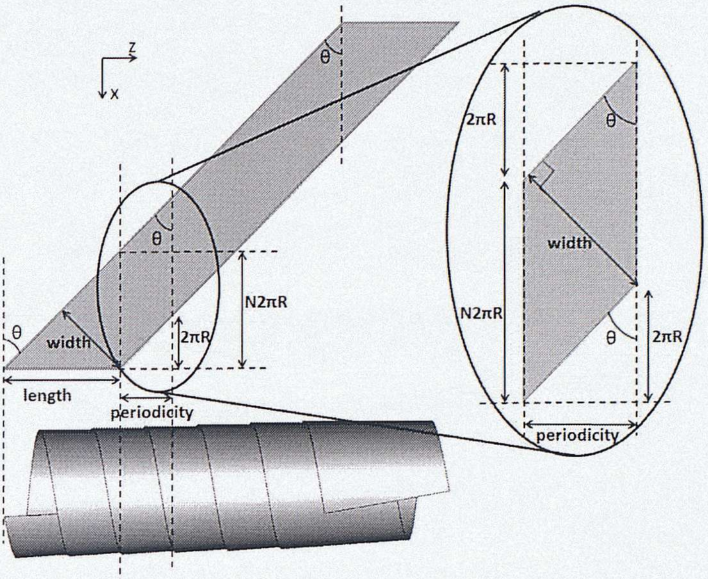

(a)

Figure 10.4: The (unfolded) conducting sheet used to create a right handed chiral Swiss Roll. When wrapped around a cylindrical mandrel, a helical conducting structure is created. The enlarged part is the unfolded section of the foil that when wrapped gives the unit cell of a chiral Swiss Roll.

macroscopically appears that 'magnetic' monopoles are flowing up and down the roll. However, the helical shape of the structure gives rise to chirality and therefore it is also expected the structure to macroscopically rotate the wave's polarization [36].

In order to derive the electromagnetic and chirality parameters of a chiral Swiss Roll (more details in Appendix G), initially consider uniform fields H_0 and E_0 applied along a right-handed chiral Swiss Roll shown in figure 10.3 (i.e along the z-axes). The H_0-field induces a current flowing in the x-y plane. The E_0-field creates charge accumulation at the edges of the foil, since it is not continuous along the z-axis, giving rise to an electric field perpendicular to the edges of the conducting sheet as shown in figure 10.5(a) (resolved to x- and z- components). The edges of the conducting foil are exposed either outside or inside the roll and since the exposed part of the conducting sheet is charged as shown in figure 10.5 (i.e. dotted lines within the grey area show the exposed part of the conducting sheet), the outer and inner surfaces of the roll are oppositely charged. Finally, note that infinite rolls are considered (i.e. periodic boundary conditions along the z-axes).

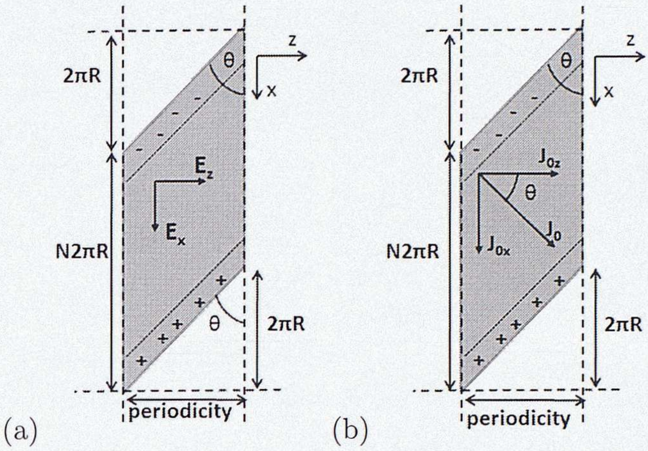

Figure 10.5: The periodic element of a chiral Swiss Roll unwrapped. The dotted lines on the unfolded sheet show the exposed part of the conducting foil to either the inside or outside of the chiral Swiss Roll. (a) The electric field due to charge accumulation at the edges of the conducting sheet, resolved in x- and z- components. (b) The current $\mathbf{J_0}$ is perpendicular to the edges of the foil (i.e. along the foil width) and is dependent on the charge accumulation at the edges.

Assuming that there are no local field effects, the cylinder has rotational symmetry and the current varies only across the width of the conducting sheet. Also, since the foil within the dotted lines is not exposed to either the outside or inside of the roll, J_0 is constant in magnitude and direction, and can be written as:

$$J_0 = J_{0x} \sin\theta + J_{0z} \cos\theta \tag{10.2}$$

where $\mathbf{J_0}$ is the current perpendicular to the edges of the unfolded conducting sheet as shown in figure 10.5(b). Furthermore, assuming that the gap between the conducting sheet is small (i.e. $R \gg d$) and that N (number of turns) is large, a large overlap of the conducting sheet is ensured, which gives rise to high capacitance. The charges accumulated at the edges of the foil, charge the capacitor (i.e. overlapping conducting sheet). Therefore, the current across the width of the foil (more details in Appendix G) is given by:

$$J_{0x} sin\theta + J_{0z} cos\theta = \frac{\varepsilon_d \varepsilon_0 2\pi R sin\theta}{(N-1)d} \tag{10.3}$$

The magnetic field along the z-axis (i.e. H_z) is given by:

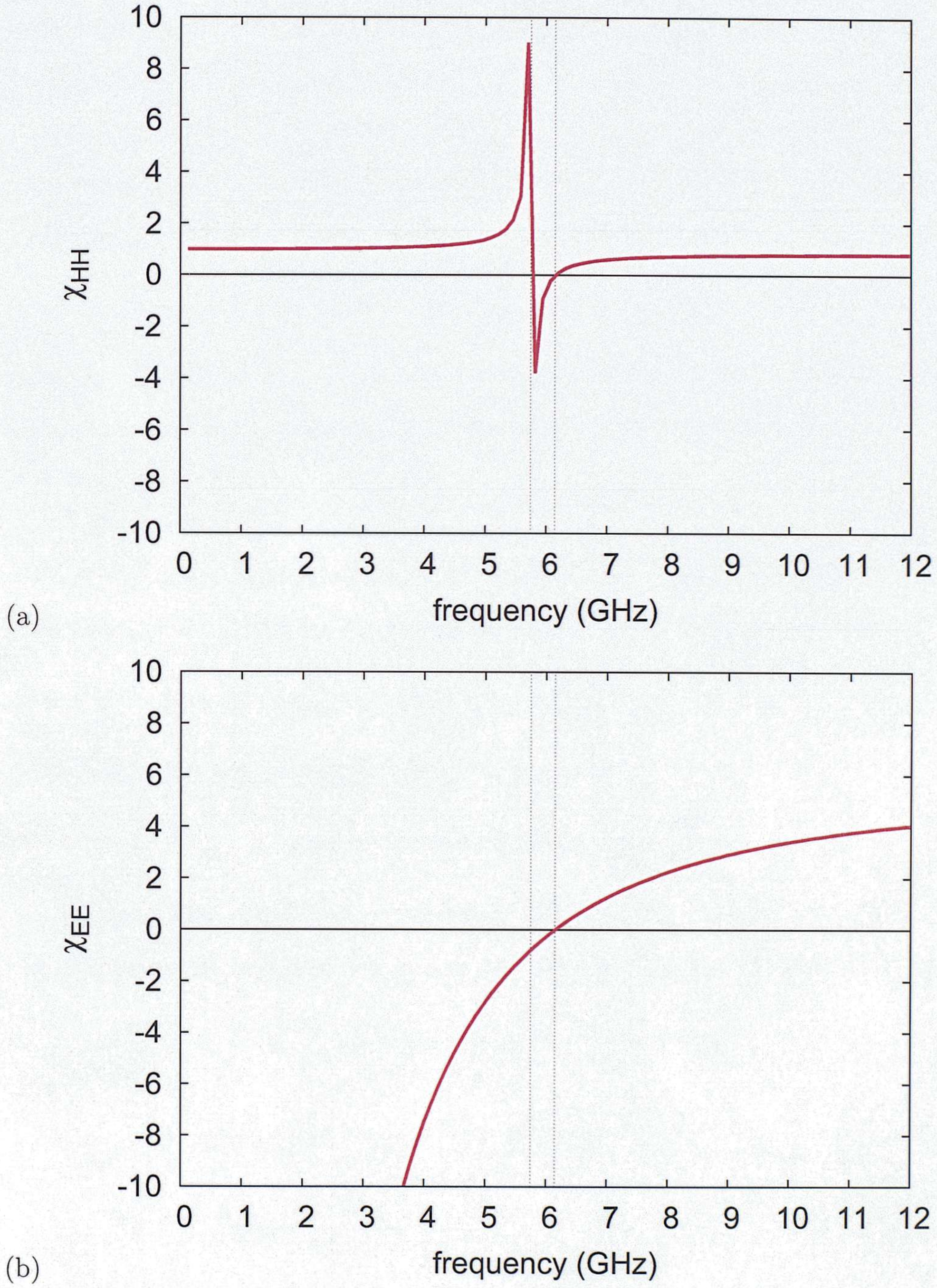

Figure 10.6: For Swiss Rolls of $N = 2$, $R = 1mm$, $l = 5mm$, $x = 0.05mm$, $d = 0.35mm$, $\theta = 21,7^{\circ}$ and $a = 5mm$ (a)The magnetic permeability (χ_{HH}) and (b)the electric permittivity tensor (χ_{EE}) are plotted.

$$H_z = H_0 + J_{0x}(1 - F) \tag{10.4}$$

where $F = \pi R^2/a^2$ is the filling factor, a the lattice constant, H_0 is the applied magnetic field and J_{0x} is the induced current from H_0. Due to J_{0x} current, an emf ($\mathcal{E}$) arises that needs to be balanced with the drop of the potential (V) (i.e. due to the capacitance of the structure) and conducting losses ($2\pi R(N-1)\rho J_{0x}$), where ρ is the resistance of the conducting sheet per unit length. Therefore,

$$\mathcal{E} = i\omega(N-1)\pi R^2 \mu_0 H_z = V + 2\pi R(N-1)\rho J_{0x} \tag{10.5}$$

Finally, the inner and outer exposed foil give rise to the capacitive element of the structure and has a potential difference of V, which is given by:

$$V = (N-1)2\pi R tan\theta(E_0 + E_P) \tag{10.6}$$

where E_P is the depolarizing field arising from the charges accumulated at the edges of the foil and are driven by J_{0z} per unit length of the circumference of the roll. Therefore:

$$E_P = \left(\frac{2\pi R}{i\omega\varepsilon_d\varepsilon_0 a^2} - \rho\right) J_{0z} \tag{10.7}$$

and hence the potential difference V is given by:

$$V = (N-1)2\pi R tan\theta \left[E_0 + \left(\frac{2\pi R}{i\omega\varepsilon_d\varepsilon_0 a^2} - \rho\right) J_{0z}\right] \tag{10.8}$$

Solving the above four equations ((10.3), (10.4), (10.5) and (10.8)), the inverse electromagnetic and chirality parameters can be obtained (derivation in Appendix G):

$$[\chi^{-1}]_{HH} = \frac{1}{(1-F)}\left(\frac{\omega^2 - \omega_0^2 + i\Gamma\omega}{\omega^2 - \omega_{mp}^2 + i\Gamma\omega/(1-F)}\right) \tag{10.9}$$

$$[\chi^{-1}]_{EE} = G\left(\frac{\omega^2 + i\omega\Gamma/(1-F)}{\omega^2 - \omega_p^2 + i\omega\Gamma/(1-F)}\right) \tag{10.10}$$

$$[\chi^{-1}]_{HE}/\varepsilon_0 = \frac{iR}{2L\tan\theta}\left(\frac{\omega_{mp}^2\omega}{\omega^2 - \omega_{mp}^2 + i\Gamma\omega/(1-F)}\right) = [\kappa^{-1}]_{HE} \tag{10.11}$$

$$[\chi^{-1}]_{EH}/\mu_0 = -\frac{iR}{2L\tan\theta}\left(\frac{\omega\omega_{mp}^2}{\omega^2 - \omega_{mp}^2 + i\Gamma\omega/(1-F)}\right) = [\kappa^{-1}]_{EH} \tag{10.12}$$

where χ^{-1} are the elements of the inverse matrix tensor in (10.1), given by:

$$\begin{bmatrix} [\chi^{-1}]_{EE} & [\chi^{-1}]_{EH} \\ [\chi^{-1}]_{HE} & [\chi^{-1}]_{HH} \end{bmatrix} = \begin{bmatrix} \chi_{EE} & \chi_{EH} \\ \chi_{HE} & \chi_{HH} \end{bmatrix}^{-1} \tag{10.13}$$

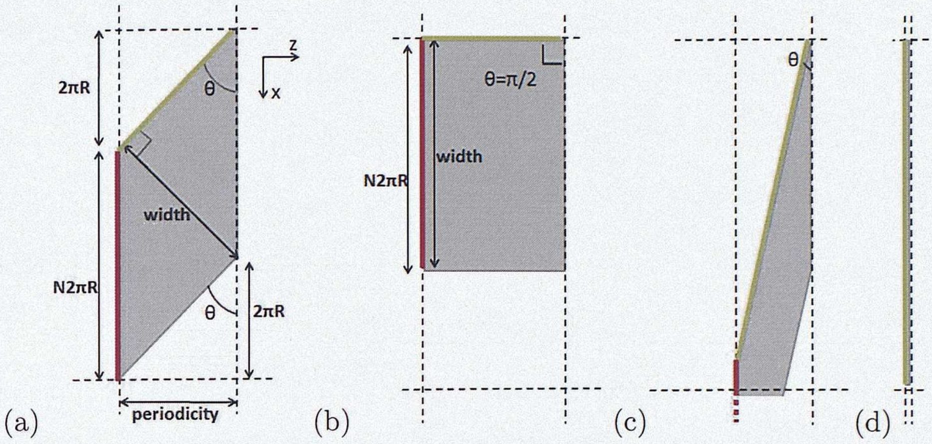

Figure 10.7: The unit cell of a chiral Swiss Roll for various values of θ. A chiral Swiss Roll with (a)a large θ, (b)$\theta = \pi/2$, creating a non-chiral Swiss Roll, where (10.18) converges to (9.7), (c) a small θ (d) $\theta \to 0$ where a non-chiral Swiss Roll is created, but note that $N \to \infty$. Also the periodicity of the unit cells changes with $\tan\theta$.

Therefore, the non-inverse electric permittivity (χ_{EE}), magnetic permeability (χ_{HH}) and chirality parameters (χ_{EH} and χ_{HE}) are obtained from the matrix identity:

$$\begin{bmatrix} \chi_{EE} & \chi_{EH} \\ \chi_{HE} & \chi_{HH} \end{bmatrix} = \begin{bmatrix} \left[\chi^{-1}\right]_{EE} & \left[\chi^{-1}\right]_{EH} \\ \left[\chi^{-1}\right]_{HE} & \left[\chi^{-1}\right]_{HH} \end{bmatrix}^{-1} = \frac{1}{det} \begin{bmatrix} \left[\chi^{-1}\right]_{HH} & -\left[\chi^{-1}\right]_{EH} \\ -\left[\chi^{-1}\right]_{HE} & \left[\chi^{-1}\right]_{EE} \end{bmatrix} \tag{10.14}$$

where $det = \left[\chi^{-1}\right]_{EE} \left[\chi^{-1}\right]_{HH} - \left[\chi^{-1}\right]_{EH} \left[\chi^{-1}\right]_{HE}$. Note that $F = \pi R^2/a^2$ in (10.9) is the filling factor and that $\left[\kappa^{-1}\right]_{EH} = -\left[\kappa^{-1}\right]_{HE}$. Additionally, ω is the frequency, R, θ and d are the dimensions of the chiral Swiss Roll as defined in figures 10.3 and 10.4, a is the lattice constant and G is given by:

$$G = \frac{a^2 d}{8\pi^3 R^3 (N-1) L \tan^2\theta + a^2 d} \tag{10.15}$$

Furthermore

$$L = 1 - \omega \frac{i\varepsilon_d \varepsilon_0 a^2 \rho}{2\pi R} \tag{10.16}$$

and

$$\Gamma = \frac{2\rho}{\mu_0 R} \tag{10.17}$$

accounts for resistivity losses of the conducting sheet and ρ is the resistance of the roll per unit length. The resonance frequencies ω_0, is given by:

$$\omega_0 = c_0\sqrt{\frac{4\pi L d \tan^2\theta}{\varepsilon_d(8(N-1)L\pi^3R^3\tan^2\theta + a^2d)}} \qquad (10.18)$$

The magnetic (ω_{mp}) and electric (ω_p) plasma frequencies take the same values and are given by:

$$\omega_{mp} = \frac{\omega_0}{\sqrt{1-F}} = \omega_p \qquad (10.19)$$

Note that the periodicity of the chiral Swiss Roll changes with θ, (periodicity: $p = 2\pi R\tan\theta$), while $N2\pi R$ (i.e. the red line) is kept constant. For $\theta = \pi/2$, the periodicity becomes infinite as expected, since an infinitely long conducting sheet is considered. On the other hand, for $\theta \to 0$, periodicity goes to zero as shown in figure 10.7(d), where an infinitesimally thin Swiss Roll is created (i.e. length: $l = 2\pi RN\tan\theta$ also goes to zero). Also, by considering that for a conducting sheet rolled along the x-axes, ω_0 is dependent by the length of the red line in figure 10.7(a) (i.e. the length of the spiral cross-section of the roll), which is $N2\pi R$ for any chiral Swiss Roll. For $\theta = \pi/2$, and keeping constant $N2\pi R$, a non-chiral Swiss Roll is created, where (10.18) converges to (9.7). As θ takes smaller values (as shown in figure 10.7(c)) and for $N2\pi R$ kept constant, the conducting sheet overlaps less which means that the Swiss Roll has a smaller capacitance. Therefore ω_0 takes smaller values, which is taken into account in (10.18) by the $\tan^2\theta$ terms. However, for the limit where $\theta \to 0$, an infinitesimally thin non-chiral Swiss Roll is created, whose magnetic response is determined by the green line in figure 10.7(d), which is infinite (i.e. $N \to \infty$), hence ω_0 cannot be defined. Therefore, (10.18) converges to (9.7) for $\theta = \pi/2$, and not for $\theta = 0$.

The (non-inverse) electromagnetic parameters are plotted in figures 10.6 and 10.8 for a PEC chiral Swiss Roll in vacuum with dimensions $N = 2$, $R = 1mm$, $l = 5mm$, $d = 0.35mm$, $\theta = 21,7°$, $a = 5mm$ and vacuum in the gap ($\varepsilon_d = 1$). Note that both $Re(\chi_{EE})$ and $Re(\chi_{HH})$ are zero at the same frequency, since $\omega_{mp} = \omega_p$ and both $Re(\chi_{EE})$ and $Re(\chi_{HH})$ are negative for frequencies $\omega_0 < \omega < \omega_{mp}$. Also, χ_{HH} in (10.9) obeys the Lorentz model, similarly to μ_z in (9.6) as expected, since the magnetic behaviour of both structures arise from the same mechanism.

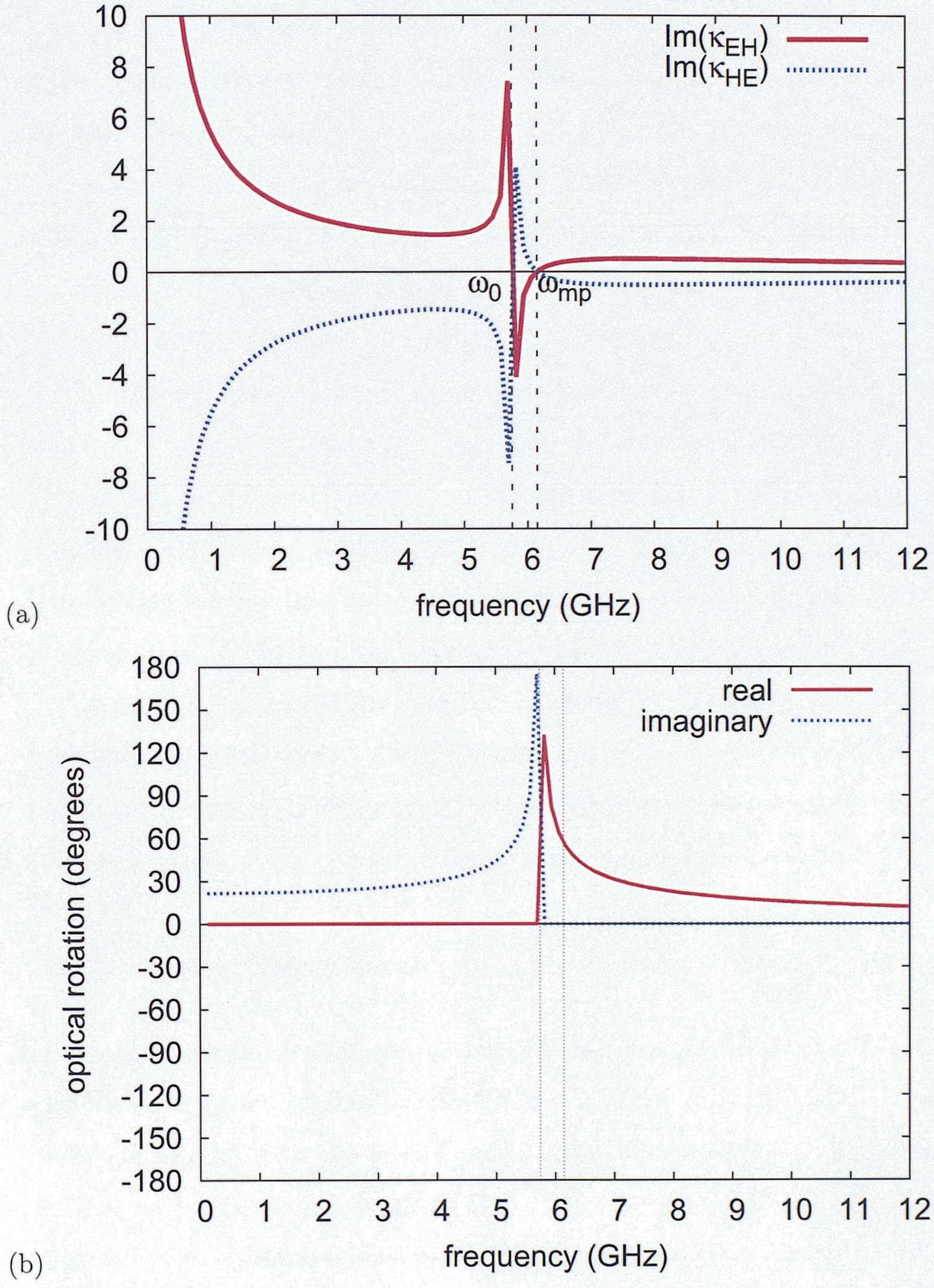

Figure 10.8: For Swiss Rolls of $N = 2$, $R = 1mm$, $l = 5mm$, $x = 0.05mm$, $d = 0.35mm$, $\theta = 21,7^\circ$ and $a = 5mm$. (a)The imaginary parts of the chirality terms (κ_{EH} and κ_{HE}), which are equal and opposite (i.e.$\kappa_{EH} = -\kappa_{HE}$). (b) The optical rotation per wavelength is plotted in degrees

Furthermore, the imaginary parts of the chirality terms, plotted in figure 10.8(a), take infinite values for $\omega \to \omega_0$ and $\omega \to 0$. Also, they pass through zero for $\omega = \omega_{mp}$. The infinite values that $Im(\kappa_{EH})$ takes at $\omega \to 0$ can be justified by noting that the structure discussed here is an infinite roll and hence an infinite current flows along the z-axes is considered analytically (not physically possible). However, if a finite resistance is considered for the conducting elements of the structure and a finite roll, the divergence of $Im(\kappa_{EH})$ disappears, since only finite currents can flow in the coils at $\omega \to 0$. This was proved experimentally in [55].

Finally, the optical activity per one wavelength (ϕ) is given by

$$\phi(rad) = \frac{i\kappa_{EH}}{\sqrt{\chi_{EE}\chi_{HH}}} \tag{10.20}$$

The real part of ϕ is the optical rotation of a chiral medium, which measures the polarization rotation of a wave travelling in a chiral medium. It can also be considered as a measure of the medium's chirality strength. The imaginary part of ϕ shows the circular dichroism of the medium, which shows the attenuation of left- or right-circularly polarized waves. Circular dichroism arises from the complex nature of the refracting indices that affect the circular ellipticity of the wave. Both the real and imaginary parts of the optical activity are plotted in figure 10.8(b).

10.2 Band Structure

A 2D chiral metamaterial can be constructed by alternating the axes-alignment of neighbouring layers of chiral Swiss Rolls, as shown in figure 10.9(a). If the Swiss Rolls are aligned with the y- and z-axes, then for propagation along the x-axes (i.e. $k_y = k_z = 0$), the fields are given by (10.1). Also, now (10.9), (10.10), (10.12), are valid for electric and magnetic fields along both the y- ans z-axes.

In order to obtain the dispersion equations of a 2D-chiral metamaterials, consider equation (10.1), Maxwell's equations, helical polarization for the electric and magnetic fields and the 2D-isotropy of the medium (details in Appendix H), which lead to:

$$\begin{bmatrix} 0 & -ik_+ \\ ik_+ & 0 \end{bmatrix} \begin{bmatrix} E_+ \\ iH_+ \end{bmatrix} = \omega^+ \begin{bmatrix} \chi_{EE} & \chi_{EH} \\ \chi_{HE} & \chi_{HH} \end{bmatrix} \begin{bmatrix} E_+ \\ iH_+ \end{bmatrix} \tag{10.21}$$

The eigenvalues of (10.21) give the dispersion equations of the medium and are given by:

$$\omega^{+\pm} = c_0 k_{+\pm} \left(i \left[\kappa^{-1}\right]_{EH} / c_0 \pm \sqrt{[\chi^{-1}]_{EE} [\chi^{-1}]_{HH}} \right) \tag{10.22}$$

$$\omega^{-\pm} = c_0 k_{-\pm} \left(-i \left[\kappa^{-1}\right]_{EH} / c_0 \pm \sqrt{[\chi^{-1}]_{EE} [\chi^{-1}]_{HH}} \right) \tag{10.23}$$

for the right-handed and left-handed circular wave-polarizations respectively and where $\left[\chi^{-1}\right]_{HH}$, $\left[\chi^{-1}\right]_{EE}$ and $\left[\kappa^{-1}\right]_{EH}$ are the inverse magnetic, electric and chirality parameters respectively given by (10.9), (10.10) and (10.12).

The analytical prediction of the real and imaginary band structure for a 2D chiral Swiss Roll medium is plotted in figures 10.9(b) and (c) respectively with lines. As it was expected, the degeneracy of the modes no longer holds, since the chirality of the medium splits the two transverse modes. Hence, a negative band for one-wave polarization has emerged for frequencies $\omega_0 < \omega < \omega_{mp}$. Furthermore, for frequencies $\omega < \omega_0$, there is a stop band as expected, since $Re(\chi_{EE})$ is negative and $Re(\chi_{HH})$ positive. Finally, the wavevector (i.e. Δk) at which the band structure takes a minimum value is dependent on the resonant frequency (ω_0) and the imaginary part of the inverse chirality at the resonant frequency ($\left[\kappa^{-1}\right]_{EH}(\omega_0)$) and is given by:

$$\Delta k = \pm \frac{\omega_0}{i \left[\kappa^{-1}\right]_{EH} (\omega_0)} \tag{10.24}$$

Using CST Microwave Studio, the band structure of a 2D chiral Swiss Roll medium with dimensions $N = 2$, $R = 1mm$, $l = 5mm$, $x = 0.05mm$, $d = 0.35mm$, $\theta = 21,7^\circ$ and $a = 5mm$ was calculated and is plotted in figure 10.9(b)(dots), together with the analytical prediction (lines) of (10.22) and (10.23). The two band structures have a similar shape, with a negative band corresponding to one-wave polarization. The agreement between analytical and numerical calculations for the resonant frequencies is approximately $\sim 80\%$ and for Δk is $\sim 84\%$. However, note that for numerical results $Re(\omega_{-+})$ and $Re(\omega_{+-})$ modes are slowly propagating and reach the Brillouin zone at relatively low frequencies, affecting the shape of the modes. This is due to the dimensions chosen for the chiral Swiss Roll, where the assumptions taken analytically, such as large N, $R \gg d$ and an infinitely thin conducting sheet, are not valid for the simulated structure. Unfortunately, the complexity of the structure's design prevents

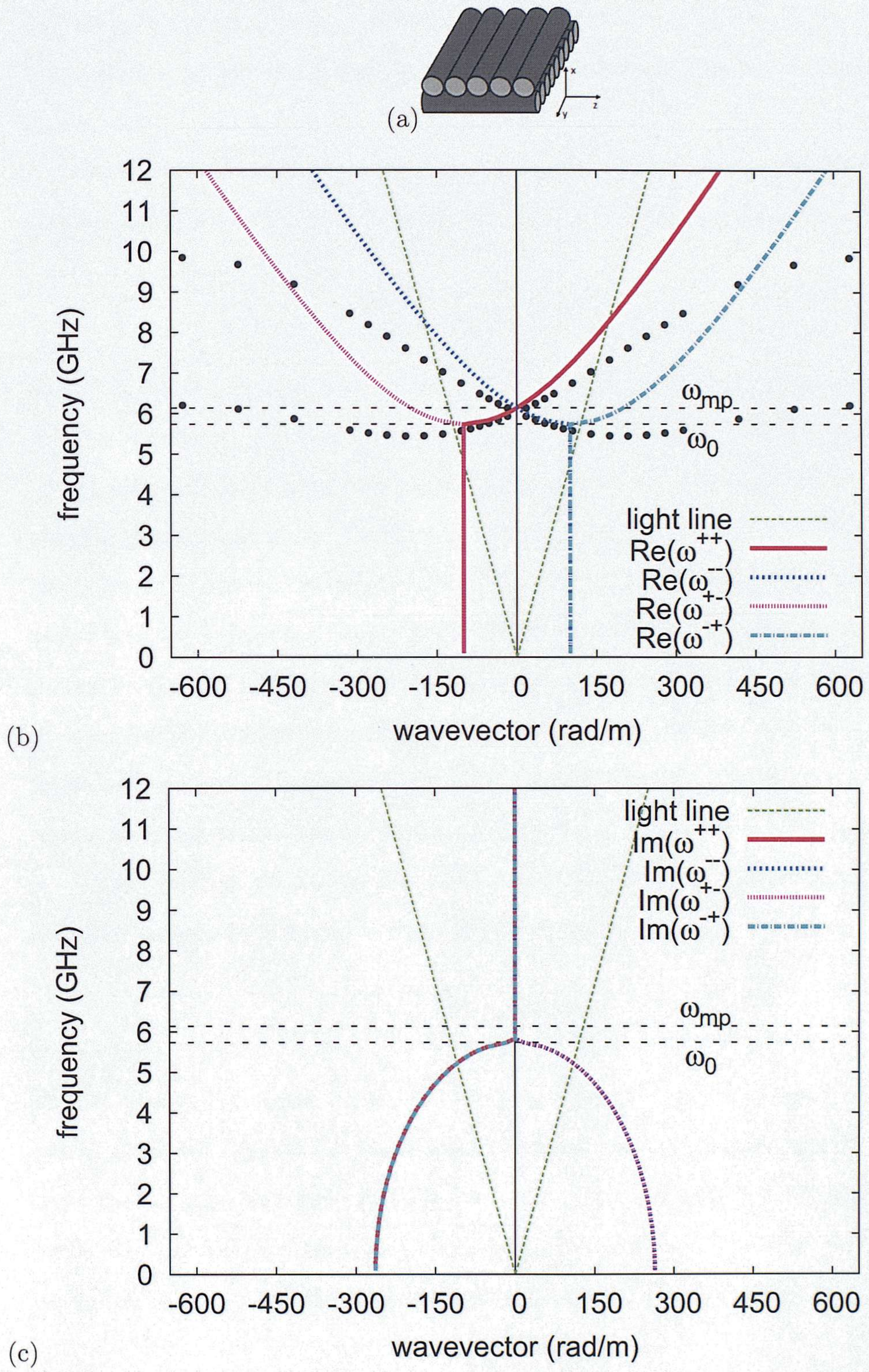

Figure 10.9: (a)Chiral Swiss Rolls are placed along the y- and z- axes, creating a 2D chiral Swiss Roll metamaterial. (b) The analytic prediction for the band structure of a 2D chiral Swiss Roll metamaterial is shown with full lines and the numerical results with dots for dimensions $N = 2$, $R = 1mm$, $l = 5mm$, $x = 0.05mm$, $d = 0.35mm$, $\theta = 21,7^\circ$ and $a = 5mm$ (c)The analytic prediction for the imaginary wavevector.

the numerical calculation of the band structure for more ideal dimensions of chiral Swiss Rolls. Nevertheless, the agreement between analytical and numerical results is significant.

The refractive index of the medium takes different values depending on the wave's polarization, as can be derived from (10.22) and (10.23), and is given by:

$$n_{\pm} = \frac{1}{\sqrt{\chi_{EE}^{-1}\chi_{HH}^{-1}} \pm i\kappa_{EH}^{-1}/c_0} \qquad (10.25)$$

which is plotted in figure 10.11 for a loss-less 2D chiral Swiss Roll metamaterial of $N = 2$, $R = 1mm$, $l = 5mm$, $x = 0.05mm$, $d = 0.35mm$, $\theta = 21,7^{\circ}$ and $a = 5mm$. A left handed circularly polarized wave (LCP) is refracted obeying n_- and a right handed circularly polarized wave (RCP) n_+. Note that for RCP, $Re(n_+)$ is always positive while for LCP $Re(n_-)$ is negative for $\omega_0 < \omega < \omega_{mp}$, passes through zero at ω_{mp} and takes positive values for higher frequencies as expected from the shape of the band structure plotted in figure 10.9. Furthermore, the real parts of both refractive indices go to infinity at lower frequencies, where $i\kappa_{EH}$ is dominant. Finally, the imaginary parts of both refractive indices are negative for stop-band frequencies (i.e. $\omega < \omega_0$, which does not violate causality since the medium is not passive at this range.

The refractive index for the same medium but in the absence of chirality (i.e. consider a racemic mixture of Swiss Rolls) is given by:

$$n = \frac{1}{\sqrt{\chi_{EE}^{-1}\chi_{HH}^{-1}}} \qquad (10.26)$$

and is plotted in figure 10.10(b). Such a medium can be constructed with chiral Swiss Rolls by aligned neighbouring rolls with opposite handedness. Note that for $\omega_0 < \omega < \omega_{mp}$, where both $Re(\chi_{EE}^{-1})$ and $Re(\chi_{HH}^{-1})$ are negative, $Re(n)$ is negative as well. Also, at frequencies where there is a stop-band $Re(n)$ is zero and $Im(n) \to \infty$. In figure 10.10(a), the impedance is plotted as well, which is given by

$$Z = \sqrt{\frac{\chi_{HH}}{\chi_{EE}}} \qquad (10.27)$$

Note that $Re(n)$ and $Re(Z)$ are zero for frequencies where there is a stop-band (i.e. $\omega < \omega_0$) and $Im(n)$ and $Im(Z)$ are zero for $\omega > \omega_0$.

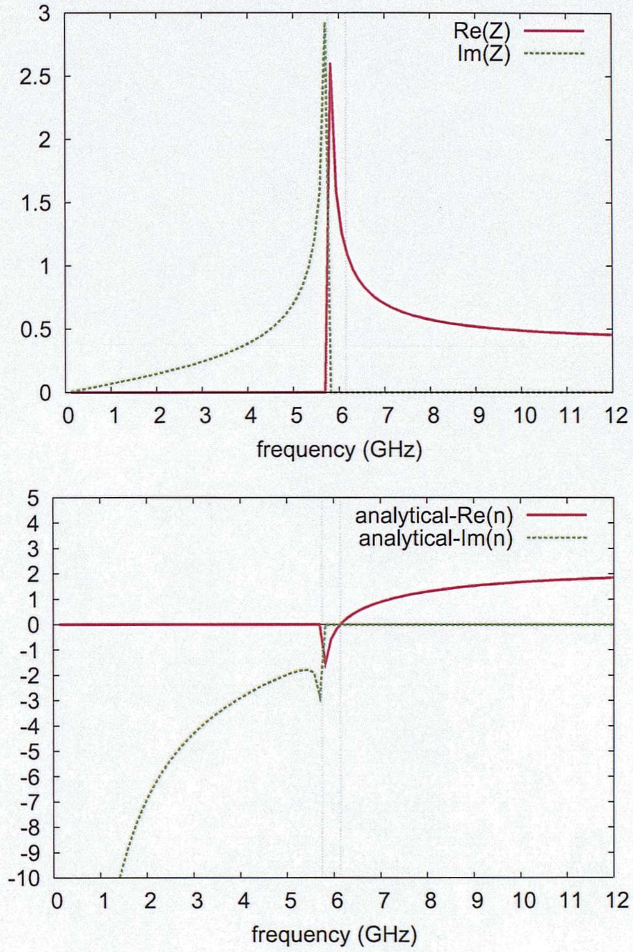

(a)

(b)

Figure 10.10: (a) The impedance (Z) and (b) refractive index (n)for a 2D-chiral Swiss Roll metamaterial of $N = 2$, $R = 1mm$, $l = 5mm$, $x = 0.05mm$, $d = 0.35mm$, $\theta = 21,7^\circ$ and $a = 5mm$ calculated analytically using equations (10.27) and (10.26) respectively.

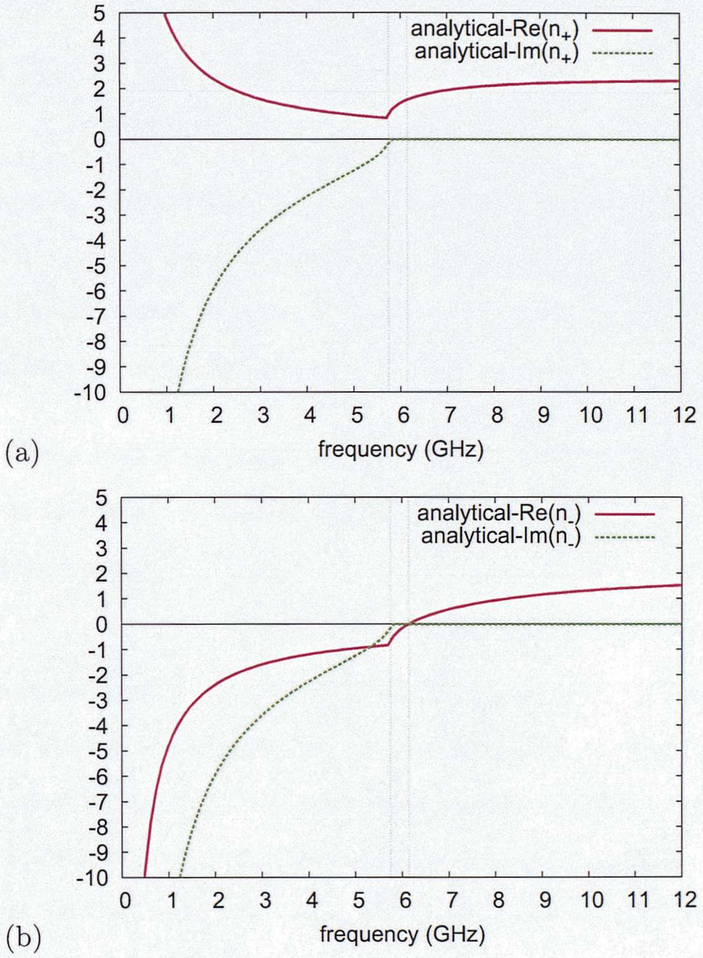

Figure 10.11: The refractive indices for (a) RCP (n_+) and (b) LCP (n_-) incident waves on a 2D-chiral Swiss Roll metamaterial of $N = 2$, $R = 1mm$, $l = 5mm$, $x = 0.05mm$, $d = 0.35mm$, $\theta = 21,7°$ and $a = 5mm$, calculated analytically using equation (10.25).

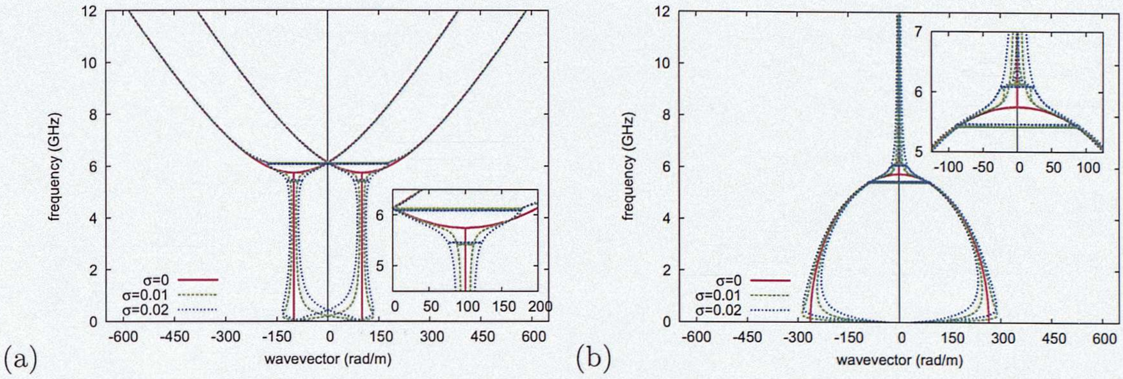

Figure 10.12: The band structure (a)real part (b)imaginary part of 2D Swiss-Roll metamaterial for various values of σ and with dimensions $N = 2$, $R = 1mm$, $l = 5mm$, $x = 0.05mm$, $d = 0.35mm$, $\theta = 21,7^\circ$ and $a = 5mm$. Red solid line:$\sigma = 0$-vacuum, green dashed line: $\sigma = 0.01$ and blue dotted line: $\sigma = 0.02$.

Losses in Swiss Roll metamaterials are dominated from the loss of the dielectric material inside the gap. In order to take them into account, consider a complex dielectric material with:

$$\varepsilon_d = \varepsilon' + i\varepsilon'' = \varepsilon' + i\frac{\sigma}{\omega\varepsilon_0} \tag{10.28}$$

where σ is the conductivity of the dielectric. In figure 10.12, the dispersion equations of (10.22) and (10.23) are plotted for various values of σ. For large enough σ the modes do not meet at Δk. Furthermore, numerical calculations for the band structure of a medium embedded in vacuum(red solid lines) and a dielectric of $\sigma = 0.0167$ (blue dotted line) are plotted in figure 10.13, where the bands slightly shift towards lower frequencies for a slightly lossy hosting medium. The resistivity losses of metals at GHz and MHz frequencies that Swiss Rolls most commonly operate, are negligibly small (i.e. for Copper resistivity $\sim 1.7 * 10^{-8}$). In figure 10.14, the band structure for various metals with different resistivity are plotted. It is clear that resistivity losses are insignificant at this frequency range, since they negligibly affect the behaviour of the structure.

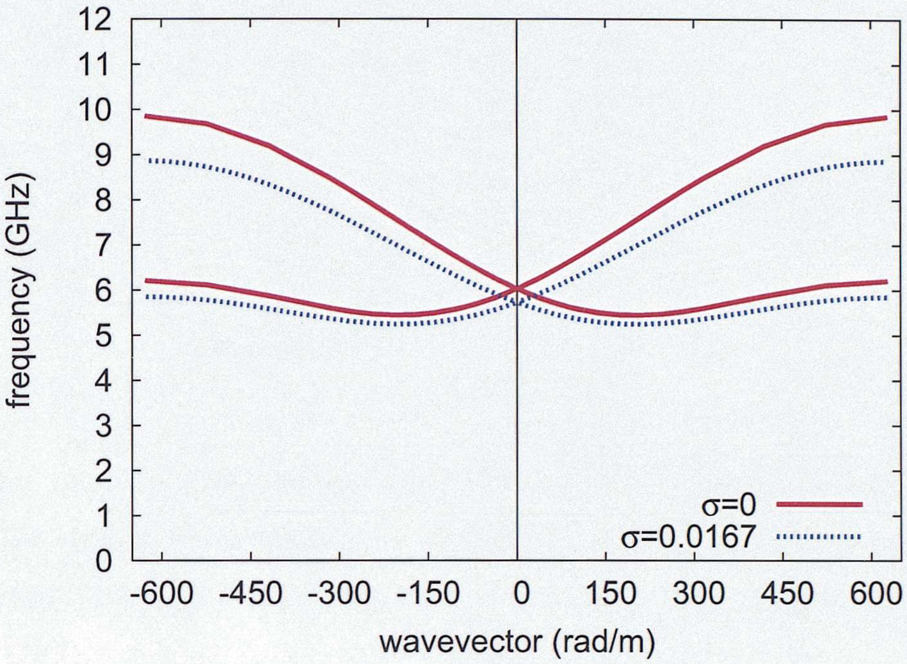

Figure 10.13: The band structure of Swiss Rolls with dimensions $N = 2$, $R = 1mm$, $l = 5mm$, $x = 0.05mm$, $d = 0.35mm$, $\theta = 21,7°$ and $a = 5mm$, calculated numerically. Red solid line for vacuum (i.e. $\sigma = 0$) between the conducting sheets and blue dotted line of $\sigma = 0.0167$.

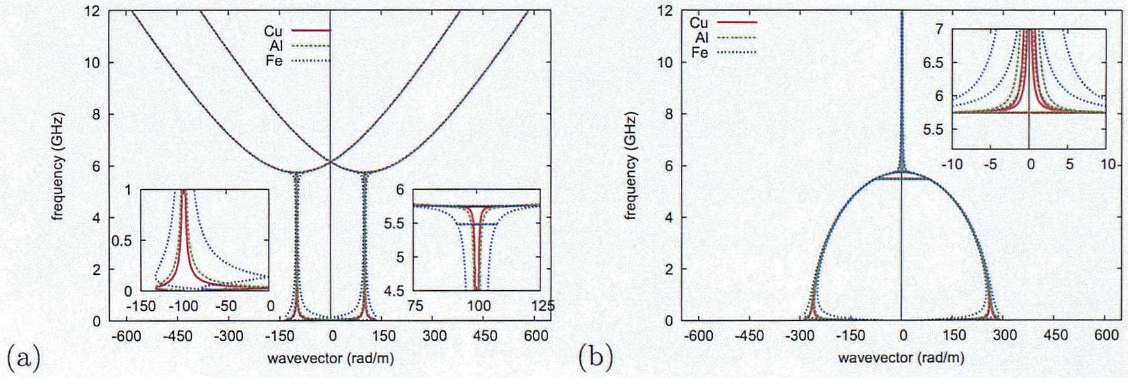

(a) (b)

Figure 10.14: The analytical band structure (a)real part (b)imaginary part of a 2D Swiss-Roll metamaterial with dimensions $N = 2$, $R = 1mm$, $l = 5mm$, $x = 0.05mm$, $d = 0.35mm$, $\theta = 21,7°$ and $a = 5mm$. Red solid line:Copper-Cu with resistivity= $(1.67 * 10^{-8})\Omega m$, green dashed lines: Aluminium with resistivity= $(2.74 * 10^{-8})\Omega m$ and blue dotted line: Iron-Fe= $(9.8 * 10^{-8})\Omega m$ which is close to the conductivity of Germanium.

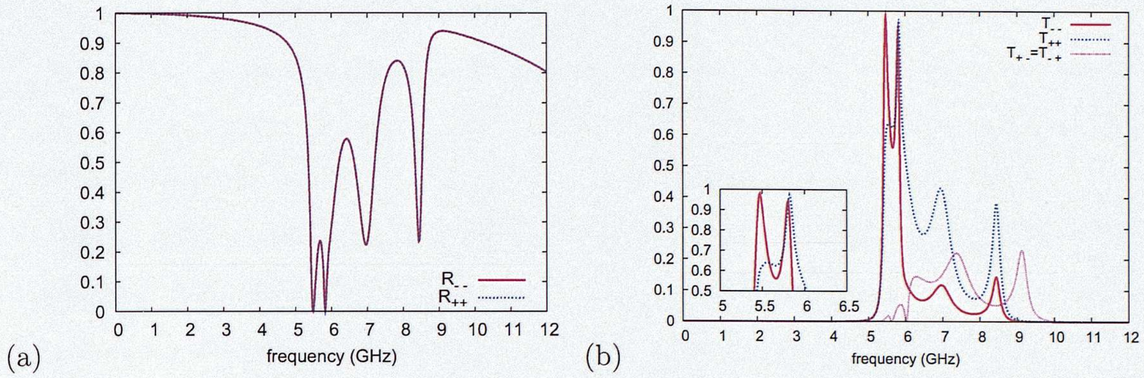

Figure 10.15: (a)The reflection and (b) transmission coefficient for right and left handed circular waves incident on a 3-unit-cell slab of chiral Swiss Rolls with dimensions $N = 2$, $R = 1mm$, $l = 5mm$, $x = 0.05mm$, $d = 0.35mm$, $\theta = 21,7^\circ$ and $a = 5mm$.

10.3 Effective Electromagnetic Behaviour

10.3.1 Scattering Parameters

Similarly to the previous part and chapter, the S-parameters of a wave incident on a finite slab of a chiral Swiss Roll metamaterial were calculated numerically in order to get an indirect insight to the electromagnetic properties of the artificial medium. Consider a circular wave normally incident (i.e. k_x-propagation) on a 2D-chiral Swiss Roll metamaterial. A different transmission coefficient is expected, depending on the wave-polarization (i.e. either left- or right-handed circularly polarized wave), since the refractive index is different for different wave-polarizations, as shown by (10.25). However. the reflection coefficient for both wave-polarizations is identical, since both waves see just the first roll and do not propagate in the medium, whose chirality induces different behaviour for RCP and LCP.

The eigensolutions of electromagnetic fields in a chiral media are two circularly polarized waves given by (10.22) and (10.23), characterized as the right-handed circularly polarized wave (RCP, $++$) and the left-handed circularly polarized wave (LCP, $--$). Therefore, four transmission coefficients T_{++}, T_{+-}, T_{-+} and T_{--} are needed to fully characterized the response of a chiral medium. Note that the cross-coupling transmission coefficients indicate RCP input and LCP output and vice-versa, given by $T_{+-} = (E^t_-/E^i_+)$ and $T_{-+} = (E^t_+/E^i_-)$ [8, 53]. However, in this case, due to the 2D-isotropy of the medium and $\kappa_{EH} = -\kappa_{HE}$, $T_{-+} = T_{+-}$.

CST Microwave Studio was used to numerically calculate the S-parameters for RCP and LCP normally incident waves on a 3-unit-cell slab consisted from chiral Swiss Rolls aligned alternatively along y- and z-axes and with dimensions $N = 2$, $R = 1mm$, $l = 5mm$, $x = 0.05mm$, $d = 0.35mm$, $\theta = 21,7^\circ$ and $a = 5mm$, (the band structure is shown in figure 10.9). Note that periodic boundary conditions were applied along the y- and z-axes and that the circular waves are propagating along the x-axes. The transmission and reflection coefficients calculated using CST Microwave studio are plotted in figure 10.15. For frequencies were the negative band is observed in figure 10.9, the transmission coefficient for the LCP wave is higher than for RCP at $\omega_0 < \omega < \omega_{mp}$, as expected. Furthermore, the reflection coefficient for both polarizations is identical as shown in figure 10.15(a). Finally, note that $T_{-+} = T_{+-}$ take small values.

10.3.2 Retrieval Method for Chiral Media

As mentioned previously, scattering parameters show significant information about the behaviour of a wave propagating in a specific medium. However, in order to get a direct insight to the electromagnetic behaviour of the structure, the electromagnetic terms need to be retrieved from S-parameters, since they directly connect **D** and **B** to **E** and **H** through (10.1).

The retrieval method for chiral media was recently developed by Plum *et.al.* [54, 53], which takes into account the different refractive indices for RCP and LCP wave polarizations. The method assumes that cross-coupling transmission parameters T_{-+} and T_{+-}, are negligibly small. Therefore, for a normally incident circularly polarized wave on a chiral medium, the impedance is given by:

$$Z = \sqrt{\frac{(1+R)^2 - T_{--}T_{++}}{(1-R)^2 - T_{--}T_{++}}} \tag{10.29}$$

where $R = R_{--} = R_{++}$ is the reflection coefficient plotted in figure 10.15(a), T_{--} and

T_{++} are the transmissions of left- and right-handed circular waves respectively. The two refractive indices are given by:

$$n_{\pm} = \frac{1}{ik_0 ma} \ln\left(\frac{1 - r_{01}R}{T_{\pm}}\right) \tag{10.30}$$

where $r_{01} = (Z-1)/(Z+1)$, m is the number of unit cells, a the lattice constant and k_0 is the wavevector in vacuum.

Now, we know from (10.22) and (10.23) that the refractive indices of the chiral Swiss Roll metamaterial are given by

$$n_{\pm} = \frac{1}{\sqrt{\chi_{EE}^{-1}\chi_{HH}^{-1}} \pm \kappa_{EH}^{-1}/c_0} \tag{10.31}$$

where κ_{EH}^{-1} is the inverse chirality term and the impedance is given by:

$$Z = \sqrt{\frac{\chi_{HH}}{\chi_{EE}}} = \frac{1}{\sqrt{\chi_{HH}^{-1}/\chi_{EE}^{-1}}} \tag{10.32}$$

Therefore, the refractive index n of the medium without the presence of chirality is given by:

$$\frac{1}{n} = \sqrt{\chi_{EE}^{-1}\chi_{HH}^{-1}} = \frac{1}{2}\left(\frac{1}{n_+} + \frac{1}{n_-}\right) \tag{10.33}$$

and from (10.32) the inverse of the electric permittivity is given by:

$$\chi_{EE}^{-1} = \frac{1}{2Z}\left(\frac{1}{n_+} + \frac{1}{n_-}\right) \tag{10.34}$$

the inverse of magnetic permeability by:

$$\chi_{HH}^{-1} = \frac{Z\left(\frac{1}{n_+} + \frac{1}{n_-}\right)}{2} \tag{10.35}$$

and finally the inverse of the chirality term

$$\kappa_{EH}^{-1} = -\kappa_{HE}^{-1} = \frac{1}{2}\left(\frac{1}{n_+} - \frac{1}{n_-}\right) \tag{10.36}$$

The non-inverse electromagnetic parameters are obtained using (10.13) and (10.14).

10.3.3 Effective Electromagnetic Parameters

For the medium whose band structure is shown in figure 10.9, the electromagnetic terms were retrieved from the scattering parameters, plotted in figure 10.15. However,

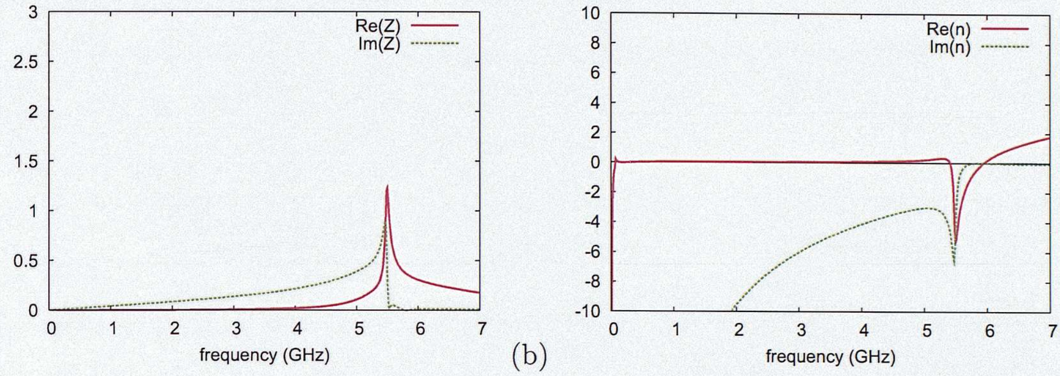

(a) (b)

Figure 10.16: (a) Retrieved impedance (Z) and (b) refractive index (n) from S-parameters calculations on a 3-unit-cell slab of a 2D-chiral Swiss Roll metamaterial of $N = 2$, $R = 1mm$, $l = 5mm$, $x = 0.05mm$, $d = 0.35mm$, $\theta = 21,7^{\circ}$ and $a = 5mm$.

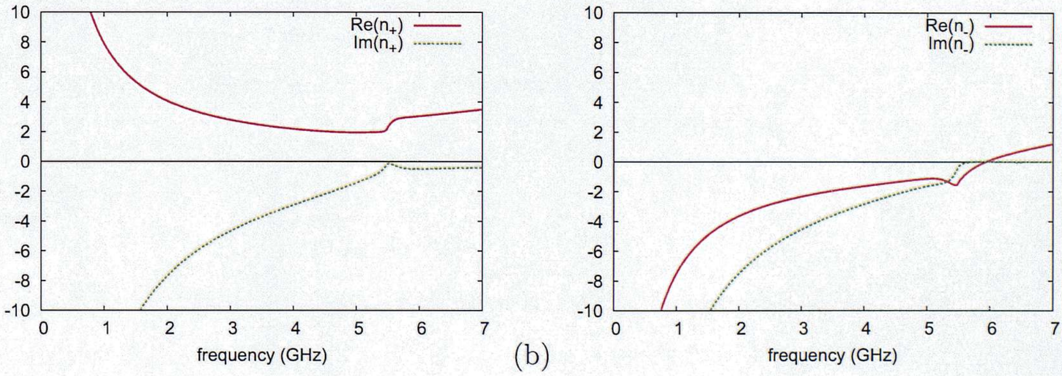

(a) (b)

Figure 10.17: Retrieved refractive indices for (a) RCP (n_+) and (b) LCP (n_-) incident waves on a 3-unit-cell slab of a 2D-chiral Swiss Roll metamaterial of $N = 2$, $R = 1mm$, $l = 5mm$, $x = 0.05mm$, $d = 0.35mm$, $\theta = 21,7^{\circ}$ and $a = 5mm$.

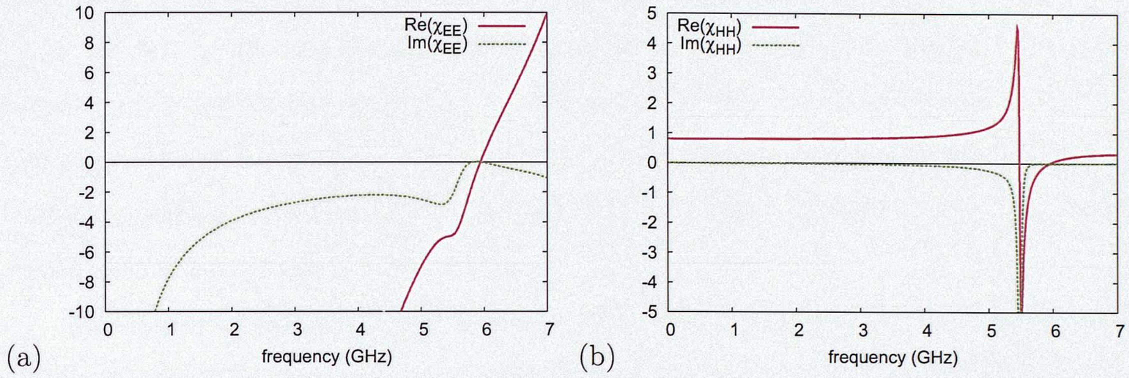

(a) (b)

Figure 10.18: Retrieved (a)electric permittivity (χ_{EE}) and (b) magnetic permeability (χ_{HH}) from S-parameter calculations on a a 3-unit-cell slab of a 2D-chiral Swiss Roll metamaterial of $N = 2$, $R = 1mm$, $l = 5mm$, $x = 0.05mm$, $d = 0.35mm$, $\theta = 21,7°$ and $a = 5mm$.

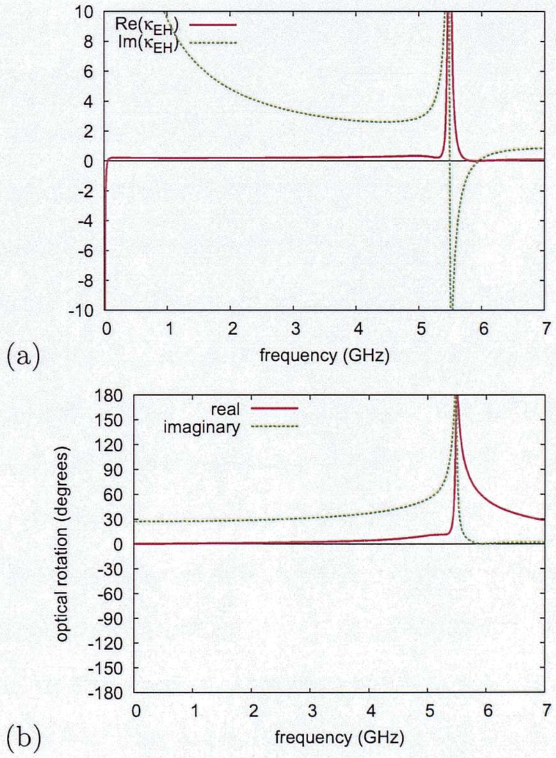

(a)

(b)

Figure 10.19: Retrieved (a) the chirality term (κ_{EH}) (b) optical rotation (ϕ) from S-parameter calculations on a a 3-unit-cell slab of a 2D-chiral Swiss Roll metamaterial of $N = 2$, $R = 1mm$, $l = 5mm$, $x = 0.05mm$, $d = 0.35mm$, $\theta = 21,7°$ and $a = 5mm$.

as shown in figure 10.15, although the cross-coupling transverse coefficient T_{+-} and T_{-+} are small, they are not negligible. In order to avoid this problem, we apply the retrieval method for frequencies up to $\sim 7GHz$, where $T_{+-} = T_{+-} \rightarrow 0$. Also, for this structure the ω_{-+} and ω_{+-} bands reach the Brillouin zone without dispersing much. This has some effect on the retrieved terms. Nevertheless, an insight to the validity of the analytical work can still be obtained.

The retrieved Z is plotted in figure 10.16(a) and is in agreement with (10.27) and figure 10.10(a). For frequencies where there is a stop-band $Re(Z) \rightarrow 0$ and $Im(Z) \neq 0$. For frequencies where the medium is transparent, $Re(Z) \neq 0$ and positive, while $Im(Z) \rightarrow 0$. Also, the refractive index of the medium in the absence of chirality was retrieved and is plotted in figure 10.16(b), and is also in agreement with the analytical prediction in (10.26) and figure 10.10(b). Note that the $Im(n)$ is negative for frequencies where there is a stop-band and that $Re(n)$ is negative for $\omega_0 < \omega < \omega_{mp}$ where both $Re(\chi_{HH})$ and $Re(\chi_{EE})$ are simultaneously negative. It passes through zero at ω_{mp} and is positive for $\omega > \omega_{mp}$.

The refractive indices for RCP and LCP waves are plotted in figure 10.17. For RCP, the real part of refractive index is always positive. For LCP, $Re(n_-)$ is negative for $\omega < \omega_{mp}$ frequencies, passes through zero at ω_{mp} and is positive for larger frequencies. Also, both $Re(n_+)$ and $Re(n_-)$ go to infinity for low frequencies as predicted by (10.25) and figures 10.11(a) and (b), since are dominated by $i\kappa_{EH}$. Note that the retrieved impedance and refractive indices are in excellent agreement with analytical calculations, with a small difference at the values of the resonant frequencies.

In figure 10.18, the retrieved electric permittivity and magnetic permeability are plotted. Both parameters follow qualitatively the same shape as predicted by (10.10) and (10.9) and plotted in figure 10.6. However, the distortion seen for retrieved χ_{EE} at $\sim 5.7GHz$ is due to the narrow dispersion of ω_{-+} mode that reaches the Brillouin zone at those frequencies. Similarly, the retrieved κ_{EH} is plotted in figure 10.19(a) and has the predicted behaviour, where the imaginary part has a strong resonance at ω_0 and at low frequencies goes to infinity, as it was analytically predicted in (10.12) and figure 10.8(a). Finally, the retrieved rotation of the wave's polarization, calculated using the retrieved values for κ_{EH}, χ_{EE} and χ_{HH}, is plotted in figure 10.19(b), which

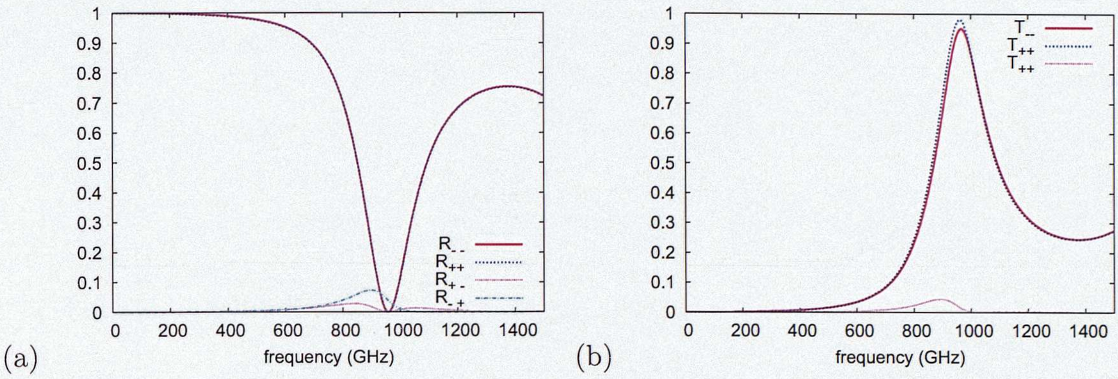

Figure 10.20: (a)The reflection and (b) transmission coefficient for right and left handed circular waves incident on a 3-unit-cell slab of chiral Swiss Rolls with dimensions $N = 3$, $R = 2.5mm$, $l = 6mm$, $x = 0.05mm$, $d = 0.21mm$, $\theta = 7^{\circ}$ and $a = 12mm$.

is in agreement with (10.20) and figure 10.8(b).

10.4 Chiral Swiss Roll Metamaterials at MHz frequencies

Similarly to non-chiral Swiss Rolls, chiral Swiss Rolls are most commonly used at MHz frequency range. However, the design complexity of Swiss Rolls at MHz frequency that demands $R \gg d$, forbids adequate computational modelling for the calculation of the band structure. Hence, a structure with smaller N and R, bigger d and θ was simulated (as discussed above), which demands significantly less computational time and capabilities. However, although there is a good agreement for a structure with resonant frequencies in the GHz range (where some assumptions taken analytically are not valid numerically), the RCP band reached the Brillouin zone at a frequency just above ω_{mp}. This has an effect on S-parameters, and affects slightly the results for retrieved electromagnetic parameters. Therefore, if the resonant frequencies are moved to lower values, the RCP band is allowed to disperse for a broader range.

Fortunately, the numerical calculation of S-parameters with CST Microwave Studio allows the use of simpler modelling of the structure (i.e. a tetrahedral meshing). Therefore, the S-parameters of a LPC and RCP waves incident on a 3-unit-cell slab of a 2D-chiral Swiss Roll metamaterial were calculated numerically and are plotted in

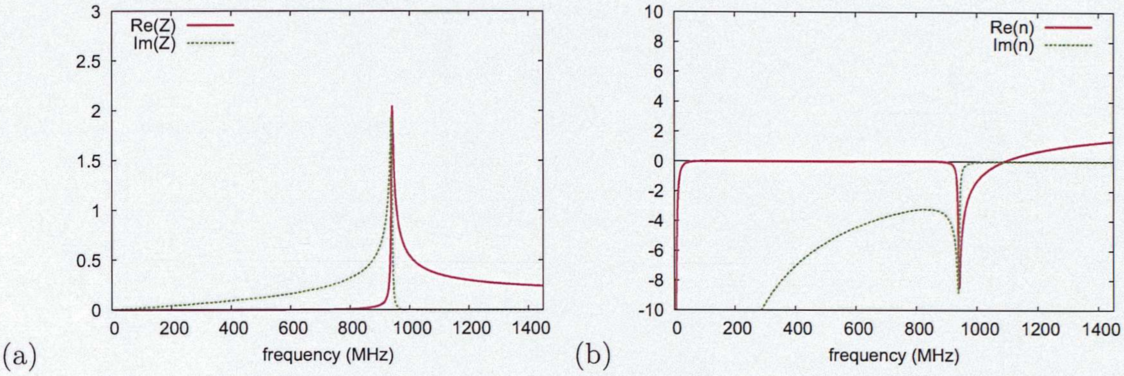

Figure 10.21: (a) Retrieved impedance (Z) and (b) refractive index (n) from S-parameters calculations on a 3-unit-cell slab of a 2D-chiral Swiss Roll metamaterial of $N = 3$, $R = 2.5mm$, $l = 6mm$, $x = 0.05mm$, $d = 0.21mm$, $\theta = 7°$ and $a = 12mm$.

figure 10.20 for rolls with dimensions $N = 3$, $R = 2.5mm$, $l = 6mm$, $x = 0.05mm$, $d = 0.21mm$, $\theta = 7°$ and $a = 12mm$. For this structure the ratio (R/d) is significantly lower, which brings the resonant frequencies to lower values. Furthermore, the cross-coupling transmission coefficients take even smaller values than figure 10.15, which is an assumption taken for the retrieval method.

Using the retrieval method described in Section 10.3.2, the electromagnetic parameters were obtained from the numerically calculated S-parameters. The impedance Z and refractive index n are shown in figure 10.21, where an agreement with the analytical prediction is observed. Similarly for n_+ and n_- refractive indices, which are plotted in figure 10.22. The differences between analytical and numerical results are observed on the values of the resonant frequencies, with an accuracy of $\sim 88\%$. In figure 10.23, the retrieved χ_{EE} and χ_{HH} are plotted as well, which also show significant agreement with the analytical predictions of (10.10) and (10.9). Note that the distortion seen in figure 10.18(a), disappears at lower frequencies as expected. Furthermore, the chirality term and the wave's polarization through an infinite structure are plotted in figure 10.24, which are also in agreement with analytical predictions.

Finally, using the retrieved parameters plotted in figures 10.23 and 10.24 and the analytically derived dispersion equations in (10.22) and (10.23), the band structure was calculated for a 2D-chiral Swiss Roll metamaterial composed from rolls with dimensions

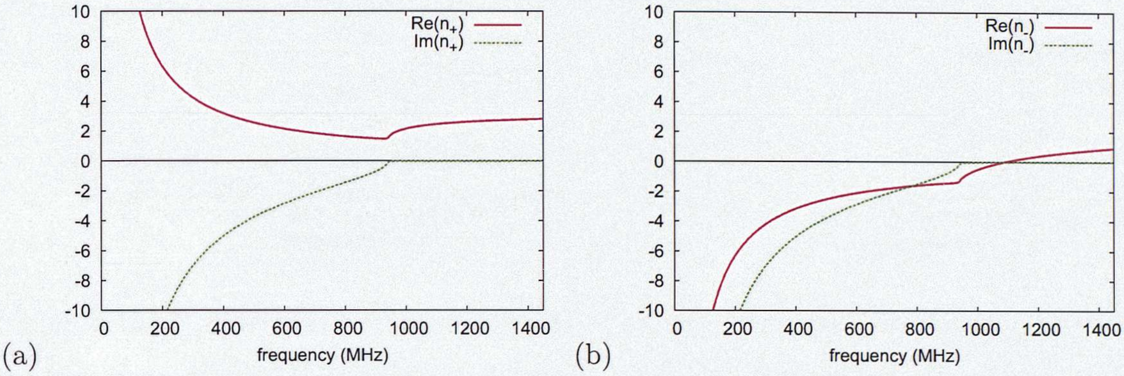

Figure 10.22: Retrieved refractive indices for (a) RCP (n_+) and (b) LCP (n_-) incident waves on a 3-unit-cell slab of a 2D-chiral Swiss Roll metamaterial of $N = 3$, $R = 2.5mm$, $l = 6mm$, $x = 0.05mm$, $d = 0.21mm$, $\theta = 7°$ and $a = 12mm$.

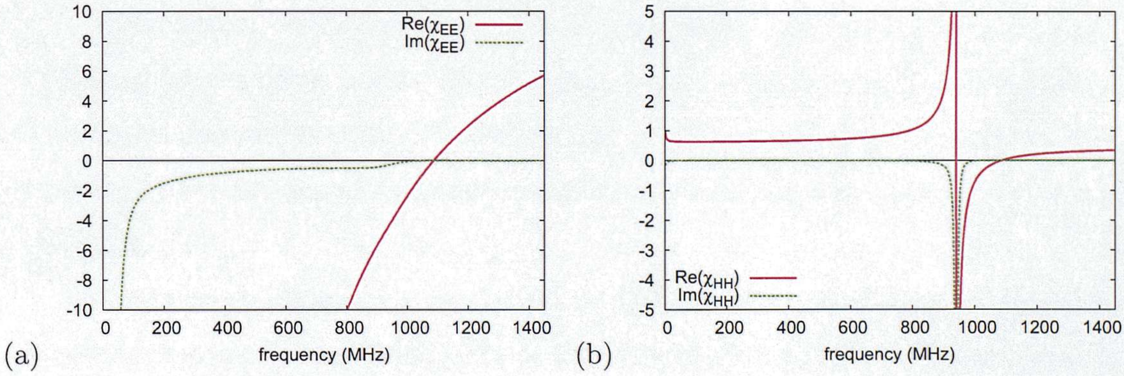

Figure 10.23: Retrieved (a)electric permittivity (χ_{EE}) and (b) magnetic permeability (χ_{HH}) from S-parameters calculations on a a 3-unit-cell slab of a 2D-chiral Swiss Roll metamaterial of $N = 3$, $R = 2.5mm$, $l = 6mm$, $x = 0.05mm$, $d = 0.21mm$, $\theta = 7°$ and $a = 12mm$.

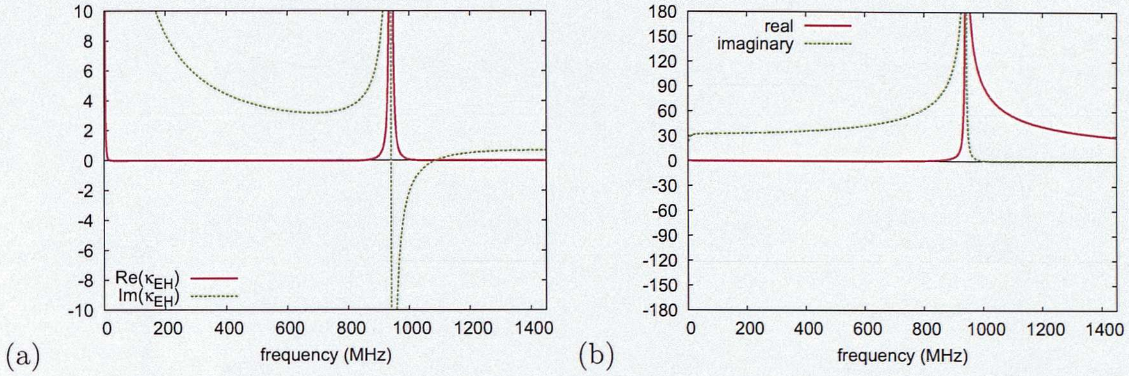

Figure 10.24: Retrieved (a) the chirality term (κ_{EH}) (b) optical rotation (ϕ) from S-parameters calculations on a a 3-unit-cell slab of a 2D-chiral Swiss Roll metamaterial of $N = 3$, $R = 2.5mm$, $l = 6mm$, $x = 0.05mm$, $d = 0.21mm$, $\theta = 7°$ and $a = 12mm$.

$N = 3$, $R = 2.5mm$, $l = 6mm$, $x = 0.05mm$, $d = 0.21mm$, $\theta = 7°$ and $a = 12mm$. The analytically and numerically predicted band structure are in agreement.

Chiral Swiss Rolls exhibit extreme chirality compared with other chiral structures discussed in the literature [50, 52], by a factor of at least two orders of magnitude This efficiency is due to the cross-section of the rolls, which is typically (1/100)th to (1/1000)th of the wavelength. Other structures proposed for chiral metamaterials such as the helical wire structure requires a much larger cross section to achieve any significant activity. This is also the main reason that for chiral Swiss Rolls a backward wave can be observed even for GHz frequencies, whereas for loop wires or helical wires, it appears for a less broad frequency range or is lost in the stop band due to sharp resonances [50].

Furthermore, this structure, in addition to Magnetic Resonance Imaging (MRI) applications that are well known [34], is ideal for polarization rotation/selection antenna applications. The extreme chirality of Swiss Rolls ensures a tremendous enhancement of the efficiency for these types of antennas, where a wave's polarization can be rotated by 90° in less than a wavelength, or a linear wave can be transformed to a circularly polarized wave in less than a wavelength [52].

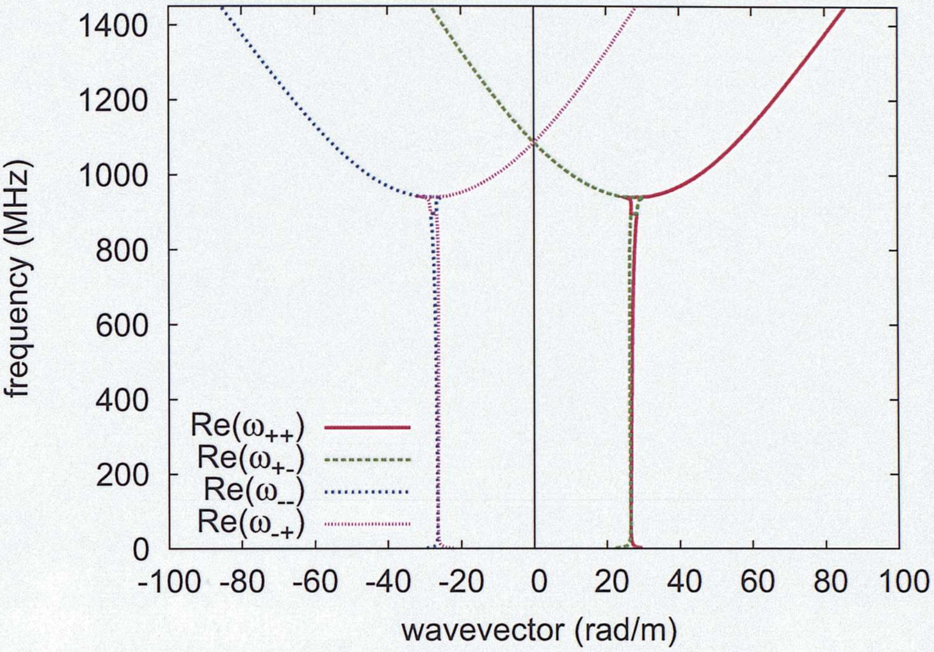

(a)

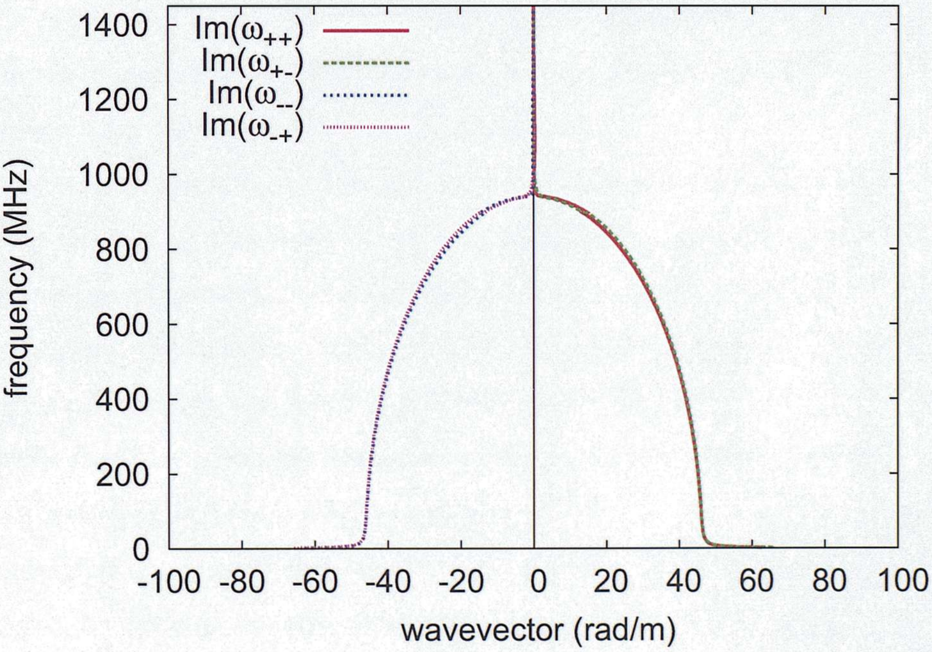

(b)

Figure 10.25: The band structure for k_x-propagation in a 2D-chiral Swiss Roll metamaterial with dimensions $N = 3$, $R = 2.5mm$, $l = 6mm$, $x = 0.05mm$, $d = 0.21mm$, $\theta = 7^\circ$ and $a = 12mm$, obtained using the retrieved electromagnetic and chirality parameters and the dispersion equations (a)real part (b) imaginary part.

Chapter 11

Conclusions

A significant advantage of Swiss Roll metamaterials (both chiral and non), is the fact that their resonant frequencies are easily tuned over a wide range of frequencies (from few MHz to tens of GHz), by simply changing the number of turns (N), or the packing (a), the radius (R) or the dielectric constant of the material in the gap (ε_d). Also, they do not require a huge lattice constant in order to have a magnetic behaviour in MHz frequency range unlike Split-Ring-Resonators.

An extensive numerical investigation was initially performed for non-chiral Swiss Rolls, by calculating the band structure and S-parameters, from which the electromagnetic parameters were retrieved. Also, the results showed a remarkable agreement with analytical predictions. Some additional resonances observed are identified as trapped modes within the spiral gap of the conducting sheet. Therefore, it can be concluded that the analytical homogenization model is exceptionally valid for Swiss Rolls operating at MHz and GHz frequencies.

Consequently, an analytical investigation of the chiral version of Swiss Rolls was performed, be deriving the electromagnetic parameters of the structure. It was found that chiral Swiss Rolls exhibit at least two orders of magnitude higher chirality compared with other structures discussed in the literature. Therefore, they ensure a broader backward wave, which is observed even at GHz frequencies, unlike other chiral structures (such as helical wires) [50]. The analytical predictions for the band structure are followed from numerical calculations, which also show a negative band for one of the wave's polarization. Finally, the electromagnetic and chirality terms were retrieved from numerical S-parameters and showed significant agreement with the analytical predictions, for both MHz and GHz frequencies

Part III

Negative Metamaterial composed of High-Dielectric structures

Chapter 12

Introduction

As mentioned in previous parts of this thesis, Pendry *et.al.* [9] proposed various ways to manufacture artificially magnetic media, made entirely from conductors, such as Swiss-Rolls and Split-Ring resonators [9, 36, 41, 35, 37]. These media are magnetically active for frequencies where conventional materials rarely show any magnetization. However, a significant drawback of these structures is that their operation and applications are limited by the lossy behaviour of metals at higher frequencies and eventually loose their conducting properties at high THz and optical ranges. Furthermore, due to their designs, it is challenging to manufacture 3D isotropic media, with small enough lattice constants.

An alternative way to create artificially magnetic-resonant metamaterials is through the excitation of the first magnetic Mie mode of high-dielectric structures, which was proposed initially by O'Brien *et.al.* [56]. Mie resonances (or single-scatterer resonances) along with Bragg scattering, are usually the main contributing mechanisms for the creation of stop-bands in photonic crystals. For photonic crystals, the dielectric inclusions have small value for the dielectric constant ε and therefore Mie resonances appear at frequencies where the wavelength is comparable to the lattice constant (a). Consequently, the concepts of a homogeneous medium and effective parameters are not valid for photonic crystals. However, by tremendously increasing the value of ε for the dielectric structures, the Mie resonances are shifted to lower frequencies. Therefore, the resonance wavelength is now larger than the lattice constant and the effective medium approach is valid [56]. On the other hand, the wavelength λ inside the high-dielectric particle is of the order of the particle's dimensions and therefore Mie theory is also valid.

In the literature, various magnetic or DNG metamaterials are discussed, whose behaviour is based on the excitation of Mie modes (electric or magnetic). Vendik *et.al.* [57, 58] and Jylha *et.al.* [59], proposed a DNG metamaterial composed of two sets of dielectric spheres of different radii and dielectric constants. The radius and ε of each sphere-set determine the frequencies of the magnetic and electric resonances and can be adjusted such as the electric Mie resonance of one sphere-set to overlap with the a magnetic Mie mode of the other sphere-set. Furthermore, Wheeler et.al [60] proposed that coated spherical particles excite both magnetic (core-sphere) and electric (coat) Mie resonances, resulting to a DNG metamaterial, if both dielectric permittivities and radii are adjusted to the right values. However, an important disadvantage of these structures is that one of the two resonances (electric or magnetic) is always significantly more narrow banded than the other, which restricts the negative band to an extremely small frequency bandwidth. Also, since the frequency value of the resonance is strongly dependent on the radius of the sphere, a small variation at the radii of spheres detunes the two resonances, destroying the negative band of the metamaterial.

In this part of the thesis, the single-scatterer (Mie) theory is initially discussed for sphere and coated-sphere dielectric particles. Then, periodic media composed of high-dielectric spheres or spherical-shells are investigated, which have an effective magnetic behaviour through the excitation of the first magnetic Mie resonance. It is shown that the effective magnetic permeability obeys the Lorentz model. Also, it is shown that a coated sphere and consequently empty spherical shells of various thicknesses, not only have an effective magnetic resonant behaviour through the excitation of the first magnetic Mie mode, but also broaden the frequency range where effective $Re(\mu)$ is negative by $\sim 75\%$ and shift the resonant frequency to higher values by $\sim 33\%$. Then, both high-dielectric sphere and spherical-shell-crystals are embedded in a wire-mesh, creating a broad-frequency negative metamaterial, which also manages to considerably tame loss for high-GHz (even low THz) negative metamaterials, compared with all conductor-based DNG metamaterials.

Chapter 13

Single Scatterer-Mie theory

The excitation of Mie resonances by a single-sphere-scatterer embedded in vacuum is initially investigated. Consider time-harmonic ($\exp(i\omega t)$) electromagnetic waves incident on a single sphere of dielectric constant ε and radius R. Since the problem discussed in this report is scattering by a particle with a spherical shape, the scalar wave equation in spherical polar coordinates (r, θ and ϕ defined in figure 13.1(c)) is considered (Appendix I) [61, 62]:

$$\frac{1}{r^2}\frac{\partial}{\partial r}\left(r^2\frac{\partial\psi}{\partial r}\right)+\frac{1}{r^2\sin\theta}\frac{\partial}{\partial\theta}\left(\sin\theta\frac{\partial\psi}{\partial\theta}\right)+\frac{1}{r^2\sin\theta}\frac{\partial^2\psi}{\partial\phi^2}+k^2\psi=0 \tag{13.1}$$

where ψ is the scalar wavefunction. The solutions of (13.1) are:

$$\begin{aligned}\psi_{emn}&=\cos m\phi P_n^m(\cos\theta)z_n(kr)\\ \psi_{omn}&=\sin m\phi P_n^m(\cos\theta)z_n(kr)\end{aligned} \tag{13.2}$$

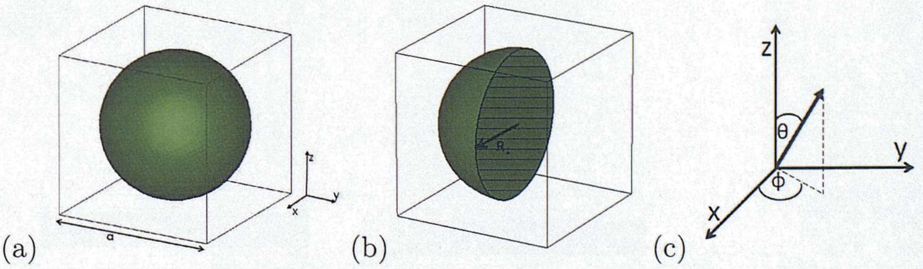

Figure 13.1: (a) A sphere of dielectric constant ε, radius R and arranged in a cubic crystal with lattice constant a. (b) A cut-plane of the unit cell at $y = 0$. (c) The definition of the polar coordinates r, θ and ϕ, with respect to orthogonal coordinates.

where P_n^m is the Legendre function, the subscripts e and o denote even and odd dependence on ϕ respectively and z_n is one of the spherical Bessel functions: j_n, y_n, $h_n^{(1)}$ and $h_n^{(2)}$. Also, any function that satisfies the scalar wave equation can be written as an infinite series of (13.2).

In order to solve the scattering problem of a plane wave from a spherical dielectric particle, we need to expand the electric and magnetic fields (incident, scattered and internal) in vector spherical harmonics (i.e. **M** and **N**-Appendix I) that satisfy the vector wave equation and are also produced from (13.2):

$$\mathbf{M}_{(e,o)mn} = \nabla \times (\mathbf{r}\psi_{(e,o)mn}) \tag{13.3}$$

$$\mathbf{N}_{(e,o)mn} = \frac{\nabla \times \mathbf{M}_{(e,o)mn}}{k} \tag{13.4}$$

Assuming that the incident plane wave has the electric field polarized along the x-axes, then:

$$\mathbf{E}_{inc} = E_0 \exp{(ikr\cos\theta)}\hat{\mathbf{e}}_{\mathbf{x}} \tag{13.5}$$

and is written in spherical polar coordinates by substituting $\hat{\mathbf{e}}_{\mathbf{x}}$ with:

$$\hat{\mathbf{e}}_{\mathbf{x}} = \sin\theta\cos\phi\hat{\mathbf{e}}_{\mathbf{r}} + \cos\theta\sin\phi\hat{\mathbf{e}}_{\theta} - \sin\phi\hat{\mathbf{e}}_{\phi} \tag{13.6}$$

and expanded (Appendix J) in vector spherical harmonics as:

$$\mathbf{E}_{inc} = \sum_{n=1}^{\infty} E_n \left(\mathbf{M}_{o1n}^{(1)} - i\mathbf{N}_{e1n}^{(1)}\right) \tag{13.7}$$

where $E_n = i^n E_0(2n+1)/(n(n+1))$, n and m are the principal and azimuthal quantum numbers (here $m = 1$, since scattering coefficients vanish for $m \neq 1$) [61]. Now, using Maxwell equations and noting that the dielectric material the sphere is made of has magnetic permeability $\mu = 1$, the magnetic field expanded in spherical harmonics is given by:

$$\mathbf{H}_{inc} = -\frac{k_0}{\omega} \sum_{n=1}^{\infty} E_n \left(\mathbf{M}_{o1n}^{(1)} + i\mathbf{N}_{e1n}^{(1)}\right) \tag{13.8}$$

Since the expansion of the fields inside the dielectric sphere are dictated by the expansion of the incident fields, the internal fields are given by [61, 62]:

$$\begin{aligned} \mathbf{E}_{int} &= \sum_{n=1}^{\infty} E_n \left(c_n\mathbf{M}_{o1n}^{(1)} - id_n\mathbf{N}_{e1n}^{(1)}\right) \\ \mathbf{H}_{int} &= -\frac{k_{int}}{\omega} \sum_{n=1}^{\infty} E_n \left(d_n\mathbf{M}_{o1n}^{(1)} + ic_n\mathbf{N}_{e1n}^{(1)}\right) \end{aligned} \tag{13.9}$$

where c_n and d_n are internal coefficients (i.e. coefficients dominating the fields inside the sphere) and k_{int} the wavevector of the wave inside the sphere. Similarly, the scattered fields are given by:

$$\begin{aligned} \mathbf{E}_{scat} &= \sum_{n=1}^{\infty} E_n \left(-b_n \mathbf{M}^{(3)}_{o1n} + i a_n \mathbf{N}^{(3)}_{e1n}\right) \\ \mathbf{H}_{scat} &= \frac{k_0}{\omega} \sum_{n=1}^{\infty} E_n \left(a_n \mathbf{M}^{(3)}_{o1n} + i b_n \mathbf{N}^{(3)}_{e1n}\right) \end{aligned} \tag{13.10}$$

where a_n and b_n are scattering coefficients (i.e. coefficients dominating the fields scattered from the sphere), and the superscript (3) on the spherical harmonic vectors denotes that the Hankel function ($h_n^{(1)}$) is used for ψ The scattering coefficients are given by:

$$a_n = \frac{N^2 j_n(N\rho)[\rho j_n(\rho)]' - j_n(\rho)[N\rho j_n(N\rho)]'}{N^2 j_n(N\rho)[\rho h_n^{(1)}(\rho)]' - h_n^{(1)}(\rho)[N\rho j_n(N\rho)]'} \tag{13.11}$$

$$b_n = \frac{j_n(N\rho)[\rho j_n(\rho)]' - j_n(\rho)[N\rho j_n(N\rho)]'}{j_n(N\rho)[\rho h_n^{(1)}(\rho)]' - h_n^{(1)}(\rho)[N\rho j_n(N\rho)]'} \tag{13.12}$$

and the internal coefficients are given by:

$$c_n = \frac{j_n(\rho)[\rho h_n^{(1)}(\rho)]' - h_n^{(1)}(\rho)[\rho j_n(\rho)]'}{j_n(N\rho)[\rho h_n^{(1)}(\rho)]' - h_n^{(1)}(\rho)[N\rho j_n(N\rho)]'} \tag{13.13}$$

$$d_n = \frac{N j_n(\rho)[\rho h_n^{(1)}(\rho)]' - N h_n^{(1)}(\rho)[\rho j_n(\rho)]'}{N^2 j_n(N\rho)[\rho h_n^{(1)}(\rho)]' - h_n^{(1)}(\rho)[N\rho j_n(N\rho)]'} \tag{13.14}$$

where N is the refracting index of the material the sphere is made from and is given by $N = \sqrt{\varepsilon}$, ρ is the size parameters given by $\rho = kR$, k is the wavevector, R the radius of the sphere and finally $[.]'$ denotes the derivative of the function in square brackets with respect to ρ. Note that the denominators of a_n and d_n are equal, as those of b_n and c_n.

When the frequency of an incident field is close to a magnetic Mie mode value, then b_n and c_n dominate (13.10) and (13.11) and when close to an electric natural mode, a_n and b_n dominate. Therefore, natural modes appear at frequencies where scattering coefficients go to infinity (i.e. the denominators approach zero). The first magnetic Mie mode (i.e. $n = 1$) for a sphere of radius R, dielectric constant ε (i.e. refractive index $N = \sqrt{\varepsilon}$) placed in vacuum, is therefore expected at frequencies where

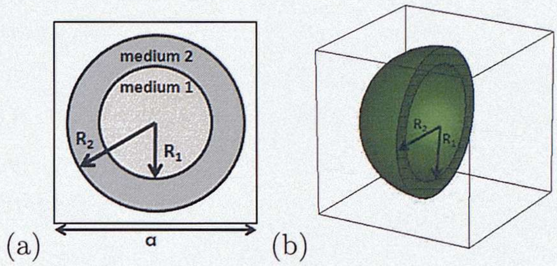

(a) (b)

Figure 13.2: (a) A sphere of dielectric constant ε_1, radius R_1, coated with a spherical-shell of ε_2 and radius R_2. A cross-section passing through the origin of the sphere is shown here and the coated sphere is arranged in a cubic lattice of constant a. (b) A cut-plane of the unit cell at $y = 0$ and for a structure with $\varepsilon_1 = 1$.

the denominator of b_n is zero, therefore:

$$\frac{[\rho h_1^{(1)}(\rho)]'}{h_1^{(1)}(\rho)} = \frac{[N\rho j_1(N\rho)]'}{j_1(N\rho)} \tag{13.15}$$

and the first electric Mie mode when:

$$\frac{[\rho h_1^{(1)}(\rho)]'}{h_1^{(1)}(\rho)} = \frac{[N\rho j_1(N\rho)]'}{N^2 j_1(N\rho)} \tag{13.16}$$

where $\rho = kR$, k is the wavevector corresponding to the resonant frequency, $j_1(\rho)$ is a spherical Bessel function and $h_1^{(1)}(\rho)$ spherical Hankel function.

13.1 Spherical-Shell Scatterer

Similarly to a dielectric-sphere-scatterer, a coated-sphere (as shown in figure 13.2(a)) scatters electromagnetic waves obeying Mie theory [61, 62]. The scattering particle is composed of a core sphere (medium 1 in figure 13.2(a)) of radius R_1 made from a material of ε_1 (i.e. assuming that $\mu_1 = 1$, the refractive index is given by: $N_1 = \sqrt{\varepsilon_1}$) and a spherical-shell (medium 2 in figure 13.2(a)) of radius R_2 with a dielectric constant of ε_2 (i.e. $N_2 = \sqrt{\varepsilon_2}$). The incident electric and magnetic fields are given by (13.7) and (13.8), the fields inside the core-sphere by (13.10) and the scattered fields by (13.11). The expansions of the fields inside the spherical-shell (i.e. $R_1 < r < R_2$

and $R_1 \neq 0$) are given by [61, 62]:

$$\mathbf{E}_{int}^{shell} = \sum_{n=1}^{\infty} E_n(f_n\mathbf{M}_{o1n}^{(1)} - ig_n\mathbf{N}_{e1n}^{(1)}) \tag{13.17}$$

$$\mathbf{H}_{int}^{shell} = -\frac{k_n}{\omega\mu_0}\sum_{n=1}^{\infty} E_n(g_n\mathbf{M}_{e1n}^{(1)} + if_n\mathbf{N}_{o1n}^{(1)}) \tag{13.18}$$

and the fields scattered by the spherical-coat are given by:

$$\mathbf{E}_{scat}^{shell} = \sum_{n=1}^{\infty} E_n(v_n\mathbf{M}_{o1n}^{(2)} - iw_n\mathbf{N}_{e1n}^{(2)}) \tag{13.19}$$

$$\mathbf{H}_{scat}^{shell} = -\frac{k_0}{\omega\mu_0}\sum_{n=1}^{\infty} E_n(w_n\mathbf{M}_{e1n}^{(2)} + iv_n\mathbf{N}_{o1n}^{(2)}) \tag{13.20}$$

where g_n, f_n, w_n and v_n are also internal and scattering coefficients for the spherical-shell and the superscript (2) on the spherical harmonics denotes their generation by $y_n(kr)$ functions.

By taking into account the boundary conditions at $r = R_1$ and $r = R_2$, the scattering coefficients (a_n and b_n) for a coated-dielectric-sphere are derived and using the Riccati-Bessel functions (i.e. $\psi_n(z) = zj_n(z)$, $\xi_n(z) = zh_n^{(1)}(z)$ and $\chi_n(z) = -zy_n(z)$) are given by [61]:

$$\begin{aligned} a_n &= \frac{\psi_n(\rho_2)\left[\psi_n'(N_2\rho_2) - A_n\chi_n'(N_2\rho_2)\right] - N_2\psi_n'(\rho_2)\left[\psi_n(N_2\rho_2) - A_n\chi_n(N_2\rho_2)\right]}{\xi_n(\rho_2)\left[\psi_n'(N_2\rho_2) - A_n\chi_n'(N_2\rho_2)\right] - N_2\xi_n'(\rho_2)\left[\psi_n(N_2\rho_2) - A_n\chi_n(N_2\rho_2)\right]} \\ b_n &= \frac{N_2\psi_n(\rho_2)\left[\psi_n'(N_2\rho_2) - B_n\chi_n'(N_2\rho_2)\right] - \psi_n'(\rho_2)\left[\psi_n(N_2\rho_2) - B_n\chi_n(N_2\rho_2)\right]}{N_2\xi_n(\rho_2)\left[\psi_n'(N_2\rho_2) - B_n\chi_n'(N_2\rho_2)\right] - \xi_n'(\rho_2)\left[\psi_n(N_2\rho_2) - B_n\chi_n(N_2\rho_2)\right]} \end{aligned} \tag{13.21}$$

where $\rho_1 = kR_1$, $\rho_2 = kR_2$, k is the wavevector and:

$$A_n = \frac{N_2\psi_n(N_2\rho_1)\psi_n'(N_1\rho_1) - N_1\psi_n'(N_2\rho_1)\psi_n(N_1\rho_1)}{N_2\chi_n(N_2\rho_1)\psi_n'(N_1\rho_1) - N_1\chi_n'(N_2\rho_1)\psi_n(N_1\rho_1)} \tag{13.22}$$

$$B_n = \frac{N_2\psi_n(N_2\rho_1)\psi_n'(N_1\rho_1) - N_1\psi_n(N_2\rho_1)\psi_n'(N_1\rho_1)}{N_2\chi_n'(N_2\rho_1)\psi_n(N_1\rho_1) - N_1\chi_n(N_2\rho_1)\psi_n'(N_1\rho_1)} \tag{13.23}$$

Note that when $N_1 = N_2 = N$ then A_n, B_n vanish and (13.21) reduce to (13.12) and when $N_2 = 1$, (13.21) reduce to (13.12) for $R = R_1$ as expected.

Similarly to the single-sphere scatterer, when a_n and b_n are infinite, the natural electric and magnetic resonances arise respectively. Also, note that the structure discussed in this paper is an empty spherical-shell of $\varepsilon_2 = \varepsilon$ and the core-sphere has

$\varepsilon_1 = 1$ and $N_1 = 1$. Consequently, by setting the denominator of b_n to zero, requiring $n = 1$ and $N_2 = N = \sqrt{\varepsilon}$, $N_1 = 1$, the first magnetic Mie mode occurs when:

$$\frac{[N\rho_2 j_1(N\rho_2)]' + B_1[N\rho_2 y_1(N\rho_2)]'}{N\rho_2 j_1(N\rho_2) + B_1 N\rho_2 y_1(N\rho_2)} = \frac{[\rho_2 h_1^{(1)}(\rho_2)]'}{N_2\rho_2 h_1^{(1)}(\rho_2)} \tag{13.24}$$

and B_1 is reduced to:

$$B_1 = \frac{N\rho_1 j_1(N\rho_1)[\rho_1 j_1(\rho_1)]' - N\rho_1 j_1(\rho_1)[N\rho_1 j_1(N\rho_1)]'}{N^2\rho_1 y_1(N\rho_1)[\rho_1 j_1(\rho_1)]' + N\rho_1 y_1(N\rho_1)[\rho_1 j_1(\rho_1)]'} \tag{13.25}$$

Chapter 14

Effective magnetization of high-dielectric crystals

When the frequency of the incident wave is close to a natural magnetic mode of a single sphere-scatterer, then the electric field inside a high-dielectric sphere is enhanced. Hence, the displacement current is amplified, resulting to an enhanced magnetic field as shown in figure 14.2(a) and (b) for the electric and magnetic fields respectively [61]. Therefore, when the spheres are placed in a periodic crystal of lattice constant a, a macroscopic bulk magnetization is obtained.

The high value of ε ensures that the incident wave sees a homogeneous medium [56], since the resonance wavelength is much larger than the lattice constant a of the crystal. However, the wave inside the sphere has a smaller wavelength than the incident wave (due to large ε), a fact that gives rise to the natural Mie modes (i.e. $\lambda_{int} \sim 2R$). Similarly, spherical-shells have an effective magnetic behaviour, since the displacement currents and the enhanced fields are not significantly affected by the vacuum core-sphere as it can be seen in figure 14.2 (discussed later).

For a sphere of radius $R = 0.45mm$ and $\varepsilon = 100 + i\sigma/(\omega\varepsilon_0)$, where $\sigma = 3.34(S/m)$ is the conductivity of the dielectric determining loss, the first magnetic Mie mode is expected at 29.6 GHz, according to (13.15). The dispersion diagram of a crystal composed of these spheres in a square lattice of $a = 1mm$ was calculated using CST Mi-

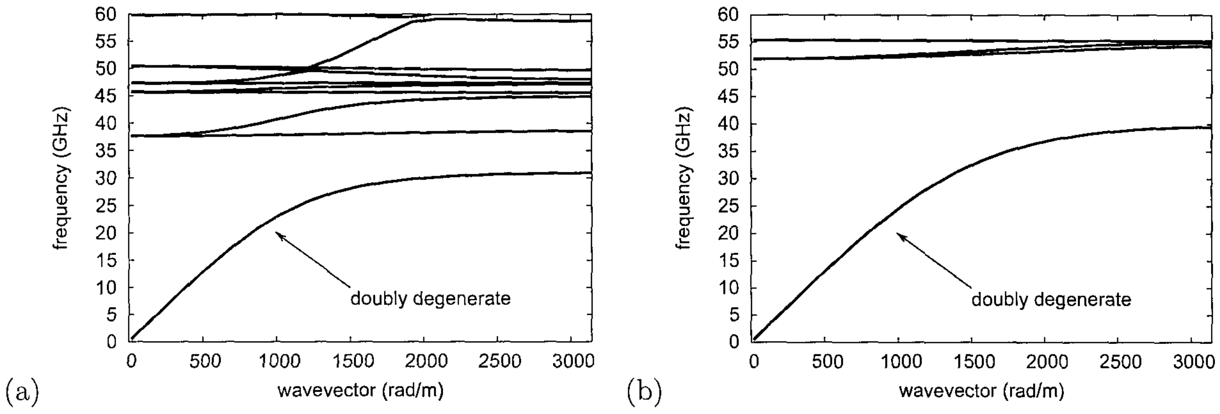

Figure 14.1: (a) Band structure for a high-dielectric crystal made of spheres of $R = 0.45mm$, $a = 1mm$, $\varepsilon = 100 + \sigma i/(\omega\varepsilon_0)$ and $\sigma = 3.34(S/m)$. (b) Band structure for a high-dielectric crystal made from spherical-shells of $R_1 = 0.35mm$, $R_2 = 0.45mm$ (as shown in figure 13.2(b), $a = 1mm$, $\varepsilon = 100 + \sigma i/(\omega\varepsilon_0)$ and $\sigma = 3.34(S/m)$. The doubly degenerate transverse modes are interrupted by a stop-band, introduced by the first Mie resonance mode.

crowave Studio[1] and is plotted in figure 14.1(a). For a spherical-shell of $R_1 = 0.35mm$, $R_2 = 0.45mm$, $\varepsilon = 100 + i\sigma/(\omega\varepsilon_0)$, $\sigma = 3.34(S/m)$ (and a vacuum core-sphere), the first magnetic resonance for a single scatterer arises at $\sim 42.5GHz$ according to (13.24) and (13.25). Using CST Microwave Studio, the dispersion diagram of a crystal composed of such spherical shells arranged in a square lattice of $a = 1mm$ was calculated as well and is plotted in figure 14.1(b). Note, that although Mie theory does not account for neighbouring particle contributions, the analytical predictions for both resonant frequencies are in good agreement with numerical results for both the sphere and spherical-shell-crystals.

The two doubly degenerate modes in figures 14.1(a) and (b), follow a linear dispersion, interrupted by a stop-band due to the excitation of the first magnetic Mie resonance. The isotropy of the structure suggests that the transverse modes (i.e. polarizations (E_y, H_z) and (E_z, H_y) for k_x-propagation) are degenerate. Note that the ratio of the wavelength at resonance over lattice constant for the sphere-crystal is $(\lambda_{res}/a) = 10$ and for the spherical-shell-crystal $(\lambda_{res}/a) = 7.5$, which are values

---

[1] CST GmbH, Darmstadt, Germany

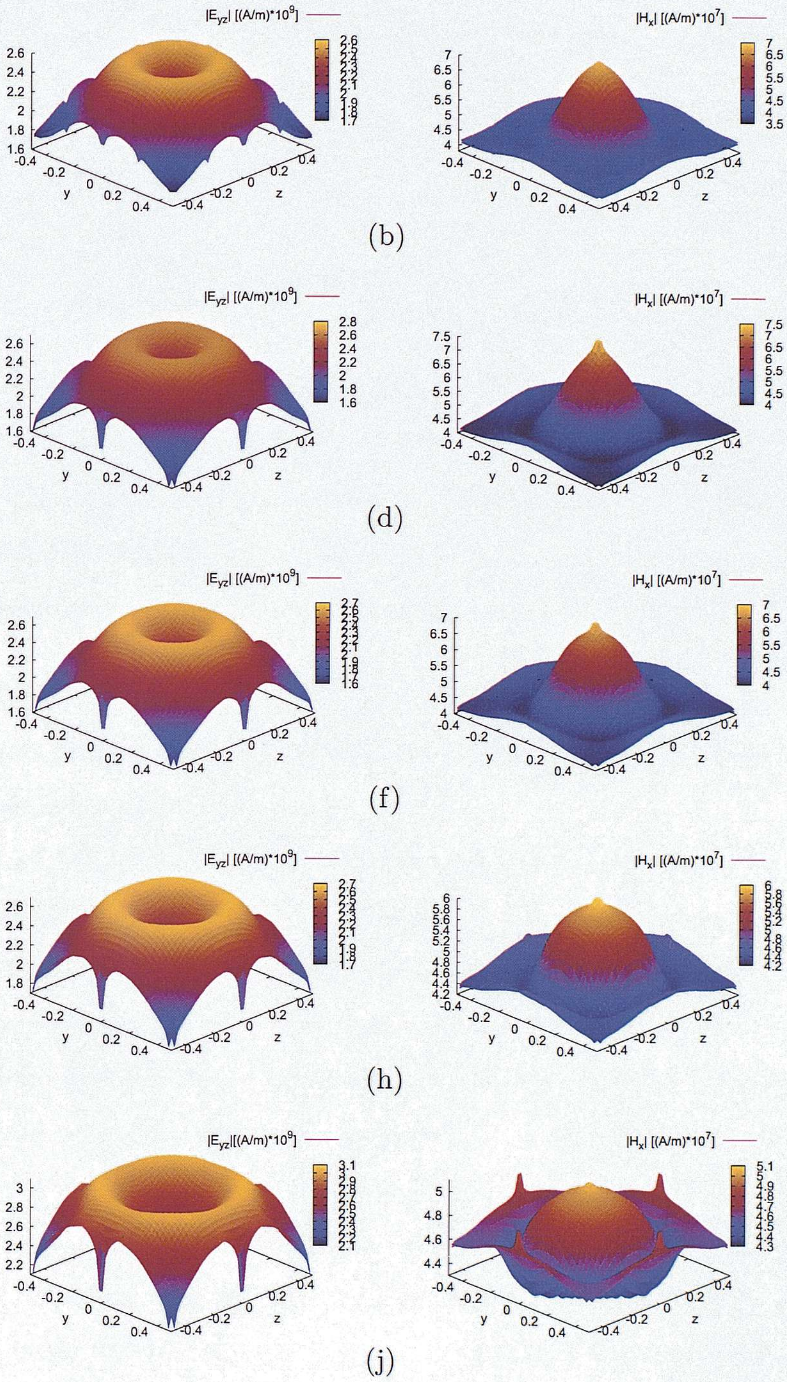

Figure 14.2: Numerically calculated field configurations for the first magnetic Mie resonance of a spherical-shell structures of radius $R_2 = 0.45mm$, dielectric constant $\varepsilon_2 = 100 + \sigma i/(\omega\varepsilon_0)$, $\sigma = 3.34(S/m)$ and arranged in a cubic lattice of constant $a = 1mm$ ($\varepsilon_1 = 1$). (a)-(b) $R_1 = 0$, (c)-(d) $R_1 = 0.05mm$, (e)-(f) $R_1 = 0.15mm$, (g)-(h) $R_1 = 0.25mm$ and (i)-(j) $R_1 = 0.35mm$. The fields are shown for k_x-propagation, on the $z = 0$-plane. Left figures is a plot of $|E_{yz}|$-field ($|E_{yz}| = \sqrt{E_y^2 + E_z^2}$) and figures on the right a plot of the magnetic field along the x-axes ($|H_x|$).

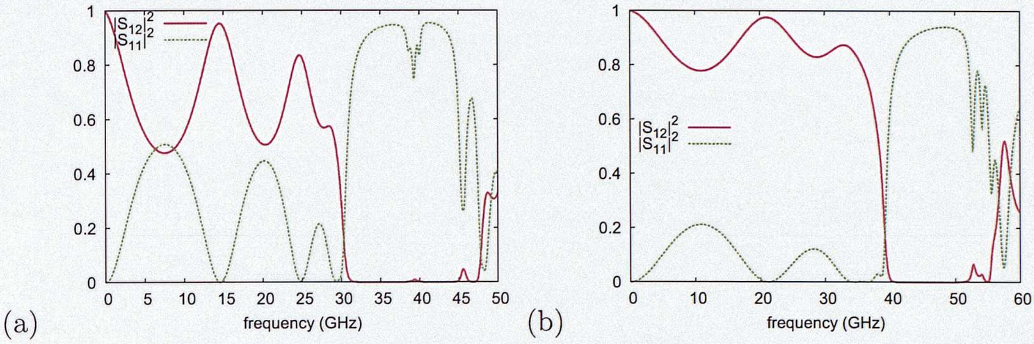

(a) (b)

Figure 14.3: S-parameters for a 4-unit-cell slab of a crystal made from (a) dielectric spheres of $R = 0.45mm$, $a = 1mm$, $\varepsilon = 100 + \sigma i/(\omega\varepsilon_0)$ and $\sigma = 3.34(S/m)$ and (b) dielectric spherical-shell of $R_1 = 0.35mm$, $R_2 = 0.45mm$, $a = 1mm$, $\varepsilon_2 = 100 + \sigma i/(\omega\varepsilon_0)$, $\sigma = 3.34(S/m)$ and $\varepsilon_1 = 1$. Solid red lines show the transmission coefficients and dotted green lines the reflection coefficients.

well within the homogenization model. Also, the linear dispersion of the two transverse modes also indicates that the resonances occur at frequencies where the effective medium approach is still valid.

The effect of the spherical-shell's thickness on the effective magnetic permeability and the resonant frequency is also investigated. The band structures for various values of R_1, while $R_2 = 0.45mm$ was kept constant, are plotted in figure 14.7(a). As R_1 becomes smaller, the band structure converges to the dispersion diagram of a sphere-crystal as expected. However, as R_1 increases, the resonant frequency and the bandwidth of the stop-band increase. In figure 14.7(b) the retrieved[2] effective magnetic permeabilities are plotted for the various spherical-shell-crystals, where it can be seen that the magnetic behaviour of the structures obey the Lorentz model for all R_1 values, but obviously with different resonant frequencies. Furthermore, the electric and magnetic fields for the resonant frequencies of spherical-shell crystals of various R_1 are plotted in figure 14.2, where for all values of R_1 the Mie mode can be identified as the first magnetic Mie resonance.

---

[2] The retrieval method is described in the following section

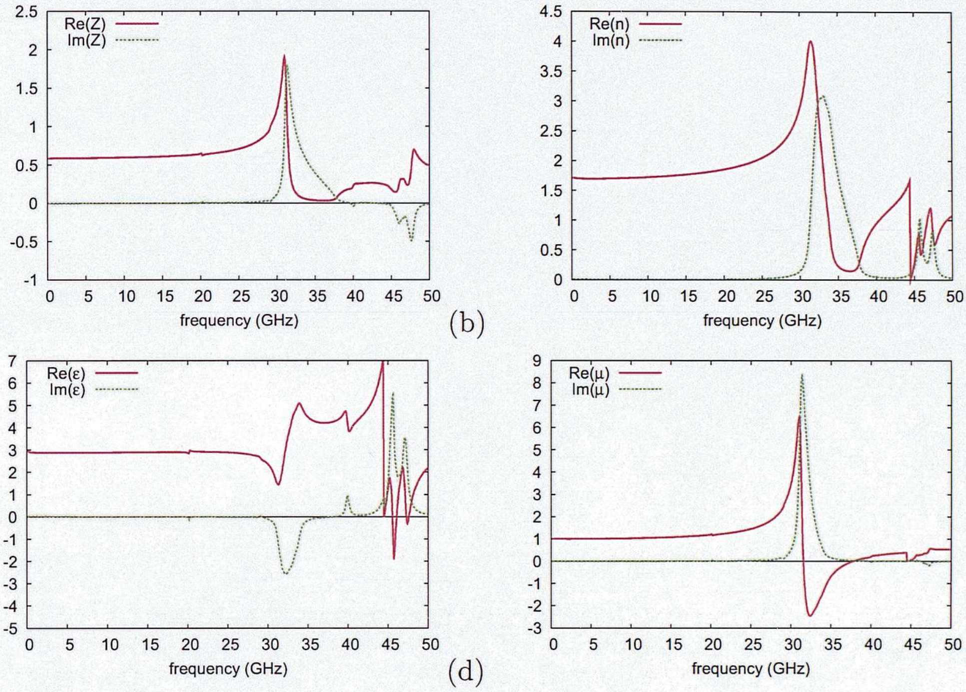

(a) (b) (c) (d)

Figure 14.4: For a crystal made from dielectric spheres of $R = 0.45mm$, $a = 1mm$, $\varepsilon = 100 + \sigma i/(\omega\varepsilon_0)$ and $\sigma = 3.34(S/m)$, the effective parameters were retrieved from numerically calculated S-parameters. The real part of the parameters is shown with a solid red line and the imaginary part with dotted green line for (a)the impedance (b) effective refractive index (c) effective electric permittivity (d) effective magnetic permeability

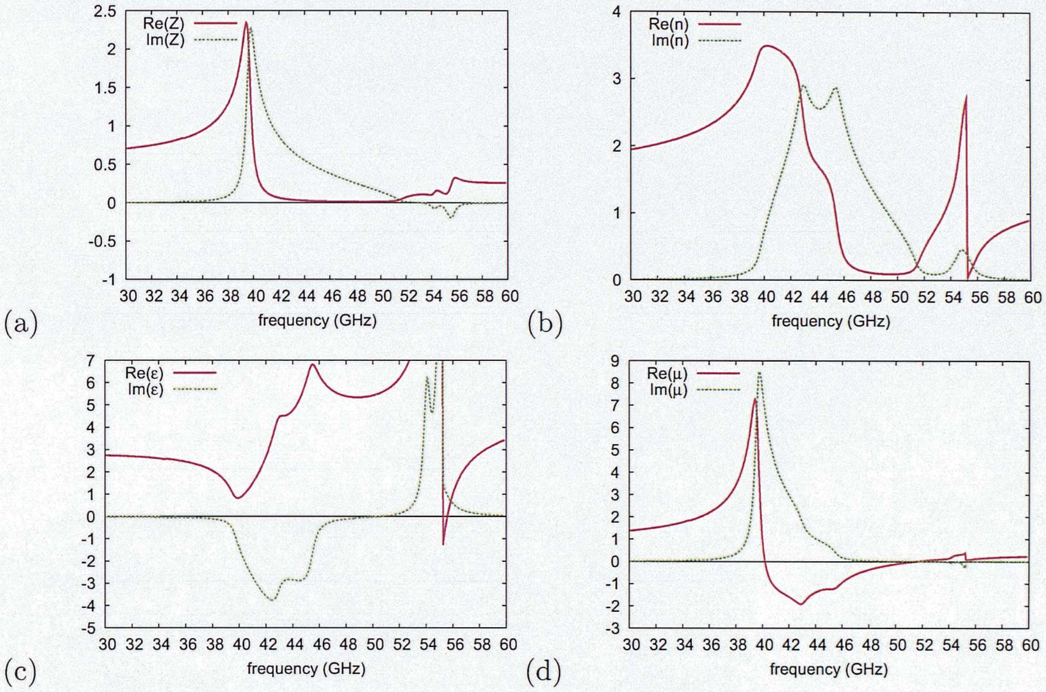

Figure 14.5: For a crystal made from dielectric spherical-shell of $R_1 = 0.35mm$, $R_2 = 0.45mm$, $a = 1mm$, $\varepsilon_2 = 100 + \sigma i/(\omega\varepsilon_0)$, $\sigma = 3.34(S/m)$ and $\varepsilon_1 = 1$, the effective parameters were retrieved from numerically calculated S-parameters. The real part of the parameters is shown with a solid red line and the imaginary part with dotted green line for (a)the impedance (b) effective refractive index (c) effective electric permittivity (d) effective magnetic permeability

14.1 Effective Electromagnetic Parameters

The S-parameters were calculated numerically using CST Microwave Studio for a slab of 4-unit-cells of the sphere and spherical-shell crystals, and are plotted in figure 14.3(a) and (b) respectively. Note that the transmission coefficient for the spherical-shell crystal is larger than for the sphere-crystal, since a bigger volume fraction of the unit-cell in the former is occupied by vacuum (i.e. less losses).

The effective electromagnetic parameters are retrieved (assuming waves of the form $\exp(-i\omega t)$) using the method described by [43, 45], where the impedance (Z) is given by:

$$Z = \pm\sqrt{\frac{(1+S_{11})^2 - S_{12}^2}{(1-S_{11})^2 - S_{12}^2}} \tag{14.1}$$

and the refractive index[3] (n) by:

$$n = \left(\frac{cos^{-1}\left(\frac{1-S_{11}^2+S_{12}^2}{2S_{12}}\right)}{kd} \right) + \frac{2\pi l}{kd} \tag{14.2}$$

and where l is an integer, S_{11} the reflection coefficient, $S_{12} = \exp(ikd)T_{12}$ and T_{12} is the transmission coefficient. Note that we ensured that causality is not violated by requiring that $Re(Z) > 0$ and $Im(n) > 0$. The electromagnetic parameters are then given by:

$$\varepsilon_{eff} = \frac{n}{Z} \tag{14.3}$$

$$\mu_{eff} = nZ \tag{14.4}$$

The effective parameters retrieved are plotted in figure 14.4 for the sphere-crystal and in figure 14.5 for the spherical-shell-crystal. Retrieved $Re(Z)$ and $Re(n)$ take negligibly small values for stop-band frequencies as expected. It can also be seen that the effective magnetic permeability for both structures becomes negative for the frequencies where there is a stop-band for the dispersion diagram. Also, note that for high frequencies $\mu \longrightarrow (1-F)$ and for low frequencies $\mu \longrightarrow 1$, as expected.

---

[3] Note that n is the effective refractive index of a crystal made from spheres in a periodic lattice and N is the refractive index of the dielectric material with constant ε that the spheres are made from.

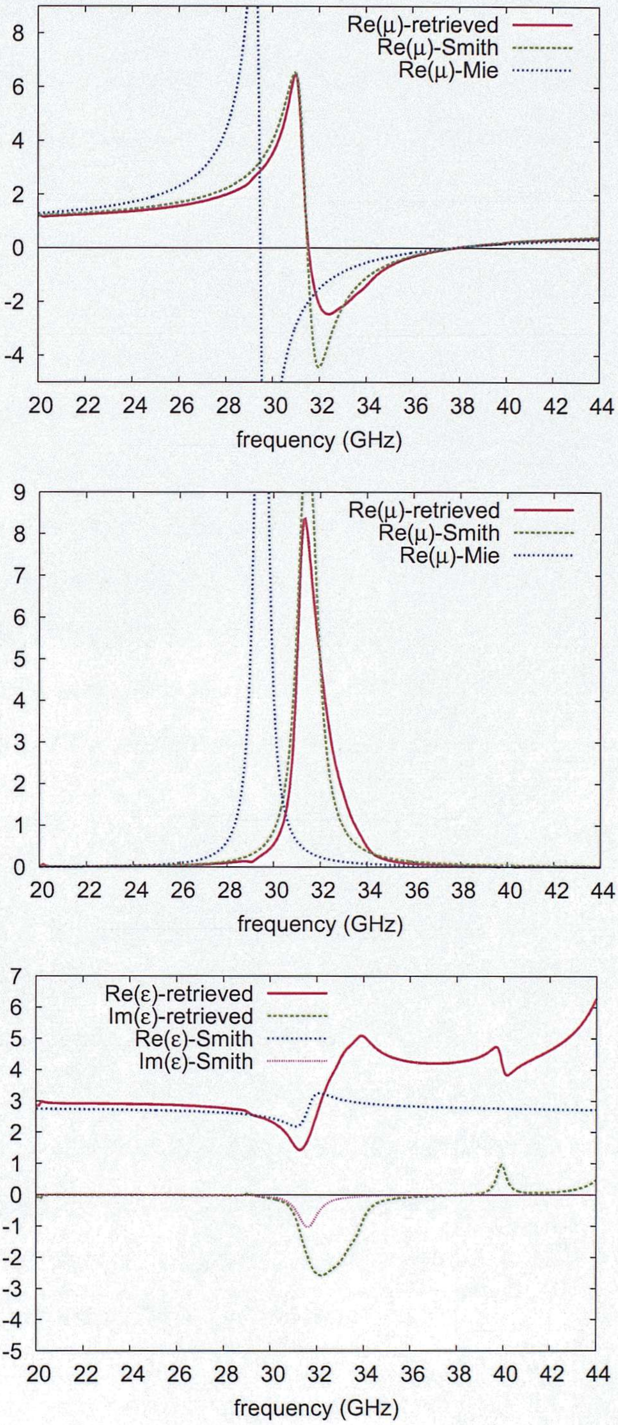

(a)

(b)

(c)

Figure 14.6: The retrieved (a) real and (b) imaginary parts of the effective magnetic permeability (solid red line) is plotted with equation (14.6) (dotted green line), which predicts the magnetic behaviour of a single spherical scatterer, Lorentz model (blue dashed line) of (14.8) that accounts for spatial dispersion is also plotted. (c) The retrieved effective electric permittivity (red solid line:real part and green dashed line:imaginary part) is plotted together with (14.9)(blue dotted line:real part and pink dashed line:imaginary part).

14.1.1 Fitting the retrieved parameters with analytical models

In order to investigate whether the retrieval method is valid for the sphere-crystal, an analytical prediction for the effective magnetic permeability was derived using microscopic field averaging (similarly to [56]) to obtain the effective permeability:

$$\mu_{eff} = \frac{< \mathbf{B} >}{\mu_0 < \mathbf{H} >} \tag{14.5}$$

where for simplicity consider averages at a plane intersection at the centre of the sphere (i.e. $z = 0$ -plane where figure 14.2(b) is plotted for) and therefore a cylindrical unit cell is considered (i.e. $a^2 = \pi R_c^2$). The average of B-field has to be taken over the whole area of the cross-section and H-field is averaged at the line between the spheres at the same plane (i.e. $r = a/2$). The magnetic fields of (13.8), (13.10) and (13.11) derived from Mie theory are used, and considering contribution only from the first magnetic Mie mode (i.e. $n = 1$), the effective magnetic permeability is obtained (more details for the derivation in [56]):

$$\mu_{eff} = \frac{2\pi}{a^2} \frac{d_1 \int_0^R r j_1(Nkr)dr + \int_R^{a/\sqrt{\pi}} r[j_1(kr) - a_1 h_1^{(1)}(kr)]dr}{j_1(ka/2) - a_1 h_1^{(1)}(ka/2)} \tag{14.6}$$

where N is the refractive index of spheres ($N = \sqrt{\varepsilon}$). For a sphere of $\varepsilon = 100 + \sigma i/(\omega\varepsilon_0)$, $\sigma = 3.34(S/m)$ and $R = 0.45mm$, (14.6) is plotted in figure 14.6, with the retrieved magnetic permeability. Both the real and imaginary parts of retrieved μ_{eff} and (14.6) have a similar shape with a small difference on the resonance frequency, which can easily be justified by noting that equation (14.6) accounts for a single-sphere scatterer and neglects contributions from neighbouring particles [63].

The effective magnetic permeability for a single sphere is a Lorentz-like resonance (also proved in [56]), given by:

$$\mu_r = 1 - \frac{F\omega^2}{\omega^2 - \omega_0^2 + i\gamma\omega} \tag{14.7}$$

where $F = 4\pi R^3/a^3$, γ accounts for the loss in the dielectrics. The finite size of the unit-cell, which although smaller than λ at resonance, is not negligible, results to spatial dispersion, and artifacts on the effective electromagnetic parameters, as described in [64, 65]. Considering that high-dielectric sphere-crystals are Lorentz-like resonators, the analytical method described by Smith *et.al.* [65] is used to derive the effective parameters by taking into account the spatial dispersion of the medium caused by the finite size of the unit cell and are given by:

$$\mu_{eff} = \mu_r \frac{\beta a/2}{\sin(\beta a/2)\cos(\beta a/2)} \tag{14.8}$$

where μ_r is the Lorentz-like resonance of (14.7). However, all magnetically resonant metamaterials show a weak resonance for the effective permittivity (and vice-versa), which is due to spatial dispersion and the phase advancement within a finite-sized unit-cell. From [64, 65], the effective permittivity of a magnetically resonant metamaterial is given by:

$$\varepsilon_{eff} = \overline{\varepsilon} \frac{\beta a/2}{\sin(\beta a/2)} \cos(\beta a/2) \tag{14.9}$$

where $\overline{\varepsilon} = 2/(1-F) = constant$ [6] and $F = (4/3)\pi R^3/a^3$ is the filling factor of the sphere. The phase advance (βa) across a unit cell is given by:

$$\beta a = 2\sin^{-1}\left(\sqrt{\mu_r}\frac{ka}{2}\right) \tag{14.10}$$

and where k is the wavevector. Applying these analytical formulae for the dielectric crystals discussed in this paper (i.e. $\omega_0 = 29.6GHz$ from (13.15), $a = 1mm$ and $R = 0.45mm$), the results obtained are plotted in figure 14.6 together with the retrieved parameters for comparison. The agreement between (14.8) and retrieved permeability is notable, as well as the agreement for the weak resonance of the effective permittivity. The differences seen for the effective parameters are due to the fact that the analytical method of (14.8) and (14.9) does not account for cell-to-cell interactions, which are expected to contribute to this structure's effective behaviour since $2R \sim a$ (i.e. spheres are closed-packed). Similarly, the retrieved effective magnetic permeability of the spherical-shell-crystal is also fitted to the Lorentz-based analytical prediction (14.8) and both are plotted in figure 14.7(b) together for comparison with thin red and thick black solid lines respectively. The agreement between them is also notable and similar to the behaviour of the sphere-crystal.

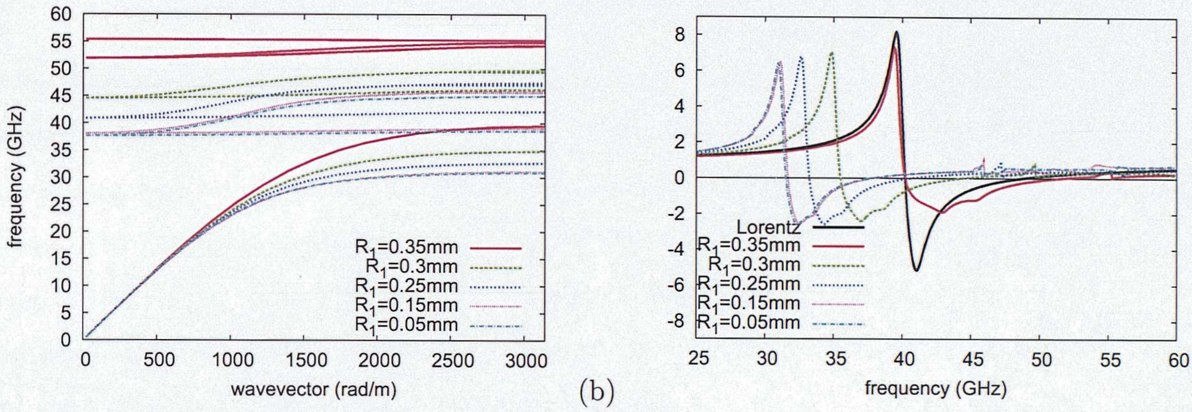

(a) (b)

Figure 14.7: (a) The band structures and (b) the retrieved effective magnetic permeability of spherical-shell crystals for various values of R_1. The effective magnetic permeability for $R_1 = 0.35mm$ is fitted to the Lorentz model of (14.8) (thick solid black line).

Chapter 15

Doubly Negative Metamaterials

Most doubly negative (DNG) metamaterials based on high-dielectric resonators are composed of two different particles, where the electric Mie resonance of the one particle is tuned at the same frequency range of the magnetic Mie mode of the other particle, in order to realize a negative refracting band. However, the bandwidth of the first electric Mie resonance for spheres is significantly more narrow-banded compared with the bandwidth of the first magnetic Mie mode. In figure 14.1(a) at about $48GHz$, the stop-band due to the first electric Mie resonance arises and is $\sim$ 92% narrower compared with the frequency range of the first magnetic Mie mode. Therefore, a negative metamaterial constructed by two sets of different dielectric spheres has an extremely narrow bandwidth for the negative band [66, 57, 59]. Furthermore, note that in the case of close-sphere-packing, a hybrid of resonances appears at slightly higher frequencies from the electric resonance [63, 67]. Also, if the spheres are not accurately enough manufactured (i.e. values of R and ε), the two resonances are detuned, destroying the negative band.

In order to avoid these problems and also take in full advantage the broad bandwidth of the first magnetic Mie resonance for both sphere- and spherical-shell-crystals, we embed both dielectric-crystals in a PEC wire-mesh [11, 12, 13]. Using CST Microwave Studio, the band structures of both metamaterials (figure 15.2) were calculated numerically for a medium composed of dielectric-crystals and a wire mesh of radius $r = 0.1mm$ and arranged in a lattice of $a = 1mm$ (i.e. plasma frequency

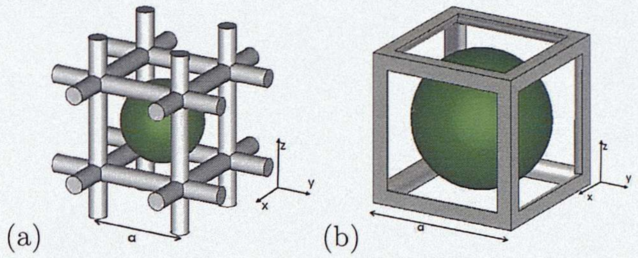

(a) (b)

Figure 15.1: (a)Embedding the high-dielectric spherical scatterers (spheres or spherical-shells) in a wire mesh, a negative refracting metamaterial is realized. The wire mesh is arranged symmetrically with the dielectric scatterer. (b) The unit cell simulated to numerically derive figures 15.2

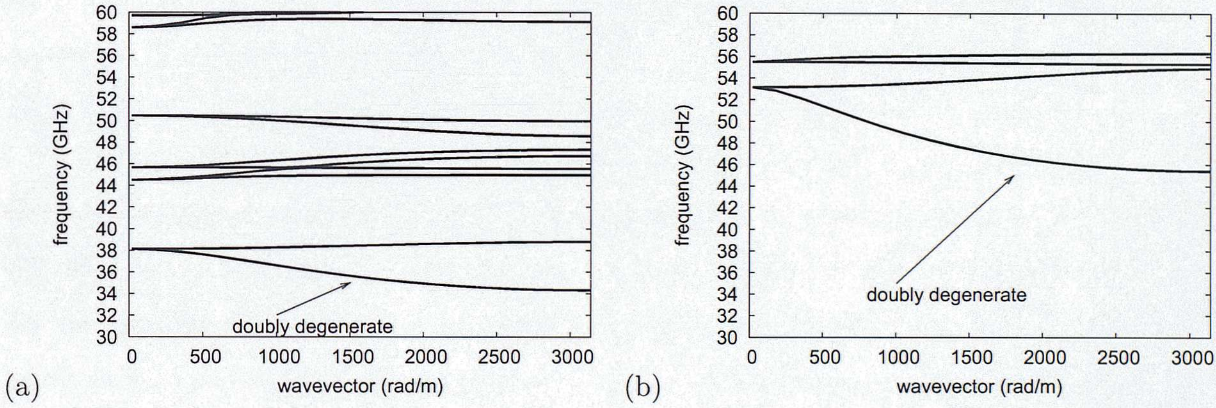

Figure 15.2: (a) Band structure for a high-dielectric crystal made of spheres of $R = 0.45mm$, $a = 1mm$, $\varepsilon = 100 + \sigma i/(\omega\varepsilon_0)$ and $\sigma = 3.34(S/m)$ and embedded in PEC wire-mesh of $r = 0.1mm$. (b) Band structure for a high-dielectric crystal made from spherical-shells of $R_1 = 0.35mm$, $R_2 = 0.45mm$ (as shown in figure 13.2(b), $a = 1mm$, $\varepsilon = 100 + \sigma i/(\omega\varepsilon_0)$ and $\sigma = 3.34(S/m)$, embedded in PEC wire-mesh of $r = 0.1mm$. There are two doubly degenerate negative modes for the frequencies where there is a stop-band for the dielectric crystals.

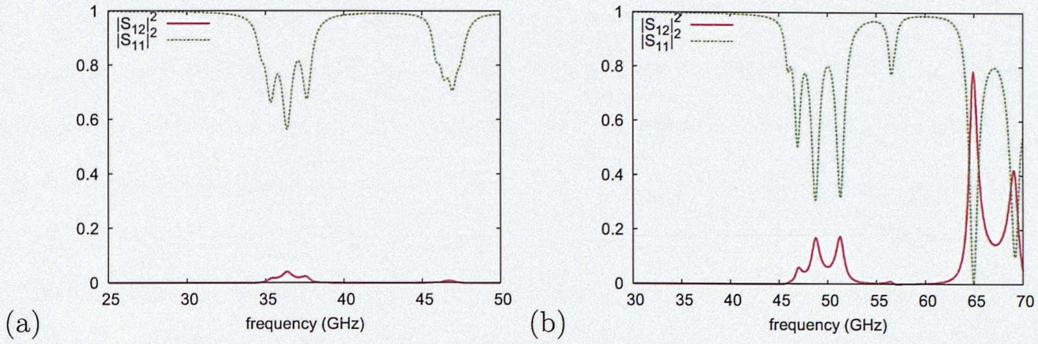

Figure 15.3: S-parameters for a 4-unit-cell slab of a negative refracting metamaterials composed of a wire mesh of $r = 0.1mm$ and a crystal made from (a) dielectric spheres of $R = 0.45mm$, $a = 1mm$, $\varepsilon = 100 + \sigma i/(\omega\varepsilon_0)$ and $\sigma = 3.34(S/m)$ and (b) dielectric spherical-shell of $R_1 = 0.35mm$, $R_2 = 0.45mm$, $a = 1mm$, $\varepsilon_2 = 100 + \sigma i/(\omega\varepsilon_0)$, $\sigma = 3.34(S/m)$ and $\varepsilon_1 = 1$. Solid red lines show the transmission coefficients and dotted green lines the reflection coefficients.

$\omega_p \sim 120GHz$), as shown in figure 15.1. The high-dielectric crystals are made from spheres of $R = 0.45mm$, $\varepsilon = 100 + \sigma i/(\omega\varepsilon_0)$, $\sigma = 3.34(S/m)$, and spherical-shells of $R_1 = 0.35mm$, $R_2 = 0.45mm$, $\varepsilon_2 = 100 + \sigma i/(\omega\varepsilon_0)$, $\sigma = 3.34(S/m)$ and $\varepsilon_1 = 1$.

The band structures derived numerically are plotted in figure 15.2, where a doubly degenerate negative band is observed, corresponding to polarizations (E_y, H_z) and (E_z, H_y) for k_x propagation. The negative bands in figures 15.2(a) and (b) appear for frequencies where there are stop-bands in figures 14.1(a) and (b). There is a small shift ($\sim 1 - 2GHz$) on the frequency that the negative band appears compared with the stop-bands of figure 14.1, which is due to the addition of the wire-mesh structure in the unit-cell, and its coupling with the magnetic resonator. However, the most outstanding observation is that the negative band is significantly more broad than other negative metamaterials [68]. The band structure of the spherical-shell-negative metamaterial, shows a negative band which is $\sim 55\%$ broader and appears at $\sim 72\%$ higher frequencies than for the sphere-negative metamaterials (as was indicated from figure 14.1). Note that the manufacture and experimental verification of a DNG composed of dielectric spheres and a wire-mesh operating at lower frequencies has been discussed in [69] with similar conclusions.

Finally, note that the spheres and spherical-shells are arranged symmetrically with respect to wire mesh, in order to obtain degenerate transverse modes. Distorting the symmetry, the two degenerate modes split, which also has significant applications, such as wave-polarization splitting devices.

The S-parameters for 4-unit-cell slabs of the two negative metamaterials were calculated numerically using CST Microwave Studio and are plotted in figure 15.3(a) and (b) for the sphere and spherical-shell negative metamaterials respectively. As it can be seen, the transmission coefficient is zero for stop-band frequencies and the reflection coefficient approaches one as expected from the band structure. Note the difference for the loss (or absorption) between the spherical-shell and the sphere-based DNG. The difference can be explained by considering the fact that less fraction of the space is filled with the high-dielectric material, which induces the losses. Nevertheless, there is no effect on the negative behaviour of the metamaterial, by using a spherical-shell as a magnetic resonator rather than a sphere.

Also, the negative band of both metamaterials is easily tuned to higher (or lower) frequencies, by either changing ε of dielectric material or scaling down (or up) the dimensions of the lattice and spherical-scatterer. For smaller values of ε, the natural Mie mode moves to higher frequencies. For example, for a sphere-crystal of $R = 0.45mm$ and $a = 1mm$, the effective medium theory holds for dielectric constants $\varepsilon \geq 40$ where $(\lambda/a) \geq 6$ and the resonant frequency is tuned up by $\sim 66\%$. Furthermore, by miniaturizing the dimensions of the lattice, the resonant frequency is obviously tuned to higher values, where the ε required is also lower. Note that ferroelectric spheres of few μm in radius and dielectric constant as low $\varepsilon = 20$, can already be manufactured and have homogeneous behaviour with resonant frequency in the low THz range [59, 60]. However, this does not come without a cost, since the loss is also increased at higher frequencies, but fortunately not as significantly as for conductor-based magnetic resonators. Limitations on the operational frequency range that the negative metamaterials described in this thesis, are dependent on manufacturing difficulties for handling ferroelectric ceramics for small enough lattices, and the losses of the conducting material of the wire-mesh, whose plasma behaviour breaks at high THz and optical frequencies.

Finally, the negative metamaterials discussed in this paper, show a negative band for frequencies where conducting-based metamaterials have difficulties to achieve isotropically, due to manufacturing problems. In [70, 68], the advancements of negative refractive metamaterials in the past few years are reviewed with respect of their operating frequencies. For the frequency range where dielectric-sphere- and spherical-shell-crystals can easily show magnetic behaviour (i.e. high GHz- low THz), to the best of our knowledge there are no other reported metamaterials that show isotropic magnetic behaviour or isotropic negative refraction. The reason of the lack of 3D-isotropic conductor-based magnetic resonators is that at high GHz-low THz frequencies, a much smaller lattice constant is demanded (approximately one order of magnitude) compared with the structures described in this report. Therefore, the manufacture of an isotropic metamaterial is practically more challenging. However, remarkable planar metamaterials have been constructed for high-GHz frequencies, such as Gokkavas *et.al.* [71] that reported double split-ring resonators operating at $\sim 100GHz$ and fishnet structures that operate from few GHz to infrared frequencies [31]. Note that high-dielectric composites can also be applied for planar applications, by simply replacing high-dielectric spheres and spherical-shells, with cylinders and rings, which show similar results but in 2D.

Chapter 16

Conclusions

High-dielectric sphere-crystals are used as magnetic resonant metamaterials, by exciting their first magnetic Mie resonance. The advantage of high-dielectric resonators (like ferroelectric ceramics) is that they exhibit significantly lower loss than conducting-based resonators, establishing them as ideal for metamaterials applications. In this report, we investigate the behaviour of high-dielectric spherical-shell-crystals that through the excitation of their first magnetic Mie resonance are also magnetically resonant, similarly to high-dielectric sphere-crystals. However, their resonant frequency is increased and the frequency range that μ_{eff} is negative is broaden for the same lattice dimensions as for sphere-crystals.

By embedding the high-dielectric crystals in a wire mesh, a doubly negatively refracting metamaterial is realized. The new negative metamaterials exhibit a broadband negative dispersion and significantly lower losses than entirely conducting-based metamaterials operating at the same frequency range. High-dielectric spherical structures can be used in order to easily manufacture isotropic metamaterials that are operational at frequencies where conductor-based magnetic metamaterials is more challenging to be constructed isotropically.

Part IV

Summary, Conclusions and Further Work

Chapter 17

Summary and Conclusions

We have discussed various metamaterial structures, by describing and characterizing their electromagnetic properties. Also, significant problems in some structures' behaviour were addressed and consequently we suggested ways to overcome them.

In the first part of the thesis, wire-mesh metamaterials were studied that simulate the electromagnetic properties of a low-density electron plasma, with the plasma frequency in the GHz range. Both the connected and non-connected designs were discussed and numerical calculations were compared with analytical work showing excellent agreement. It was shown that the behaviour of wire structures is strongly modified by spatial dispersion. Longitudinal waves incident on a wire-mesh metamaterials cause charges to accumulate periodically. The local fields produced from the periodic charge accumulation on wires, give rise to spatial dispersion, which causes the longitudinal mode to disperse with frequency and spoils the simple local model description for the permittivity tensor.

Spatial dispersion can be minimized in wire metamaterials by increasing either the capacitance or the inductance of the system. The capacitance can be increased by attaching conducting structures on the wires, where the charges associated with spatial dispersion are now stored on. The inductance of the metamaterial system is increased by coating the wires with a magnetic material, and therefore the magnetic field -and consequently the electric field- of the wave are enhanced. However, the static charge associated with spatial dispersion remains undisturbed. Therefore, the relative importance of spatial dispersion on the behaviour of the structure is reduced. Various designs were also proposed and numerically examined that manage to minimize spatial dispersion and create a dispersion-free longitudinal mode. Hence, the new wire-structures can be described by a simple local permittivity tensor, since only the transverse mode propagates in the metamaterial.

In part II of this thesis, Swiss Roll metamaterials are discussed. Initially, numerical calculations for non-chiral rolls are compared with analytical work, showing an excellent agreement. Therefore, it can be concluded that the analytical homogenization model is exceptionally valid for Swiss Rolls operating at the MHz-GHz frequency range. Additional resonances were observed and identified as trapped modes within the spiral gap, created by the shape of the conducting sheet. Furthermore, the more complicated design of chiral Swiss Rolls is discussed analytically and numerically, showing that chiral Swiss Rolls exhibit extreme chirality. The chirality of Swiss Rolls is significantly higher compared with other structures discussed in the literature, and allows for the macroscopic rotation of the wave's polarization by 90° in less than a wavelength.

A significant advantage of Swiss Roll metamaterials (both chiral and non), is the fact that their resonant frequencies are easily tuned over a wide range of frequencies (from few MHz to tens of GHz), by simply changing the number of turns (N), the packing (a), the radius (R) or the dielectric constant of the material in the gap (ε_d). Therefore, Swiss Rolls can be manufactured that are two orders of magnitude smaller than other magnetic resonators with the same resonant frequency, giving a much higher value to the (λ/a) ratio.

Finally in part III, by exciting the first magnetic Mie mode of high-dielectric spheres and spherical-shells in a crystal, a magnetically resonant medium is created. Their advantage over conductor-based particles (i.e. split-ring resonators) is that they exhibit significantly lower losses, a property that establishes them ideal for metamaterial applications. Also, the frequency range that the effective permeability of the crystals is negative, is significantly broader than other magnetic resonators. Hence, when the high-dielectric crystals are embedded in a wire-mesh metamaterial, a broadband double negative metamaterial is realized, with less losses compared with other negative metamaterials.

Chapter 18

Further Work

The work discussed in this thesis has a lot of potential to inspire further technological applications, theoretical and experimental work.

- Eliminating spatial dispersion from wire structures has significant advantages, since wire structures are widely used for technological purposes. A 2D version of the wire-mesh structure has been discussed in the literature and has resulted in many improved applications, like low-profile antennas [72, 73], leaky-wave antennas [74, 75], quasi-TEM and impedance waveguides [76, 77, 78]. The discussion in this thesis can provide more insight into the behaviour and properties of such structures, and tools towards experimentalists and engineers for more efficient designs.

- The conveniently small size of chiral Swiss Rolls for microwave frequencies and their extreme chirality, establish them as ideal for magnetic resonance imaging (MRI) applications [41, 34, 40, 33, 32], as well as for polarization rotation/selection antenna applications. Chiral Swiss Rolls have high optical rotation, which makes them ideal for replacing the helical wires that exist in polarization rotation/selection antennas, and therefore tremendously reducing antenna's size and enhance its efficiency.

- Applications and properties of metamaterials are frequently limited by loss, especially at higher than microwave frequencies. A solution to that problem could possibly be the use of high-dielectric materials that exhibit low-losses, serving as magnetic resonators. This structure can be tuned up to few hundreds of GHz, a range where significantly smaller lattice are required for other magnetic resonators (such as split-ring resonators).

- Finally, further developments can be achieved on the double negative metamaterial proposed in this thesis, by placing the spherical dielectric crystal non-isotropically with respect to the wire-mesh. Then, the two transverse negative bands are not degenerate any more, a property that can be used for numerous applications such as wave-polarization splitting devices.

Bibliography

[1] Pendry JB. Negative refraction. *Contemporary Physics*, 45:191–202, 2004.

[2] Ramakrishna SA. Physics of negative refractive index materials. *Reports on Progress in Physics*, 68:449, 2005.

[3] Pendry JB. Negative refraction makes a perfect lens. *Physical Review Letters*, 85:3966–69, 2000.

[4] Pendry JB, Schurig D, and Smith DR. Controlling electromagnetic fields. *Science*, 312:1780, 2006.

[5] Belov PA, Marques R, Maslovski SI, Nefedov IS, Silveirinha M, Simovski CR, and Tretyakov SA. Strong spatial dispersion in wire media in the very large wavelength limit. *Physical Review B*, 67:113103, 2003.

[6] Smith DR and Pendry JB. Homogenization of metamaterials by field averaging. *J. Opt. Soc. Am. B*, 23:391, 2006.

[7] Veselago VG. The electrodynamics of substances with simultaneously negative values of ε and μ. *Soviet Phys. Ups.*, 10:509, 1968.

[8] Jackson JD. *Classical Electrodynamics*. Singapore: Wiley, 1999.

[9] Pendry JB, Holden AJ, Robbins DJ, and Stewart WJ. Magnetism form conductors and enhanced nonlinear phenomena. *IEEE Transactions on Microwave Theory and Techniques*, 47:2075, 1999.

[10] Shelby RA, Smith DR, and Schultz S. Experimental verification of a negative index of refraction. *Science*, 292:77–79, 2001.

[11] Pendry JB, Holden AJ, Stewart WJ, and Young I. Extremely low frequency plasmons in metallic mesostructures. *Physical Review Letters*, 76:4773–6, 1996.

[12] Pendry JB, Holden AJ, Robbins DJ, and Stewart WJ. Low frequency plasmons in thin - wire structures. *Journal of Physics: Condensed Matter*, 10:4785–809, 1998.

[13] Demetriadou A and Pendry JB. Taming spatial dispersion in wire metamaterial. *J. Phys.: Condens. Matter*, 20:295222, 2008.

[14] Pendry JB and Ramakrishna SA. Focusing light using negative refraction. *Journal of Physics: Condensed Matter*, 15:6345–6364, 2003.

[15] Pendry JB. Perfect cylindrical lenses. *Optics Express*, 11:755–760, 2003.

[16] Ramakrishna SA and Pendry JB. Spherical perfect lens: Solutions of maxwell's equations for spherical geometry. *Physical Review B*, 69:115115, 2004.

[17] Schurig D, Mock JJ, Justice BJ, Cummer SA, Pendry JB, Starr AF, and Smith DR. Metamaterial electromagnetic cloak at microwave frequencies. *Science*, 314:977, 2006.

[18] Cummer SA, Popa BI, Schurig D, Smith DR, Pendry JB, Rahm M, and Starr AF. Scattering theory derivation of a 3d acoustic cloaking shell. *Physical Review Letters*, 100:024301, 2008.

[19] Brown J. Artificial dielectrics. *Progress in Dielectrics*, 2:195, 1960.

[20] Rotman W. Plasma simulation by artificial dielectrics and parallel-plate media. *IEEE Transactions on Antennas and Propagation*, 10:82–95, 1962.

[21] Belov PA, Tretyakov SA, and Viitanen A. Dispersion and reflection properties of artificial media formed by regular lattices of ideally conducting wires. *J. of Electromagnetic Waves and Applications*, 16:1153–70, 2002.

[22] Simovski CR and Belov PA. Low-frequency spatial dispersion in wire media. *Physical Review E*, 70:046616, 2004.

[23] Zhao Y, Belov PA, and Hao Y. Spatially dispersive finite-difference time domain analysis of subwavelength imaging by the wire medium slabs. *Optics Express*, 14:5154– 5167, 2006.

[24] Belov PA and Silveirinha MG. Resolution of subwavelength transmission devices formed by a wire medium. *Physical Review E*, 73:056607, 2006.

[25] Belov PA, Simovski CR, and Ikonen P. Canalization of subwavelength images by electromagnetic crystals. *Physical Review B*, 71:193105, 2005.

[26] Silveirinha MG and Fernandes CA. Homogenization of 3d-connected and nonconnected wire metamaterial. *IEEE Transactions on Microwave Theory and Techniques*, 53:1418–30, 2005.

[27] Silveirinha M. Nonlocal homogenization model for a periodic array of ϵ-negative rods. *Physical Review E*, 73:046612, 2006.

[28] Shapiro MA, Shvets G, Sirigiri LR, and Temkin RJ. Spatial dispersion in metamaterials with negative dielectric permittivity and its effect on surface waves. *Optics Letters*, 31(13):2051–53, 2006.

[29] Dolling G, Enkrich C, Wegener M, Zhou JF, Soukoulis CM, and Linden S. Cut-wire pairs and plate pairs as magnetic atoms for optical metamaterials. *Optics Letters*, 30:3198, 2005.

[30] Klein MW, Enkrich C, Wegener M, Soukoulis CM, and Linden S. Single-slit split-ring resonators at optical frequencies: limits of size scaling. *Optics Letters*, 31:1259, 2006.

[31] Valentine J, Zhang S, Zentgraf T, Ulin-Avila E, Genov DA, Bartall G, and Zhang X. Three-dimensional optical metamaterial with a negative refractive index. *Nature*, 455:376, 2008.

[32] Wiltshire MCK, Pendry JB, Young IR, Larkman DJ, Gilderdale DJ, and Hajnal JV. Microstructured magnetic materials for rf flux guides in magnetic resonance imaging. *Science*, 291:849, 2001.

[33] Wiltshire MCK, Hajnal JV, Pendry JB, Edwards DJ, and Stevens CJ. Metamaterial endoscope for magnetic field transfer: near field imaging with magnetic wires. *Optics Express*, 11:709–15, 2003.

[34] Wiltshire MCK, Pendry JB, and Hajnal JV. Sub-wavelength imaging at radio frequency. *J. of Phys.:Condensed Matter*, 19:456216, 2006.

[35] Demetriadou A and Pendry JB. Numerical analysis of swiss roll metamaterials. *J. Phys.: Condens. Matter*, submitted, 2009.

[36] Pendry JB. A chiral route to negative refraction. *Science*, 306:1353–1355, 2004.

[37] Demetriadou A and Pendry JB. Extreme chirality in swiss roll metamaterials. *J. Phys.: Condens. Matter*, submitted, 2009.

[38] Wood B and Pendry JB. Metamaterial at zero frequency. *J. Phys.: Condensed Matter*, 19:076208, 2007.

[39] Shurig D, Pendry JB, and Smith DR. Calculation of material properties and ray tracing in transformation media. *Optics Express*, 14:9794–9804, 2006.

[40] Wiltshire MCK. Radio frequency (rf) metamaterials. *Physica Status Solidi*, 244:1227–36, 2007.

[41] Wiltshire MCK, Pendry JB, Williams W, and Hajnal JV. An effective medium description of ‘swiss rolls’, a magnetic metamaterial. *J. of Phys.:Condensed Matter*, 18:L315–L321, 2007.

[42] Zolla F, Nicolet A, and Guenneau S. Swiss roll lattices:numerical and asymptotic modelling. *Waves in Random and Complex Media*, 17:571–9, 2007.

[43] Smith DR, Schultz S, Markos P, and Soukoulis CM. Determination of effective permittivity and permeability of metamaterials from reflection and transmission coefficients. *Physical Review B*, 65:195104–1, 2002.

[44] Chen X, Grzegorczyk TM, Wu BI, Pacheco J, and Kong JA. Robust method to retrieve the constitute effective parameters of metamaterials. *Physical Review E*, 70:016608–1, 2004.

[45] Smith DR, Vier DC, Koschny T, and Soukoulis CM. Electromagnetic parameter retrieval from inhomogeneous metamaterials. *Physical Review E*, 71:03667–1 – 11, 2005.

[46] Chen X, Wu BI, Kong JA, and Grzegorczyk TM. Retrieval of the effective constitutive parameters of bianisotropic metamaterial. *Physical Review E*, 71:046610–1, 2005.

[47] Potts A, Papakostas A, Bagnall DM, and Zheludev NI. Planar chiral metamaterials for optical applications. *Microelectronic Engineering*, 73-74:367–71, 2004.

[48] Plum E, Fedotov VA, Schwanecke AS, Zheludev NI, and Chen Y. Giant optical gyrotropy due to electromagnetic coupling. *Applied Physics Letters*, 90:223113, 2007.

[49] Rogacheva AV, Fedotov VA, Schwanecke AS, and Zheludev NI. Giant gyrotropy due to electromagnetic-field coupling in a bilayered chiral structure. *Physical Review Letters*, 97:177401, 2006.

[50] Tretyakov S, Sihvola A, and Jylha L. Backward-wave regime and negative refraction in chiral composites. *Photonics and Nanostructures - Fundamentals and Applications*, 3:107–115, 2005.

[51] Sihvola Ari. Metamaterials in electromagnetics. *Metamaterials*, 1:2–11, 2007.

[52] Silveirinha MG. Design of linear-to-circular polarization transformers made of long densely packed metallic helices. *IEEE Transactions on Antennas and Propagation*, 56:390–401, 2008.

[53] Zhou J, Dong J, Wang B, Koschny T, Kafesaki M, and Soukoulis CM. Negative refractive index due to chirality. *Physical Review B*, 79:121104, 2009.

[54] Plum E, Zhou J, Dong J, Fedotov VA, Koschny T, Soukoulis CM, and Zheludev NI. Metamaterials with negative index due to chirality. *Physical Review B*, 79:035407, 2009.

[55] MCK Wiltshire, JB Pendry, and JV Hanjal. Chiral swiss rolls show a negative refractive index. *J. Phys.:Condended Matter*, 21:292201, 2009.

[56] O'Brien S and Pendry JB. Photonic band-gap effects and magnetic activity in dielectric composites. *Journal of Physics: Condensed Matter*, 14:4035–4044, 2002.

[57] OG Vendik and MS Gashinova. Artificial double negative (dng) media composed by two different dielectric sphere lattices embedded in a dielectric matrix. *Proceedings European Microwave Conference*, page 1209, 2004.

[58] I Vendik, O Vendik, I Kolmakov, and M Odit. Modelling of isotropic double negative media for microwave applications. *Opto-electronics Review*, 14:178, 2006.

[59] L Jylha, I Kolmakov, M Maslovski, and S Tretyakov. Modelling of isotropic backward-wave materials composed of resonant spheres. *Journal of Applied Physics*, 99:043102, 2006.

[60] MS Wheeler, JS Aitchison, and M Mojahedi. Coated nonmagnetic spheres with a negative index of refraction at infrared frequencies. *Physical Review B*, 73:045105, 2006.

[61] Bohren CF and Huffman DR. *Absorption and Scattering of Light by Small Particles.* New York: Wiley- Interscience, 1983.

[62] JD Stratton. *Electromagnetic Theory.* McGraw-Hill Book Company, 1941.

[63] MI Antonoyiannakis and JB Pendry. Mie resonances and bonding in photonic crystals. *Europhysics Letters*, 40:613, 1997.

[64] R Liu, T J Cui, D Huang, B Zhao, and D R Smith. Description and explanations of electromagnetic behaviors in artificial metamaterials based on effective medium theory. *Physical Review E*, 76:026606, 2007.

[65] D R Smith. Analytic expressions for the constitutive parameters for magnetoelectric metamaterials. *to be published*, 2009.

[66] CL Holloway, EF Kuester, J Baker-Jarvis, and P Kabos. A double negative (dng) composite medium composed of magnetodielectric spherical particles embedded in a matrix. *IEEE Transactions on antennas and propagation*, 51:2596, 2003.

[67] MI Antonoyiannakis and JB Pendry. Electromagnetic forces in photonic crystals. *Physical Review B*, 60:2363, 1999.

[68] Soukoulis CM, Zhou J, Koschny T, Kafesaki M, and Economou EN. The science of negative index materials. *Journal of Physics: Condensed Matter*, 20:304217, 2008.

[69] X Caia, R Zhua, and G Hu. Experimental study for metamaterials based on dielectric resonators and wire frame. *Metamaterials*, 2:220–226, 2008.

[70] Soukoulis CM, Linden S, and Wegener M. Negative refractive index at optical wavelengths. *Science*, 315:47–49, 2007.

[71] Gokkavas M, Guven K, Bulu I, Aydin K, Penciu RS, Kafesaki M, Soukoulis CM, and Ozbay E. Experimental demonstration of a left-handed metamaterial operating at 100 ghz. *Physical Review B*, 73:193103, 2006.

[72] AP Feresidis, G Goussetis, W Shenhong, and JC Vardaxoglou. Artificial magnetic conductor surfaces and their application to low-profile high-gain planar antennas. *IEEE Trans. Antennas Propag.*, 53:209–215, 2005.

[73] JM Bell and MF Iskander. A low-profile archimedean spiral antenna using an ebg ground plane. *IEEE Antennas Wireless Propag. Lett.*, 3:223–226, 2004.

[74] D Sievenpiper, J Schaffner, JJ Lee, and S Livingston. A steerable leaky-wave antenna using a tunable impedance ground plane. *IEEE Antennas Wireless Propag. Lett.*, 1:179–182, 2002.

[75] D Sievenpiper. Forward and backward leaky wave radiation with large effective aperture from an electronically tunable textured surface. *IEEE Antennas Propag.*, 53:236–247, 2005.

[76] JFR Yang, KP Ma, Y Qian, and T Itoh. A novel tem waveguide using uniplanar compact photonic-bandgap (uc-pbg) structure. *IEEE Trans. Mircowave Theory Tech.*, 47:2092–2098, 1999.

[77] JA Higgins, H Xin, A Sailer, and M Rosker. Ka-band waveguide phase shifter using tunable electromagnetic crystal sidewalls. *IEEE Trans. Mircowave Theory Tech.*, 51:1281–1287, 2003.

[78] O Luukkonen, C Simovski, AV Raisanen, and S A Tretyakov. An efficient and simple analytical model for analysis of propagation properties in impedance waveguides. *IEEE Trans. Mircowave Theory Tech.*, 56:1624–1632, 2008.

Appendix A

Effective electron mass in an artificial plasma

Consider the parallel-wire medium in figure 3.1 arranged in a square lattice of constant a with the wires placed at the centre of the unit cell and aligned with the z-axis. When current flows in a wire, a magnetic field is created around the wire [11, 12], which is given by:

$$H(r) = \frac{j}{2\pi R} = \frac{\pi r_0^2 nve}{2\pi r} \tag{A.1}$$

where r is the distance from the wire, v the mean electron velocity, r_0 the wire's radius, n the density of the electrons in the wire and $j = \pi r_0^2 nve$ the current flowing in the wire. Now, consider a plasmon-like longitudinal excitation for the system shown in figure 3.1 (i.e. the wavevector and the electric field of the incident radiation are parallel to the wires and along the z-axis) and $\mathbf{q}a \ll 1$. Therefore, the applied electric field is:

$$D = [0, 0, D_0]exp[i(kz - \omega t)] \tag{A.2}$$

From Maxwell's equations: $\nabla \times \mathbf{H} = \frac{\partial \mathbf{D}}{\partial t} + \mathbf{j}$ where $\mathbf{j}$ is the current confined in the thin wires, and $\mathbf{D}$ is the electric field, which is uniform in the x-y plane for $\mathbf{q}a \ll 1$ [8]. Now, approximate the cubical unit cell with a cylindrical of the same cross-section area (i.e. $\pi R_c^2 = a^2 \Rightarrow R_c = \frac{a}{\sqrt{\pi}}$), where R_c is the radius of the cylindrical unit cell and a the lattice constant. For simplicity, assume that there are no contributions to the magnetic field from neighbouring wires. Therefore, the magnetic field inside a circle of radius r is given by:

$$H_c(r) = \begin{cases} \frac{j}{2\pi r}\left(1 - \frac{\pi r^2}{\pi R_c^2}\right) & \text{for } 0 < r < R_c \\ 0 & \text{for } r \geq R_c \end{cases} \tag{A.3}$$

Also: $\mathbf{H}(r) = \mu_0^{-1}\nabla \times \mathbf{A}$ and therefore the vector potential $\mathbf{A}$ can be written as $\nabla \times \mathbf{A} = \mu_0 \mathbf{H_c(r)} = \frac{\mu_0 j}{2\pi}\left[\frac{1}{r} - \frac{r}{R_c^2}\right]$. Applying Stokes' theorem, the vector potential becomes:

$$A_c(r) = \begin{cases} \frac{\mu_0 j}{2\pi}\left[\ln(\frac{R_c}{r}) - \frac{R_c^2 - r^2}{2R_c^2}\right] & \text{for } 0 < r < R_c \\ 0 & \text{for } r \geq R_c \end{cases} \tag{A.4}$$

Note that the integration constant is chosen such that the vector potential to be zero outside the cylindrical unit cell, in order to ensure no mutual inductance between the wires (i.e. no neighbouring contributions). By substituting for $R_c = \frac{a}{\sqrt{\pi}}$, the vector potential at the surface of the wire (i.e $r = r_0$) is:

$$A_c(r_0) = \frac{\mu_0 j}{2\pi}\left[\ln\left(\frac{a}{r_0\sqrt{\pi}}\right) - \frac{1}{2} + \frac{\pi r_0^2}{2a^2}\right] \tag{A.5}$$

but since $r_0 \ll a$, then $\frac{\pi r_0^2}{2a^2} \rightarrow 0$ and $\ln\left(\frac{a}{r_0\sqrt{\pi}}\right) \gg \frac{1}{2}$, therefore the vector potential approximately becomes:

$$A_c(r) \approx \frac{\mu_0 r_0^2 nve}{2\pi} \ln\left(\frac{a}{r_0\sqrt{\pi}}\right) \tag{A.6}$$

From classical mechanics, the electrons in a magnetic field have an additional contribution to their momentum of $e\mathbf{A}$. Therefore, the total momentum per unit length of the wire is:

$$eA(r)n\pi r_0^2 = m_{eff}\pi r_0^2 nv \approx \frac{\pi\mu_0 v(er_0^2 n)^2}{2} \ln\left(\frac{a}{r_0\sqrt{\pi}}\right) \tag{A.7}$$

and therefore, the effective electron mass is given by:

$$m_{eff} \approx \frac{\mu_0 e^2 r_0^2 n}{2} \ln\left(\frac{a}{r_0\sqrt{\pi}}\right) \tag{A.8}$$

However, by accounting for the neighbouring wire-contributions, a more precise form for the effective electron mass is derived given by:

$$m_{eff} = \frac{\mu_0 e^2 r_0^2 n}{2}\left[\ln\left(\frac{a}{2\pi r_0}\right) + F(x)\right] \tag{A.9}$$

where $F(x)$ accounts for contributions from neighbouring wires and for a square lattice $F(x = 1) = 0.5275$ [5]. For wires arranged in an orthogonal lattice of constants a and b, (A.9) is valid and where $x = \frac{\mathrm{a}}{\mathrm{b}}$ and $F(x) = -\frac{1}{2}ln(x) + \sum_{n=1}^{+\infty}\left(\frac{coth(\pi nx)-1}{n}\right) + \frac{\pi x}{6}$.

Appendix B

Dispersion Equations of Parallel-Wire Medium

Consider the parallel-wire metamaterial shown in figure 3.1, with the wires along the z-axes and arranged in a square lattice of constant a. The aim is to find self-consistent solutions of Maxwell's equations, where the current in the wires support the surrounding fields. In order to do this, we need to consider:

1. the mean electric field averaged over the unit cell $(\overline{E_z})$
2. the difference of the electric field across the unit cell $(\Delta E_z(r_0))$

B.1 Mean Electric field:

The current induced in each wire, averaged over the unit cell is given by:

$$< \mathbf{j} >= \frac{I\hat{\mathbf{z}}}{a^2} exp(iq_x x + iq_y y + iq_z z - i\omega t) \tag{B.1}$$

where I is the current induced on the wire and q the wavevector inside the metamaterial. Using the continuity equation:(i.e. $\nabla \mathbf{j} + \frac{\partial \rho}{\partial t} = 0$), the charge density in each wire averaged over the unit cell is:

$$< \rho >== \frac{Iq_z}{\omega a^2} exp(iq_x x + iq_y y + iq_z z - i\omega t) \tag{B.2}$$

Also, from Maxwell equations and the gauge of **A** through Lorentz condition in free space (i.e. $\nabla \cdot \mathbf{A} + \frac{1}{c_0^2}\frac{\partial \phi}{\partial t} = 0$) [8], two differential equations of **A** and ϕ emerge (where **A** is the vector potential and ϕ the scalar potential):

$$\nabla^2 \mathbf{A} - \frac{1}{c_0^2}\frac{\partial^2 \mathbf{A}}{\partial t^2} = -\mu_0 < \mathbf{j} > \tag{B.3}$$

$$\nabla^2 \phi - \frac{1}{c_0^2}\frac{\partial^2 \phi}{\partial t^2} = -\frac{< \rho >}{\varepsilon_0} \tag{B.4}$$

which can be solved and give:

$$\mathbf{A} = \frac{\mu_0 I \hat{\mathbf{z}}}{(q^2 - k_0^2)a^2} \exp(iq_x x + iq_y y + iq_z z - i\omega t) \tag{B.5}$$

$$\phi = \frac{I q_z}{(q^2 - k_0^2)\varepsilon_0 a^2 \omega} \exp(iq_x x + iq_y y + iq_z z - i\omega t) \tag{B.6}$$

where $k_0 = \omega / c_0$. Consequently, the mean electric and magnetic fields averaged over the unit cell are given by:

$$\overline{\mathbf{B}} = i\mathbf{q} \times \mathbf{A} = \frac{i\mu_0 I (q_y \hat{\mathbf{x}} + q_x \hat{\mathbf{y}})}{(q^2 - k_0^2)a^2} exp(iq_x x + iq_y y + iq_z z - i\omega t) \tag{B.7}$$

$$\overline{\mathbf{E}} = i\omega \mathbf{A} - i\mathbf{q}\phi = \left[i\omega\mu_0 \hat{\mathbf{z}} - \frac{iq_z \mathbf{q}}{\varepsilon_0 \omega} \right] \frac{I}{(q^2 - k_0^2)a^2} \exp(iq_x x + iq_y y + iq_z z - i\omega t) \tag{B.8}$$

However, we are interested for the mean electric field along the z-direction which is:

$$\overline{E_z} = \frac{-iI}{\varepsilon_0 \omega a^2} \left(\frac{k_0^2 - q_z^2}{k_0^2 - q^2} \right) \exp(iq_x x + iq_y y + iq_z z - i\omega t) \tag{B.9}$$

B.2 Difference of the Electric Field across the unit cell:

Now, the difference of the electric field from the edge of the unit cell to the surface of the wire needs to be calculated. For simplicity, replace the square unit cell with a cylindrical unit cell of the same cross-sectional area (i.e. $R_c = a/\sqrt{\pi}$). **A** and ϕ in (B.6) are converted in cylindrical coordinates:

$$A_z = A_0 H_0^{(1)} \left(r\sqrt{k_0^2 - q_z^2} \right) \exp(iq_z z - i\omega t) \tag{B.10}$$

$$\phi = \phi_0 H_0^{(1)} \left(r\sqrt{k_0^2 - q_z^2} \right) \exp(iq_z z - i\omega t) \tag{B.11}$$

where $H_0^{(1)}(x) \approx i\frac{2}{\pi}\ln(x) + 1 + ...$ is Hankel function.The local electric field at distance r from the centre of a wire is given by $E_z(r) = -\frac{\partial \phi}{\partial z} - \frac{\partial A_z}{\partial t}$, and hence:

$$E_z(r) = -i\frac{2}{\pi}\frac{(k_0^2 - q_z^2)I}{4k_0}\sqrt{\frac{\mu_0}{\varepsilon_0}}H_0^{(1)}\left(r\sqrt{k_0^2 - q_z^2}\right)\exp(iq_z z - i\omega t) \tag{B.12}$$

The difference of the electric field from R_c to just above the surface of the wire (r_0) is given by :

$$\Delta E_z(r_0) = E_z\left(\frac{a}{\sqrt{\pi}}\right) - E_z(r_0) = -i\frac{(k_0^2 - q_z^2)I}{k_0 k_p^2 a^2}\sqrt{\frac{\mu_0}{\varepsilon_0}}\exp(iq_z z - i\omega t) \tag{B.13}$$

where $k_p^2 = \frac{2\pi}{a^2 \ln\left(\frac{a}{r\sqrt{\pi}}\right)}$ is the wavevector associated with plasma frequency ω_p.

B.3 Dispersion equations:

Assuming that there are no contributions from neighbouring wires, the electric field at $R_c = a/\sqrt{\pi}$ should be zero and therefore, the difference between $\overline{E_z}$ and $\Delta E_z(r_0)$, gives the electric field in the wire. However, the electric field in the wire is zero, since the wires are made from a perfect conducting material. Hence:

$$E_z - \Delta E_z(r_0) = -\frac{iI}{a^2 k_0}\sqrt{\frac{\mu_0}{\varepsilon_0}}(k_0^2 - q_z^2)\left[\frac{1}{k_0^2 - q^2} - \frac{1}{k_p^2}\right]e^{(iq_z z - i\omega t)} = 0 \tag{B.14}$$

The solutions of (B.14) give the dispersion equations for the thin-parallel-wire structure:

(a) transverse electric (TE) mode: $k_0 = \omega/c_0$, but $k_0 = 0$ for q_z-propagation.

(b) transverse magnetic (TM) mode: $k_0^2 = q^2 + k_p^2$

(c) transverse electric and magnetic (TEM) mode: $q_z = k_0 = \omega/c_0$

Appendix C

Dispersion Equations of Wire-Mesh Metamaterials

Similarly to Appendix B, the aim is to find self-consistent solutions of Maxwell's equations, where the current induced on the wires supports the surrounding fields. Consider a wire-mesh metamaterial (as shown in figure 4.1) with wires along the three orthogonal axes (the difference between connected and non-connected structures is stressed in the text). As before, we need to calculate the mean electric field averaged over the unit cell ($\overline{E_x}$) and the difference of the electric field from the edge of the unit cell to the surface of the wire ($\Delta E_x(r_0)$).

C.1 Mean Electric field:

The current in the wire averaged over the unit cell is:

$$< \mathbf{j} >= \frac{\mathbf{j_0}}{a^2} exp(iq_x x + iq_y y + iq_z z - i\omega t) \tag{C.1}$$

where q is the wavevector inside the metamaterial and $\mathbf{j_0} = I(\hat{\mathbf{x}} \sin\theta\cos\phi + \hat{\mathbf{y}} \sin\theta\sin\phi + \hat{\mathbf{z}}\cos\theta)$ The charge density averaged over the unit cell is derived through the continuity equation, and is given by:

$$< \rho >= \frac{\mathbf{j_0} \cdot \mathbf{q}}{a^2 \omega} exp(iq_x x + iq_y y + iq_z z - i\omega t) \tag{C.2}$$

From Maxwell equations and the gauge of **A** through Lorentz condition in free space $(=\nabla \cdot \mathbf{A} + \frac{1}{c_0^2}\frac{\partial \phi}{\partial t} = 0)$ [8], differential equations for **A** and ϕ are obtained:

$$\nabla^2 \mathbf{A} - \frac{1}{c_0^2}\frac{\partial^2 \mathbf{A}}{\partial t^2} = -\mu_0 < \mathbf{j} > \tag{C.3}$$

$$\nabla^2 \phi - \frac{1}{c_0^2}\frac{\partial^2 \phi}{\partial t^2} = -\frac{< \rho >}{\varepsilon_0} \tag{C.4}$$

Solving the above differential equations, **A** and ϕ are derived:

$$\mathbf{A} = \frac{\mu_0 \mathbf{j}_0}{(q^2 - k_0^2)a^2}\exp(iq_x x + iq_y y + iq_z z - i\omega t) \tag{C.5}$$

$$\phi = \frac{\mathbf{j}_0 \cdot \mathbf{q}}{(q^2 - k_0^2)\varepsilon_0 a^2 \omega}\exp(iq_x x + iq_y y + iq_z z - i\omega t) \tag{C.6}$$

Hence, the average electric and magnetic fields over the unit cell are given by:

$$\overline{\mathbf{B}} = i\mathbf{q} \times \mathbf{A} = \frac{i\mu_0 \mathbf{q} \times \mathbf{j}_0}{(q^2 - k_0^2)a^2} exp(iq_x x + iq_y y + iq_z z - i\omega t) \tag{C.7}$$

$$\overline{\mathbf{E}} = i\omega \mathbf{A} - i\mathbf{q}\phi = \left[i\omega\mu_0 \mathbf{j}_0 - i\mathbf{q}\frac{\mathbf{j}_0 \cdot \mathbf{q}}{\varepsilon_0 \omega} \right] \frac{1}{(q^2 - k_0^2)a^2}\exp(iq_x x + iq_y y + iq_z z - i\omega t) \tag{C.8}$$

However, for simplicity consider the average electric field along one of the wire axes (i.e. along x-axis):

$$\overline{E_x} = \left[i\omega\mu_0 j_{0x} - iq_x\frac{\mathbf{j}_0 \cdot \mathbf{q}}{\varepsilon_0 \omega} \right] \frac{1}{(q^2 - k_0^2)a^2}\exp(iq_x x + iq_y y + iq_z z - i\omega t) \tag{C.9}$$

C.2 Difference of the Electric Field across the unit cell:

Similarly to Appendix B, replace the square unit cell with a cylindrical of the same area (i.e. $R_c = a/\sqrt{\pi}$). Therefore, **A** and ϕ can be written for cylindrical coordinates, as:

$$A_x = A_0 H_0^{(1)}\left(r\sqrt{k_0^2 - q_x^2} \right)\exp(iq_x x - i\omega t) \tag{C.10}$$

$$\phi = \phi_0 H_0^{(1)}\left(r\sqrt{k_0^2 - q_x^2} \right)\exp(iq_x x - i\omega t) \tag{C.11}$$

where $H_0^{(1)}(x) \approx i\frac{2}{\pi}\ln(x) + 1 + ...$ is a Hankel function. The electric field at a distance r from the centre of the wire and along one of the wires is given by $E_x(r) = -\frac{\partial \phi}{\partial x} - \frac{\partial A_x}{\partial t}$, hence:

$$E_x(r) = iH_0^{(1)}\left(r\sqrt{k_0^2 - q_x^2} \right)\sqrt{\frac{\mu_0}{\varepsilon_0}}\left[\frac{j_{0x}k_0^2 - q_x \mathbf{q} \cdot \mathbf{j}_0}{(q^2 - k_0^2)a^2 k_0} \right]\exp(iq_x x - i\omega t) \tag{C.12}$$

The difference of the electric field from R_c to just above the surface of the wire (r_0) is given by :

$$\Delta E_x(r_0) = E(R_c) - E(r_0) = i\frac{2}{\pi}\sqrt{\frac{\mu_0}{\varepsilon_0}}\ln\left(\frac{a}{r_0\sqrt{\pi}}\right)\left[\frac{Cq_x - k_0^2 j_{0x}}{4k_0}\right]\exp(iq_x x - i\omega t) \tag{C.13}$$

The first term in the square brackets is due to charge accumulation on the wires. For connected wires, where the current at nodes is distributed over the three wires is given by:

$$C = \frac{\mathbf{q}\cdot\mathbf{j}_0}{3} \tag{C.14}$$

and for non-connected wires:

$$C = \mathbf{q}\cdot\mathbf{j}_0 \tag{C.15}$$

C.3 Dispersion equations:

Finally, by assuming that there are no contributions from neighbouring wires, the difference of $\overline{E_x}$ and ΔE_x, gives the electric field in the wire, which is zero since PEC wires are considered. Therefore:

$$\begin{aligned} \overline{E_x} - \Delta E_x &= 0 \\ \frac{\left[k_0^2 j_{0x} - q_x \mathbf{q}\cdot\mathbf{j}_0\right]}{q^2 - k_0^2} + \frac{k_0^2 j_{0x}}{k_p^2} - \frac{Cq_x}{k_p^2} &= 0 \end{aligned} \tag{C.16}$$

where $k_p^2 = \frac{2\pi}{a^2\ln\left(\frac{a}{r\sqrt{\pi}}\right)}$ is the plasma wavevector.

C.3.1 Connected wires:

For connected 3D wires, $C = \mathbf{q}\cdot\mathbf{j}_0/3$ and (C.16) becomes:

$$\frac{\left[k_0^2 j_{0x} - q_x \mathbf{q}\cdot\mathbf{j}_0\right]}{q^2 - k_0^2} + \frac{k_0^2 j_{0x}}{k_p^2} - \frac{q_x \mathbf{q}\cdot\mathbf{j}_0}{3k_p^2} = 0 \tag{C.17}$$

For the transverse mode $\mathbf{q}\cdot\mathbf{j}_0 = 0$ and therefore:

$$k_0^2 = q_T^2 + k_p^2 \tag{C.18}$$

For the longitudinal mode $\mathbf{q}\times\mathbf{j}_0 = 0$ (i.e. $\mathbf{q} = q_x\hat{\mathbf{x}}$ and $\mathbf{j}_0 = j_{0x}\hat{\mathbf{x}}$) and hence:

$$k_0^2 = (q_L^2/3) + k_p^2 \tag{C.19}$$

where q_L is the longitudinal wavevector and q_T the transverse wavevector.

C.3.2 Non-Connected wires:

For non-connected 3D wires, $C = \mathbf{q} \cdot \mathbf{j}_0$ and (C.16) becomes:

$$\frac{\left[k_0^2 j_{0x} - q_x \mathbf{q} \cdot \mathbf{j}_0\right]}{q^2 - k_0^2} + \frac{k_0^2 j_{0x}}{k_p^2} - \frac{q_x \mathbf{q} \cdot \mathbf{j}_0}{k_p^2} = 0 \tag{C.20}$$

Again for the transverse mode $\mathbf{q} \cdot \mathbf{j}_0 = 0$ and therefore:

$$k_0^2 = q_T^2 + k_p^2 \tag{C.21}$$

For the longitudinal mode $\mathbf{q} \times \mathbf{j}_0 = 0$ and hence:

$$k_0^2 = q_L^2 + k_p^2 \tag{C.22}$$

where q_L is the longitudinal wavevector and q_T the transverse wavevector

Appendix D

Reflection Coefficient for Parallel-Wire media

D.1 Semi-infinite slab:

Consider a P-polarized wave incident on a semi-infinite slab of a parallel-wire metamaterial, as shown in figure 5.1. Assuming that the wave is incident at $z = 0$ interface, then by matching the electric and magnetic fields at this interface, the reflection coefficient can be derived.

D.1.1 Reflected Fields:

The incident and reflected magnetic field:

$$\mathbf{H} = \hat{\mathbf{y}} H_0 exp(iq_x x + iq_y y + iq_z z - i\omega t) + \hat{\mathbf{y}} R H_0 exp(iq_x x + iq_y y - iq_z z - i\omega t) \quad \text{(D.1)}$$

where R is the reflection coefficient. The electric field is derived from Maxwell equation:

$$\frac{\partial D}{\partial t} = \nabla \times \mathbf{H} \Rightarrow \mathbf{E} = -\frac{1}{i\varepsilon_0 \omega} \nabla \times \mathbf{H} \quad \text{(D.2)}$$

and is given by:

$$\mathbf{E} = \frac{q_z \hat{\mathbf{x}} - q_x \hat{\mathbf{z}}}{\varepsilon_0 \omega} H_0 exp(iq_x x + iq_y y + iq_z z - i\omega t) - \frac{q_z \hat{\mathbf{x}} + q_x \hat{\mathbf{z}}}{\varepsilon_0 \omega} R H_0 exp(iq_x x + iq_y y - iq_z z - i\omega t) \quad \text{(D.3)}$$

D.1.2 Transmitted Fields:

The electric and magnetic fields inside the metamaterial are derived in (B.8) and given by:

$$\mathbf{H} = \frac{iIq_x\hat{\mathbf{y}}}{(q^2-k_0^2)a^2} exp(iq_x x + iq_y y + iq_z z - i\omega t) \tag{D.4}$$

$$\mathbf{E} = \left[i\omega\mu_0\hat{\mathbf{z}} - \frac{iq_z\mathbf{q}}{\varepsilon\omega} \right] \frac{I}{(q^2-k_0^2)a^2} \exp(iq_x x + iq_y y + iq_z z - i\omega t) \tag{D.5}$$

For a P-polarized wave, two modes are propagating in the parallel-wire medium, the TEM and longitudinal mode.

D.1.2.1 TEM mode:

The dispersion equation of TEM mode is: $k_0 = q_z$ and assume that the current induced in the wires due to this mode is T_1. Therefore, from (D.4), the magnetic field driven by TEM mode is:

$$H_y^1 = \frac{iT_1H_0q_x}{(q^2-k_0^2)a^2} exp(iq_x x + iq_z z - i\omega t) \tag{D.6}$$

and since the wavevector in the x-y plane can take arbitrary values, then $(q^2 - k_0^2) = q_x^2$. Hence, the H_y^1 takes the form:

$$H_y^1 = \frac{iT_1H_0}{q_x a^2} exp(iq_x x + iq_z z - i\omega t) \tag{D.7}$$

Now, the electric field is given by (D.5), but consider the electric field on surface $z = 0$:

$$E_x^1 = -\frac{ik_0T_1H_0}{\varepsilon\omega q_x a^2} \exp(iq_x x + iq_z z - i\omega t) \tag{D.8}$$

D.1.2.2 Longitudinal mode:

The dispersion equation of the longitudinal mode is: $q^2 = k_0^2 - k_p^2$, and assume the current induced in the wires due to this mode is T_2. Therefore, from (D.4), the magnetic field driven by longitudinal mode is:

$$H_y^2 = -\frac{iT_2H_0q_x}{k_p^2a^2} exp(iq_x x + iq_z z - i\omega t) \tag{D.9}$$

and the tangential component of the electric field from (D.5) is given by:

$$E_x^2 = \frac{iT_2H_0q_x\sqrt{k_0^2 - k_p^2 - q_x^2}}{\varepsilon\omega k_p^2 a^2} \exp(iq_x x + iq_z z - i\omega t) \tag{D.10}$$

At surface $z = 0$, the capacitance of thin wires is zero which indicates that the current at this surface should be zero as well. Hence:

$$T_1 = -T_2 \tag{D.11}$$

Therefore, the total magnetic and electric fields transmitted in the wire medium due to both modes are given by:

$$H_y = \frac{iT_1H_0}{a^2}\left[\frac{1}{q_x} + \frac{q_x}{k_p^2}\right] exp(iq_x x + iq_z z - i\omega t) \tag{D.12}$$

$$E_x = -\frac{iT_1H_0}{\varepsilon\omega a^2}\left[\frac{k_0}{q_x} + \frac{q_x\sqrt{k_0^2 - k_p^2 - q_x^2}}{k_p^2}\right] \exp(iq_x x + iq_z z - i\omega t) \tag{D.13}$$

D.1.2.3 Local model Paradox:

Assuming that the local model holds for the parallel-wire medium, then just one mode can propagate in the metamaterial. Therefore, the current associated with that mode would not be zero at the surface of the medium. This implies charge accumulation at the ends of the wires, which is a paradox, since the capacitance of the wires at the surface $z = 0$ is zero. This paradox can be avoided by considering a second mode, whose current compensates the first mode's charge accumulation, and allowing the current in the wires to be zero at the surface of incidence.

D.1.3 Reflection Coefficient:

By matching the magnetic fields reflected and transmitted in the medium:

$$1 + R = \frac{iT_1}{a^2}\left[\frac{1}{q_x} + \frac{q_x}{k_p^2}\right] \tag{D.14}$$

and matching the electric fields reflected and transmitted:

$$1 - R = \frac{iT_1}{a^2}\left[\frac{k_0}{q_z q_x} + \frac{q_x\sqrt{k_0^2 - k_p^2 - q_x^2}}{q_z k_p^2}\right] \tag{D.15}$$

Solving these two equations, the reflection coefficient can be derived for a semi-infinite slab of a parallel wire medium.

$$R_{non-local} = \frac{q_z k_p^2 + q_x^2 q_z - k_0 k_p^2 - q_x^2 q_{2z}}{q_z k_p^2 + q_x^2 q_z + k_0 k_p^2 + q_x^2 q_{2z}} \tag{D.16}$$

where $q_{2z} = \sqrt{k_0^2 - k_p^2 - q_x^2}$.

D.2 Finite Slab:

By matching the electric and magnetic fields at the $z = d$ surface, and following the same calculation procedure as above, the reflection coefficient for a finite slab of a parallel-wire medium can be derived and is given by:

$$R = \frac{1 + A^2 - B^2}{1 + 2B - A^2 + B^2} \tag{D.17}$$

where

$$A = \frac{i}{q_z(k_p^2 + q_x^2)} \left[\frac{k_0 k_p^2}{sin(k_0 d)} + \frac{k_x^2 q_{2z}}{sin(q_{2z} d)} \right] \tag{D.18}$$

$$B = \frac{i}{q_z(k_p^2 + q_x^2)} \left[\frac{k_0 k_p^2 cos(k_0)}{sin(k_0 d)} + \frac{k_x^2 q_{2z} cos(q_{2z} d)}{sin(q_{2z} d)} \right] \tag{D.19}$$

where $q_{2z} = \sqrt{k_0^2 - k_p^2 - q_x^2}$.

Appendix E

Reflection Coefficient for Wire-Mesh media

Consider a P-polarized wave incident on a semi-infinite slab of a 3D-connected wire-mesh metamaterial as shown in figure 4.1. Assuming that the wave is incident at the plane $z = 0$, then by matching the electric and magnetic fields at this surface, the reflection coefficient can be derived.

E.1 Reflected Fields:

The incident and reflected magnetic fields:

$$\mathbf{H} = \hat{y} H_0 exp(iq_x x + iq_y y + iq_z z - i\omega t) + \hat{\mathbf{y}} R H_0 exp(iq_x x + iq_y y - iq_z z - i\omega t) \quad \text{(E.1)}$$

and the electric fields derived from Maxwell equations:

$$\mathbf{E} = \frac{q_z \hat{\mathbf{x}} - q_x \hat{\mathbf{z}}}{\varepsilon_0 \omega} H_0 exp(iq_x x + iq_y y + iq_z z - i\omega t) - \frac{q_z \hat{\mathbf{x}} + q_x \hat{\mathbf{z}}}{\varepsilon_0 \omega} R H_0 exp(iq_x x + iq_y y - iq_z z - i\omega t) \quad \text{(E.2)}$$

E.2 Transmitted Fields:

The electric and magnetic fields propagating in the metamaterial are derived in C.8 and given by:

$$\mathbf{B} = \frac{i\mu_0 \mathbf{q} \times \mathbf{j_0}}{(q^2 - k_0^2)a^2} exp(iq_x x + iq_y y + iq_z z - i\omega t) \quad \text{(E.3)}$$

$$\mathbf{E} = \left[i\omega\mu_0 \mathbf{j_0} - i\mathbf{q}\frac{\mathbf{j_0}\cdot\mathbf{q}}{\varepsilon\omega} \right] \frac{1}{(q^2 - k_0^2)a^2} \exp(iq_x x + iq_y y + iq_z z - i\omega t) \qquad \text{(E.4)}$$

For P-polarized incident wave, both the longitudinal and transverse modes are propagating in the connected wire-mesh metamaterial.

E.2.1 Longitudinal mode:

The dispersion equation of the longitudinal mode is: $q^2 = 3(k_0^2 - k_p^2)$, and the current induced in the wires due to the longitudinal mode is $\mathbf{j_L} = J_L H_0 \mathbf{q_L} = J_L H_0 (q_L \hat{\mathbf{x}} + q_z \hat{\mathbf{z}})$. Therefore, the magnetic field driven by the longitudinal mode is:

$$B_L = \frac{i\mu_0 \mathbf{q_L} \times \mathbf{j_L}}{(q^2 - k_0^2)a^2} exp(iq_x x + iq_z z - i\omega t) = 0 \qquad \text{(E.5)}$$

and is equal to zero, since the $\mathbf{q_L}$ is parallel to $\mathbf{j_L}$ and therefore $\mathbf{q_L} \times \mathbf{j_L} = 0$. Now, the electric field driven by the longitudinal mode is given by:

$$\mathbf{E}_L = \left[i\omega\mu_0 J_L H_0 (q_L \hat{\mathbf{x}} + q_z \hat{\mathbf{z}}) - i\frac{J_L H_0 q_L^2}{\varepsilon\omega}\mathbf{q_L} \right] \frac{1}{(q^2 - k_0^2)a^2} \exp(iq_x x + iq_z z - i\omega t) \qquad \text{(E.6)}$$

and for simplicity consider the electric field tangential to surface $z = 0$ and since the longitudinal wavevector is always parallel to the electric field, then $\mathbf{q_L} = q_x \hat{\mathbf{x}}$ can be substituted in the above equation giving:

$$E_L^x = -\frac{i\omega\mu_0 J_L H_0 q_x}{k_0^2 a^2} \exp(iq_x x + iq_z z - i\omega t) \qquad \text{(E.7)}$$

E.2.2 Transverse mode:

The dispersion equation of the transverse mode is: $q^2 = k_0^2 - k_p^2$, and the current induced in the wires due to transverse mode is $\mathbf{j_T} = J_T H_0 \mathbf{q_T} = J_T H_0 (q_T \hat{\mathbf{x}} + q_x \hat{\mathbf{z}})$. Therefore, the magnetic field driven by transverse mode is:

$$\mathbf{H_T} = \frac{iJ_T H_0 q_T^2 \hat{\mathbf{y}}}{(q_T^2 - k_0^2)a^2} exp(iq_x x + iq_z z - i\omega t) = -\frac{iJ_T H_0 (k_0^2 - k_p^2)\hat{\mathbf{y}}}{k_p^2 a^2} exp(iq_x x + iq_z z - i\omega t) \qquad \text{(E.8)}$$

and the electric field:

$$\mathbf{E_T} = \left[i\omega\mu_0 J_T H_0 (q_T \hat{\mathbf{x}} + q_x \hat{\mathbf{z}}) - i\frac{J_T H_0 q_T^2}{\varepsilon\omega}\mathbf{q_T} \right] \frac{1}{(q^2 - k_0^2)a^2} \exp(iq_x x + iq_z z - i\omega t) \qquad \text{(E.9)}$$

Consider the electric field tangential to surface $z = 0$:

$$E_T^x = -\frac{i\omega\mu_0 J_T H_0 q_{Tz}}{k_p^2 a^2}\exp(iq_x x + iq_z z - i\omega t) \tag{E.10}$$

It is required that the current at surface $z = 0$ to be zero, since thin wires are considered which have zero capacitance at this surface. Therefore, the currents induced from the two modes should add to zero.

$$\mathbf{j_T} + \mathbf{j_L} = -J_T H_0 \mathbf{q}_T + J_L H_0 \mathbf{q_L} = 0 \tag{E.11}$$

and by considering current flowing in the wires along the z-axis:

$$J_L = \frac{J_T q_x}{q_{Lz}} \tag{E.12}$$

Hence, the total magnetic and electric fields transmitted due to both modes are:

$$H = -\frac{iJ_T H_0(k_0^2 - k_p^2)}{k_p^2 a^2} exp(iq_x x + iq_z z - i\omega t) \tag{E.13}$$

$$E_x = -\frac{i\omega\mu_0 J_T H_0}{a^2}\left[\frac{q_x^2}{k_0^2 q_{Lz}} + \frac{q_{Tz}}{k_p^2}\right]\exp(iq_x x + iq_z z - i\omega t) \tag{E.14}$$

E.2.3 Reflection Coefficient:

By matching the magnetic fields at the surface $z = 0$:

$$1 + R = -\frac{iJ_T(k_0^2 - k_p^2)}{k_p^2 a^2} \tag{E.15}$$

and by matching the tangential electric fields at the surface of incidence:

$$1 - R = -\frac{iJ_T k_0^2}{a^2 q_z}\left[\frac{q_x^2}{k_0^2 q_{Lz}} + \frac{q_{Tz}}{k_p^2}\right] \tag{E.16}$$

Solving the above two equations, the non-local reflection coefficient can be derived for a semi-infinite slab of a connected wire-mesh metamaterial.

$$R = \frac{q_z q_{Lz}(k_0^2 - k_p^2) - \left[q_{Tz} q_{Lz} k_0^2 + q_x^2 k_p^2\right]}{q_z q_{Lz}(k_0^2 - k_p^2) + \left[q_{Tz} q_{Lz} k_0^2 + q_x^2 k_p^2\right]} \tag{E.17}$$

Appendix F

Dispersion Equations for (non-chiral) Swiss Roll media

Consider a metamaterial consisted from Swiss Rolls placed in a square lattice of constant a, aligned with the z-axes and a monochromatic wave with wavevector $\mathbf{k}$. Maxwell equations for a monochromatic wave are:

$$\begin{aligned} \nabla \times \mathbf{E} &= -\frac{d\mathbf{B}}{dt} \Rightarrow i\mathbf{k} \times \mathbf{E} = i\omega\mu\mu_0\mathbf{H} \\ \nabla \times \mathbf{H} &= \frac{d\mathbf{D}}{dt} \Rightarrow i\mathbf{k} \times \mathbf{H} = -i\omega\varepsilon\varepsilon_0\mathbf{E} \end{aligned} \tag{F.1}$$

For simplicity, consider a wave propagating in xz-plane $\mathbf{k}(k_x, 0, k_z)$. Since the metamaterial is electrically inactive along the z-axes, the electric field is $\mathbf{E}(0, E_y, 0)$ and the magnetic field $\mathbf{H}(H_x, 0, H_z)$ [40]. From (F.1):

$$i\mathbf{k} \times \mathbf{E} = i \begin{vmatrix} \overrightarrow{i} & \overrightarrow{\mathrm{j}} & \overrightarrow{\mathrm{k}} \\ k_x & 0 & k_z \\ 0 & E_y & 0 \end{vmatrix} = i\left[\overrightarrow{\mathrm{k}}\, k_x E_y - \overrightarrow{i}\, k_z E_y\right] = i\omega\mu\mu_0(\overrightarrow{\mathrm{k}}\, H_z + \overrightarrow{i}\, H_x) \tag{F.2}$$

$$i\mathbf{k} \times \mathbf{H} = i \begin{vmatrix} \overrightarrow{i} & \overrightarrow{\mathrm{j}} & \overrightarrow{\mathrm{k}} \\ k_x & 0 & k_z \\ H_x & 0 & H_z \end{vmatrix} = i\left[\overrightarrow{\mathrm{j}}\,(k_z H_x - k_x H_z)\right] = -i\omega\varepsilon\varepsilon_0 E_y\, \overrightarrow{\mathrm{j}} \tag{F.3}$$

and therefore:

$$k_x E_y = \omega\mu_z\mu_0 H_z \Rightarrow H_z = \frac{k_x E_y}{\omega\mu_z\mu_0} \tag{F.4}$$

$$-k_z E_y = \omega \mu_x \mu_0 H_x \Rightarrow H_x = -\frac{k_z E_y}{\omega \mu_x \mu_0} \tag{F.5}$$

$$k_z H_x - k_x H_z = -\omega \varepsilon_y \varepsilon_0 E_y \tag{F.6}$$

Solving the above three equations, the dispersion equation is derived [40]:

$$\omega = c_0 \sqrt{\frac{k_x^2}{\varepsilon_y \mu_z} + \frac{k_z^2}{\varepsilon_y \mu_x}} \tag{F.7}$$

Appendix G

Electromagnetic and chirality terms for Swiss Rolls

Consider uniform fields H_z and E_z applied along a right handed chiral Swiss Roll and assume that:

1. there are no local field effects therefore the cylinder is rotational symmetric and the current varies only across the width of the conducting sheet. Consequently, only J_0 (figure 10.5(b)) is driven by *emf.*

2. the foil within the dotted lines is not exposed to either the outside or inside of the chiral Swiss Roll, and therefore it can be assumed that there is no charge accumulation in this area, and current J_0 is constant in magnitude and direction, written by:
$$J_0 = J_{0x} \sin\theta + J_{0z} \cos\theta \tag{G.1}$$

3. the number of turns (N) is large, ensuring a large overlap of the conducting sheet.

4. the current outside the dotted lines rotates until is parallel to the edges of the foil, and therefore the rotation is assumed to be linear with distance.

5. and finally assume that all fields are of the form $\exp(-i\omega t)$

Let us consider initially the current flowing through the capacitive elements of the structure. The charge accumulated at the edges of the foil (i.e. outside the dotted lines) needs to be considered, which charges the capacitor created from the overlapping conducting sheet. Therefore, the current across the width of the foil (figure 10.5(b))is given by:

$$J_0 = J_{0x}\sin\theta + J_{0z}\cos\theta = \frac{\partial Q}{\partial t} = (N-1)C\frac{\partial V}{\partial t} \tag{G.2}$$

where Q is the charge accumulated outside of the dotted lines, V is the potential difference between two parallel conducting plates and C is the capacitance per unit length of each exposed turn, given by:

$$C = \frac{\varepsilon_d \varepsilon_0 (width)}{(separation\ of\ the\ plates) * (no.\,of\ turns)} = \frac{\varepsilon_d \varepsilon_0 2\pi R \sin\theta}{(N-1)d} \tag{G.3}$$

Since V is of the form $V_0 exp(-i\omega t)$, then:

$$\therefore J_{0x}\sin\theta + J_{0z}\cos\theta = -\frac{i\omega\varepsilon_d\varepsilon_0 2\pi R\sin\theta}{d}V \tag{G.4}$$

Also, the magnetic field along the Swiss Roll is given by:

$$H_z = H_0 + J_{0x} - \frac{\pi R^2}{a^2}J_{0x} \tag{G.5}$$

where H_0 is the external magnetic field, the second term of the above equation is caused directly by the current flow on the conducting sheet and the last term is due to depolarizing fields with sources at the remote ends of the cylinders. If the cylinders are very long, then the depolarizing field uniformly spreads over the unit cell.

Furthermore, the emf can be calculated by considering k_y-propagation and E_x-field, ensuring a magnetic field along the z-axis, which in its turn induces current that flow around the spiral ring. Using Faraday's law of induction, emf is given by:

$$\mathcal{E} = -(N-1)\frac{d\Phi}{dt} = -(N-1)\pi R^2 \mu_0 \frac{\partial H_z}{\partial t} \tag{G.6}$$

$\mathcal{E}$ needs to be balanced by the ohmic drop in the potential (V) due to the capacitance of the structure and conductivity losses ($= 2\pi R(N-1)\rho J_{ox}$), therefore:

$$\therefore i\omega(N-1)\pi R^2\mu_0 H_z = V + 2\pi R(N-1)\rho J_{0x} \tag{G.7}$$

where ρ is the resistance of the conducting sheet per unit length.

Finally, the potential difference (V) across $(N-1)$ conducting sheets can be calculated by integrating around a loop in the y-z plane (from r=inner-radius to r=R) of the structure, giving:

$$V = \int E\partial x = (E_0 + E_p)(N-1)2\pi R \tan\theta \tag{G.8}$$

where E_p is the electric field driven by the current per unit length of the circumference of the coil, which is induced by charge accumulation. Therefore:

$$E_P = \left[\frac{2\pi R}{i\omega\varepsilon_d\varepsilon_0 a^2} - \rho\right] J_{0z} \tag{G.9}$$

and

$$E_0 + E_P = E_0 + \left[\frac{2\pi R}{i\omega\varepsilon_d\varepsilon_0 a^2} - \rho\right] J_{0z} = \frac{V}{(N-1)2\pi R \tan\theta} \tag{G.10}$$

Now, solving (G.4), (G.5), (G.7) and (G.10) with respect to J_{0x} and J_{0z}:

$$J_{0x} = \frac{-\left[AL\tan^2\theta + B\right]\omega^2 H_0 - C\omega\tan\theta E_0}{\omega^2 D(AL\tan^2\theta + B) + \omega(KL\tan^2\theta + C\rho) - L\tan^2\theta} \tag{G.11}$$

$$J_{0z} = -\frac{B\omega^2}{L\tan\theta}H_0 + \left(\frac{BD\omega^2 + C\rho\omega}{L\tan\theta}\right)\frac{\left[AL\tan^2\theta + B\right]\omega^2 H_0 + C\omega\tan\theta E_0}{\omega^2 D(AL\tan^2\theta + B) + \omega(KL\tan^2\theta + C\rho) - L\tan^2\theta} - \frac{C\omega}{L}I \tag{G.12}$$

where

$$\begin{aligned}
A &= \frac{2\pi^2 R^3 \varepsilon_d (N-1)}{dc_0^2} \\
B &= \frac{\varepsilon_d a^2}{4\pi c_0^2} \\
C &= \frac{i\varepsilon_d\varepsilon_0 a^2}{2\pi R} \\
D &= 1 - \frac{\pi R^2}{a^2} = 1 - F \\
K &= \frac{i\varepsilon_d\varepsilon_0 4\pi^2 R^2 \rho (N-1)}{d} && \text{(G.13)} \\
L &= 1 - C\rho\omega && \text{(G.14)}
\end{aligned}$$

and where F is the filling factor and $F = \frac{\pi R^2}{a^2}$ and ρ is the resistance of the roll per unit area.

Finally, since the average H-field is given by the sum of H_0 and the depolarizing fields from the coils $H_{ave} = H_0 - J_{0x}\frac{\pi R^2}{a^2}$ and $\mu = B_{ave}/(\mu_0 H_{ave})$ then χ_{HH}, χ_{HE} are given by:

$$[\chi^{-1}]_{HH} = \frac{1}{(1-F)} \frac{\omega^2 - \omega_0^2 + i\Gamma\omega}{\omega^2 - \omega_{mp}^2 + i\Gamma\omega/D} \tag{G.15}$$

$$[\chi^{-1}]_{HE}/\varepsilon_0 = \frac{iR}{2L\tan\theta}\left(\frac{\omega_{mp}^2\omega}{\omega^2 - \omega_{mp}^2 + i\Gamma\omega/D}\right) = [\kappa^{-1}]_{HE} \tag{G.16}$$

where

$$\omega_0^2 = \frac{L\tan^2\theta}{AL\tan^2\theta + B} = \frac{\tan^2\theta}{\varepsilon_d\left(\frac{2\pi^2R^3(N-1)}{dc_0^2}\tan^2\theta + \frac{a^2}{4\pi c_0^2}\right)} \tag{G.17}$$

$$\omega_{mp}^2 = \frac{L\tan^2\theta}{D(AL\tan^2\theta + B)} = \frac{\tan^2\theta}{\varepsilon_d\left(1 - \frac{\pi R^2}{a^2}\right)\left(\frac{2\pi^2R^3(N-1)}{dc_0^2}\tan^2\theta + \frac{a^2}{4\pi c_0^2}\right)} = \frac{\omega_0^2}{1-F} \tag{G.18}$$

are the resonant and the magnetic plasma frequencies respectively and

$$\Gamma = -i\frac{(KL\tan^2\theta + C\rho)}{AL\tan^2\theta + B} = \frac{2\rho}{\mu_0 R} \tag{G.19}$$

Similarly for ε, where $\varepsilon = D_{ave}/(\varepsilon_0 E_{ave}) = E_0/(E_0 + E_P)$, χ_{EE} and χ_{EH} are given by:

$$[\chi^{-1}]_{EE} = G\left(\frac{\omega^2 + i\omega\Gamma/D}{\omega^2 - \omega_p^2 + i\omega\Gamma/D}\right) \tag{G.20}$$

where G is a constant given by:

$$G = \frac{B}{AL\tan^2\theta + B} = \frac{\frac{a^2}{4\pi c_0^2}}{\frac{2\pi^2R^3(N-1)L}{dc_0^2}\tan^2\theta + \frac{a^2}{4\pi c_0^2}} = \frac{a^2 d}{8\pi^3R^3(N-1)L\tan^2\theta + a^2 d} \tag{G.21}$$

and

$$\omega_p = \omega_{mp} \tag{G.22}$$

are the plasma frequency, and finally:

$$[\chi^{-1}]_{EH}/\mu_0 = -\frac{iR}{2L\tan\theta}\left(\frac{\omega\omega_{mp}^2}{\omega^2 - \omega_{mp}^2 + i\Gamma\omega/D}\right) = [\kappa^{-1}]_{EH} \tag{G.23}$$

Appendix H

Dispersion equations for chiral Swiss Rolls

For a 2D chiral medium:

$$\begin{bmatrix} D_y \\ D_z \\ B_y \\ B_z \end{bmatrix} = \begin{bmatrix} \chi_{EE} & 0 & \chi_{EH} & 0 \\ 0 & \chi_{EE} & 0 & \chi_{EH} \\ \chi_{HE} & 0 & \chi_{HH} & 0 \\ 0 & \chi_{HE} & 0 & \chi_{HH} \end{bmatrix} \begin{bmatrix} E_y \\ E_z \\ H_y \\ H_z \end{bmatrix} \tag{H.1}$$

From Maxwell's equations:

$$\mathbf{k} \times \mathbf{H} = -\omega \mathbf{D} \Rightarrow \begin{bmatrix} 0 & -k_z & k_y \\ k_z & 0 & -k_x \\ -k_y & k_x & 0 \end{bmatrix} \begin{bmatrix} H_x \\ H_y \\ H_z \end{bmatrix} = -\omega \begin{bmatrix} D_x \\ D_y \\ D_z \end{bmatrix} \tag{H.2}$$

$$\mathbf{k} \times \mathbf{E} = -\omega \mathrm{B} \Rightarrow \begin{bmatrix} 0 & -k_z & k_y \\ k_z & 0 & -k_x \\ -k_y & k_x & 0 \end{bmatrix} \begin{bmatrix} E_x \\ E_y \\ E_z \end{bmatrix} = \omega \begin{bmatrix} B_x \\ B_y \\ B_z \end{bmatrix} \tag{H.3}$$

For k_x propagation, then $k_y = k_z = 0$ and the above equations lead to:

$$\begin{bmatrix} 0 & 0 & 0 & k_x \\ 0 & 0 & -k_x & 0 \\ 0 & -k_x & 0 & 0 \\ k_x & 0 & 0 & 0 \end{bmatrix} \begin{bmatrix} E_y \\ E_z \\ H_y \\ H_z \end{bmatrix} = \omega \begin{bmatrix} \chi_{EE} & 0 & \chi_{EH} & 0 \\ 0 & \chi_{EE} & 0 & \chi_{EH} \\ \chi_{HE} & 0 & \chi_{HH} & 0 \\ 0 & \chi_{HE} & 0 & \chi_{HH} \end{bmatrix} \begin{bmatrix} E_y \\ E_z \\ H_y \\ H_z \end{bmatrix} \tag{H.4}$$

If we use helical polarization, then: $k_x = ksin\theta$, $k_y = 0$ and $k_z = kcos\theta$, (and where $\theta = 90°$ for k_x-propagation), the electric field is given by: $E_x = Ecos\theta$, $E_y = -iE$ and $E_z = -Esin\theta$ and the magnetic field: $H_x = iHcos\theta$, $H_y = H$ and $H_z = -iHsin\theta$. Now, depending on handedness of chiral Swiss Rolls, the magnetic behaviour of the metamaterial

$$\mathbf{F}^+ = \begin{bmatrix} E_+cos\theta \\ -iE_+ \\ -E_+sin\theta \\ iH_+cos\theta \\ H_+ \\ -iH_+sin\theta \end{bmatrix} = \begin{bmatrix} 0 \\ -iE_+ \\ -E_+ \\ 0 \\ H_+ \\ -iH_+ \end{bmatrix} \tag{H.5}$$

for right handedness and for left handedness:

$$\mathbf{F}^- = \begin{bmatrix} E_-cos\theta \\ iE_- \\ -E_-sin\theta \\ -iH_-cos\theta \\ H_- \\ iH_-sin\theta \end{bmatrix} == \begin{bmatrix} 0 \\ -iE_+ \\ -E_+ \\ 0 \\ H_+ \\ -iH_+ \end{bmatrix} \tag{H.6}$$

Let's take the positive solution, which means that:

$$\begin{bmatrix} 0 & 0 & 0 & k_x \\ 0 & 0 & -k_x & 0 \\ 0 & -k_x & 0 & 0 \\ k_x & 0 & 0 & 0 \end{bmatrix} \begin{bmatrix} -iE_+ \\ -E_+ \\ H_+ \\ -iH_+ \end{bmatrix} = \omega^+ \begin{bmatrix} \chi_{EE} & 0 & \chi_{EH} & 0 \\ 0 & \chi_{EE} & 0 & \chi_{EH} \\ \chi_{HE} & 0 & \chi_{HH} & 0 \\ 0 & \chi_{HE} & 0 & \chi_{HH} \end{bmatrix} \begin{bmatrix} -iE_+ \\ -E_+ \\ H_+ \\ -iH_+ \end{bmatrix} \tag{H.7}$$

Due to the 2D-isotropy of the medium, the above equation can be reduced to:

$$\begin{bmatrix} 0 & -ik_+ \\ ik_+ & 0 \end{bmatrix} \begin{bmatrix} E_+ \\ iH_+ \end{bmatrix} = \omega^+ \begin{bmatrix} \chi_{EE} & \chi_{EH} \\ \chi_{HE} & \chi_{HH} \end{bmatrix} \begin{bmatrix} E_+ \\ iH_+ \end{bmatrix} \tag{H.8}$$

and therefore:

$$\begin{bmatrix} \chi_{EE}^{-1} & \chi_{EH}^{-1} \\ \chi_{HE}^{-1} & \chi_{HH}^{-1} \end{bmatrix} \begin{bmatrix} 0 & -1 \\ 1 & 0 \end{bmatrix} \begin{bmatrix} E_+ \\ iH_+ \end{bmatrix} = \frac{\omega^+}{ik_+} \begin{bmatrix} E_+ \\ iH_+ \end{bmatrix} \tag{H.9}$$

leading to:

$$\begin{bmatrix} \chi_{EH}^{-1} & -\chi_{EE}^{-1} \\ \chi_{HH}^{-1} & -\chi_{HE}^{-1} \end{bmatrix} \begin{bmatrix} E_+ \\ iH_+ \end{bmatrix} = \frac{\omega^+}{ik_+} \begin{bmatrix} E_+ \\ iH_+ \end{bmatrix} \tag{H.10}$$

and hence the eigen-equation is derived:

$$\begin{bmatrix} \chi_{EH}^{-1} + \frac{i\omega^+}{k_+} & -\chi_{EE}^{-1} \\ \chi_{HH}^{-1} & -\chi_{HE}^{-1} + \frac{i\omega^+}{k_+} \end{bmatrix} \begin{bmatrix} E_+ \\ iH_+ \end{bmatrix} = 0 \tag{H.11}$$

whose eigenvalues are given by:

$$det \begin{vmatrix} \chi_{EH}^{-1} + \frac{i\omega^+}{k_+} & -\chi_{EE}^{-1} \\ \chi_{HH}^{-1} & -\chi_{HE}^{-1} + \frac{i\omega^+}{k_+} \end{vmatrix} = 0 \tag{H.12}$$

which leads to the dispersion equation for the right handed polarization:

$$\omega^{+\pm} = k_{+\pm} \left(i\chi_{EH}^{-1} \pm \sqrt{\chi_{EE}^{-1}\chi_{HH}^{-1}} \right) \tag{H.13}$$

Similarly, the dispersion equation for the left handed polarization is given by:

$$\omega^{-\pm} = k_{-\pm} \left(-i\chi_{EH}^{-1} \pm \sqrt{\chi_{EE}^{-1}\chi_{HH}^{-1}} \right) \tag{H.14}$$

where i and j in $\omega^{ij}$and k_{ij}, show the polarization of the wave and the sign of the group velocity respectively.

Appendix I

The vector spherical harmonics (M and N)

The electric (**E**) and magnetic (**H** fields of a wave with time dependent fields of $\exp(i\omega t)$ propagating in a linear isotropic homogeneous medium, obey the wave equations [61]:

$$\nabla^2 \mathbf{E} + k^2 \mathbf{E} = 0 \qquad \nabla^2 \mathbf{H} + k^2 \mathbf{H} = 0 \tag{I.1}$$

and their divergence is zero:

$$\nabla \cdot \mathbf{E} = 0 \qquad \nabla \cdot \mathbf{H} = 0 \tag{I.2}$$

Also, from Maxwell equations we know that **E** and **H** are not independent from each other:

$$\nabla \times \mathbf{E} = i\omega\mu \mathbf{H} \qquad \nabla \times \mathbf{H} = -i\omega\varepsilon \mathbf{E} \tag{I.3}$$

Now, we introduce two vector functions **M** and **N** that satisfy the above properties of an electromagnetic field, in order to simplify the problem of finding solutions to the field equations. **M** and **N** are constructed from a scalar function ψ and a constant vector **r**, as:

$$\mathbf{M} = \nabla \times (\mathbf{r}\psi) \qquad \mathbf{N} = \frac{\nabla \times \mathbf{M}}{k} \tag{I.4}$$

whose divergence is also zero:

$$\nabla \mathbf{M} = 0 \qquad \nabla \mathbf{N} = 0 \tag{I.5}$$

and satisfy the wave equation:

$$\nabla^2\mathbf{M} + k^2\mathbf{M} = \nabla \times \left(r(\nabla^2\psi + k^2\psi)\right) = 0 \tag{I.6}$$

$$\nabla^2\mathbf{N} + k^2\mathbf{N} = 0 \tag{I.7}$$

and from (I.7), ψ satisfies the scalar wave equation:

$$\therefore \nabla^2\psi + k^2\psi = 0 \tag{I.8}$$

Therefore, the problem is reduced to the simpler problem of finding solutions to (I.8). (Note that the usual terminology is $\mathbf{M}$, $\mathbf{N}$: vector harmonics, ψ: generating function and $\mathbf{r}$: pilot or guiding vector)

In this report, the scattering of a plane wave by a spherical particle is considered. Therefore, ψ is chosen to satisfy the wave equation in spherical coordinates:

$$\frac{1}{r^2}\frac{\partial}{\partial r}\left(r^2\frac{\partial\psi}{\partial r}\right) + \frac{1}{r^2\sin\theta}\frac{\partial}{\partial\theta}\left(\sin\theta\frac{\partial\psi}{\partial\theta}\right) + \frac{1}{r^2\sin\theta}\frac{\partial^2\psi}{\partial\phi^2} + k^2\psi = 0 \tag{I.9}$$

which has solutions:

$$\psi_{emn} = \cos m\phi P_n^m(\cos\theta) z_n(kr) \tag{I.10}$$

$$\psi_{omn} = \sin m\phi P_n^m(\cos\theta) z_n(kr) \tag{I.11}$$

where n,m are the principal and azimuthal quantum numbers respectively, P_n^m the Legendre function, the subscripts e and o denote even and odd dependence on ϕ respectively and z_n is one of the spherical Bessel functions: j_n, y_n, $h_n^{(1)}$ and $h_n^{(2)}$.

The vector spherical harmonics generated by $\psi_{(e,o)mn}$ are given by:

$$\mathbf{M}_{(e,o)mn} = \nabla \times (\mathbf{r}\psi_{(e,o)mn}) \qquad \mathbf{N}_{(e,o)mn} = \frac{\nabla \times \mathbf{M}_{(e,o)mn}}{k} \tag{I.12}$$

which are resolved in polar coordinates as:

$$\mathbf{M}_{emn} = -\frac{m}{\sin\theta}\sin m\phi P_n^m(\cos\theta) z_n(\rho)\hat{\mathbf{e}}_\theta - \cos m\phi \frac{dP_n^m(\cos\theta)}{d\theta} z_n(\rho)\hat{\mathbf{e}}_\phi \tag{I.13}$$

$$\begin{aligned}\mathbf{N}_{emn} = -\frac{z_n(\rho)}{\rho}\cos m\phi\, n(n+1) P_n^m(\cos\theta)\hat{\mathbf{e}}_{\mathrm{r}} + \cos m\phi \frac{dP_n^m(\cos\theta)}{d\theta}\frac{1}{\rho}\frac{d}{d\rho}\left[\rho z_n(\rho)\right]\hat{\mathbf{e}}_\theta \\ -\frac{m}{\sin\theta}\sin m\phi P_n^m(\cos\theta)\frac{1}{\rho}\frac{d}{d\rho}\left[\rho z_n(\rho)\right]\hat{\mathbf{e}}_\phi\end{aligned} \tag{I.14}$$

$$\mathbf{M}_{omn} = \frac{m}{\sin\theta}\cos m\phi P_n^m(\cos\theta) z_n(\rho)\hat{\mathbf{e}}_\theta - \sin m\phi \frac{dP_n^m(\cos\theta)}{d\theta} z_n(\rho)\hat{\mathbf{e}}_\phi \tag{I.15}$$

$$\begin{aligned}\mathbf{N}_{omn} = \frac{z_n(\rho)}{\rho}\sin m\phi n(n+1)P_n^m(\cos\theta)\hat{\mathbf{e}}_\mathrm{r} + \sin m\phi \frac{dP_n^m(\cos\theta)}{d\theta}\frac{1}{\rho}\frac{d}{d\rho}\left[\rho z_n(\rho)\right]\hat{\mathbf{e}}_\theta \\ + \frac{m}{\sin\theta}\cos m\phi P_n^m(\cos\theta)\frac{1}{\rho}\frac{d}{d\rho}\left[\rho z_n(\rho)\right]\hat{\mathbf{e}}_\phi\end{aligned} \tag{I.16}$$

where $\rho = kr$

Appendix J

A plane wave in vector spherical harmonics

Consider a plane wave with the electric field polarized along the x-axes, incident on an arbitrary sphere of radius R. The incident electric field in spherical polar coordinates is given by:

$$\mathbf{E}_{inc} = E_0 \exp ikr \cos\theta \hat{\mathbf{e}}_{\mathbf{x}} \tag{J.1}$$

where

$$\hat{\mathbf{e}}_{\mathbf{x}} = \sin\theta\cos\phi\hat{\mathbf{e}}_{\mathbf{r}} + \cos\theta\sin\phi\hat{\mathbf{e}}_{\theta} - \sin\phi\hat{\mathbf{e}}_{\phi} \tag{J.2}$$

Now expanding (J.1) in vector spherical harmonics:

$$\mathbf{E}_{inc} = \sum_{m=0}^{\infty}\sum_{n=m}^{\infty} \left(B_{emn}\mathbf{M}_{emn} + B_{omn}\mathbf{M}_{omn} + A_{emn}\mathbf{N}_{emn} + A_{omn}\mathbf{N}_{omn} \right) \tag{J.3}$$

where $B_{(e,o)mn}$ and $A_{(e,o)mn}$ are coefficients. Taking into account that the vector spherical harmonics are mutually orthogonal (i.e. $\mathbf{M}_{emn}$ is orthogonal to $\mathbf{M}_{omn}$):

$$\int_0^{2\pi}\int_0^{\pi} \mathbf{M}_{em'n'} \cdot \mathbf{M}_{omn} \sin\theta d\theta d\phi = 0 \qquad \text{for all } m,\ m',\ n \text{ and } n' \tag{J.4}$$

Since (J.4) is also valid for ($\mathbf{N}_{omn}$,$\mathbf{N}_{emn}$), ($\mathbf{M}_{omn}$,$\mathbf{N}_{omn}$) and ($\mathbf{M}_{emn}$,$\mathbf{N}_{omn}$), the coefficients are given by:

$$B_{emn} = \frac{\int_0^{2\pi}\int_0^{\pi} \mathbf{E}_{inc} \cdot \mathbf{M}_{emn} \sin\theta d\theta d\phi}{\int_0^{2\pi}\int_0^{\pi} |\mathbf{M}_{emn}|^2 \sin\theta d\theta d\phi} \tag{J.5}$$

with similar derivations for B_{omn}, A_{emn} and A_{omn} coefficients. Now, from (I.13), (I.17) and (J.2) and accounting for the orthogonality of the sine and cosine, it can be obtained that

$$B_{emn} = A_{omn} = 0 \qquad \text{for all } m,\, n \tag{J.6}$$

and only for $m = 1$:

$$B_{omn} \neq 0 \qquad A_{emn} \neq 0 \tag{J.7}$$

Therefore, (J.1) is expanded to spherical harmonics as:

$$\mathbf{E}_{inc} = \sum_{n=1}^{\infty} \left(B_{o1n}\mathbf{M}^{(1)}_{o1n} + A_{e1n}\mathbf{N}^{(1)}_{e1n} \right) \tag{J.8}$$

Note that since the incident field at the origin is finite, the Bessel function required to be used is j_n in (I.11). Therefore, in order to distinguish what Bessel function is used for the spherical vector harmonics, the superscript (1) is used for j_n and (3) for spherical Hankel functions $h^{(1)}_n$. We can also derive the coefficients, which are given by:

$$\begin{aligned} B_{o1n} &= i^n E_0 \frac{2n+1}{n(n+1)} \\ A_{e1n} &= -i^{n+1} E_0 \frac{2n+1}{n(n+1)} \end{aligned} \tag{J.9}$$

Substituting these to (J.8), the expanded plane wave to spherical harmonics is given by:

$$\mathbf{E}_{inc} = \sum_{n=1}^{\infty} E_n \left(\mathbf{M}^{(1)}_{o1n} - i\mathbf{N}^{(1)}_{e1n} \right) \tag{J.10}$$

where $E_n = i^n E_0 (2n+1)/(n(n+1))$. Now, using Maxwells equation (I.3) and noting that the materials considered in this report (i.e. high-dielectrics) have magnetic permeability $\mu = 1$, the magnetic field expanded in spherical harmonics is obtained:

$$\mathbf{H}_{inc} = -\frac{k_0}{\omega} \sum_{n=1}^{\infty} E_n \left(\mathbf{M}^{(1)}_{o1n} + i\mathbf{N}^{(1)}_{e1n} \right) \tag{J.11}$$

Appendix K

Internal and scattered fields by a dielectric sphere

Consider a sphere of radius R and dielectric constant ε (and $\mu = 1$) and a plane wave incident on the sphere, with fields (expanded in spherical harmonics):

$$\begin{aligned} \mathbf{E}_{inc} &= \sum_{n=1}^{\infty} E_n \left(\mathbf{M}^{(1)}_{o1n} - i\mathbf{N}^{(1)}_{e1n}\right) \\ \mathbf{H}_{inc} &= -\frac{k_0}{\omega} \sum_{n=1}^{\infty} E_n \left(\mathbf{M}^{(1)}_{o1n} + i\mathbf{N}^{(1)}_{e1n}\right) \end{aligned} \tag{K.1}$$

where $E_n = i^n E_0(2n+1)/(n(n+1))$.

In order to expand the scattered and internal electromagnetic fields of an incident wave on the sphere, we apply the condition that at the surface of the sphere the electric and magnetic fields obey:

$$(\mathbf{E}_{inc} + \mathbf{E}_{scat} - \mathbf{E}_{int}) \times \hat{\mathbf{e}}_{\mathbf{r}} = (\mathbf{H}_{inc} + \mathbf{H}_{scat} - \mathbf{H}_{int}) \times \hat{\mathbf{e}}_{\mathbf{r}} = 0 \tag{K.2}$$

Also, note that both the scattered and internal fields' expansion is dictated by the expansion of the incident field, which means that the coefficients $B_{emn} = A_{omn} = 0$ and that B_{omn}, A_{emn} vanish for all values of m, except for $m = 1$.

The vector harmonics inside the sphere are descried by $j_n(k_{int}\mathbf{r})$ Bessel function, since the field at the origin of the sphere is finite. Therefore, the electric and magnetic fields inside a dielectric sphere (with $\mu = 1$) are expanded to spherical harmonics as:

$$\begin{aligned} \mathbf{E}_{int} &= \sum_{n=1}^{\infty} E_n \left(c_n \mathbf{M}^{(1)}_{o1n} - i d_n \mathbf{N}^{(1)}_{e1n} \right) \\ \mathbf{H}_{int} &= -\frac{k_{int}}{\omega} \sum_{n=1}^{\infty} E_n \left(d_n \mathbf{M}^{(1)}_{o1n} + i c_n \mathbf{N}^{(1)}_{e1n} \right) \end{aligned} \tag{K.3}$$

where c_n and d_n are internal coefficients (i.e. coefficients dominating the fields inside the sphere) and k_{int} the wavevector of the wave inside the sphere.

However, outside of the sphere, the scattered fields are well-described by both j_n and y_n Bessel functions. Therefore, the Hankel functions $h_n^{(1)}$ and $h_n^{(2)}$ are used for the spherical harmonics (i.e. $h_n^{(1)}(x) = j_n(x) + i y_n(x)$ and $h_n^{(2)}(x) = j_n(x) - i y_n(x)$), and therefore a superscript of (3) is used. Therefore, the scattered fields are expanded to spherical harmonics as:

$$\begin{aligned} \mathbf{E}_{scat} &= \sum_{n=1}^{\infty} E_n \left(-b_n \mathbf{M}^{(3)}_{o1n} + i a_n \mathbf{N}^{(3)}_{e1n} \right) \\ \mathbf{H}_{scat} &= \frac{k_0}{\omega} \sum_{n=1}^{\infty} E_n \left(a_n \mathbf{M}^{(3)}_{o1n} + i b_n \mathbf{N}^{(3)}_{e1n} \right) \end{aligned} \tag{K.4}$$

where a_n and b_n are scattering coefficients (i.e. coefficients dominating the fields scattered from the sphere), and the superscript (3) on the spherical harmonic vectors denotes that the Hankel function is used for ψ

The scattering coefficients are given by:

$$a_n = \frac{N^2 j_n(N\rho)[\rho j_n(\rho)]' - j_n(\rho)[N\rho j_n(N\rho)]'}{N^2 j_n(N\rho)[\rho h_n^{(1)}(\rho)]' - h_n^{(1)}(\rho)[N\rho j_n(N\rho)]'} \tag{K.5}$$

$$b_n = \frac{j_n(N\rho)[\rho j_n(\rho)]' - j_n(\rho)[N\rho j_n(N\rho)]'}{j_n(N\rho)[\rho h_n^{(1)}(\rho)]' - h_n^{(1)}(\rho)[N\rho j_n(N\rho)]'} \tag{K.6}$$

The internal coefficients are given by:

$$c_n = \frac{j_n(\rho)[\rho h_n^{(1)}(\rho)]' - h_n^{(1)}(\rho)[\rho j_n(\rho)]'}{j_n(N\rho)[\rho h_n^{(1)}(\rho)]' - h_n^{(1)}(\rho)[N\rho j_n(N\rho)]'} \tag{K.7}$$

$$d_n = \frac{N j_n(\rho)[\rho h_n^{(1)}(\rho)]' - N h_n^{(1)}(\rho)[\rho j_n(\rho)]'}{j_n(N\rho)[\rho h_n^{(1)}(\rho)]' - h_n^{(1)}(\rho)[N\rho j_n(N\rho)]'} \tag{K.8}$$

where N is the refracting index of the material the sphere is made from and is given by $N = \sqrt{\varepsilon}$, ρ is the size parameters given by $\rho = kR$, k is the wavevector in vacuum and R the radius of the sphere and finally $[.]'$ denotes the derivative of the function in square brackets with respect to ρ. Note that the denominators of a_n and d_n are equal, as those of b_n and c_n.